Institute for Circuit Theory and Signal Processing
Technical University of Munich

Signal Processing for Optical Communication Systems

Israa H. Slim

Vollständiger Abdruck der von der Fakultät für Elektrotechnik und Informationstechnik der Technischen Universität München zur Erlangung des akademischen Grades eines

Doktor-Ingenieurs

genehmigten Dissertation.

Vorsitzender: Prof. Dr.-Ing. Eckehard Steinbach
Prüfer der Dissertation:

1. Prof. Dr. techn. Josef A. Nossek
2. Prof. Dr.-Ing. Norbert Hanik

Die Dissertation wurde am 19.04.2017 bei der Technischen Universität München eingereicht und durch die Fakultät für Elektrotechnik und Informationstechnik am 17.08.2017 angenommen.

Contents

1. Introduction

1.1 Motivation

Optical-fiber communication systems have revolutionized the telecommunications industry and they continue to be vital in enabling the proliferating use of the Internet. To meet their capacity requirements, tremendous telecommunication services intensely rely on optical-fiber communication systems. Optical links provide enormous bandwidth; and the optical fiber is the only medium which can meet modern society's needs for transporting massive amounts of data over long distances. No other known medium can support the massive demands for data-rate, reliability and energy efficiency.

The data traffic transported over the telecommunication networks has grown exponentially in the past. A foreseeable increased usage of data transport in combination with new types of applications will most likely stimulate an interest in more throughput [1]. Applications range from global high-capacity networks, which constitute the backbone of the Internet, to the massively parallel interconnects that provide data connectivity inside data-centers and supercomputers. Commercially deployed wavelength division multiplexing (WDM) optical-fiber systems in 2010 supported approximately 100 wavelength channels for an approximate 10 Tbit/s of aggregate per-fiber WDM capacity. With a 40% traffic growth rate, the need for commercial systems supporting per-fiber capacities of 1 Pbit/s around 2024 should be expected [1]. This demand for higher capacities drives the evolution of fiber-optic communication systems.

One of the most promising approaches to cope with the ever increasing demand for capacity is by increasing the spectral efficiency of WDM systems. This is procured through employing high order modulation schemes and through densely packing the wavelength channels. Nevertheless, this should be accomplished without sacrificing reach, performance, power consumption or cost in long-haul optical communication systems. Coherent detection using digital signal processing (DSP) has been and still proves to be a key enabling technology in optical communication systems to engineer such opposing yet indispensable objectives. It is once again considered a feasible detection method particularly beneficial for long-haul optical communication systems with high data-rates. Many of the problems hindering the use of coherent detection have been eliminated with the advancements of analog-to-digital converters (ADCs) speeds [2]. Most notably, DSP alleviates the need for hardware phase-locking and polarization tracking, which can now be achieved in the digital domain. Only coherent detection as compared to the other two detection schemes, namely non-coherent and differentially-coherent, enables the full recovery of the optical field at the receiver. This feature opens up the possibility of sending high order modulation schemes by modulating either the amplitude, the phase or the frequency of an optical carrier. Moreover, the conversion of the optical signal to the electrical digital domain enables the use of powerful DSP

algorithms to mitigate linear optical impairments in the electrical domain as powerful as traditional optical compensation techniques. Currently, optical transponders supporting 112 Gbits/s data rates per wavelength channel are feasible employing coherent transmission technology using two polarizations, a quadrature phase shift keying (QPSK) modulation format and DSP to equalize for optical-fiber impairments with a baud-rate as low as 28 GBaud. At the transmitter side of a coherent optical system DSP can be also employed in conjunction with digital-to-analog converters (DACs) in order to digitally filter the signal of each wavelength channel. Pulse shaping controls the spectrum of the signals to be modulated and sent over an optical fiber. This allows to densely pack the wavelength channels in WDM systems as a way to efficiently use the available optical bandwidth. Densely packing of the channels thus enhances the spectral efficiency of the system and provides aggregate capacities of Tbit/s. It can be concluded that the degrees of freedom that the DSP provides introduce a myriad of research options and possibilities for future long-haul WDM transmission systems.

Operating at data rates of 112 Gbit/s per wavelength channel and densely packing the separate wavelength channels at baud-rate spacing limit the overall performance of long-haul coherent optical communication systems due to the induced interference. Linear impairments like chromatic dispersion (CD) induce intersymbol interference (ISI) at such high data rates. Dense packing of the wavelength channels at baud-rate induces interchannel interference (ICI). For a robust system both types of interference should be compensated. Nonetheless, the techniques for interference compensation should keep the complexity for filtering minimal. Therefore, the first objective of this thesis is to develop novel DSP techniques at the receiver with cost-effective methods for CD equalization to mitigate ISI. The developed techniques improve the performance of the system drastically with the same or a marginal increase in complexity as compared to the benchmark design. The second objective is to develop DSP methods at the receiver to minimize or compensate ICI in baud-rate channel spaced WDM systems while using DSP for pulse shaping at the transmitter. The different developed techniques give a compromise between performance and complexity.

1.2 Overview and Contributions

In accordance to the main objectives targeted for the thesis, we organize it in three main parts:

Chapter 2: Optical Transmission

In this chapter, we give an overview of long-haul optical transmission systems employing wavelength division multiplexing (WDM) techniques. The setup introduced is widely used in experiments and in commercially available products enabling high data-rates per wavelength channel. We present polarization-division multiplex quadrature amplitude modulation (PDM-QAM) transmitter architecture necessary for the generation of different QAM signals. For the receiver we depict an architecture necessary for coherent detection systems.
As part of long-haul optical transmission systems, we present single-mode fibers (SMFs) showing its physical structure and characteristics. In these fibers, the most important linear deterministic impairments that arise are also reviewed. Specifically, we focus on chromatic dispersion (CD) for which we provide the corresponding mathematical model as an optical channel. We also revisit the different dominant sources of noise in long-haul transmission systems.

Chapter 3: Chromatic Dispersion Compensation in Long-haul Transmission Systems

In this chapter, we mainly focus on the compensation of CD in long-haul transmission systems carrying data rates of 112 Gbit/s per wavelength channel. The main obstacle for implementation at a such high data rate is the complexity of the filtering algorithms in terms of multiplications. This is directly related to power consumption and the availability of DSP circuits that offer very high gate density and very high processing speeds.
Digital signal processing with coherent detection schemes, richer constellations, and fast analog-to-digital converters (ADCs) plays an important role in CD compensation. Digital CD equalization can be either done in time-domain (TD) or in the frequency-domain (FD). We show in this chapter that FD equalization becomes more efficient than TD equalization with respect to implementation complexity over a wide range of CD values. Namely, the overlap-and-save (OLS) and overlap-and-add (OLA) are the most efficient FD methods for CD equalization.
The OLS method with an overlap factor of 50% (OLS-50%) is considered as the benchmark for FD CD compensation. Starting from this, we show how this method can be implemented as a non-maximally decimated discrete Fourier transform (DFT) filter bank (FB) with trivial prototype filters i.e. filters with rectangular impulse response. The equalization using such a structure is done per sub-band paving the way for more sophisticated sub-band processing. Based on this observation and exploiting the nature of the CD channel, we design a delayed single-tap filter in each sub-band that equalizes not only the phase of the CD channel but also its group delay. Furthermore, we derive a delayed dual-tap equalizer from the delayed single-tap equalizer that aims at smoothing the group delay function of the latter equalizer. We show that both designs provide improved equalization abilities as compared to the benchmark with the same complexity in terms of multiplications. Just additional delay elements are required for the delayed single-tap equalizer and the delayed dual-tap equalizer requires besides this some adders and/or subtractors. Finally, we derive the coefficients of the FD equalizer that takes into account the response of the transmitter and receiver besides the propagating CD channel. The equalization abilities for low and moderate CD value improve for this design. All the proposed equalization methods are implemented with a fractionally spaced equalizer operating at two samples per symbol.

Chapter 4: Baud-rate Channel Spacing in Wavelength Division Multiplexing Systems

In this chapter, we present three approaches to either minimize or compensate interchannel interference (ICI). The latter arises due to considerable overlap between the spectra of the adjacent wavelength channels. The overlap occurs because we consider that the channels are spaced at the baud-rate as a way to efficiently use the available optical bandwidth.
In the first approach for ICI equalization, offset-QAM (OQAM) is used as modulation format implemented through staggering and destaggering, in the transmitter and receiver, respectively, of the real and imaginary parts of the signal. Ideally, there is no ICI in the system and the equalizer in each wavelength channel reduces to a single-channel equalizer. In the second technique where standard QAM (SQAM) is used as modulation format, we design an ICI equalizer in each wavelength channel which treats ICI in the same way as the additive noise for the regularization term of the minimum mean squared equalizer. The third approach for ICI cancellation is based on utilizing SQAM as modulation scheme and ICI is canceled at the receiver with the help of digital signal processing. It is based on a super-receiver architecture which builds on conventional Nyquist WDM systems. For such an architecture each received signal of the neighboring wavelength chan-

nel is fed into the receiver of the wavelength channel of interest for multi-receiver equalization. We compare the different developed techniques for ICI equalization or cancellation in terms of performance, complexity and system requirements.
For all the different approaches for ICI equalization, a digital root-raised-cosine (RRC) pulse shaper characterized with a non-zero roll-off factor is implemented in the transmitter and in the receiver. This choice is justified by the fact that the resulting overall RC response satisfies the first Nyquist criterion for intersymbol interference (ISI)-free transmission.

1.3 Notation and Definition

We present here the notations and definitions which we will use frequently throughout the thesis.

Scalars are expressed in italic font. Vectors are written as lower case letters in bold face. Matrices are written as upper case letters in bold face. The operators $(\bullet)^*$, $(\bullet)^{\mathrm{T}}$, and $(\bullet)^{\mathrm{H}}$ denote the complex conjugate, transposition and Hermitian operators, respectively, where the Hermitian operator represents a complex conjugate transposition. The symbol $*$ denotes convolution, unless it appears as a superscript in which it represents complex conjugation. The expectation is denoted as $\mathrm{E}[\bullet]$.

The real and imaginary part of a signal, an impulse response or any matrix in the time domain are written as $\mathrm{Re}[(\bullet)] = (\bullet)^{\mathrm{R}}$ and $\mathrm{Im}[(\bullet)] = (\bullet)^{\mathrm{I}}$, i.e.

$$(\bullet) = (\bullet)^{\mathrm{R}} + j(\bullet)^{\mathrm{I}}, \quad \text{with } j = \sqrt{-1}. \tag{1.1}$$

The conjugate of a complex argument is defined as

$$(\bullet)^* = (\bullet)^{\mathrm{R}} - j(\bullet)^{\mathrm{I}}. \tag{1.2}$$

The z-domain representation of a signal $y[n]$ is denoted as $Y(z) = \mathcal{Z}\{y[n]\}$. The *frequency domain* argument z corresponds wherever it appears to technical angular frequencies ω according to $z = \exp(j\omega T)$. This means that z is associated with the sampling time interval T.

The z-transform representation of an impulse response $h[n]$ of a finite impulse response (FIR) filter with P coefficients $h_p, p = 0, \cdots, P-1$, is given by

$$h[n] = \sum_{p=0}^{P-1} h_p \delta[n-p] \longleftrightarrow H(z) = \sum_{p=0}^{P-1} h_p z^{-p} = \sum_{p=0}^{P-1} h[p] z^{-p} \tag{1.3}$$

where $\delta[i]$ is unity for $i = 0$ and is zero else. Therefore, the transfer function $H(z)$ can be equally expressed by the filter coefficients h_p or the impulse response of the filter $h[n]$. Applying the linear time invariant (LTI) filter $h[n]$ to a sequence $x[n]$ corresponds to a convolution between $h[n]$ and $x[n]$

$$y[n] = h[n] * x[n] = \sum_{p=0}^{P-1} h_p x[n-p]. \tag{1.4}$$

The *discrete Fourier transform* (DFT) matrix of dimension $N \times N$ is defined as

$$\boldsymbol{W}_N = \frac{1}{\sqrt{N}} [W_N^{kn}]_{k+1,n+1} \tag{1.5}$$

with $W_N = \exp(-j2\pi/N)$, $k = 0, 1, \cdots, N-1$ and $n = 0, 1, \cdots, N-1$. Consequently, the conjugate complex and transposed matrix

$$\boldsymbol{W}_N^{\mathrm{H}} = \boldsymbol{W}_N^{*} = \boldsymbol{W}_N^{-1} = \frac{1}{\sqrt{N}}[W_N^{-kn}]_{k+1,n+1} \tag{1.6}$$

is the *inverse discrete Fourier transform* (IDFT) matrix.

The definition of the N-point DFT of a sequence $x[n], n = 0, 1, \cdots, N-1$ and its inverse can be expressed by (1.5) and (1.6), respectively, according to

$$X[k] = \sum_{n=0}^{N-1} x[n] W_N^{kn} = \sqrt{N}\boldsymbol{e}_k^{\mathrm{T}} \boldsymbol{W}_N \boldsymbol{x} \tag{1.7}$$

and

$$x[n] = \sum_{n=0}^{N-1} X[k] W_N^{-nk} = \frac{1}{\sqrt{N}}\boldsymbol{e}_n^{\mathrm{T}} \boldsymbol{W}_N^{*} \boldsymbol{X}, \tag{1.8}$$

with $\boldsymbol{x} = [x[0], x[1], \cdots, x[N-1]]^{\mathrm{T}}$ and $\boldsymbol{X} = [X[0], X[1], \cdots, X[N-1]]^{\mathrm{T}}$ and the unit-vectors $\boldsymbol{e}_k$ and $\boldsymbol{e}_n$.

2. Optical Transmission

In this chapter, we present an overview of long-haul optical transmission systems which transport the largest amount of data over the longest distances. To meet the increasing demand for high capacities and data-rates, these systems use wavelength division multiplexing (WDM) technology, employ polarization-division multiplex quadrature amplitude modulation (PDM-QAM) at the transmitter and coherent reception in the receiver. In particular, we illustrate the overall structure of the transmitter and the receiver showing the necessary components in both entities and their functionality. As part of the optical transmission systems, the optical fiber link contributes to the overall performance due to its characteristics. For long-haul transmissions, single-mode fibers (SMFs) are employed. We present not only the physical structure and characteristics of such fibers but also the most important linear deterministic impairments induced in them. We derive also the corresponding mathematical model of the optical channel relevant to this thesis.

2.1 Introduction

The optical transmission links in the backbone of the telecommunication network can be classified into access, metro or long-haul networks depending on their *regenerator-free* transmission distance. A transmission link in (ultra) long-haul core network transports the largest amount of data over the longest distances ($>$1000 km) for trans-national, trans-continental and trans-oceanic communication. To allow a manifold increase in the data-rates of long-haul optical transmission systems, WDM technology is deployed. By multiplexing a number of wavelength channels of lower data-rates onto a single fiber, a WDM transmission link transports large amount of data traffic.

Figure 2.1 shows the typical layout of a long-haul optical transmission system. The main role of the optical transmitter of each channel wavelength is to modulate the electrical data sequence onto an optical carrier generated by an optical source. The separate wavelength channels are then multiplexed together using a wavelength multiplexer and sent over the same fiber link. At the receiver side of the transmission link, the WDM channels are demultiplexed using demultiplexers. Each of the de-multiplexed channels is then fed into an optical receiver, which converts the signal back to the electrical domain for further processing. The transmission link itself consists of cascaded fiber spans with optical amplifiers (OAs) in-between. The OAs amplify the weak input signal from the previous span and launch it again into the next span. This allows long-haul transmission while maintaining a sufficiently high optical signal-to-noise ratio (OSNR) at the output of the fiber link.

To cope with the ever growing demand for increasing the aggregate capacity for example from telecommunication transports [3], new technologies in WDM long-haul transmission systems need to be deployed. This is attained through increasing spectral efficiency (SE) without resorting to ex-

panding the bandwidth of optical amplifiers. The bit rate and wavelength channel spacing of a transmission system is often expressed in terms of the SE, which is the transmitted capacity per unit bandwidth. One way to increase SE is to increase the bit rate per wavelength channel by using advanced modulation formats. The other way is to pack WDM wavelength channels closer together. For both ways, coherent detection is ideally suited. The rebirth of coherent systems which occurred around the turn of the century was remarked by the need to increase SE in long-haul transmission systems. Originally, the rise of coherent systems occurred in the seventies as means to increase the repeater spacing which was typically 60-70 km. The optical signal had to be regenerated periodically using electronic repeaters due to fiber losses. An increased repeater spacing of 10-20 km was achieved by using coherently-detected systems because their use required less power at the receiver. Compared to direct-detection systems [4–6] available at that time, coherent systems showed their improved receiver sensitivity approaching the shot noise limit [6–8] which have been extensively also demonstrated [6]. At that time the main drawback of coherent systems was the complexity of the receiver. For example, polarization-matching is needed between the received signal and local oscillator (LO) laser [9]. Additionally, coherent receivers that used homodyne optical front-ends where the optical signal is down-mixed directly to baseband needed accurate phase tracking between the LO and signal carrier [7, 9]. Early homodyne receivers used optical phase-locked loops (OPLLs), which were technically demanding to implement. The invention and rapid commercialization of erbium-doped fiber amplifiers (EDFAs) [10] for optical amplification led to the demise of coherent systems [9]. This is because EDFAs provided a cheaper and simpler way to increase repeater spacing. Additionally, EDFA systems are limited by amplified spontaneous emission (ASE) instead of shot noise. Therefore, coherent receivers being limited by shot-noise became less interesting [7].

One way to increase SE is to increase the bit rate per wavelength channel by using advanced modulation formats. They are generated based on amplitude and phase modulation such as differential quadrature phase shift keying ((D)QPSK) and quadrature amplitude modulation (QAM) with polarization division multiplexing (PDM). PDM doubles the number of information bits by transmitting independent information in each of the two orthogonal polarizations of an optical fiber. Since coherent detection techniques enables the detection of both the amplitude and the phase of the received optical signal, sending information by modulating either the amplitude, or the phase or the frequency of an optical carrier becomes feasible. The two other available detection techniques, namely direct detection and differential detection, do not provide this possibility. Direct detection does not allow phase or frequency modulation, as all phase information of the signal is lost. Differential detection is a form of coherent detection also known as self-coherent or pseudo-coherent detection. It is generally used with simple receiver signal processing. Although differential detection enables greater receiver sensitivity than direct detection, it is still limited by linear distortions such as chromatic dispersion (CD) and polarization-mode dispersion (PMD), and may not be used easily with polarization multiplexing. A further problem with differential detection is that the signal is itself noisy, so the receiver sensitivity is reduced considerably. Since with a coherent receiver all four dimensions of the optical field (amplitude and phase in two orthogonal polarizations) can be detected, digital signal processing (DSP) may be utilized to mitigate linear optical impairments such as CD and PMD in the digital electrical domain. Mitigation of the impairments in the aforementioned domain is as powerful as traditional optical compensation techniques to the extent that only non-deterministic effects degrade the performance. The advances in integrated circuits and DSP technologies over the years had improved and could now operate at speeds high enough to process the baseband electrical signal. They have made it possible to build

coherent receivers with relatively low optical complexity [11]. Problems such as polarization- and carrier phase-compensation, which were difficult to solve previously, could now be solved digitally [7, 12]. Independent of the optical channel, the choice of the optical front-end at the receiver (direct, differential or coherent detection) systematically defines the system properties such as the noise statistics, being linear or nonlinear system and loosing phase information of the optical signal or not. Coherent detection systems are predominantly linear with Gaussian noise characteristics and full transfer of all information from the optical domain into the electrical domain is possible.

The other way to increase SE in WDM long-haul transmission systems is to closely pack the wavelength channels. The channel spacing could be less than, greater than or equal to the the symbol-rate (baud-rate). Packing the wavelength channels at channel spacing less than the symbol-rate achieves the greatest SE as compared to the other two channel spacing techniques. This concept which is referred to as *faster-than-Nyquist* (FTN) signaling was introduced by Mazo [13]. The main motivation with FTN signaling was the potential increase of SE by fitting more signals than the orthogonality principle allows in a specific frequency range. It is a non-orthogonal signaling method where inter-channel interference (ICI) arises. Inter-symbol interference (ISI) is inherit in the structure because the symbols overlap in both the time-domain (TD) and in the frequency-domain (FD). Notwithstanding, the detection implementation for such systems relies on very complex techniques. This is because the transmitted symbols can not be detected independently making the complexity at the receiver high [14]. For a channel spacing greater than the symbol-rate, neighboring wavelength channels do not considerably overlap. This means that the power of ICI is low. However, the main drawback of such a technique is the loss in SE. Channel packing at exactly the symbol-rate gives rise to considerable ICI due to spectra overlap. However, there exist classes of orthogonal-signaling systems where despite symbol-rate spacing, ICI is ideally not present in the system and the reconstruction of the transmitted data symbols at the receiver side becomes simple. The first system is *orthogonal frequency division multiplexing* (OFDM) [15–33]. In OFDM, each wavelength channel is shaped in the FD with a sinc function. Neighboring channels cross ideally exactly at the symbol-rate leading to zero ICI. Simple equalization of the transmitting channel is done at the receiver in the FD through a single-tap equalizer because a cyclic prefix (CP) is inserted in each transmitted block. However, the insertion CP leads to a loss in SE. Another major drawback of OFDM is the high *peak-to-average power ratio* (PAPR) values incurred which give rise to non-linearities in the optical channel. The second technology to generate symbol-rate spaced channels is the Nyquist WDM approach [34–47]. It is complementary to OFDM where each channel has an ideal rectangular shaped spectrum in FD with bandwidth equal to the symbol-rate obtained by employing pulse shaping filters in the transmitter. However, practical issues are raised by the requirement of perfect rectangular spectral shaping which is difficult to realize. This leads to both ISI and ICI. One challenge in Nyquist WDM systems with symbol-rate spacing of the channels is to simultaneously minimize ISI and ICI impairments which can be achieved by adopting transmitter-side and receiver-side approaches. The third technology to generate symbol-rate spaced channels is by employing offset QAM (OQAM) as a modulation scheme for Nyquist WDM systems [48–53]. In OQAM-WDM [54, 55], orthogonality between the wavelength channels is attained by alternately staggering the real and the imaginary parts of the signal of the even and the odd wavelength channels in the transmitter. At the receiver side, destaggering of the real and the imaginary parts of the signal in each wavelength channel is done. Theoretically, OQAM Nyquist systems are ICI-free systems.

This chapter deals specifically with the design of coherent long-haul WDM transmission systems. It is organized as follows. In Section 2.2, we describe a transmitter employing WDM PDM-

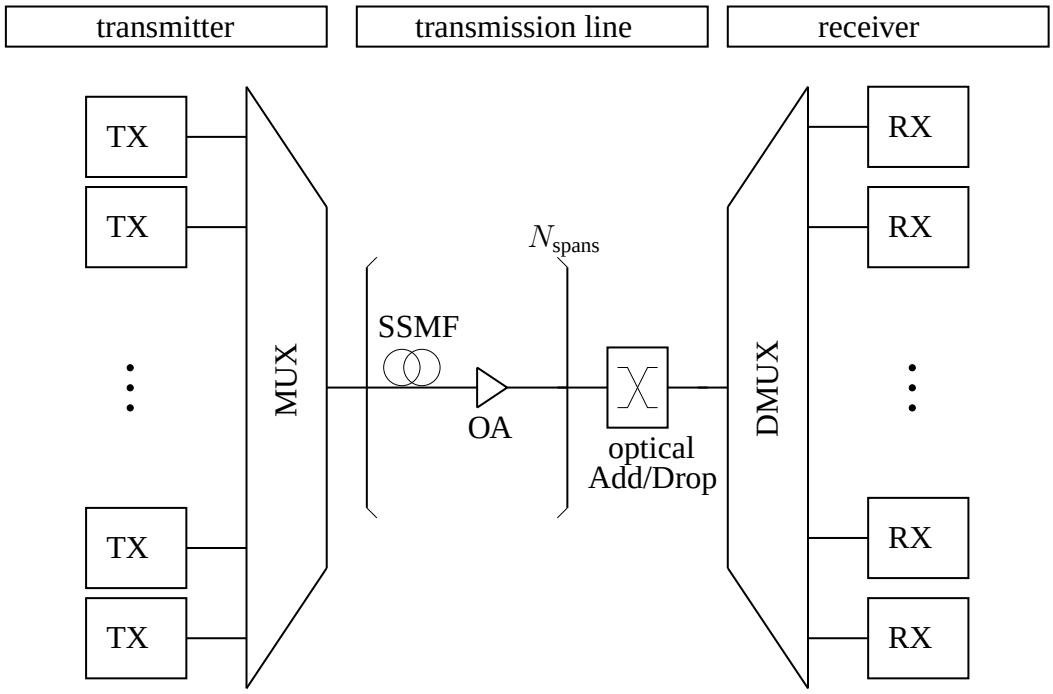

Fig. 2.1. Generic WDM Long-haul Optical Communication System

QAM technology and the different wavelength channel packing techniques. In Section 2.3, we explain the concept of coherent reception relevant to this thesis and we present accordingly a coherent receiver structure. The setup introduced is widely used in experiments and in commercially available products for WDM long-haul transmission systems with high data-rates per wavelength channel. In Section 2.4, we present the different dominant sources of noise in long-haul transmission systems. In Sections 2.5 and 2.6 we describe, respectively, the single-mode fiber usually employed in long-haul transmissions, and give the mathematical model of the CD channel relevant to this thesis.

2.2 WDM PDM-QAM Optical Transmitter

The main role of an optical transmitter is to convert the electrical signal into an optical form and launch the resulting optical signal into the optical fiber. The building blocks of an optical transmitter are optical source, optical modulators, digital-to-analog converters (DACs), DSP module, and a channel multiplexer.

The block diagram of the transmitter is shown in Fig. 2.2. In each wavelength channel, the unmodulated optical pulses coming from the same optical source can be optionally pulse-carved through an optical modulator before they are split into the two orthogonal (vertical and horizontal) linear polarizations. For generating polarization-division multiplex (also named as dual-polarization (DP) or polarization multiplexing (PolMUX)) QAM modulation formats, typically two inphase-quadrature (IQ) modulators are used in parallel, each modulating the (optionally modulated) pulses generated by the optical source in each orthogonal polarization as depicted in the block diagram in Fig. 2.2. In each polarization, two digital sources generate binary information. In the horizontal polarization, the bit sequences $x_{\text{H}}^{\text{R}}[n]$ and $x_{\text{H}}^{\text{I}}[n] \in \{0,1\}$ are generated. In the vertical polarization, the bit sequences $y_{\text{V}}^{\text{R}}[n]$ and $y_{\text{V}}^{\text{I}}[n] \in \{0,1\}$ are generated. A symbol, which

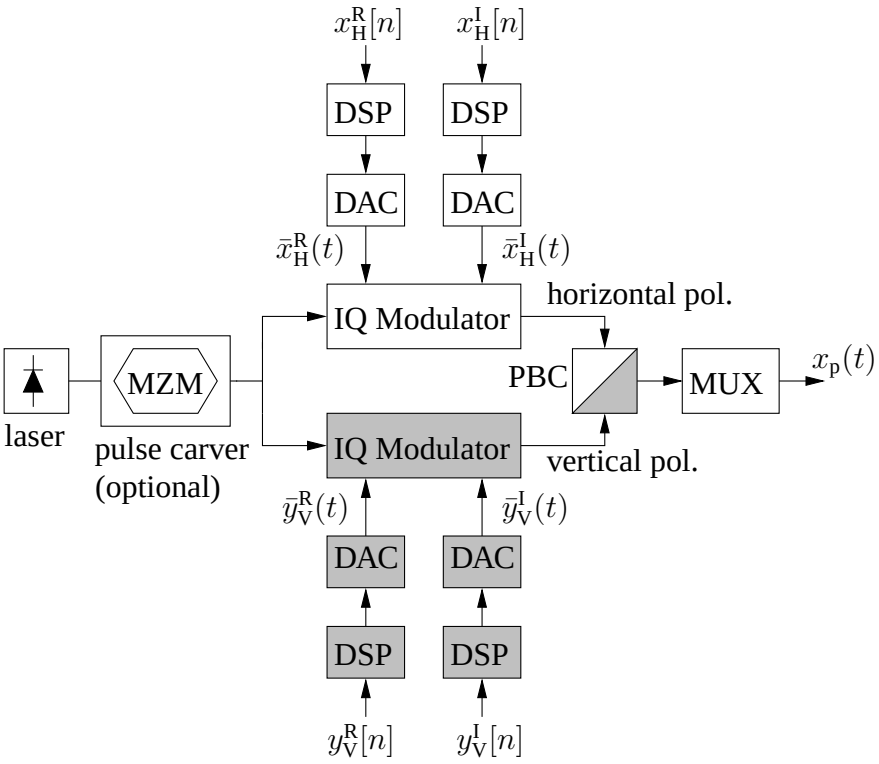

Fig. 2.2. Transmitter for Polarization Multiplexing

is formed of two bits, has a duration of T_s in seconds and accordingly a symbol-rate of $B = 1/T_s$ also called the *baud rate*. These electrical signals could be pulse shaped in the digital domain to meet some requirements for example ISI-free pulse transmission or pre-distortion of the DAC and optical front-end. The continuous-time representation of the electrical signals is denoted, respectively, by $\bar{x}_{\mathrm{H}}^{\mathrm{R}}(t)$, $\bar{x}_{\mathrm{H}}^{\mathrm{I}}(t)$, $\bar{y}_{\mathrm{V}}^{\mathrm{R}}(t)$ and $\bar{y}_{\mathrm{V}}^{\mathrm{I}}(t)$. Therefore, in each wavelength channel the continuous-time electrical signals of both polarizations are first modulated by the (optionally pulse-curved) optical pulses and then combined together with a polarization beam combiner (PBC). The signal transmitted over the fiber is generated by multiplexing the independently generated optically modulated PDM-QAM signal in each wavelength channel.

This section presents optical sources (Section 2.2.1), the most common optical modulation principles (Section 2.2.2), optical pulse carving (Section 2.2.3), electrical pulse forming (Section 2.2.4), WDM schemes (Section 2.2.5) and multiplexers (Section 2.2.6).

2.2.1 Optical Source: Laser

Most of the optical transmission systems based on single-mode fiber operating at data rates greater than 5 Gbit/s use semiconductor lasers (*Light Amplification by Stimulated Emission of Radiation*) as light sources. Light emission can occur through two fundamental processes known as *spontaneous* and *stimulated emission*. The later is the dominant process in lasers. With stimulated emission, a narrow beam of coherent light is generated and used as the optical carrier.

The quality of a carrier light wave and detection highly depends on the quality of the lasers. Ideally, the carrier is a light-wave with constant amplitude, frequency and phase, that translates into zero laser spectral line-width. Unfortunately, the perfect carrier cannot be generated in practice. The process of spontaneous emission takes place along with stimulated emission, causing fluctuations in the intensity and the phase of the signal, named respectively, amplitude and laser phase

noise. This subsequently results in broadening the spectral width of the signal. The requirements on the laser linewidth depend on the data rate and the modulation format used to transmit data. Nowadays, with the modern technologies like single-mode distributed feedback lasers (DFB) and external cavity lasers (ECL), carrier signal with linewidths in the kHz range can be generated [56]. Therefore, phase noise is not of concern for the system investigated in this thesis.

2.2.2 Optical Modulation

Optical modulation is the process by which data, conveyed in an electrical signal, is converted into an optical signal with the same information. There are basically two techniques to encode the information on the optical carrier; these are namely direct modulation or external modulation. In direct modulation, the output of the laser is directly modulated by varying the injection electrical current. External modulation is achieved by biasing the laser with a constant injection electrical current and an external modulator is used to convert the electrical signal into an optical modulated signal with a certain modulation format. Although direct modulation simplifies the transmitter and is cost-effective, the frequency chirp imposed by current modulation limits the system performance at data rates larger than 5 Gbit/s. Instead, external modulators are used to modulate the continuous wave (CW) output of a laser.

Two types of external modulators are commonly used in optical communications systems which are the electro-absorption modulators (EAMs) and electro-optic modulators (EOMs). EOMs have been preferred over EAMs due to the advantages that the electro-optic materials offer such as linear response characteristic, high extinction ratio, and in particular, the possibility to generate chirp-free signals.

There exist three external optical modulator structures, of fundamental importance for today's optical high speed transmitters, which employ one or more EOMs. These are phase modulator (PM), Mach-Zehnder modulator (MZM), and IQ modulator.

2.2.2.1 Phase Modulator

A PM can be implemented as an integrated optical device by embedding an optical waveguide e.g. Ti:$LiNbO_3$ in an electro-optical substrate e.g. $LiNbO_3$. The electrical field is applied to the waveguide using electrodes causing a change in the effective refractive index. This results in an in-phase modulation of the incoming optical signal. A PM is shown in Fig. 2.3. According to the Pockels effect, the phase shift experienced by the light in each branch due to the change in refractive index varies linearly with the applied voltage $v(t)$. It can be expressed by $\Delta\varphi = \pi\frac{v(t)}{V_\pi}$ where V_π denotes the drive voltage necessary to produce a phase shift of π between the two branches and the constant optical phase shift of the modulator was neglected. Typical values for V_π range between 3 to 6 Volts.

2.2.2.2 Mach-Zehnder Modulator

The most widely used device for external modulation is the MZM which employs PMs to modulate the intensity of an optical carrier by arranging them in the interferometric structure depicted in Fig. 2.4.

In a MZM, the CW light of the laser $E_{\text{in}}(t)$ is split equally (ideally) into two branches. The refractive index of the waveguide material is changed by means of the externally applied voltages $v_1(t)$ and $v_2(t)$ in each branch, respectively, therefore, producing a phase shift in the optical field.

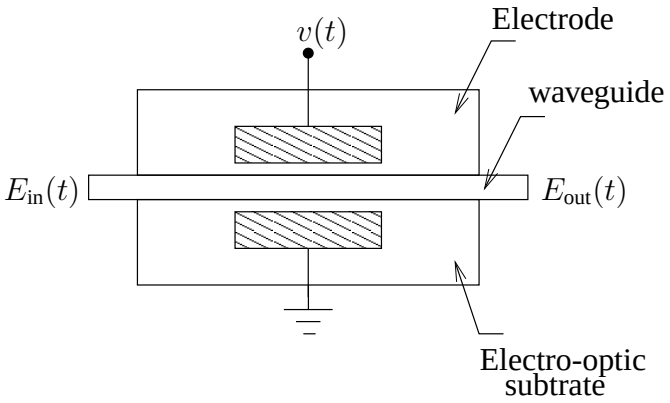

Fig. 2.3. Phase Modulator

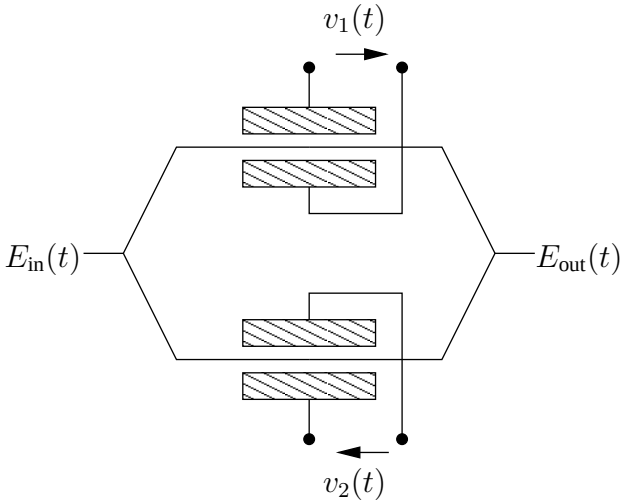

Fig. 2.4. Integrated optical Mach-Zehnder modulator

Depending on the applied electrical voltages, the interference which varies from destructive to constructive produces intensity modulation. If no voltage is applied, the optical field in the two branches experiences equal phase shift and interferes constructively. If different voltages are applied to the arms of the MZM, constructive interference no longer occurs, and the intensity of the light at the output of the MZM is reduced proportionally to the phase difference between the two arms. When the phase difference between the arms is π, destructive interference occurs and no light is transmitted.

For the case $v_1(t) = v_2(t) = v(t)$ and $V_{\pi 1} = V_{\pi 2} = V_\pi$, pure phase modulation is achieved and the MZM operates in the push-push mode. In case $v_1(t) = -v_2(t) = \frac{1}{2}v(t)$ and $V_{\pi 1} = V_{\pi 2} = V_\pi$ the two branches have opposite phase shift and chirp-free amplitude modulation is obtained. In this case, the MZM operates in the push-pull mode with the following time response

$$\frac{E_{\text{out}}(t)}{E_{\text{in}}(t)} = \cos\left(\frac{\pi}{2V_\pi}v(t)\right). \tag{2.1}$$

2.2.2.3 In-phase and Quadrature Modulator

Arbitrary complex optical waveforms can be generated using an optical IQ modulator. An IQ modulator is composed of a PM and two MZMs, which is commercially available in an integrated

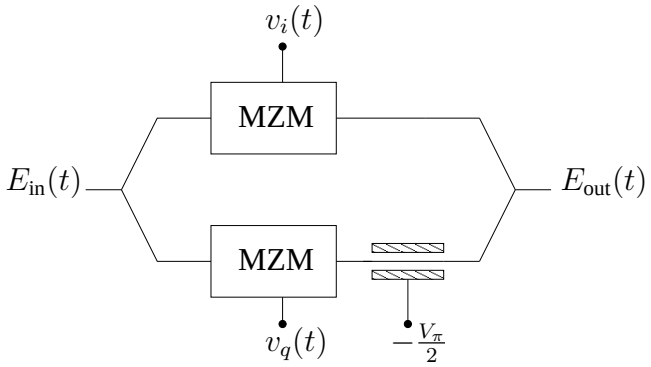

Fig. 2.5. Integrated optical IQ Modulator

form schematically shown in Fig. 2.5. The incoming CW light of the laser $E_{\text{in}}(t)$ is equally split into two arms namely the in-phase and the quadrature arm. A field amplitude modulation can be performed by operating the MZM in the push-pull mode in both arms which is used to produce the in-phase and quadrature components of the signal, respectively. Furthermore, a relative phase shift of $\pi/2$ is adapted in one arm by a PM. With this method any constellation point can be generated in the complex IQ-plane. The response of an optical IQ modulator can be expressed by

$$\frac{E_{\text{out}}(t)}{E_{\text{in}}(t)} = \frac{1}{2}\left(\cos\left(\frac{\pi}{2V_\pi}v_i(t)\right) + j\cos\left(\frac{\pi}{2V_\pi}v_q(t)\right)\right). \tag{2.2}$$

2.2.3 Optical Pulse Carvers

The shape of the generated optical pulses significantly affects the overall performance of a communication system. An advantage of pulse carving is that it increases the robustness of the system against imperfections in the transmitter. In high bit-rate optical transmitters this can help to reduce the stringent requirements on, for example, the bandwidth of the modulator and driver amplifier voltage swing [57]. Additionally, pulse carving reduces the unwanted chirp that arises between successive symbols [56]. The optimum pulse shape will depend on the transmission scenario, e.g. available bandwidth, transmission distance and type of link.

The most straightforward pulse form is the non-return-to-zero (NRZ) where a pulse filling the entire symbol period is transmitted. Another common pulse shape is known as return-to-zero (RZ), where the optical power goes to zero in each symbol period. RZ pulses are generated in the optical domain by means of an MZM used for pulse carving.
Optical pulse carving using an MZM is done as follows. The CW light coming from the laser $E_{\text{in}}(t)$ is modulated by the electrical sinusoidal driving voltage $v(t) = V_p\cos(2\pi f_s' t + \phi) + v_{\text{bias}}$ with peak voltage V_p, frequency f_s', phase ϕ and bias voltage v_{bias}. The four parameters $\{V_p, f_s', \phi, v_{\text{bias}}\}$ determine the characteristics of the generated pulses with a time response of the pulse carver MZM given by (2.1). Typical values for such parameters as listed in Table 2.1 give rise to three different pulses with a duty-cycle of 33% (RZ-33%), 50% (RZ-50%) and 67% (RZ-67%).

2.2.4 Electrical Pulse Forming

The signal to be transmitted over the optical fiber can be shaped such that an ISI-free received signal is obtained. Nyquist pulses meet this requirement despite band-limitation [58]. In WDM architectures, Nyquist pulses are generated to alleviate the need of guard symbols necessary in

Pulse shape	Peak Voltage V_p	Drive frequency f_s'	Bias voltage v_{bias}	phase ϕ
RZ-67%	V_π	$1/(2T_s)$	V_π	-$\pi/2$
RZ-50%	$V_\pi/2$	$1/(T_s)$	$V_\pi/2$	0
RZ-33%	$V_\pi/2$	$1/(2T_s)$	0	0

Table 2.1. Parameters of the drive signal for pulse carving

OFDM systems as a way to improve SE. Moreover, to avoid performance degradation due to optical front-end and the bandwidth limitation of DAC, the transmitted signal is pre-distorted. By using different DSP algorithms the electrical signal in the transmitter can be both pulse shaped and pre-distorted. Electrical pulse forming in the FD is superior over both TD and optical pulse forming. For FD pulse forming, discrete Fourier transform (DFT) and inverse DFT (IDFT) operations are to be applied on the signal.

A filter which satisfies first Nyquist condition for ISI-free transmission is the raised-cosine (RC) filter. A root-raised cosine (RRC) filter is derived from an RC filter according to the requirement that the receive filter should be matched to the transmit filter in order to get sufficient statistics for the subsequent symbol decision based on sampling at the symbol rate. In this way, the signal-to-noise ratio at the sampling instants is maximized. The frequency response of an RRC filter is obtained by taking the square root of the frequency response of an RC filter. It reads as

$$H_{\text{RRC}}(f) = \begin{cases} \sqrt{T_s}, & 0 \leq |f| < \frac{1-\rho}{2T_s}, \\ \sqrt{T_s}\cos\left(\frac{\pi T_s}{2\rho}\left(|f| - \frac{1-\rho}{2T_s}\right)\right), & \frac{1-\rho}{2T_s} \leq |f| \leq \frac{1+\rho}{2T_s}, \\ 0, & |f| > \frac{1+\rho}{2T_s}. \end{cases} \tag{2.3}$$

The frequency response of an RRC filter in the passband of the filter is perfectly flat, the transition from the passband to the stopband characterizes this filter as an RRC filter, and the stopband is the band where the frequency components of the signal are perfectly attenuated. The parameter ρ with $0 < \rho \leq 1$ is called the roll-off factor and can be adjusted to determine the steepness of the transition band and therefore the bandwidth of the filter. Figure 2.6 shows the frequency response of an RRC filter with different values for ρ.

To avoid the significant degradation of the signal to be sent over the fiber link due to the DAC and optical front-end, a pre-distorter is operated in the digital domain at the baseband. Pre-distortion of the DAC and optical filtering is simply performed on the input signal by filtering it by the inverse of the combined impulse response of the DAC and the optical filter. Pre-distortion of the input signal by filtering with the inverse of the propagating channel impulse response can be also done. However, due to possible high induced PAPR values, and the need for a fast feedback channel from the receiver and for exact knowledge of the constellation of the system, pre-distortion of the channel impulse response is not further discussed in the thesis.

2.2.5 Wavelength Division Multiplexing Schemes

WDM corresponds to the scheme in which the output of several transmitters, each operating at its own carrier frequency f_c (or correspondingly wavelength λ_c), is multiplexed together. The multiplexer combines the output of several transmitters such that the frequency separation $\Delta f = f_c^u - f_c^{u-1}$ between the neighboring carrier frequencies f_c^{u-1} and f_c^u of user $u-1$ and u,

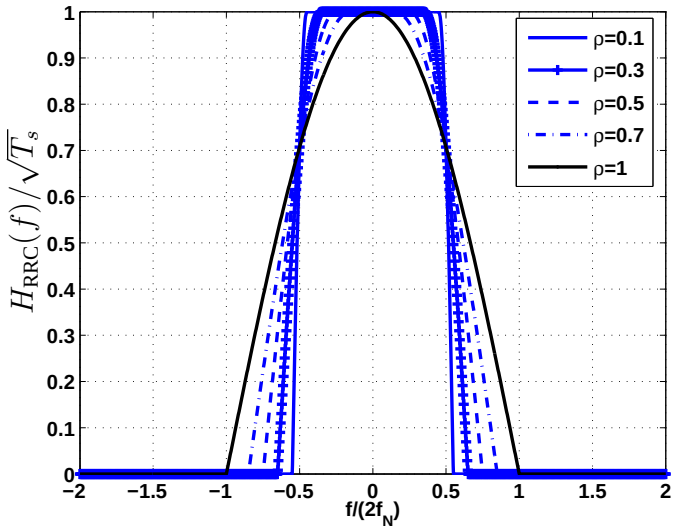

Fig. 2.6. Frequency response of a Root Raised Cosine filter

respectively, is only a fraction α_{sp} of the inverse of the symbol period T_s, i.e.

$$\alpha_{\text{sp}} = \Delta f T_s \tag{2.4}$$

where α_{sp} could be equal to, less than or greater than 1.
For long-haul fiber links forming the backbone or the core of a telecommunication network, the role of WDM is simply to increase the total capacity of the system. The ultimate capacity of WDM fiber links depends on how closely the wavelength channels can be packed. The minimum channel spacing Δf is limited by inter-channel crosstalk or inter-channel interference. A measure of the spectral efficiency of a WDM system is given as $\eta_{\text{sp}} = \frac{1}{\alpha_{\text{sp}}}$. Attempts are made to make η_{sp} as large as possible.

For $\alpha_{\text{sp}} < 1$ through which the maximum SE is obtained, neighboring channels are spaced below the symbol-rate i.e. $\Delta f < B$. This is a non-orthogonal signaling method where in addition to ICI, ISI is inherit in the structure even in the absence of a transmission channel because the symbols overlap in both TD and FD. Notwithstanding, the detection implementation for such systems relies on very complex techniques since the transmitted symbols can not be detected independently due to the system's inherent ISI and ICI. This makes the complexity at the receiver high [14].

For $\alpha_{\text{sp}} = 1$, neighboring channels are spaced exactly at the symbol-rate i.e. $\Delta f = B$ which gives rise to considerable ICI due to spectra overlap. There are classes of orthogonal-signaling systems where despite symbol-rate spacing ICI is ideally not present in the system structure. Thanks to orthogonality, the reconstruction of the transmitted data symbols at the receiver side becomes simple. Three orthogonal multiplexing schemes exist which are known from radio communications and have been later adapted in optical communications [16–33]. The first scheme is the multicarrier OFDM [15] scheme where the pulse in each wavelength channel has a sinc-shape and adjacent pulses have zero-crossings at the symbol-rate. In OFDM, a DFT is present at the transmitter and a IDFT at the receiver requiring DAC and analog-to-digital converter (ADC), respectively, at both entities. ICI is combated by introducing a guard interval between the transmitted blocks. This leads to loss in SE. Moreover, OFDM is sensitive to frequency mismatch between the transmitter and receiver. Additionally, an OFDM signal exhibits high PAPR values giving rise to non-linearities in

the optical channel. For these reasons, we do not consider OFDM as a multiplexing scheme in this thesis. The second orthogonal scheme is complementary to OFDM; it is the Nyquist WDM scheme where each wavelength channel has an ideal rectangular shaped spectrum with bandwidth equal to the baud-rate. Electrical as well optical filters are used to generate such a spectrum as reported in [34–47]. However, practical issues are raised by the requirement of perfect rectangular spectral shaping which is difficult to realize which leads to ISI and ICI. The requirement on an ideal rectangular spectrum is relaxed by varying ρ of the RRC filter to obtain Nyquist pulses. The resulting Nyquist WDM system is non-orthogonal. One challenge in these systems is to simultaneously minimize ISI and ICI impairments achieved by adopting transmitter-side and receiver-side approaches. The third orthogonal signaling scheme which is known from the radio communications [54,55] and is applied in optical Nyquist WDM systems is the multicarrier OQAM modulation [48–53]. Orthogonal multiplexing is achieved by alternately staggering the the real and the imaginary parts of the signal in the transmitter of each wavelength channel while in the receiver, destaggering is done. However, this is achieved by setting strict requirements on the frequency, time and phase offsets between the wavelength channels in the transmitter and receiver. In this thesis, we will consider the last two schemes for Nyquist WDM systems with baud-rate for channel spacing.

For $\alpha_{\text{sp}} > 1$, the spacing between neighboring channels is greater than the baud-rate which means $\Delta f > B$. In this case, the ICI induced in such a system is smaller than in systems where $\alpha_{\text{sp}} = 1$ and $\alpha_{\text{sp}} < 1$. For sufficiently large spacing, ICI is even negligible. This simplifies the design of both the transmitter and the receiver. However, the main disadvantage of such systems is the great loss in SE. For this reason, we will not consider this multiplexing scheme in this thesis.

2.2.6 Multiplexer

Optical signals of different wavelength channels in the transmitter of a WDM system are combined by a multiplexer. The most frequently used techniques to optically multiplex multiple WDM channels are arrayed waveguide gratings (AWG), thin-film filters [9, 59] or wavelength selective switching (WSS) components.

For experiments, optical filters are used as multiplexers. Optical band-pass filters are modeled as non-causal Gaussian filters with real-valued transfer function. The transfer function of a Gaussian band-pass filter $H_{\text{BP}}(f)$ can be given by

$$H_{\text{BP}}(f) = \exp\left(-\frac{2^{2n_{\text{od}}}\ln(2)}{2(2\pi B_{\text{O3dB}})^{2n_{\text{od}}}}(2\pi(f-f_c))^{2n_{\text{od}}}\right) \tag{2.5}$$

where n_{od} is the order of the filter, f_c is the center frequency and B_{O3dB} is the double-sided 3-dB bandwidth of the filter, both given in Hz.

A low-pass equivalent of the optical filter in (2.5) can be simplified to

$$H_o(f) = \exp\left(-\ln(\sqrt{2})\left(\frac{2f}{B_{\text{O3dB}}}\right)^{2n_{\text{od}}}\right). \tag{2.6}$$

The transfer function of the optical low-pass filter $H_o(f)$ for different orders $n_{\text{od}} = 1, 2, 3$ are plotted in Fig. 2.7 for $B = 28$ GHz and $B_{\text{O3dB}} = 35$ GHz.

2.3 Coherent Optical Receiver

The role of an optical receiver is to convert the optical signal back into the electrical form and recover the data transmitted through the lightwave system. It consists of photodiodes, optical and

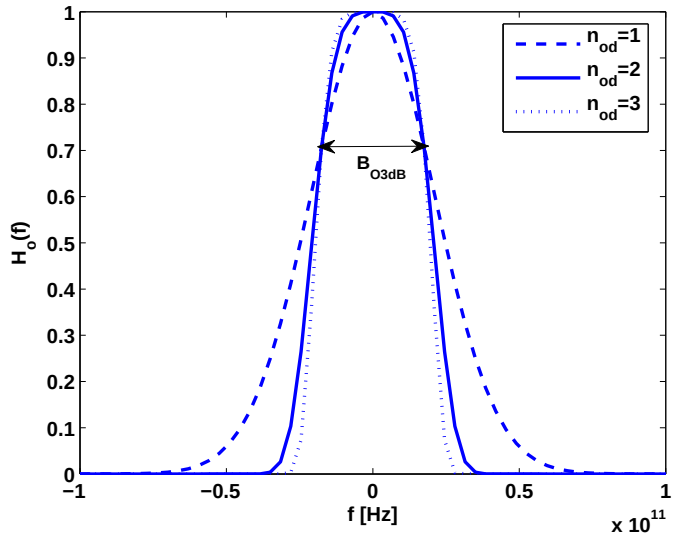

Fig. 2.7. Transfer function of an optical filter modeled as a Gaussian band-pass filter for various order n_{od}

electrical filters (laboratory channel demultiplexers), polarization beam splitters (PBSs), coherent detection modules (2×4 90°-hybrid), ADCs, and DSP module.

In Section 2.3.1, we present the three different coherent detection concepts. In Section 2.3.2, we present a coherent receiver employed in commercially available products.

2.3.1 Concept of Coherent Detection

In order to decode information bits from the complex phase modulated optical signal, the receiver needs to detect both the absolute phase and amplitude of the received signal. For this a LO is used at the receiver to beat with the incoming optical signal before it falls on the detector.

There are three types of coherent detection methods that can be differentiated. These are homodyne, intradyne and heterodyne detection. All employ the same principle of operation. The signal-LO beat term mixes the signal either down to the baseband (homodyne detection) or to an intermediate frequency (heterodyne detection) using 2×4 90°-hybrid. The term intradyne detection is used if the intermediate frequency is smaller than the frequency of the signal. The most commonly used and implemented methods in commercially available products for coherent detection are homodyne and intradyne detection.

Homodyne detection generates an electrical signal in the baseband such that the frequency of the LO is the same as the frequency of the carrier signal. The main advantage of this scheme is that an DSP for residual frequency recovery is not needed. However, the main disadvantage is its phase sensitivity. Ideally, the phase of the LO should be kept constant, but in practice it fluctuates randomly over time. Therefore, it should be optically controlled. Such changes could be tracked by an optical phase-locked loop (PLL). However, it is not simple to implement such an analog loop making the design of optical homodyne receivers quite complicated. In addition, the condition that the frequency of LO and the carrier signal should be the same puts stringent requirements on the laser used at the transmitter and the one used for the LO. These problems can be overcome by the use of intradyne detection [60].

Intradyne detection generates an electrical signal at an intermediate frequency near to frequency zero. Compared to homodyne detection, the LO laser does not need to be coherent with the

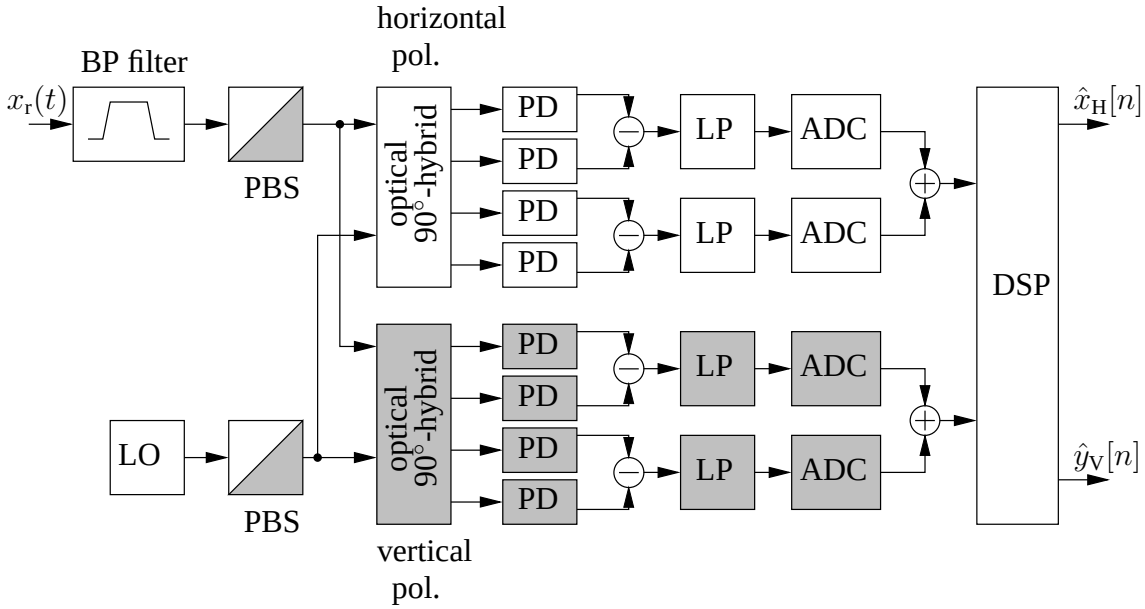

Fig. 2.8. Simplified block diagram of a typical polarization-diverse, intradyne coherent demodulation with a free-running LO mixing with the modulated optical signal in two optical 90°-hybrids

incoming optical carrier. The difference in terms of frequency and phase between the LO and the laser in the transmitter is compensated in the DSP module and an automatic frequency controller is employed. Intradyne detection requires optical and electrical components with bandwidth only slightly larger than the signal's bandwidth. This allows certain relaxation on the requirements of the optical sources. Today's commercially available digital coherent receivers are based on polarization and phase diversity intradyne coherent detection supported by DSP.

2.3.2 Coherent Receiver Design

In coherent receivers, all the information of the optical signal such as amplitude, frequency, phase and polarization can be transferred into the electrical domain. A first advantage, thus, of coherent receivers is that the demodulation can be performed completely in the electrical domain and the complexity for the optical components can be reduced. The further advantages are the possibility for electronic compensation of transmission impairments and the existence of tunable WDM receivers with highly selective channel separation.

Here we present polarization diverse intradyne demodulation; a setup widely used in experiments and also in commercially available products. It is composed of an optical front-end and subsequent digital signal processing for data recovery. The polarization and phase coherent receiver model is shown in Fig. 2.8.

For wavelength channel demultiplexing, band-pass optical filters are used in the simulations of WDM systems at the receiver. An optical bandpass filter as given in (2.5) is convolved with the receive signal $x_{\mathrm{r}}(t)$ to separate the wavelength channels. Afterward, the modulated signal is split by a PBS into its vertical and horizontal polarizations. Intradyne downconversion by mixing the LO with the signal can be achieved by an optical 90°-hybrid in each polarization. The inphase and quadrature components in each of the orthogonal polarizations is transferred into the electrical domain by the balanced photodiodes. The electrical signal from the quadrature front-ends is filtered by a low-pass filter and then digitized with ADCs before being fed into the DSP unit. In the DSP

unit, the linear impairments of the channel like CD and PMD and timing and carrier recovery are compensated for to obtain the equalized signals $\hat{x}_{\mathrm{H}}[n] = \hat{x}_{\mathrm{H}}^{\mathrm{R}}[n] + j\hat{x}_{\mathrm{H}}^{\mathrm{I}}[n]$ and $\hat{y}_{\mathrm{V}}[n] = \hat{y}_{\mathrm{V}}^{\mathrm{R}}[n] + j\hat{y}_{\mathrm{V}}^{\mathrm{I}}[n]$ in the horizontal and vertical polarization, respectively.

We give the details on the components of a coherent receiver in the what follows.

2.3.2.1 2×4 90°-Hybrid

Since photodiodes can only detect the power of light signal, an additional component is necessary in coherent receiver for the detection of phase information. With the 2×4 90°-hybrid, the detection of the in-phase and quadrature components of the optical signal is enabled to demodulate the received signal with the LO. It is composed of two power splitters and a relative phase shift of $\pi/2$ between the inphase and quadrature arm.

2.3.2.2 Photodetector

Photodetection is the process by which an optical signal is converted to an electrical signal. The main requirements for a photodetector are high sensitivity, high response bandwidth, low noise, low cost and high reliability. A photodetector is usually composed of a photodiode and a receiver electronic circuit.

In this thesis, we consider that the photodiode is an ideal $p - i - n$ photodiode with unity responsivity. The responsivity is proportional to the quantum efficiency of the photodiode defined as the quotient between the electron generation rate and the photon incident rate.

2.3.2.3 Electrical Filters

At the receiver side, electrical filters are used in order to further filter the noise after photodetection since optoelectronic components like photodetectors are bandwidth limited. In digital receivers, electrical filters can be used as image rejection filters before ADCs.

Electrical filters are usually modeled as low-pass Bessel filters since they can be physically implemented, exhibit a linear phase response and an excellent step response with minimal overshoot and ringing [56]. In this thesis, fifth-order Bessel low-pass filters are used with normalized transfer function given by

$$H_e(f) = \frac{945}{jF^5 + 15F^4 - 105jF^3 - 420F^2 + 945jF + 945}, \tag{2.7}$$

where $F = \dfrac{K_{\mathrm{3dB}}}{B_{\mathrm{E3dB}}} f$, $K_{\mathrm{3dB}} = 2.4274$ is the 3-dB normalization constant and B_{E3dB} is the single-sided 3-dB bandwidth of the filter given in Hz.

2.3.2.4 Analog to Digital Convertor

The four output analog electrical signals of the coherent receiver are digitized. For simplicity, the signals are digitized at 2 samples per symbol. This rate of oversampling is not strictly necessary, but reduces the constraints on the required anti-aliasing filters and enables compensation of a larger range of frequency offset. As these ADCs operate in the region of 56 GSa/s (for $B = 28$ GHz), the performance of these components is critical. Both the number of bits of resolution and timing jitter introduce uncertainty into the digitized signal. A metric of performance for ADCs is the effective number of bits (ENOBs). The greater the ENOBs in the digital word, the finer the resolution of the DAC.

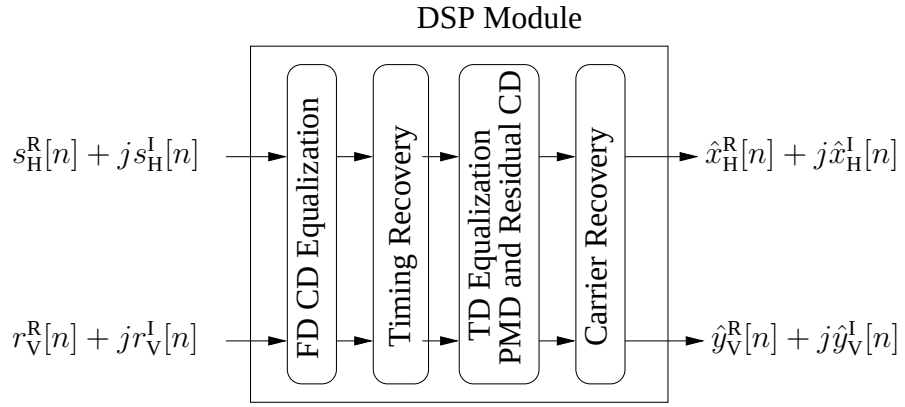

Fig. 2.9. DSP module in polarization multiplexed coherent receiver

2.3.2.5 Digital Signal Processing Module

For receivers with coherent detection, DSP is required to recover the data information. There are different modules in the DSP. These are modules for FD equalization of CD, TD equalization of PMD, and modules for the timing and carrier recovery.

The memory length of CD channel increases quadratically with the baud-rate. For baud-rates of 28 GBaud and more, the memory spread is in the order of hundreds of symbols. We show in Sec. 3.3.3 that for such high data-rates it is more efficient in terms of complexity, defined as the number of real multiplications, to equalize CD channel in FD rather than in TD. The memory spread of PMD for such high baud-rate is in the order of tens of symbols. Therefore, PMD equalization is done in TD. Since CD equalization can operate without timing synchronization whereas PMD can not because of the need to adapt the coefficients for TD FIR PMD equalizer, timing recovery can be done after CD equalization but must be done before PMD equalization. Most methods available for carrier recovery can not operate in the presence of channel distortions. Therefore, carrier recovery is performed as a last step in the DSP module.

Putting all the modules in a nut shell, the order of the different modules of DSP is shown in Fig. 2.9. FD equalization (FDE) is done in a first step for CD compensation. Afterward, the sample-rate synchronization and the optimal sample-time estimation can be performed with one of the different timing recovery algorithms e.g., Gardner timing recovery [61], square timing recovery [62], Mueller & Mueller timing recovery [63], and histogram based timing recovery [64, 65]. Timing recovery is applied after FD equalization of CD and before TD equalization. Following timing recovery, PMD and residual CD are compensated for with an adaptive TD FIR filter having butterfly structure. The adaptation of the coefficients of the FIR filter can be implemented with either non-data-aided algorithms such as constant modulus algorithm (CMA) [66] or the decision directed least mean square (LMS) [67] algorithm or with data-aided adaptation algorithms such as CMA, LMS and minimum mean square error (MMSE) [68]. Finally carrier synchronization is applied after TD equalization.

We assume in this thesis that timing and carrier recovery as well as the TD equalization of PMD perfectly work. Therefore, we focus on the FD equalization module to improve the performance of the overall system in terms of increasing the dispersion tolerance and decreasing the required optical signal-to-noise ratio (ROSNR) values through designing different FD equalizers. We propose, therefore, two novel FD equalization methods of the group delay of the CD channel that have the same complexity in terms of multiplications as the benchmark method. In baud-rate

spacing of the wavelength channels in WDM systems we design different equalization methods that take into account the incurred ICI to improve the overall performance of the system. In such systems considerable ICI arises because of the baud-rate spacing of the channels.

2.4 Noise in Coherent Systems

There are different noise sources in optical communication systems. These sources include amplified spontaneous emission (ASE), shot and thermal noise of the receiver. ASE is induced by optical amplification. It results from spontaneous emission within EDFAs, which is then subsequently amplified. Shot noise arises when an avalanche photo diode is applied. Thermal noise arises in the electrical circuits.

The dominant source of additive noise in long-haul coherent optical transmission systems is ASE. Besides, the linear transfer function of the receiver in coherent optical systems preserves the Gaussian noise statistics of ASE. ASE noise is polarization-independent; it can be modeled as an additive white Gaussian noise (AWGN) with identical power spectral density (PSD) in each polarization. Although filtering at the receiver with an optical and an electrical filter weakens the assumption of white noise, the noise process in the electrical domain can be described as AWGN with a Gaussian power density function (PDF) with a certain mean and variance.

2.5 Optical Fiber

In 1966, Kao and Hockham proposed to use glass fibers as a waveguide for long distance communication at optical frequencies [69]. Since its introduction, many different fiber types have been developed. In this section, we present first the characteristics of the fiber being used throughout this thesis, then the linear impairments induced in an optical fiber and finally the mathematical model of the optical channel of interest in this thesis.

2.5.1 Fiber Structure

An optical fiber consists of a circular glass core surrounded by a cladding layer as shown in Fig. 2.10(a) having a refractive index n_{cl} which is slightly lower than the core index n_{co}. Such fibers are generally referred to as step-index fibers to distinguish them from graded-index fibers in which the refractive index of the core decreases gradually from center to core boundary and is function of the radius as shown in Fig. 2.10(b). Most of the fibers are made from glass, i.e. Silica. For silica fibers, $n_{\text{co}} \approx 1.48$ and depending on the fiber type, n_{cl} is 0.2 to 3% lower [70]. The cladding confines the light into the core through total internal reflection and reduces the scattering loss at the core-cladding boundary. The coating or jacket of the fiber provides mechanical strength and protection against moisture.

Optical fibers are designed to support either a single-mode or multiple-mode (> 100) transmission. The main difference between the single-mode fibers (SMFs) and multimode fibers (MMFs) is the core size. The core radius a_{co} is typically 25-30 μm for MMFs. However, SMFs require a_{co} to be < 5 μm. The numerical value of the outer radius is less critical as long as it is large enough to confine the fiber modes entirely. Because MMFs have larger core size than SMFs, they support more than one propagation mode. The different modes in MMFs travel at different group velocities causing intermodal dispersion. This leads to pulse broadening when the signal travels along the MMFs giving rise to ISI. Thus, intermodal dispersion limits the feasible transmission distance

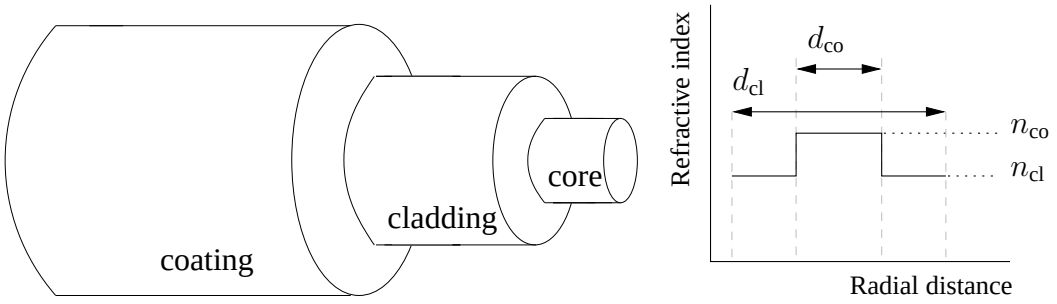

(a) Fiber structure

(b) Index profile of a step-index fiber where $d_{\text{co}} = 2a_{\text{co}}$ and $d_{\text{cl}} = 2a_{\text{cl}}$

Fig. 2.10. Fiber structure and refractive index profile of a step-index fiber

in MMFs. For this reason, all long-distance communications fibers are single-mode fibers [9]. Although SMFs do not suffer from intermodal dispersion, principal deterministic linear (attenuation and dispersion) and nonlinear effects cause signal degradation. These effects depend on the concentration of dopants in the material, the refractive index profile, the effective area and the wavelength of the propagating field. The various types of single-mode fibers are typically characterized by measurable parameters.

The term optical fiber in this thesis refers to standard single-mode fibers (SSMFs) unless noted otherwise.

2.5.2 Fiber Loss

The optical signal losses its power as it propagates through a fiber due to absorption by the glass particles and scattering by microscopic imperfections in the fiber. This loss is called attenuation. If P_{in} in W is the power launched at the input end of a fiber, the signal power $P(\ell)$ in W after traveling distance ℓ_d is given by

$$P(\ell) = P_{\text{in}}\exp(-\alpha_{\text{att}}\ell_d), \tag{2.8}$$

where α_{att} is the attenuation coefficient in Neper per kilometer which is assumed to be constant in the vicinity of the carrier angular frequency ω_c. Conventionally, the attenuation coefficient is expressed in dB/km, which is related to Neper by

$$\alpha_{\text{att}}[\text{dB}] = 10\log_{10}\exp(\alpha_{\text{att}}) \approx 4.343\alpha_{\text{att}}. \tag{2.9}$$

The attenuation coefficient α_{att} is a measure of the total fiber losses from all sources. It depends on the wavelength λ_c and the carrier frequency f_c which are related according to $\lambda_c = c/f_c$ where $c = 2.998 \times 10^8$ m/s represents the speed of light in vacuum. Several factors contribute to overall losses; the two most important among them are material absorption and Rayleigh scattering. Material absorption can be divided into two categories intrinsic and extrinsic absorption. Intrinsic absorption losses α_{UV} (dominating for short wavelengths) and α_{IR} (dominating for long wavelengths) occur due to electronic and vibrational resonances associated with silica (SiO_2) molecules, respectively. Extrinsic absorption α_{OH} is related to losses caused by impurities within state-of-the-art silica fibers due to the presence of water vapors. Rayleigh scattering results from local microscopic fluctuations in the material density that are created during the manufacturing process. It is strongly wavelength dependent and varies as $1/\lambda_c^4$.

Band	**Description**	**Wavelength Range** [nm]
O-band	Original	1260 to 1360 nm
E-band	Extended	1360 to 1460 nm
S-band	Short wavelength	1460 to 1530 nm
C-band	Conventional	1530 to 1565 nm
L-band	Long wavelength	1565 to 1625 nm
U-band	Ultra-long wavelength	1625 to 1675 nm

Table 2.2. SSMF spectral bands

In modern lightwave systems, λ_c is chosen from a set of frequencies standardized by the International Telecommunication Union (ITU) which defined six bands for transmission using single-mode fiber: the O, E, S, C, L and U-band ranging from 1260 nm to 1675 nm as shown in Table. 2.2 [71]. As the name implies, the original band (O-band) was used in early long-haul transmission systems. Nowadays, practically no long-haul system employs the O-band. However, the O-band is used almost exclusively for the client interface in the access network [72–75]. Due to the relatively high attenuation, the extended band (E-band) and the ultra long-wavelength band (U-band) are less interesting for most fiber-optic applications. Most commercial transmission systems employ the conventional band (C-band), from 1530 nm to 1565 nm, where the fiber loss is the lowest. When more bandwidth is required, the transmission capacity can be increased by using the long-wavelength band (L-band), from 1565 nm to 1625 nm. Alternatively, the short-wavelength band (S-band) from 1460 nm to 1530 nm can be used.

Modern fibers exhibit a loss of $\alpha_{\text{att}}[\text{dB}] \approx 0.2$ dB/km near the wavelength $\lambda_c = 1.55\mu$m, which is the reference wavelength for most long-haul optical transmission systems [60]. Therefore, transmission in the C-band will be considered in this thesis.

2.5.3 Chromatic Dispersion

The angular frequency dependence of the refractive index $n(\omega)$ causes the effect of material dispersion that contributes the greatest to chromatic dispersion. As a result, different spectral components of an optical pulse propagating in a fiber travel at slightly different group velocities given by $c/n(\omega)$ leading to ISI.

Mathematically, the effects of chromatic dispersion are accounted for by expanding the mode-propagation constant $\beta(\omega) = n(\omega)\frac{\omega}{c}$ of the fundamental mode in SSMF into a Taylor series with the assumption that $\Delta\omega = \omega - \omega_c \ll \omega_c$

$$\beta(\omega) = \beta_0 + \beta_1 \cdot (\omega - \omega_c) + \frac{1}{2}\beta_2 \cdot (\omega - \omega_c)^2 + \cdots \tag{2.10}$$

where

$$\beta_m = \left.\frac{d^m \beta(\omega)}{d\omega^m}\right|_{\omega=\omega_c}, m = 0, 1, 2, \cdots \tag{2.11}$$

The constant phase shift is represented by β_0 in rad/km. The first two derivatives β_1 in ps/km and β_2 in ps^2/km correspond to the group-velocity and the group velocity dispersion (GVD), respectively.

Both are related to the refractive index $n(\omega)$ and can be derived as follows, respectively,

$$\beta_1 = \frac{1}{v_g} = \frac{n_g}{c} = \frac{1}{c}\left(n(\omega) + \omega\frac{dn(\omega)}{d\omega}\right)\Big|_{\omega=\omega_c}, \tag{2.12}$$

$$\beta_2 = \frac{1}{c}\left(2\frac{dn(\omega)}{d\omega} + \omega\frac{d^2n(\omega)}{d\omega^2}\right)\Big|_{\omega=\omega_c}, \tag{2.13}$$

where n_g is the group index and v_g is the group velocity. Instead of the propagation constant β_2, it is more common to use the dispersion parameter D_{CD} expressed in s/m^2 but usually measured in ps/nm/km to characterize optical fibers, which is related to β_2 as

$$D_{\text{CD}} = \frac{d\beta_1}{d\lambda} = -\frac{2\pi c}{\lambda_c^2}\beta_2. \tag{2.14}$$

The term β_3 in ps^3/km represents the slope of CD. It is also called third-order dispersion which is the change in dispersion as a function of the reference angular frequency ω_c. Often, the dispersion slope parameter S expressed in ps/nm^2/km is used instead of β_3 to characterize optical fibers [9]

$$S = \frac{dD_{\text{CD}}}{d\lambda} = \frac{4\pi c}{\lambda_c^3}\beta_2 + \left(\frac{2\pi c}{\lambda_c^2}\right)^2\beta_3. \tag{2.15}$$

The bandwidth of most signals at bit rates up to 100 Gb/s is much narrower than the bandwidth over which β_2 varies for the most common fibers. Consequently, β_3 represents an effective change of β_2 from one channel to another in WDM systems rather than having a significant impact in single-channel systems. Therefore, when considering only single-channel transmission, the effect induced by β_3 can be neglected.

In optical fibers, CD results from material dispersion D_{M}. Apart from material dispersion D_{M}, another important dispersion effect that occurs in SMFs is waveguide dispersion D_{W}. Waveguide dispersion is caused by the fact that the optical field is not totally confined to the core of a fiber and thus partly propagates through the cladding [70]. And as the refractive index of the core and the cladding is different, waveguide dispersion arises. The contribution of the waveguide dispersion is dependent on fiber parameters such as the radius of the core and the difference in refractive index between the core and the cladding. Therefore, the fiber design determines the dispersion profile of the fiber. Fig. 2.11 shows the chromatic dispersion D_{CD} and the relative contributions of materiel dispersion D_{M} and waveguide dispersion D_{W} for SSMFs.

In SSMFs, the dispersion profile is mainly determined by the material dispersion D_{M}. In the C-band the dispersion parameter for SSMF around the carrier wavelength $\lambda_c = 1550$ nm varies between $D_{\text{CD}} = 15 - 18$ ps/nm/km. We consider in this thesis that $D_{\text{CD}} = 17$ ps/nm/km. The dispersion slope is typically $S = 0.06$ ps/nm^2/km.

2.5.4 Birefringence

Two orthogonally polarized fundamental modes are able to propagate in a single-mode fiber. In a perfectly cylindrical and stress-free fibers, these modes are indistinguishable and degenerate. This means a mode excited in the horizontal polarization would not couple with the mode in the orthogonal vertical polarization and both modes have identical propagation properties. However, in practice, fibers exhibit a certain amount of anisotropy due to intrinsic geometrical asymmetries or due to external stress. As a consequence, a perfect circular core shape with a constant refractive

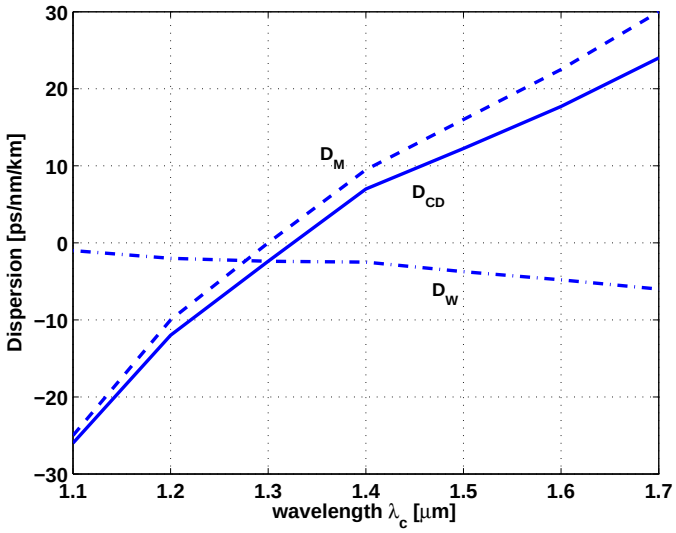

Fig. 2.11. Chromatic dispersion D_{CD} and the relative contributions of materiel dispersion D_{M} and waveguide dispersion D_{W} for SSMFs.

index along the fiber cannot be achieved. As a result, both modes will propagate with different velocities and exchange power along the way. This is referred to as *modal birefringence* and *mode coupling*, respectively. The strength of modal birefringence is defined by [60]

$$\Delta n = |n_{\mathrm{H}} - n_{\mathrm{V}}| = \frac{\lambda_c \left| \beta_1^{\mathrm{H}} - \beta_1^{\mathrm{V}} \right|}{2\pi} \tag{2.16}$$

where n_{H} and n_{V} are the modal refractive indices of the two orthogonally polarized fiber modes. The axis along which the mode index is smaller is called the fast axis because the group velocity is larger for light propagating in that direction. For the same reason, the axis with the larger mode index is called the slow axis. Due to the different group velocities β_1^{H} and β_1^{V} of the fundamental mode of both polarization components, respectively, the pulse becomes broader as the two components disperse along the fiber. In a short piece of fiber of length L_{F}, where birefringence can be considered constant, the broadening can be estimated from the time delay $\Delta\tau$ between the two polarization components during propagation of the pulse. The time delay $\Delta\tau$ is usually referred to as *differential group delay* (DGD) and is given by

$$\Delta\tau = L_{\mathrm{F}} |\beta_1^{\mathrm{H}} - \beta_1^{\mathrm{V}}| = \frac{\omega_c \Delta n}{c}. \tag{2.17}$$

Birefringence leads to a periodic power exchange between the two polarization components. The period, referred to as the beat length, is given by

$$L_{\mathrm{B}} = \lambda_c / \Delta n. \tag{2.18}$$

In SSMFs, typical values of L_{B} are in the range of 10 to 30 meters [76]. SSMFs do not behave like a single birefringence segment since the birefringence changes over the fiber. Therefore, real SSMFs need to be modeled by concatenating multiple fiber segments in which the birefringence properties are locally constant.

2.5.5 Polarization Mode Dispersion

Birefringence leads to the linear effect of polarization mode dispersion (PMD). For real fibers, the birefringence is not constant and changes randomly over time, frequency and fiber length because of change in the shape of the core due to fabrication imperfections, mechanical stress applied to the fiber, temperature changes, etc. PMD causes, for an arbitrary input polarization, a pulse with sufficiently low bandwidth to be split into pulses at the output of the PMD section. The resulting pulses are delayed against each other by DGD. As a result, PMD arises as a stochastic process where the DGD in $\Delta\tau$ in (2.17), also called first-order PMD, is not constant and changes randomly.

The mean DGD value denoted as $\mathrm{E}\{\Delta\tau\}$ is referred to as the PMD value. The evolution of PMD for light propagating through a long span of fiber with randomly changing birefringence sections can be modeled by concatenating N_{PMD} sections. The effect of local birefringence does not accumulate linearly from section to section as it can add up and subtract in each section. For this reason the PMD needs to be statistically described. The probability density function for the DGD, $p(\Delta\tau)$, of a fiber section at any particular time can be characterized by a Maxwellian distribution [77]

$$p(\Delta\tau) = \sqrt{\frac{2}{\pi}}\frac{(\Delta\tau)^2}{q_{\mathrm{T}}^3}\exp\left(-\frac{(\Delta\tau)^2}{2q_{\mathrm{T}}^2}\right), \tag{2.19}$$

where $q_{\mathrm{T}} = \sqrt{\frac{\pi}{8}}\mathrm{E}\{\Delta\tau\}$. The frequency dependence of the DGD, $\Delta\tau$, causes higher order PMD effects. For numerical simulations of all-order PMD, a model with $N_{\mathrm{PMD}} \geq 20$ fiber sections has been found to approximate the statistics sufficiently well.

PMD impairs the performance of a transmission system through ISI. The impact of DGD scales with the symbol rate. Higher data rates go along with smaller bit-slots and therefore more ISI occurs with the same DGD. For long-haul transmission systems, the PMD increases due to its random birefringence behavior with the square root of the transmission distance. The PMD-coefficient D_{PMD} can in this case be expressed by [77]

$$D_{\mathrm{PMD}} = \mathrm{E}\{\Delta\tau\}/\sqrt{L_{\mathrm{F}}} \tag{2.20}$$

where D_{PMD} is expressed in ps/$\sqrt{\mathrm{km}}$. The PMD-coefficient of a fiber is a measure for the quality of the fiber. PMD is especially problematic when old fibers with a high PMD coefficient ($D_{\mathrm{PMD}} \approx 1$ ps/$\sqrt{\mathrm{km}}$) are used for transmission. In this case, PMD compensation schemes can be employed to enable high bit-rate transmission. In the transmission experiments conducted in this thesis, high quality transmission fibers were used with a low PMD value ($D_{\mathrm{PMD}} \approx 0.02$ ps/$\sqrt{\mathrm{km}}$). Therefore no PMD compensation is required.

2.6 Optical Channel Model

The discussion of attenuation in Section 2.5.2 and the linear distortions in Sections 2.5.3, 2.5.4 and 2.5.5 in optical fibers is based on an intuitive phenomenological approach. In this Section, we discuss attenuation and linear distortions by using the wave equation that governs propagation of light in fiber. The numerical methods used to solve the resulting propagation equation are also presented.

Maxwell's equations can be used to obtain the wave equation that describes light propagation in optical fibers. The wave equation in an optical fiber is expressed by [60]

$$\nabla \times \nabla \times \mathbf{E} = -\epsilon_0\mu_0\frac{\partial^2\mathbf{E}}{\partial t^2} - \mu_0\frac{\partial^2\mathbf{P}}{\partial t^2}, \tag{2.21}$$

where ϵ_0 and μ_0 represent the vacuum permittivity and the vacuum permeability, respectively, which are related to speed of light in vacuum c as $\mu_0\epsilon_0 = 1/c^2$. The three dimensional vectors $\mathbf{E} = \begin{bmatrix} E_x(\mathbf{r},t) & E_y(\mathbf{r},t) & E_z(\mathbf{r},t) \end{bmatrix}^{\mathrm{T}}$ and $\mathbf{P} = \begin{bmatrix} P_x(\mathbf{r},t) & P_y(\mathbf{r},t) & P_z(\mathbf{r},t) \end{bmatrix}^{\mathrm{T}}$ represent the strength of the electric field and the induced electric polarization, respectively, and are given in Cartesian coordinates $\mathbf{r} = (x, y, z)$. The variable t denotes time. The generalized linear[1] Schrödinger equation (GLSE) which governs the propagation of a pulse in an optical fiber represents the solution of the wave equation [60].

Since the wave equation in (2.21) is difficult to handle, it is necessary to make several simplifying assumptions to solve it. It is assumed that a single-mode fiber in long-haul transmission with pulse widths larger than 1 ps is employed. In single-mode fiber only the fundamental mode is supported and all higher-order modes are cut-off at the operating wavelength. The fundamental mode is uniquely determined by its propagation constant $\beta(\omega)$ given in (2.10). The optical field is assumed to maintain its polarization along the fiber length so that a scalar approach for solving (2.21) is valid. It is assumed to be quasi-monochromatic i.e. the pulse spectrum centered at ω_c is assumed to have a spectral width $\Delta\omega$ such that $\Delta\omega/\omega_c \ll 1$ (this is valid for pulses as short as 0.1 ps). Under these assumptions the following LSE is typically employed that describes the propagation of a pulse in optical fibers

$$\frac{\partial A_x(z,t)}{\partial z} = -\frac{\alpha_{\text{att}}}{2}A_x(z,t) + \beta_1^x\frac{\partial A_x(z,t)}{\partial t} + j\frac{1}{2}\beta_2\frac{\partial^2 A_x(z,t)}{\partial t^2} - \frac{1}{6}\beta_3\frac{\partial^3 A_x(z,t)}{\partial t^3}, \tag{2.22}$$

$$\frac{\partial A_y(z,t)}{\partial z} = -\frac{\alpha_{\text{att}}}{2}A_y(z,t) + \beta_1^y\frac{\partial A_y(z,t)}{\partial t} + j\frac{1}{2}\beta_2\frac{\partial^2 A_y(z,t)}{\partial t^2} - \frac{1}{6}\beta_3\frac{\partial^3 A_y(z,t)}{\partial t^3}, \tag{2.23}$$

where $A_x(z,t)$ and $A_y(z,t)$ are the slowly varying amplitude envelopes of the transverse components $E_x(z,t)$ and $E_y(z,t)$, respectively, of the optical field. In the literature [60], $A_x(z,t)$ and $A_y(z,t)$ are often normalized such that $|A_x(z,t)|^2$ and $|A_y(z,t)|^2$ represent power values. Fiber losses explained in Section 2.5.2 are accounted for by attenuation coefficient is α_{att}. Linear birefringence is considered in (2.22) and (2.23) which means that the β_0 and β_1 of the propagation constant $\beta(\omega)$ in (2.10) are different for both polarizations i.e. $\beta_0^x \neq \beta_0^y$ and $\beta_1^x \neq \beta_1^y$. This also means that the quadratic and cubic terms β_2 and β_3 in (2.10) are assumed to be equal for both polarizations i.e. $\beta_2^x = \beta_2^y = \beta_2$ and $\beta_3^x = \beta_3^y = \beta_3$. The GVD coefficient β_2 is related to the dispersion D_{CD} as in (2.14) whereas β_3 is related to the dispersion slope S through (2.15). Here z indicates the propagation direction along the longitudinal axis of the fiber. Note that (2.22) and (2.23) are entirely in the time-domain.

In single-channel transmission over the fiber, further terms for intra-channel impairments like all-order PMD or self-phase modulation (SPM) can be added to (2.22) and (2.23).
In WDM systems, $A(z,t)$ comprises a comb of K_{ch} independently modulated optical signals at different optical frequencies propagating along the fiber. It is of the form

$$A_{x,y}(z,t) = \sum_{k=1}^{K_{\text{ch}}} A_{x,y}^{(k)}(z,t)\exp\left(-j\Delta\omega_k t\right) \tag{2.24}$$

where $A_{x,y}^{(k)}(z,t)$ is the slowly varying envelope of the signal in channel k in either polarization and $\Delta\omega_k = \omega_k - \omega_c$ represents channel spacing in terms of angular frequency which is defined as the difference between the center angular frequency of channel k and the angular frequency of the

[1] We do not consider non-linearities in this thesis

center channel of the WDM comb.
By substituting (2.24) in (2.22) and (2.23) and by using the superposition principle, the propagation equation for channel k in each polarization can be expressed by, respectively,

$$\frac{\partial A_x^{(k)}(z,t)}{\partial z} = -\frac{\alpha_{\text{att}}}{2}A_x^{(k)}(z,t) + \beta_1^{x,(k)}\frac{\partial A_x^{(k)}(z,t)}{\partial t} + j\frac{1}{2}\beta_2^{(k)}\frac{\partial^2 A_x^{(k)}(z,t)}{\partial t^2} - \frac{1}{6}\beta_3^{(k)}\frac{\partial^3 A_x^{(k)}(z,t)}{\partial t^3}, \tag{2.25}$$

$$\frac{\partial A_y^{(k)}(z,t)}{\partial z} = -\frac{\alpha_{\text{att}}}{2}A_y^{(k)}(z,t) + \beta_1^{y,(k)}\frac{\partial A_y^{(k)}(z,t)}{\partial t} + j\frac{1}{2}\beta_2^{(k)}\frac{\partial^2 A_y^{(k)}(z,t)}{\partial t^2} - \frac{1}{6}\beta_3^{(k)}\frac{\partial^3 A_y^{(k)}(z,t)}{\partial t^3}, \tag{2.26}$$

where each WDM signal propagates with a different propagation constant denoted as $\beta^{(k)}(\omega) = \beta_0^{(k)} + \beta_1^{(k)}\omega + \frac{1}{2}\beta_2^{(k)}\omega^2 + \frac{1}{6}\beta_3^{(k)}\omega^3 + \cdots$, and the signals in the WDM comb experience *walk-off*, i.e., each propagates with a different group velocity. Note that the derivation of (2.25) and (2.26) do not consider the spectrum overlap of neighboring wavelength channels. Further terms for intra-channel impairments like linear effects of all-order PMD or the non-linear effects of SPM, or inter-channel nonlinear interference like cross-phase modulation (XPM), cross-polarization modulation (XPolM) and four wave mixing (FWM) can be added.

Closed form solutions of (2.22) and (2.23) (correspondingly of (2.25) and (2.25)) exist only in special cases where chromatic dispersion, DGD or attenuation is neglected. In this thesis, we focus on the effects of CD in long-haul transmissions. Therefore, we neglect the effects of attenuation i.e. $\alpha_{\text{att}} = 0$, and birefringence $\beta_0^x = 0, \beta_1^x = 0, \beta_0^y = 0$ and $\beta_1^y = 0$. In this case, equations (2.22) and (2.23) reduce to the effects of CD as

$$\frac{\partial A(z,t)}{\partial t} = \frac{1}{2}j\beta_2\frac{\partial^2 A(z,t)}{\partial t^2} \tag{2.27}$$

which is polarization-independent and the cubic term β_3 was neglected, however, it must be included when the signal propagates near the zero-dispersion wavelength, i.e., when $\beta_2 \approx 0$.
Equation (2.27) can be solved by the Fourier transform and the solution reads in the FD

$$\tilde{A}(z,\omega) = \tilde{A}(0,\omega)\text{exp}\left(-j\frac{\beta_2}{2}z\omega^2\right). \tag{2.28}$$

A TD function $A(z,t)$ whose FD transform satisfies (2.28) broadens essentially linearly with z in the time domain. The constant β_2 is responsible for the spreading of the pulse. As can be seen from (2.28), $|\tilde{A}(z,\omega)| = |\tilde{A}(0,\omega)|,\ \forall z$; that is the Fourier transform has constant modulus and in particular the magnitude of the frequency components does not change during propagation. In other words, equation (2.28) provides a simple all-pass transfer function.
We adopt in this thesis a FD representation of the CD channel derived from (2.28) by substituting $\omega = 2\pi f$ (where the angular frequency ω is centered around the carrier angular frequency ω_c) and considering a signal propagating a distance $z = \ell_d$ along the fiber. It reads as

$$H_{\text{CD}}(f) = \text{exp}\left(-j\alpha_{\text{CD}}f^2\right) \tag{2.29}$$

where $\alpha_{\text{CD}} = \frac{\pi\lambda_c^2}{c} \times \text{CD}$ and CD represents the chromatic dispersion value given in ps/nm.

3. Chromatic Dispersion Compensation in Long-haul Transmission Systems

In this chapter, we report on the performance of long-haul optical systems that enable 112 Gbit/s polarization division multiplexed quadrature phase shift keying (PDM-QPSK) data transmission over a standard single-mode fiber (SSMF). Specifically, since chromatic dispersion (CD), among the various linear impairments present in optical fibers, limits the performance in long-haul optical systems [78], we focus on the different compensation techniques to mitigate it in these systems.

3.1 Introduction

The dramatic revolution in optical transmission systems brought by the introduction of coherent technologies, has been multi-faceted. One of its many aspects involves the possibility to mitigate dispersions in the link. Coherent optical receivers allow significant compensation of CD in the electrical domain instead of the compensation in the optical domain [79–82] or by dispersion compensating fibers (DCFs) [83, 84] or dispersion compensating modules (DCMs) [85, 86]. This provides a range of benefits with respect to cost effectiveness, power budget and non-linearity tolerance [87].

Equalization in the electrical domain can be implemented by analog or digital electronics either at the transmitter or at the receiver. In coherent optical systems with a predominant linear channel, the stable implementation of a butterfly structure with a large number of analog feed-forward equalizers (FFEs) is most challenging and has not been considered hitherto. With coherent detection schemes, richer constellations, and fast analog-to-digital converters (ADCs), digital signal processing plays an important role in CD compensation [88, 89]. The development of signal processing algorithms for optical communications aggregated rapidly with the feasibility of coherent detection. In this thesis, we consider that CD compensation is done at the receiver at the first stage of the digital filtering since it is polarization independent and time-invariant. This allows for the compensation of large amounts of CD without the need to frequently adapt the coefficients of the CD equalizer providing advantages for the implementation of digital signal processing methods.

Linear digital CD equalization can be either done in time-domain (TD) with finite impulse response (FIR) filters [90–97] or infinite impulse response (IIR) filters [98–101] or in frequency-domain (FD) with multi-carrier (MC) [18, 102, 103] or single-carrier (SC) [104–110] approaches. In Sec. 3.3.1 and Sec. 3.3.2 we review these different methods available in the literature for CD compensation. The equalization choice between TD and FD mainly depends on the maximum dispersion in the channel and the resulting number of coefficients for the equalizer. One of the main challenges is that the filtering algorithms have to be as simple as possible to enable high-

speed real time processing. This is because the main obstacle for implementation at such data rates is the complexity of the filtering algorithms and thus power consumption and availability of digital signal processing circuits that offer both very high gate density and speed.

The way the complexity of an algorithm to be quantified depends heavily on the platform it is implemented on. For digital signal processing algorithms, multiply-accumulate operation is a common step that computes the product of two numbers and adds that product to an accumulator. The hardware unit that performs the operation is known as a multiplier-accumulator (MAC, or MAC unit). The multiplication and addition introduce the same latency which is the relevant figure of merit although the hardware effort is much higher for a multiplier than for an adder. For the implementation of a digital signal processing algorithm on an application specific integrated circuit (ASIC) or a field programmable gate array (FPGA), however, power consumption and chip space are important. Here, the effort for a multiplier is much higher than for an adder. Therefore, in this thesis that the complexity of an algorithm measured in terms of the required number of real multiplications is the figure of merit.

As we show in Sec. 3.3.3, in long haul communications, FD equalization becomes more efficient than TD equalization with respect to implementation complexity over a wide range of CD values [18, 108–110] owing that to its block-to-block operation by using fast Fourier transform (FFT) and inverse FFT (IFFT). Specifically, the overlap methods [111–115], namely overlap-and-save (OLS) and overlap-and-add (OLA) are the more efficient FD methods for CD equalization. The OLS method with an overlap factor of 50% (OLS-50%) is considered as the benchmark for long-haul FD CD compensation. Starting from this, we show in Sec. 3.4 that the OLS-50% method can be implemented as a non-maximally decimated discrete Fourier transform (DFT) filter bank (FB) (see Appendix C) with trivial prototype filters i.e. filters with rectangular impulse response, and the equalization is done per sub-band. Filter banks [112, 115, 116] are digital signal processing systems that are candidates for applications in various fields of wireless communications beyond the current long-term evolution (LTE) systems. An important class of FBs is the DFT FB [116], which can be efficiently implemented based on the use of polyphase networks (see Appendix A), FFT and IFFT. We present DFT FB in Appendix C. FD equalization using DFT FB paves the way for more sophisticated sub-band processing. Based on this observation, we investigate in Sec. 3.5.2 the possibility of using a low complexity delayed single-tap equalizer in the frequency sub-bands. A delayed single-tap equalizer is a multi-tap equalizer with several delay elements and just one active tap. It aims at equalizing the group delay of the propagating CD channel in addition to its phase. It turns out that this approach provides much better equalization ability with no extra complexity as compared to the benchmark apart from additional delay elements. In Sec. 3.5.3, we derive a delayed dual-tap equalizer from the delayed single-tap equalizer that further improves the performance of the system by smoothing the group delay function. For a special weighting factor of the two active taps, no extra complexity apart from adders and/or subtractors is incurred as compared to the system with delayed single-tap equalizer. In [117], the idea of sub-band processing with modulated FB for CD channels has been introduced. The complexity of the method in [117] as compared to our method is higher since it requires more active taps for the sub-band equalizer. Additionally, the author in [117] considers fractional delays which lead to a non-efficient structure for the FB, whereas we consider integer delays per sub-band leading to an efficient implementation of the FB.

Any linear channel distortion can in principle be compensated by a digital receiver operating at one sample per symbol [118]. This requires that, prior to sampling, the receiver employs an analog matched filter (matched to the convolution between the transmitted pulse shape and the propagating

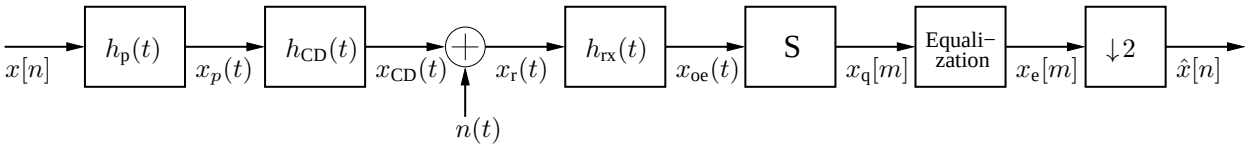

Fig. 3.1. Generic Single-channel Optical System Model

channel). Also, the performance of a symbol-rate equalizer is sensitive to sampling time error. A fractionally spaced equalizer (FSE) can implement the matched filter and equalizer as a single unit and can compensate for sampling time errors, provided that the baseband signal is sampled above the Nyquist rate [118–121]. The experiments in coherent optical transmission invariably use an oversampling rate of two for CD compensation [122–125]. Therefore, the different equalizers that we present for CD compensation are FSEs operating at two samples per symbol. In Sec. 3.6, we design a FDE that equalizes not only the propagating CD channel but also the impulse responses of the transmit and receive filter. Moreover, the design of the equalizer takes into account the aliasing terms that arise because of the receive filter.

3.2 System Model for CD Equalization

A 28 GBaud PDM return-to-zero (RZ-50%) QPSK transmission with digital coherent receiver applying two-fold oversampling with 56 GSample/s is used to verify the different methods for CD equalization. The setup of a single-channel optical transmission system under investigation in this chapter is shown in Fig. 3.1.

The discrete-time complex quadrature amplitude modulation (QAM) input data $x[n]$ of variance $\mathrm{E}[|x[n]|^2] = \sigma_x^2$ is passed through the waveform generator $h_{\mathrm{p}}(t)$ to get the continuous-time complex signal $x_{\mathrm{p}}(t)$

$$x_{\mathrm{p}}(t) = \sum_{n=-\infty}^{\infty} x[n] h_p(t - nT_s) \tag{3.1}$$

where T_s is the symbol period. The waveform generator $h_{\mathrm{p}}(t)$ employs a RZ-50% line code given as

$$h_{\mathrm{p}}(t) = \begin{cases} \cos\left(\frac{\pi}{4} + \frac{\pi}{4}\cos\left(\frac{2\pi t}{T_s}\right)\right), & \text{for} \quad 0 \le t \le T_s, \\ 0, & \text{elsewhere.} \end{cases} \tag{3.2}$$

The signal $x_{\mathrm{p}}(t)$ has variance σ_t^2

$$\begin{aligned} \sigma_t^2 = \mathrm{E}\left[|x_{\mathrm{p}}(t)|^2\right] = \mathrm{E}\left[\left|\sum_{n=-\infty}^{\infty} x[n] h_p(t - nT_s)\right|^2\right] = \sum_{n=-\infty}^{\infty} \mathrm{E}[|x[n]|^2] |h_{\mathrm{p}}(t - nT_s)|^2 \\ = \sigma_x^2 \sum_{n=-\infty}^{\infty} |h_{\mathrm{p}}(t - nT_s)|^2, \end{aligned} \tag{3.3}$$

which follows from the assumption that the entries of the input signal $x[n]$ are independent and identically distributed (i.i.d)

$$\mathrm{E}\left[x[n]x[n']\right] = \begin{cases} \sigma_x^2, & \text{for} \quad n = n', \\ 0, & \text{elsewhere.} \end{cases}$$

The band-limited transmitted signal $x_{\mathrm{p}}(t)$ is then coupled into the standard single mode fiber which is modeled as a linear CD channel

$$x_{\mathrm{CD}}(t) = h_{\mathrm{CD}}(t) * x_{\mathrm{p}}(t). \tag{3.4}$$

An equivalent baseband linear time invariant model for the CD channel can be written in terms of its frequency response as $h_{\mathrm{CD}}(t) = \int_{-\infty}^{+\infty} H_{\mathrm{CD}}(f)\mathrm{exp}(j2\pi ft)\mathrm{d}f$ where

$$H_{\mathrm{CD}}(f) = \mathrm{exp}\left(-j\alpha_{\mathrm{CD}} f^2\right). \tag{3.5}$$

The argument f in (3.5) is the frequency of the baseband electrical signal and not the optical signal. It is defined in the frequency interval $-f_s/2 \leq f \leq +f_s/2$ with f_s representing the sampling frequency at the ADC (modeled as a 5th-order Bessel filter in (2.7)). The coefficient α_{CD} is defined by

$$\alpha_{\mathrm{CD}} = \frac{\pi\lambda_c^2}{c}\mathrm{CD}, \tag{3.6}$$

where the value of the chromatic dispersion CD is expressed in ps/nm, the carrier wavelength λ_c in nm and the speed of light in vacuum c in m/s. In the receiver, the signal $x_{\mathrm{CD}}(t)$ is perturbed with white Gaussian noise (WGN) $n(t)$, originating from different sources as we explained in Sec. 2.4, which is added to the signal

$$x_{\mathrm{r}}(t) = x_{\mathrm{CD}}(t) + n(t). \tag{3.7}$$

The noise $n(t)$ has variance σ_n^2 is related to optical signal-to-noise ratio (OSNR) commonly used in optical communication systems as

$$\sigma_n^2 = \frac{\sigma_t^2}{\mathrm{OSNR}}\frac{B}{B_{\mathrm{ref}}}, \tag{3.8}$$

where $B = 28$ GHz is the symbol rate and $B_{\mathrm{ref}} = 12.5$ GHz is the reference bandwidth over $|\Delta\lambda_c| = 0.1$ nm resolution bandwidth of optical spectrum analyzers at $\lambda_c = 1550$ nm carrier wavelength calculated as $B_{\mathrm{ref}} = (c/\lambda_c^2) \times |\Delta\lambda_c|$.

The perturbed signal $x_{\mathrm{r}}(t)$ is then optically filtered at the receiver

$$x_{\mathrm{o}}(t) = h_o(t) * x_{\mathrm{r}}(t) \tag{3.9}$$

where the low-pass equivalent transfer function of the optical filter $h_o(t)$ is modeled in the FD as a Gaussian function given in (2.6) with order $n_{\mathrm{od}} = 2$ expressed by

$$H_o(f) = \mathrm{exp}\left[-\ln(\sqrt{2})\left(\frac{2f}{B_{\mathrm{O3dB}}}\right)^4\right] \tag{3.10}$$

and $B_{\mathrm{O3dB}} = 35$ GHz represents the double-sided 3-dB bandwidth of the filter.

The optical signal $x_{\mathrm{o}}(t)$ is then converted to an electrical signal $x_{\mathrm{oe}}(t)$

$$x_{\mathrm{oe}}(t) = h_e(t) * x_{\mathrm{o}}(t) \tag{3.11}$$

where $h_e(t)$ represents the low-pass characteristics of the electrical components. It can be modeled in the FD as a 5th-order Bessel function defined in (2.7) given by

$$H_e(f) = \frac{945}{jF^5 + 15F^4 - j105F^3 - 420F^2 + j945F + 945} \tag{3.12}$$

where $F = \frac{K_{\text{3dB}}}{B_{\text{E3dB}}} f$, $K_{\text{3dB}} = 2.4274$ is the 3-dB normalization constant and we choose $B_{\text{E3dB}} = 0.7 \times B = 19.6$ GHz as the single-sided 3-dB bandwidth of the filter. The optical and electrical filters define the opto-electronic front-end of the coherent receiver modeled by $h_{\text{rx}}(t) = h_o(t) * h_e(t)$ in Fig. 3.1 which has the frequency response of $H_{\text{rx}}(f) = H_o(f)H_e(f)$.

The electrical signal $x_{\text{oe}}(t)$ is sampled with sampling time equal to $T_s/2$ i.e. at twice the symbol rate. The m-th sample of the electrical signal after the receive filter is

$$x_{\text{q}}[m] = x_{\text{oe}}(mT_s/2). \tag{3.13}$$

The signal $x_{\text{q}}[m]$ is then equalized by one of the different available methods either in the TD or in FD. The target of the investigation here is to examine solely the equalization penalty. No other impairment, laser phase or carrier frequency offset is considered in the simulation. The equalized signal is denoted as $x_{\text{e}}[m]$ which is finally downsampled by a factor of 2 to get the symbol-based signal $\hat{x}[n]$.

The system performance is quantified by the required OSNR to tolerate different CD values (accordingly different lengths of the fiber) to get a bit-error-ratio (BER) of 10^{-3} evaluated over 0.1 nm resolution noise bandwidth and for 10^6 bits.

3.3 Literature Review: Time-domain and Frequency-domain CD Compensation Methods

We revisit the popular digital filters for CD compensation encompassing TD and FD designs.

3.3.1 Time-domain CD Compensation Methods

Time-domain CD compensation methods include the use of adaptive and non-adaptive digital filters. Adaptive methods for CD equalization have been suggested and intensively researched. The authors in [90, 91] reported their CD equalization work using the maximum likelihood sequence estimation (MLSE) method, which was the first proposed digital equalizer. The MLSE electronic equalizer is implemented by using the Viterbi algorithm [126], where the most likely bit sequence formed by a series of distorted signals is looked for. The MLSE is not tailored to a specific distortion but is optimum for any kind of optically distorted signal detected by the photodiode. Later the authors in [92, 93] developed a least mean squared (LMS) adaptive filter to compensate CD in a 112 Gbit/s non return-to-zero (NRZ)-PDM-QPSK coherent optical transmission system. In general, adaptive filters show the best performance in CD equalization. However, their convergence speed is slow and the update of the tap weights increases the computational complexity of the system. Additionally, CD is time invariant and it is polarization-independent. So we restrict ourselves to non-adaptive linear digital filters for long-haul CD compensation.

3.3.1.1 FIR Filters

S. J. Savory designed in [94–96] a TD FIR filter to compensate for large CD values. To derive the equalizer, the impulse response of the CD channel is firstly obtained by taking the inverse Fourier transform of (3.5). Then, the realization of the FIR filter for equalization arises from the digitization of the inverse of the TD impulse response of the CD channel. The impulse response of the FIR CD equalizer is truncated by a window filter to get a finite duration causal FIR filter and to avoid aliasing that arises in digital systems. A closed form expression of the complex coefficients of the

FIR CD equalizer was given in [94–96]. The required number of taps $N_{\text{TD-FIR}}$ for the compensation of CD channel is given by

$$N_{\text{TD-FIR}} = 2 \times \left\lfloor \frac{\alpha_{\text{CD}}}{2\pi} \left(\frac{o_s}{T_s} \right)^2 \right\rfloor + 1 \tag{3.14}$$

which has an odd value and o_s is the oversampling factor.

Although the simulations presented with this approach show an almost penalty-free performance for moderate and high CD values, this method suffers from high complexity. For an FIR of $N_{\text{TD-FIR}}$ taps, the number of real multiplications per output symbol is

$$C_{\text{TD-FIR}} = 4N_{\text{TD-FIR}}. \tag{3.15}$$

This arises from the well-known realization of complex multiplications of two symbols which requires four real multiplications and two real additions. The complexity for TD FIR filtering grows linearly with $N_{\text{TD-FIR}}$. The square dependence of the complexity on the baud-rate and the linear dependence on CD indicates how quickly TD FIR filtering becomes computationally intense. For example, to compensate for a CD value of 32,000 ps/nm with baud-rate value of $B = 28$ GHz and an oversampling factor $o_s = 2$, the number of taps for the equalizer $N_{\text{TD-FIR}}$ is 803. Moreover, a longer FIR filter introduces a longer delay and requires more area on a DSP chip. This method also suffers from another two drawbacks. The first drawback is that the quality of CD compensation does not improve by increasing the number of coefficients for the equalizer. The second drawback is that the method shows suboptimal performance especially for modulation formats with higher spectral efficiencies.

To overcome these drawbacks, the authors in [97] presented an optimal least-squares (LS) FIR digital filter design for CD compensation. Their methodology is based on the convex minimization of the complex error between the frequency response of the desired CD equalizer (taken as the inverse of CD channel in (3.5)) and an equalizer designed over the whole frequency bandwidth $-f_s/2 \leq f \leq +f_s/2$ or over a limited bandwidth obtained for example when employing a pulse shaping filter with a given roll-off factor at both the transmitter and the receiver. The impulse response of the LS TD-FIR filter is obtained by taking the IDFT of the designed FD equalizer. A comparison between the coefficients of the closed form expression of the TD-FIR filter in [94–96] and the designed impulse response by the LS method reveals that both are partly similar. However, the superiority of the LS-FIR method arises by the obtained more constant group delay. Additionally, the LS-FIR filter is not only designed to obtain arbitrarily good CD compensation but also requires fewer taps for the same BER performance as in [95] such that a reduction by 63% of the number of taps is incurred for equalizing the same value of CD of 1000 ps/nm. A straightforward alternative to this proposed optimization is to get the underlying TD FIR impulse response of CD equalizer by taking the M-point IDFT of the inverse of the CD channel in (3.5)

$$H_{\text{FSM}}(f_k) = H_{\text{CD}}^{-1}(f_k) = \exp\left(+j\alpha_{\text{CD}} f_k^2\right). \tag{3.16}$$

The frequency response of the CD equalizer $H_{\text{FSM}}(f_k)$ is evaluated at M uniformly-spaced discrete frequencies $f_k, k = 0, 1, \cdots, M-1$ (corresponding to those frequencies of an M-point DFT) defined as

$$f_k = \begin{cases} \frac{o_s}{MT_s} k, & \text{for } 0 \leq k \leq M/2 - 1, \\ -\frac{o_s}{MT_s}(M-k), & \text{for } M/2 \leq k \leq M-1. \end{cases} \tag{3.17}$$

This method is called the frequency sampling method (FSM). A TD FIR filter obtained by the FSM method has a lower design complexity as the proposed LS-FIR design since for the former

the underlying FD response is to be evaluated just at M discrete frequency points whereas for the latter it is to be evaluated at all the frequencies of the available bandwidth. With 4-QAM modulation schemes, the LS-FIR and the underlying TD FIR filter obtained by FSM have a very good and same performance for large CD values. The authors in [97] concluded that for high spectral efficiency modulation formats like 512-QAM, the performance of the system with LS-FIR filter is superior as compared to system where the equalizer is obtained by FSM method. However, since high spectral efficiency modulation formats are very sensitive to non-linear effects due to the high required OSNR, smaller modulation formats are desired where in this case both methods for equalizer design deliver the same performance.

3.3.1.2 IIR Filters

An efficient alternative to FIR filtering for CD compensation is clearly highly desirable. IIR filters inherently require a reduced number of taps for a similar response compared to FIR counterparts due to the feedback path.

In [99], the author designed an all-pass IIR filter with both real and complex-valued coefficients to approximate the desired phase response of the CD channel. The real-valued IIR filtering scheme requires a Hilbert transformer and time reversal operations. In paper [98], the authors showed that CD compensation with real-valued coefficients for IIR filtering delivers similar performance as FIR filtering with a substantially reduced number of multiplications. For large dispersion values, the IIR equalizer has half the number of taps as compared to the counterpart FIR equalizer

$$N_{\text{TD-IIR}} = \frac{1}{2} N_{\text{TD-FIR}}. \tag{3.18}$$

The large overhead from the Hilbert transformer and the special design considerations of the time reversal device limit the overall performance of the system with real-valued coefficients of the IIR equalizer. These are overcome by designing complex-valued coefficients for the IIR filter [99]. As stated by the author in [99], complex-coefficient IIR filter is practically impossible to design such that the response is matched in the entire frequency bandwidth [127]. However it can be designed to match well within a limited bandwidth, so some degree of oversampling is required when complex IIR filtering is to be employed. The tradeoff between computational efficiency and higher sampling rate must be considered. Moreover, the total amount of CD compensation that can be achieved using this filtering approach is limited. Nevertheless, complex IIR filtering is highly efficient for small dispersion values, and its advantage shows up when distributed compensation is considered.

In [100], a stable complex-valued IIR all-pass filter for CD equalization over the whole desired frequency bandwidth was designed. The authors present a design methodology for finding the complex coefficients of the IIR filter that incorporate the desired group delay as well as desired phase behavior in a multi-step multi-objective optimization framework. This approach delivers better performance in comparison with other FIR-based equalization. The benefit obtained by this approach is that the number of taps for the equalizer reduces to a range of 65% to 70% as compared to FIR filtering in [95] for the same performance. However, it is not advantageous to use the proposed framework for high CD values since the computational complexity grows linearly with the order of the filter. One possible way to reduce the complexity for long fiber lengths is to divide the long CD channel into narrow sub-bands using a FB structure [112, 115, 116] and to design low order IIR equalizer for each of them as in [101].

However, the inherent feedback of IIR equalizers makes it impossible to implement in high speed applications with parallel signal processing.

3.3.2 Frequency-domain CD Compensation Methods

FDE is well established in electrical communications and known in the literature [128, 129]. It has been proposed for the equalization of wireless channels [130–134] and is a strong candidate for applications beyond the current LTE systems. In optical communications, FDE is very attractive for CD equalization in long-haul transmissions. This is because it has much lower complexity than TDE for large dispersion values when the equalizer has many taps [18, 108–110] owing that to its block-to-block operation by using FFT and IFFT.

The temporal dispersion of the received signal is decreased by FDE. Therefore, the computational complexity of the timing and frequency synchronization is significantly reduced because they can be performed after the stage of FDE of CD. Additionally, since CD is time-invariant and polarization independent, the FD equalizers for CD are static i.e. non-adaptive. As a result, we stick to the method of FDE of CD with static filters where the equalization is done at the first stage in the DSP module.

There are two classes of FDE techniques: namely MC-FDE [18, 102] and SC-FDE [104–110]. In MC-FDE, cyclic-prefix orthogonal frequency division multiplexing (CP-OFDM) with IFFT and FFT at the transmitter and the receiver, respectively, is used. Thus, digital-to-analog converters (DACs) are required at the transmitter for filtering the signal. However, multi-carrier systems suffer from high peak-to-average power ratio (PAPR) values which make them vulnerable to the nonlinearities in the fiber [102, 135]. Moreover, there is a loss in spectral efficiency due to the cyclic prefix. Although CP-OFDM transmission has low computational complexity because of its block-wise operation, SC-FDE remain advantageous due to the aforementioned problems.

For SC-FDE there are two configurations which are CP-FDE and Overlap-FDE (OFDE). In CP-FDE [104] the input symbol sequence in the transmitter is divided into blocks each having M symbols. The last N_{cp} symbols of the FFT block are copied and inserted, exactly as in OFDM, at the beginning of the block. If the duration of the CP is longer than the maximum time delay difference of the channel impulse response, CP can avoid the inter-block-interference (IBI) from the previous block. In SC-FDE transmission, unique word (UW) can be used as CP [130]. A UW of N_{cp} symbols is inserted at the end of each DFT block and the previous UW is used as the CP for the present block. Since each UW is a known symbol sequence, it can be used not only for CP but also for synchronization and for equalization. After CP insertion, the symbol sequence is transmitted. At the receiver, CP is removed. An M-point DFT is applied to decompose the received signal into M frequency components. Then single tap equalization is carried out in the frequency-domain to each block through point-wise multiplication with the transfer function of the equalizer given in (3.16). Finally IDFT with M-point is done to get the serial equalized signal. In long-haul communication systems, the block length M must be large to compensate the large temporal dispersion created by CD. Although the guard interval or the CP is effective to eliminate the inter-symbol interference due to the temporal dispersion, the large length of the CP degrades the transmission efficiency. Furthermore, the block-to-block operation with large block length is vulnerable to synchronization errors and this increases the computational complexity of the receiver. To overcome the aforementioned problems of CP for SC for FDE, the second method was suggested which is the OFDE presented in [111–115] for long-haul CD compensation [105–

110]. OFDE was proposed for wireless systems to improve transmission efficiency of FDE by dispensing with the guard interval [136].

Overlap techniques perform linear convolution in the FD. In OFDE, the sequence is divided into blocks of length M which is processed piecewise. Then the filtered segments are carefully pieced back together. The building blocks of OFDE are: I/DFT of length M, the formation of input blocks for filtering and the formation of the output sequence. The overlap is required because filtering a signal in the FD results in cyclic convolution when using DFTs and IDFTs. IBI is eliminated by overlapping either the input blocks or the output blocks. These methods are named, respectively, OLS and OLA. The number of overlapped samples is denoted as v. Block-wise use of circular convolution to accomplish linear convolution is also referred to as fast convolution.

The overall complexity of FD filtering is composed of the complexity of DFT, IDFT and the point-wise multiplication in the FD. For OLS and OLA FD filtering, the number of real multiplications per output symbol can be expressed by

$$C_{\text{FD-OLS/OLA}} = \frac{2C_{\text{DFT/IDFT}} + C_{\text{filtering}}}{v}. \tag{3.19}$$

In what follows, we explain the OLS and OLA fast convolution methods that are relevant to this work.

3.3.2.1 Overlap-and-save Method

The schematic for FDE of $x_{\text{q}}[m]$ with the overlap-and-save method is illustrated in Fig. 3.2. Serial to parallel conversion is applied to the signal $x_{\text{q}}[m]$ forming blocks $x_{\text{q}}^{(i)}[m]$ with a certain overlap factor, where the block length M is the I/DFT-length. Each block $x_{\text{q}}^{(i)}[m]$ consists of $M - v$ new samples and is extended by v samples from its trailing neighbor $x_{\text{q}}^{(i+1)}[m]$. Afterward, an DFT is applied on each block $x_{\text{q}}^{(i)}[m]$ to get the FD signal $X_{\text{q}}^{(i)}[k], k = 0, 1, \cdots, M-1$. Filtering of $X_{\text{q}}^{(i)}[k]$ in FD is done through point-wise multiplication of it with the coefficients of the equalizer $E[k]$. For equalizing the CD channel $E[k] = H_{\text{CD}}^{-1}(f_k)$ as given in (3.16). Each block of the FD filtered signal $X_{\text{eq}}^{(i)}[k]$ is transformed into the TD through performing IDFT of length M to get $y_{\text{eq}}^{(i)}[m]$. Finally, the processed data blocks are combined together, and the bilateral overlap samples are symmetrically discarded before converting the parallel blocks into the serial signal $x_{\text{e}}[m]$.

In OFDE, the overlap length v is an important factor. In general it should be larger than the length of the propagating channel impulse response. We assume throughout this thesis that the factor of overlap is 50% of the block size M i.e. $v = M/2$ independent from the channel memory. The OLS method with $v = M/2$ is denoted as OLS-50%.

3.3.2.2 Overlap-and-add Method

The structure of the FDE of $x_{\text{q}}[m]$ with overlap-and-add one-side zero-padding (OLA-OSZP) method is shown in Fig. 3.3. In OLA method, serial to parallel conversion is applied to the signal $x_{\text{q}}[m]$ forming small blocks denoted as $x_{\text{q}}^{(i)}[m]$ having $M - v$ samples without any overlap with the adjacent block $x_{\text{q}}^{(i+1)}[m]$. Each block $x_{\text{q}}^{(i)}[m]$ is appended with a vector of zeros of length v at the tail. The formed block is denoted as $x_{\text{qa}}^{(i)}[m]$ which is of length M (length of I/DFT) in order to be consistent with the OLS method. Each block $x_{\text{qa}}^{(i)}[m]$ is transformed by an DFT into the FD to get the signal $X_{\text{qa}}^{(i)}[k], k = 0, 1, \cdots, M-1$. Filtering of $X_{\text{qa}}^{(i)}[k]$ in FD is done through point-wise multiplication of it with the coefficients of the equalizer $E[k]$. For equalizing the CD channel

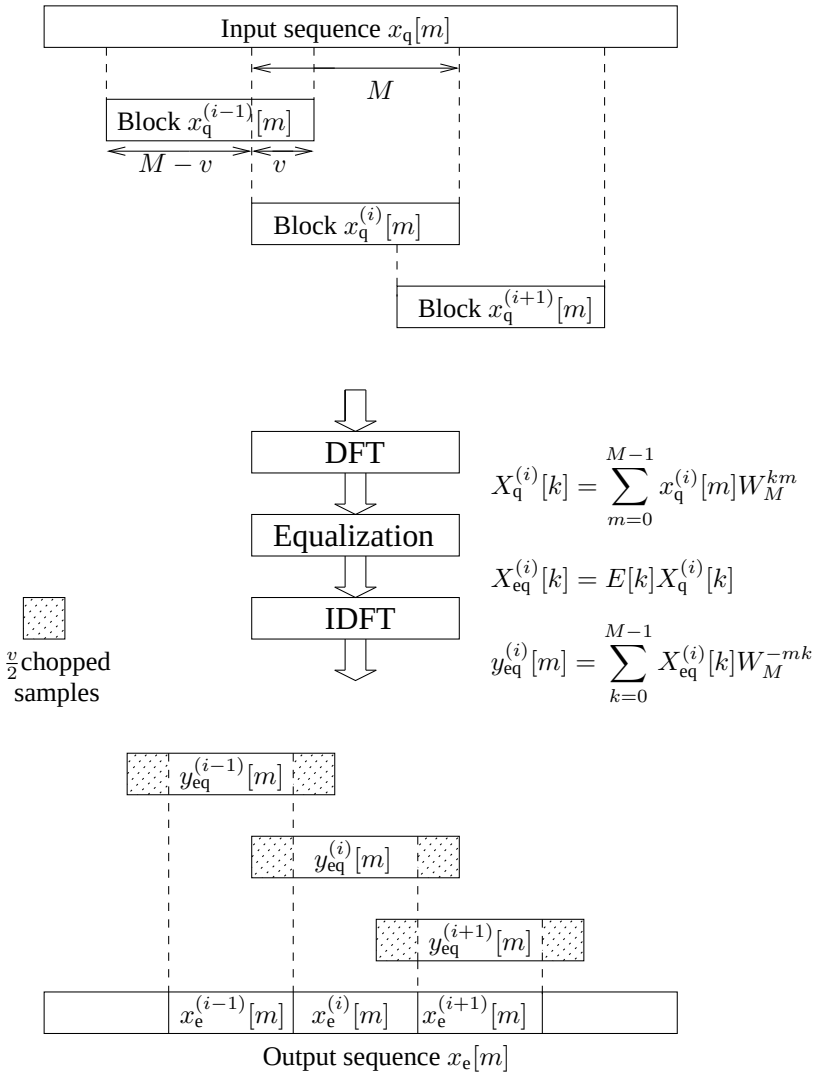

Fig. 3.2. Concept of Overlap-and-save for Filtering: forming of overlapping blocks, DFT, FD filtering, IDFT, discarding and forming of output sequence

$E[k] = H_{\text{CD}}^{-1}(f_k)$ as given in (3.16). Each block of the FD filtered signal $X_{\text{eq}}^{(i)}[k]$ is transformed into the TD through performing IDFT of length M to get $y_{\text{eq}}^{(i)}[m]$. Parallel to serial conversion is applied to the filtered blocks. Finally the processed data sequences are combined by overlapping and adding as shown in Fig. 3.3 to get the signal $x_{\text{e}}[m]$. The OLA method with $v = M/2$ (same as in the OLS-50% method) is denoted as OLA-50%.

3.3.3 Implementation Complexity: TD vs. FD Filtering

If the I/DFT length M is power of two (which is assumed throughout this thesis), the I/DFT can be efficiently implemented as FFT. There is a large pool of different FFT algorithms. The most widespread one is the classical radix-2 algorithm, for which the length of the vector to be transformed needs to be a power of 2.

The number of real multiplications for an M-point I/FFT using split-radix algorithm on a block of length M of complex data is given in [137] as

$$C_{\text{I/FFT}} = M(\log_2 M - 3) + 4. \tag{3.20}$$

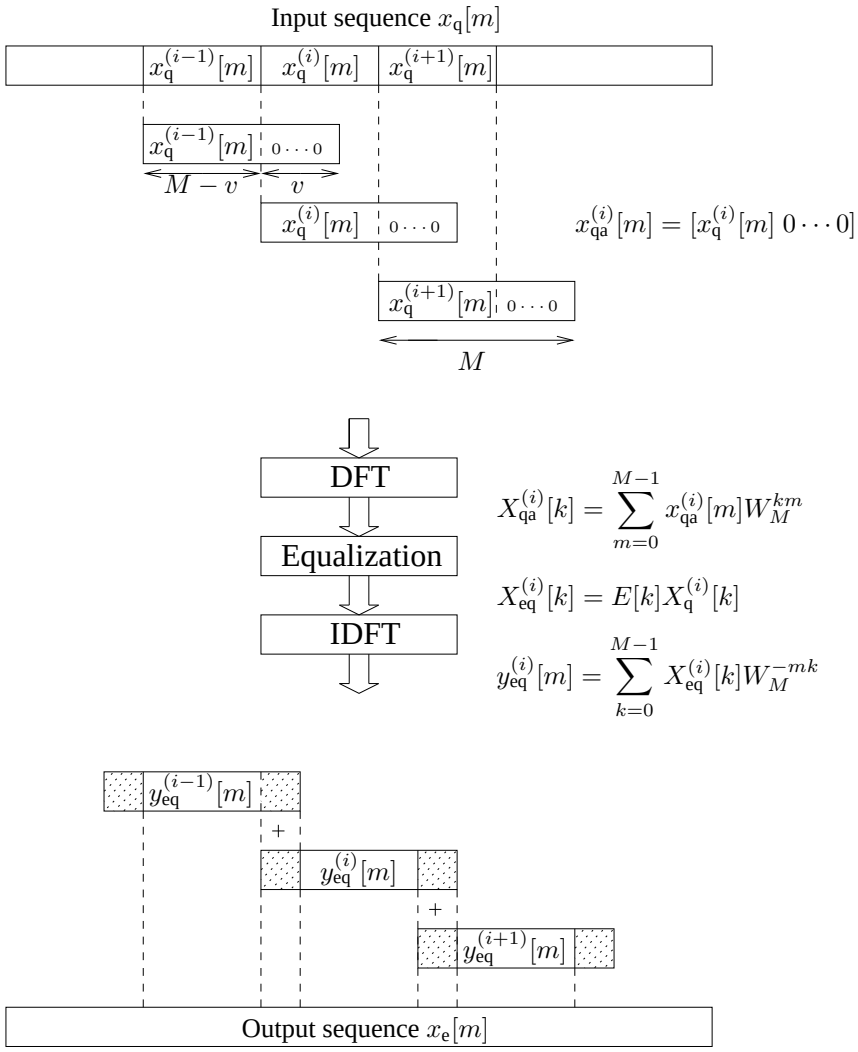

Fig. 3.3. Concept of Overlap-and-add for Filtering: forming of non-overlapping blocks, DFT, FD Filtering, IDFT, addition of the overlapping blocks for the formation of the output sequence

For OLS-50% and OLA-50%, the complexity in (3.19) becomes

$$C_{\text{FD-OLS/OLA}} = \frac{2C_{\text{I/FFT}} + 4M}{M/2} = 4\log_2 M - 4 + \frac{16}{M}. \tag{3.21}$$

Note that for the calculation of the complexity for OLS-50% and OLA-50%, the complete internal butterfly structures of IFFT and FFT, respectively, are considered for getting the output signal although half of the output in OLS-50% in discarded and half the input symbols to the FFT in OLA-50% is zero.

In Fig. 3.4, the complexity is plotted for TD and FD filtering for different values of M. Given that M is the I/FFT length for FD filtering, the filter (equalizer) in the TD has $M/2$ coefficients for exact linear convolution with TD filtering. Thus the complexity with TD filtering is $2M$. In comparison, the complexity with TD filtering increases linearly with M while with FD it increases logarithmically with M. When the number of taps for equalization is greater than 4, the multiplication complexity of OFDE is much less than the complexity of TDE. For CD compensation in

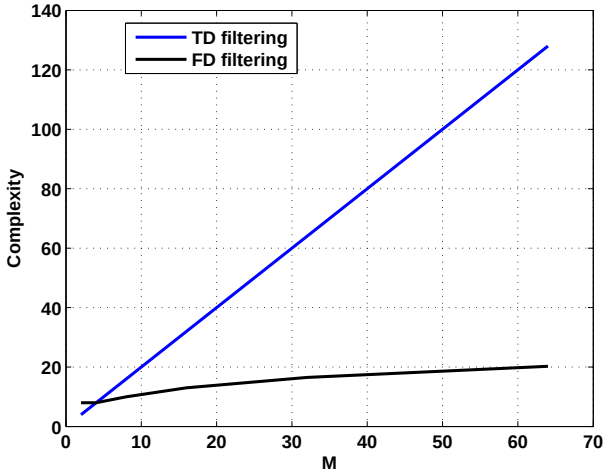

Fig. 3.4. Total number of complex multiplications per output sample for TD and FD equalization

long-haul transmission the equalizer requires more than 4 taps. Therefore, it is more efficient to perform FDE of CD.

3.4 Filter Bank Structure for Frequency-domain CD Compensation

Filter banks [112, 115, 116] are digital signal processing systems that could be used in FD CD compensation. An important class of FBs is the non-maximally decimated DFT FB [116], which can be efficiently implemented based on the use of polyphase networks (see Appendix A), DFT and IDFT. The filter bank structure is presented in detail in Appendix C.

To operate the FB structure as FD equalizer, FIR filters denoted as $E_k(z_{M/2})$ are placed between the analysis FBs (see Appendix C.2) and the synthesis FBs (see Appendix C.3). The resulting structure is shown in Fig. 3.5.

The FIR sub-band equalizer $E_k(z_{M/2})$ can have N_t coefficients

$$\begin{aligned} E_k(z_{M/2}) &= \sum_{\ell=0}^{N_t-1} e_k[\ell] z_{M/2}^{-\ell} \\ &= \sum_{\ell=0}^{N_t-1} e_k[\ell] \exp\left(-j2\pi f_k \ell MT/2\right), \end{aligned} \tag{3.22}$$

where the value of the tap $e_k[\ell]$ can be designed according to zero-forcing (ZF), matched-filter (MF) or minimum mean-squared error (MMSE) criterion.

Equalization with a multitap filter introduces a latency time τ_c dependent on N_t

$$\tau_c = rMT/2, r \in \{0, \cdots, N_t - 1\}. \tag{3.23}$$

The latency time τ_c adds a degree of freedom for the design of the equalizer.

The sub-band equalizer $E_k(z_{M/2})$ can have a single tap

$$E_k(z_{M/2}) = E_k = e_k, \tag{3.24}$$

where the value of e_k can be derived according to ZF, MF or MMSE criterion.

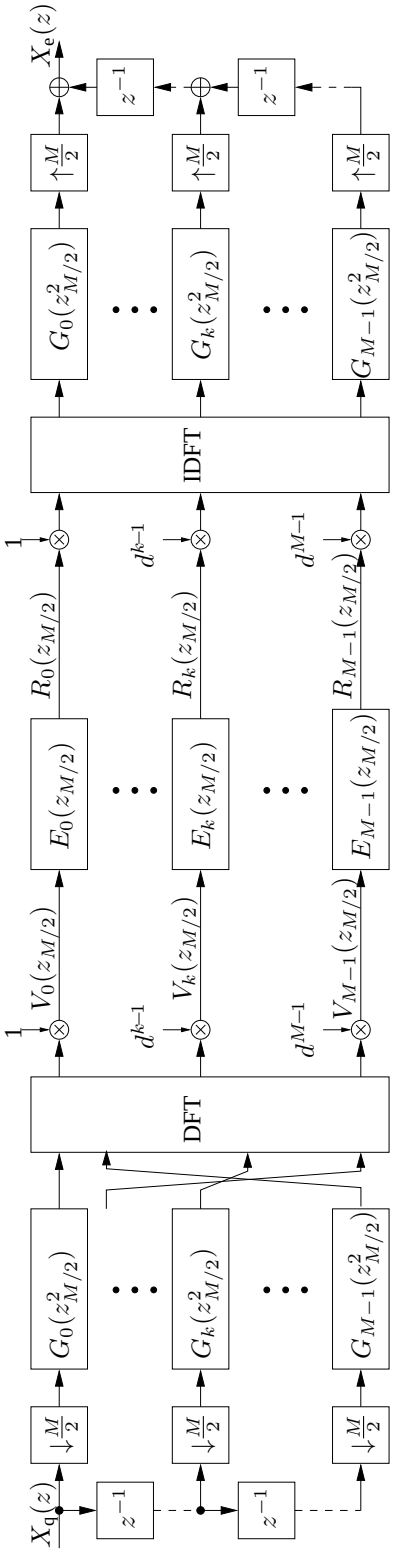

Fig. 3.5. Filter Bank for FD equalization: efficient analysis and synthesis DFT Filter Bank with polyphase components $G_k(z^2_{M/2})$; sub-band equalization is done through $E_k(z_{M/2})$ for CD compensation.

3.4.1 Filter Bank with Trivial Prototype Filters for FD CD Compensation

The OLS-50% method can be implemented as a non-maximally decimated DFT FB. This is achieved by having trivial filters i.e. rectangular impulse response for the analysis and the synthesis prototype filters $h_{\mathrm{P}}[l]$ and $s_{\mathrm{P}}[l]$, respectively, (c.f. (C.3) and (C.4) in Appendix C) of length $P = M$. However, the filter $s_{\mathrm{P}}[l]$ has $M/2$ zero coefficients due to discard part of the OLS method. The prototype filter in the analysis filter bank (AFB) and in the synthesis filter bank (SFB) is, respectively, given by

$$h_{\mathrm{P}}[l] = \sum_{k=0}^{M-1} h[k]\delta[l-k], \tag{3.25}$$

$$s_{\mathrm{P}}[l] = \sum_{k=\frac{M}{4}}^{\frac{3M}{4}-1} s[k]\delta[l-k], \tag{3.26}$$

where

$$h[k] = \begin{cases} \frac{1}{\sqrt{M}}, & \text{for } 0 \leq k \leq M-1, \\ 0, & \text{elsewhere.} \end{cases}$$

and

$$s[k] = \begin{cases} \frac{1}{\sqrt{M}}, & \text{for } \frac{M}{4} \leq k \leq \frac{3M}{4}-1, \\ 0, & \text{elsewhere.} \end{cases}$$

The z-transform representation of $h_{\mathrm{P}}[l]$ and $s_{\mathrm{P}}[l]$ is, respectively,

$$H_{\mathrm{P}}(z) = \mathcal{Z}\{h_{\mathrm{P}}[l]\} = \sum_{l=-\infty}^{l=+\infty} h_{\mathrm{P}}[l]z^{-l} = \sum_{k=0}^{M-1} h[k]z^{-k} = \frac{1}{\sqrt{M}} \sum_{k=0}^{M-1} z^{-k}, \tag{3.27}$$

$$S_{\mathrm{P}}(z) = \mathcal{Z}\{s_{\mathrm{P}}[l]\} = \sum_{l=-\infty}^{l=+\infty} s_{\mathrm{P}}[l]z^{-l} = \sum_{k=\frac{M}{4}}^{\frac{3M}{4}-1} s[k]z^{-k} = \frac{1}{\sqrt{M}} \sum_{k=\frac{M}{4}}^{\frac{3M}{4}-1} z^{-k}, \tag{3.28}$$

which when substituting $z = e^{j\omega T}$ can be expressed by

$$H_{\mathrm{P}}(z = e^{j\omega T}) = \frac{1}{\sqrt{M}} \sum_{k=0}^{M-1} e^{-j\omega Tk} = \frac{1}{\sqrt{M}} e^{-j\omega(M-1)\frac{T}{2}} \frac{\sin\frac{\omega MT}{2}}{\sin\frac{\omega T}{2}}, \tag{3.29}$$

$$S_{\mathrm{P}}(z = e^{j\omega T}) = \frac{1}{\sqrt{M}} \sum_{k=\frac{M}{4}}^{\frac{3M}{4}-1} e^{-j\omega Tk} = \frac{1}{\sqrt{M}} e^{-j\omega(M-1)\frac{T}{2}} \frac{\sin\frac{\omega MT}{4}}{\sin\frac{\omega T}{2}}. \tag{3.30}$$

The proof of (3.29) and (3.30) is given in Appendix D. It follows accordingly that the per sub-band analysis filter $H_k(z)$ and synthesis filter $S_k(z)$ is, respectively,

$$\begin{aligned} H_k(z) &= H_{\mathrm{P}}(zW_M^k) = H_{\mathrm{P}}\left(z = e^{j\left(\omega - 2\pi\frac{k}{MT}\right)T}\right) \\ &= \frac{1}{\sqrt{M}} e^{-j\omega(M-1)\frac{T}{2}} e^{j\pi\frac{k}{M}(M-1)} \frac{\sin(\frac{\omega MT}{2} - \pi k)}{\sin((\omega - 2\pi\frac{k}{MT})\frac{T}{2})}, \qquad (3.31) \\ S_k(z) &= S_{\mathrm{P}}(zW_M^k) = S_{\mathrm{P}}\left(z = e^{j\left(\omega - 2\pi\frac{k}{MT}\right)T}\right) \\ &= \frac{1}{\sqrt{M}} e^{-j\omega(M-1)\frac{T}{2}} e^{j\pi\frac{k}{M}(M-1)} \frac{\sin(\frac{\omega MT}{4} - \pi k)}{\sin((\omega - 2\pi\frac{k}{MT})\frac{T}{2})}. \qquad (3.32) \end{aligned}$$

The delay τ_{FB} introduced by the FB in this case is the sum of the delay introduced by the AFB and SFB

$$\tau_{\mathrm{FB}} = (M-1)T. \qquad (3.33)$$

Since the prototype filters for OLS-50% are trivial filters of length $P = M$, each polyphase component $G_m(z^M), m = 0, 1, \cdots, M-1$ of $H_k(z)$ in the AFB and $S_k(z)$ in the SFB has one coefficient which is equal to $1/\sqrt{M}$.

The following further step is needed to operate the FB structure as OLS-50%. The phase factors $\boldsymbol{D}$ in (C.13) of the prototype filters for an even P in the FD result in a cyclic shift of the signal in the TD. This can be proved by multiplying $\boldsymbol{D}$ by the DFT matrix $\boldsymbol{W}_M$ in AFB and the IDFT matrix $\boldsymbol{W}_M^{\mathrm{H}}$ in the SFB. This leads to the following permutation matrix

$$\boldsymbol{W}_M^{\mathrm{H}} \boldsymbol{D}^2 \boldsymbol{W}_M = \begin{bmatrix} 0 & 0 & \cdots & 1 \\ 1 & 0 & \cdots & 0 \\ 0 & 1 & \cdots & 0 \\ \vdots & \vdots & \ddots & \vdots \\ 0 & \cdots & 1 & 0 \end{bmatrix} \qquad (3.34)$$

which results in having direct connections of the signal input to the DFT in the AFB as opposed to cross connections seen in Fig. C.2.

Fig. 3.6 shows the OLS-50% method for linear convolution implemented as an efficient non-maximally decimated DFT FB. CD equalization is done in each sub-band through point-wise multiplication of the DFT transformed overlapping blocks of $X_{\mathrm{q}}(z)$ each of length M with the M-point vector equalizer $\boldsymbol{e} = [E_0(z_{M/2}), \cdots, E_{M-1}(z_{M/2})]$ where $E_k(z_{M/2}) = H_{\mathrm{CD}}^{-1}(f_k)$ given in (3.16). The equalizer per sub-band has only one tap i.e. $N_t = 1$. This method is denoted as the benchmark for FD CD compensation.

In general, to model linear convolution with an efficient non-maximally decimated DFT FB, the following inequality regarding the lengths (number of non-zero coefficients) of the filters should be fulfilled [112, 115]

$$L_E + L_h + L_s - 1 \leq 2M, \qquad (3.35)$$

where L_E, L_h, and L_s is the length of the equalizer, the analysis prototype filter $h_{\mathrm{P}}[l]$, and the synthesis prototype filter $s_{\mathrm{P}}[l]$, respectively. In the case of OLS-50%, since $L_h = P = M$ and $L_s = M/2$, the length of the equalizer L_E should be

$$L_E \leq M/2 + 1. \qquad (3.36)$$

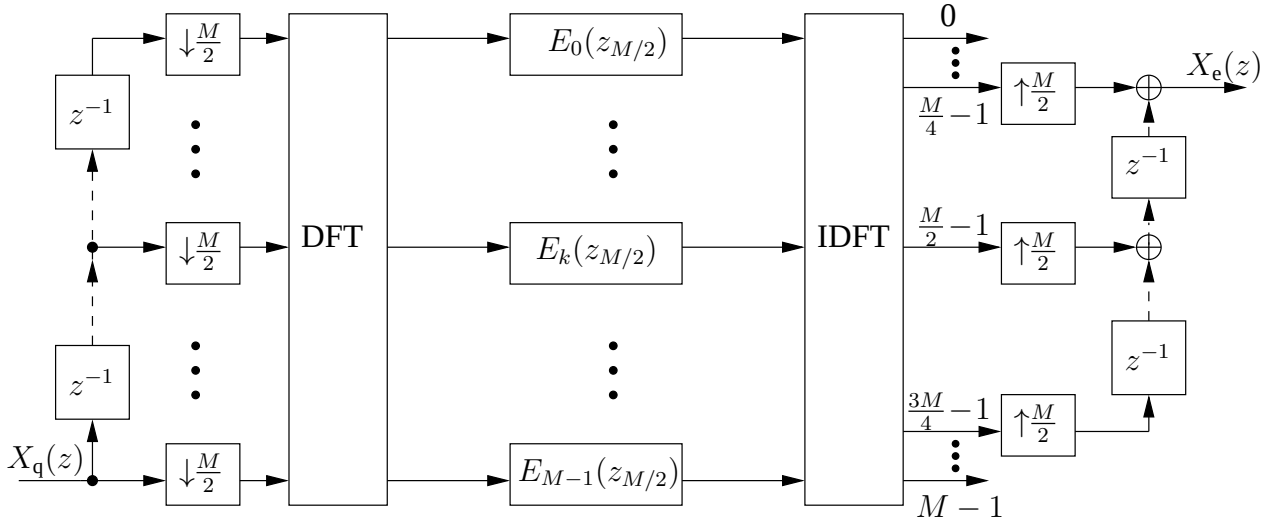

Fig. 3.6. The method of OLS-50% realized as a non-maximally decimated with trivial prototype filters DFT FB with sub-band equalizer $E_k(z_{M/2})$ for CD compensation.

In the method for CD compensation presented so far, all M degrees of freedom have been used for the design of the overall equalizer. So, it is no longer strictly the OLS method that implements linear convolution with the aid of DFT and IDFT, but it is a FB based CD equalization with trivial prototype filters. The system thus belongs to the class of linear periodically time variant systems.

In Fig. 3.7, CD tolerance for $M = 512$ is plotted with both methods for equalization which are the exact linear convolution and the approximate linear convolution based on the efficient non-maximally decimated DFT FB with trivial prototype filters. Exact linear convolution for CD compensation is attained by having an equalizer in the TD which has $M/2$ coefficients. The $M/2$ coefficients are obtained by taking an M-point IFFT of equalizer's transfer function in (3.16), out of which just $M/2$ TD coefficients are chosen (in our case we choose the middle $M/2$ points) which are appended with $M/2$ zeros and finally transformed back into the frequency domain by an M-point FFT. The resulting M-point FD equalizer is then used for CD compensation. As expected, CD tolerance is extended with the FD equalization based on the approximate linear convolution since more degrees of freedom are exploited for the design of the equalizer whose memory is therefore prolonged.

3.4.2 Filter Bank with Non-trivial Prototype Filters for FD CD Compensation

Another approach for FD CD compensation is based on an efficient non-maximally decimated DFT FB presented in Appendix C with non-trivial prototype filters (NTFs) for the analysis and synthesis filters. The same prototype filter is used in both AFB and SFB. We choose the extended lapped transform (ELT) for the prototype filter given in (C.21) which is a low pass filter of length $P = 2M$ with linear phase and has real coefficients. Each polyphase component $G_m(z^M), m = 0, 1, \cdots, M-1$ of the analysis and synthesis filter thus has two coefficients.

In Fig. 3.8, this method and the benchmark for CD compensation have been compared by evaluating their applicability for different I/FFT lengths M and for compensating different CD values. The simulations reveal that for the same required OSNR value, higher CD values are compensated for the same I/FFT length with the method of FD CD compensation with FB structure having non-trivial prototype filters. This is because the memory of the equalizer is further increased by the

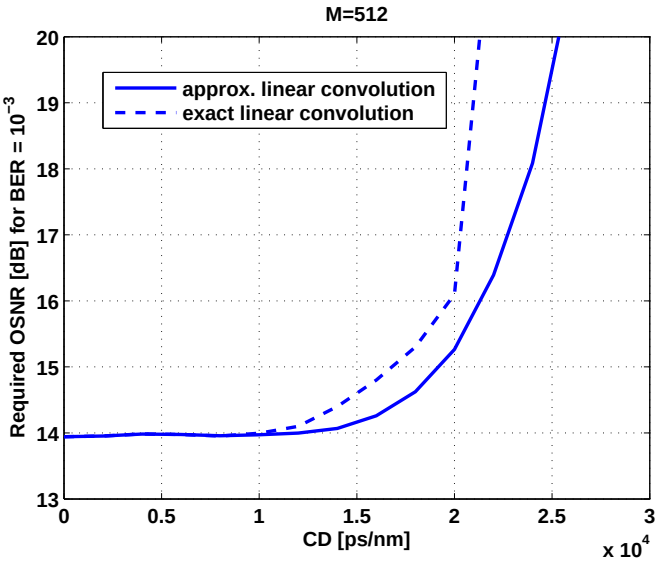

Fig. 3.7. Approximate linear convolution vs. exact linear convolution for FD CD equalization

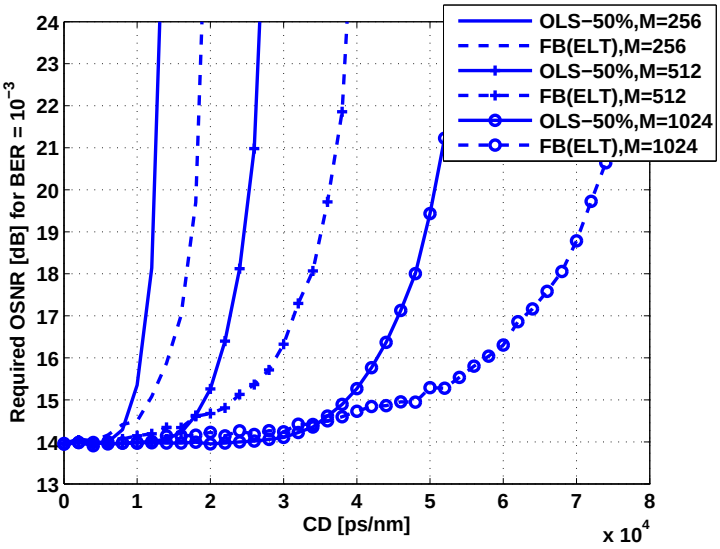

Fig. 3.8. Required OSNR for the compensation of different CD values given different I/FFT length M: Non-maximally decimated DFT FB with trivial prototype filter and non-trivial ELT prototype filter structures.

prototype filters as compared to the case with trivial prototype filters (for the benchmark method) and because the input signal for equalization is filtered by the ELT prototype filter before being further processed. For the same CD tolerance a lower value for the OSNR is required with the FB based FDE with non-trivial prototype filters. This structure in contrast to the benchmark allows to extend the reach even further for acceptable OSNR penalties up to 3 dB. Moreover, this benefit increases for large I/FFT length.

However the improved performance obtained comes at the cost of increased complexity as compared to the benchmark due to filtering by the prototype filter in the AFB and SFB. Since the prototype filter has real coefficients of length KM, an additional term of $2(2KM)/(M/2)$ is to be added for the complexity calculations in (3.21). For the case of ELT $K = 2$. Therefore, the

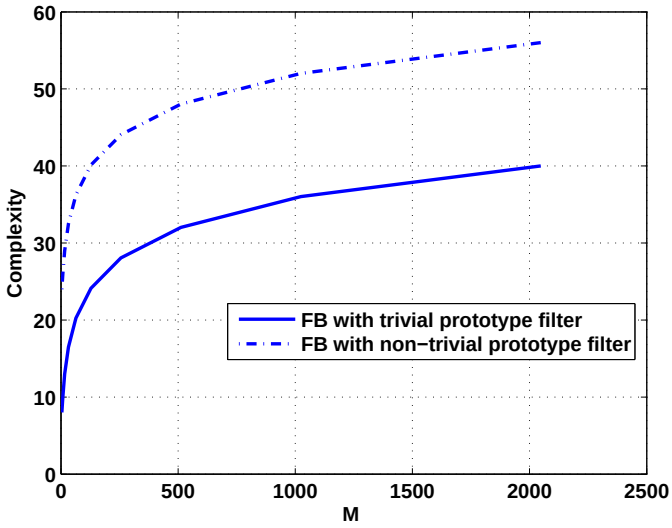

Fig. 3.9. Complexity Comparison: FB structure with trivial and non-trivial prototype filters for FD CD compensation.

complexity in (3.21) for FB structure with non-trivial prototype filters can be expressed by

$$C_{\text{FB-NTF}} = 4\log_2 M + 12 + \frac{16}{M}. \tag{3.37}$$

Fig. 3.9 shows the complexity of the FB structure for FD CD compensation with trivial and non-trivial prototype filters for different values of I/FFT M. The constant gap between the two curves is due to the additional filtering by the non-trivial prototype filter in the non-maximally decimated DFT FB structure.

To get the same complexity for both structures, the I/FFT length M for OLS-50% should be increased. Concretely, to achieve a complexity of $C_{\text{FD-OLS}}$=40 real multiplications per output symbol, the I/FFT length of $M_{\text{FD-OLS}}$=2048 is needed for OLS-50% while $M_{\text{FB-NTF}}$=128 is needed for the non-maximally decimated FB structure with non-trivial prototype filters. The former shows a dramatic performance advantage in terms of CD tolerance as the latter for $M_{\text{FD-OLS}}$=2048. Therefore, in the coming subsections and for the next chapter the benchmark (i.e. OLS-50%) is adopted and further improved for CD equalization.

In paper [138], we presented the method of FD CD compensation based on a maximally decimated efficient DFT FB structure with non-trivial prototype filters. The maximally decimated FB structure utilizes more efficiently the spectral bandwidth as the non-maximally decimated FB since the up- and down-sampling rate L per subband is equal to the number of sub-bands M ($L = M$ in Fig. C.1). However, the signal at the output of a back-to-back connection of analysis and synthesis FB is no longer alias-free. This disadvantage can be overcome by offsetting the real and the imaginary parts of the signal in the SFB, a process known as staggering operation, and performing destaggering in the AFB (refer to Sec. 4.3 for detailed explanation of both operations). Additionally, upon inserting a single tap CD equalizer into this structure the output is still not necessarily alias-free. However, we were able to find a special arrangement of the equalizer that preserves an alias-free output. FD CD equalization with this method delivered the same performance as the non-maximally decimated decimated FB with a non-trivial prototype filter since both structures are inherently alias-free.

3.5 Group Delay Equalization of CD

3.5.1 Motivation

The phase of the CD channel perceived from (3.5) reads as

$$\phi_{\text{CD}}(f) = -\alpha_{\text{CD}} f^2 \tag{3.38}$$

which has a quadratic behavior with respect to frequency f. The group delay $\tau_{\text{CD}}(f)$ of the CD channel which is obtained by differentiating the phase $\phi_{\text{CD}}(f)$ with respect to the angular frequency $\omega = 2\pi f$ and taking the negative sign of the result reads as

$$\tau_{\text{CD}}(f) = -\frac{\partial \phi_{\text{CD}}(f)}{\partial 2\pi f} = \frac{\alpha_{\text{CD}}}{\pi} f \tag{3.39}$$

which changes linearly with the frequency f. Therefore, not only does the CD channel distort the phase of the signal but also its group delay.

The benchmark for CD compensation in (3.16) provides only a constant phase compensation of $+\alpha_{\text{CD}} f_k^2$ in each frequency subband $k = 0, 1, \cdots, M-1$. Compensating not only the phase value of the CD channel $\phi_{\text{CD}}(f)$ but also the slope of the quadratically varying phase i.e. the group delay $\tau_{\text{CD}}(f)$ at each discrete frequency point f_k, which is the center of each frequency subband, improves the performance to a great extent. We present, therefore, the idea of a delayed single-tap and delayed dual-tap equalizer in Sec. 3.5.2 and in Sec. 3.5.3, respectively. Adding appropriate delay elements for the equalizer in each frequency sub-band increases enormously the memory of the equalizer. For large CD values, where usually large I/FFT lengths are needed for compensation, small I/FFT lengths with an equalizer having delay elements and a single or two active taps are now needed leading almost to the same performance. We demonstrated this work in [139–141].

3.5.2 Delayed Single-tap Equalizer for FD CD Compensation

3.5.2.1 Derivation

The idea of the delayed single-tap equalizer is to take into account in the design of it the group delay (in samples) of the CD channel. It targets at compensating the group delay distortions $\tau_{\text{CD}}(f)$ caused by the CD channel in addition to its phase at each discrete frequency point f_k. This necessitates that the sub-band equalizer should be a multi-tap FIR filter with N_t taps as given in (3.22). However, to avoid any extra complexity as compared to the benchmark equalizer only one single tap $e_k[\ell_k]$ out of the N_t taps at each frequency point f_k in (3.22) is assumed to be active at position ℓ_k performing single-tap phase equalization. The other $(N_t - 1)$ taps are set to zero. This simplifies (3.22) to the following expression for the equalizer

$$E_k^{\text{S}}(f) = e_k[\ell_k] \exp\left(-j2\pi f \ell_k MT/2\right). \tag{3.40}$$

Fig. 3.10 illustrates the idea of a delayed single-tap equalizer where the delay elements $\ell_k MT/2$ realize a sub-band group delay necessary to compensate the group delay of the CD channel $\tau_{\text{CD}}(f_k)$ and it takes into account the latency time τ_c in (3.23). Note that ℓ_k is an integer multiple of the sampling time period $MT/2$ having discrete values from the set $\ell_k \in \{0, 1, \cdots, N_t - 1\}$ (for the case $\ell_k = 0$, the equalizer is the single-tap equalizer). Therefore, the delayed single-tap equalizer requires just additional delay elements as compared to the single-tap equalizer in (3.16).

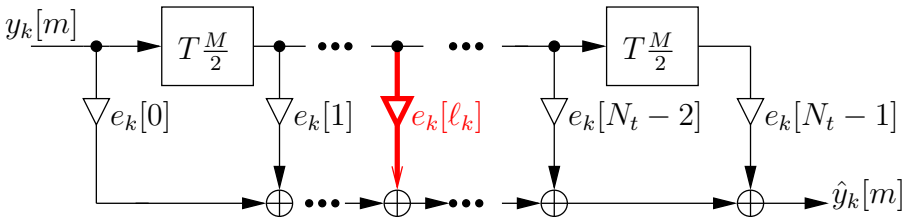

Fig. 3.10. The idea of a delayed single-tap equalizer: only $e_k[\ell_k]$ is active for the k-th sub-band. All other taps ($e_k[p]$ for $p \neq \ell_k$) are zero.

In order to find $e_k[\ell_k]$ and ℓ_k in (3.40), we recall that in general the desired equalizer in each sub-band k aims at equalizing the CD channel as follows

$$E'_k(f) = H^{-1}_{\text{CD}}(f_k)\exp\left(-j2\pi f_k \tau_c\right). \tag{3.41}$$

The latency time τ_c defined in (3.23) is needed and necessary to get an overall causal equalization.

In order to find ℓ_k, we first examine the group delay per sub-band that the equalizer defined in (3.41) introduces. It is obtained by differentiating the phase of (3.41) with respect to the angular frequency ω and taking the negative sign of the result. It is denoted as $\tau'_{\text{Eq}}(f_k)$ and it therefore reads as

$$\tau'_{\text{Eq}}(f_k) = -\tau_{\text{CD}}(f_k) + \tau_c \tag{3.42}$$

which can take any value and is not necessarily an integer multiple of the sampling time period $MT/2$. In order words, $\tau'_{\text{Eq}}(f_k)$ can be expressed by

$$\tau'_{\text{Eq}}(f_k) = \ell'_k MT/2, \tag{3.43}$$

where $\ell'_k \in \mathbb{R}$ is a non-integer number. By setting (3.42) and (3.43) equal, ℓ'_k can be re-arranged as

$$\ell'_k = \frac{-\tau_{\text{CD}}(f_k) + \tau_c}{MT/2}. \tag{3.44}$$

Now, the integer multiple ℓ_k of the sampling period time $MT/2$ necessary for realizing the delayed single-tap equalizer in (3.40) is found by the quantization of ℓ'_k. We choose to round the value of ℓ'_k to get ℓ_k

$$\begin{aligned}\ell_k &= \text{round}(\ell'_k) \\ &= \text{round}\left(\frac{-\tau_{\text{CD}}(f_k) + \tau_c}{MT/2}\right).\end{aligned} \tag{3.45}$$

As a result, the number of delay elements ℓ_k required for the delayed single-tap equalizer depends on the group delay of the CD channel $\tau_{\text{CD}}(f_k)$ and the latency time τ_c. Note that ℓ'_k and ℓ_k are pre-calculated offline.

In order to find $e_k[\ell_k]$, both equalizers in (3.40) and (3.41) are set equal resulting in

$$e_k[\ell_k] = H^{-1}_{\text{CD}}(f_k)\exp\left(+j2\pi f_k\left(\frac{MT}{2}\ell_k - \tau_{\text{c}}\right)\right), \tag{3.46}$$

which is complex-valued containing the term for equalizing the phase of the CD channel.

In brief, the delayed single-tap equalizer can be interpreted as a sub-band group delay filter with linear all-pass filtering of the CD channel in each sub-band.

3.5.2.2 Performance Analysis

Based on linear simulations, the performance of the system with delayed single-tap equalizer and the benchmark i.e. with a single-tap equalizer is evaluated for different N_t (accordingly different τ_c values), I/FFT lengths (i.e. different values for M) and for compensating different CD values. It should be noted that on top of the demonstrated filtering penalty, OSNR penalties resulting from the fiber attenuation and the according optical amplification need to be added as well as penalties from non-linearity and implementation constraints.

In Fig. 3.11, ℓ'_k and ℓ_k are plotted for CD = 36,000 ps/nm, $M = 512$, an even N_t of value $N_t = 2$. For this value of N_t, τ_c can have infinitely many values bounded between 0 and $MT/2$ as given in (3.23). We choose the following values for $\tau_c = \{0, \frac{1}{2}\frac{MT}{2}, \frac{MT}{2}\}$. As can be seen in Fig. 3.11(a), ℓ'_k takes non-integer values which is dependent on the CD value, M and τ_c. The integer values of ℓ_k for $N_t = 2$ can be either 0 or 1 as can be seen in Figs. 3.11(b), 3.11(c), and 3.11(d). The value of $\ell_k = 0$ means that in the subband k (correspondingly at the discrete frequency point f_k) no delay element exists i.e. a single-tap equalizer is applied. The value of $\ell_k = 1$ means that in the subband k (correspondingly at the discrete frequency point f_k) the delayed single-tap equalizer is applied having one delay element. For each value of τ_c, the group of frequency points at which either the single-tap equalizer ($\ell_k = 0$) or the delayed single-tap equalizer ($\ell_k = 1$) is identified. Only for the case $\tau_c = \frac{1}{2}\frac{MT}{2}$ which corresponds to $\tau_c = \frac{N_t-1}{2}\frac{MT}{2}$, the number of sub-bands requiring one delay element for the equalizer (a delayed single-tap equalizer) is the same as the number of sub-bands requiring no delay element for the equalizer (single-tap equalizer). This can be observed by the symmetry in ℓ_k in Fig. 3.11(c). In general for an even N_t and $\tau_c = \frac{N_t-1}{2}\frac{MT}{2}$, the rounding of ℓ'_k to get ℓ_k is an operation performed by a mid-rise quantizer.

For the same settings as in Fig. 3.11, ℓ'_k and ℓ_k are plotted in Fig. 3.12 for an odd value of N_t namely $N_t = 3$. In this case, τ_c can have larger values as compared to the case for $N_t = 2$. We choose the following values for $\tau_c = \{0, \frac{1}{2}\frac{MT}{2}, \frac{MT}{2}, \frac{3}{2}\frac{MT}{2}, 2\frac{MT}{2}\}$. Accordingly, ℓ'_k has larger non-integer values as well. For $N_t = 3$, ℓ_k can have three different integer values of 0 or 1 or 2. The value of $\ell_k = 2$ means that the delayed single-tap equalizer have 2 delay elements in sub-band k (the interpretation of $\ell_k = 0$ and $\ell_k = 1$ is the same as in the case of $N_t = 2$). Only for the case $\tau_c = \frac{MT}{2}$ corresponding to $\tau_c = \frac{N_t-1}{2}\frac{MT}{2}$ the number of sub-bands requiring two delay elements for the equalizer and the number of sub-bands requiring one delay element for the equalizer and the number of sub-bands requiring no delay element for the equalizer (single-tap equalizer) is equal. This is observed by the symmetry in ℓ_k shown in Fig. 3.12(d). In general for an odd N_t and $\tau_c = \frac{N_t-1}{2}\frac{MT}{2}$, the rounding of ℓ'_k to get ℓ_k is an operation performed by a mid-thread quantizer.

The difference between ℓ'_k and ℓ_k causes a low value of residual CD in each sub-band, which is compensated by a single-tap all-pass filtering function realizing the according parabolic phase transfer function (c.f. (3.46)).

In Fig. 3.13, the required OSNR to compensate for different CD values is plotted for $M = 512$, $N_t = 2$ and the different τ_c values considered for Fig. 3.11. The advantage of a delayed single-tap equalizer can be clearly seen where significantly higher CD values are compensated for any value of τ_c as compared to the system with a single-tap equalizer. The maximum CD tolerance is obtained for $\tau_c = \frac{1}{2}\frac{MT}{2}$, corresponding to $\tau_c = \frac{N_t-1}{2}\frac{MT}{2}$, with a small penalty for small CD values. This is due to the value of the active tap for the equalization of the phase of the CD channel (c.f. (3.46)). For $\tau_c > \frac{1}{2}\frac{MT}{2}$, the CD tolerance does not increase and the system performance is the same for $\tau_c < \frac{1}{2}\frac{MT}{2}$. For example, for $\tau_c = \frac{MT}{2}$, the same system performance is obtained as compared for the case of $\tau_c = 0$ as can be seen in Fig. 3.13. This can be interpreted by examining the obtained

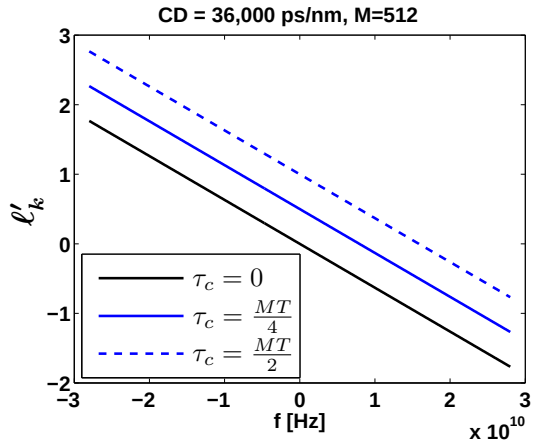

(a) ℓ'_k for CD = 36,000 ps/nm, $M = 512$ and different τ_c values

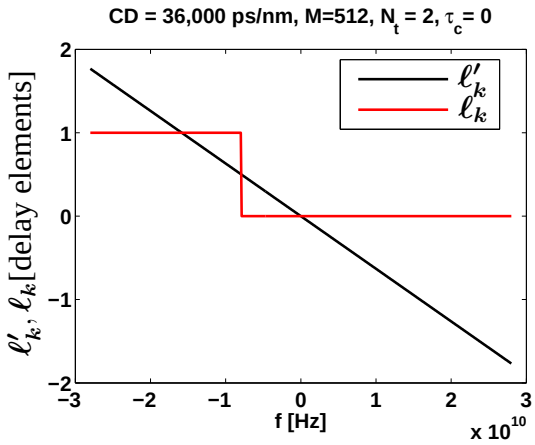

(b) ℓ_k and ℓ'_k for CD = 36,000 ps/nm, $M = 512$, $N_t = 2$ and $\tau_c = 0$

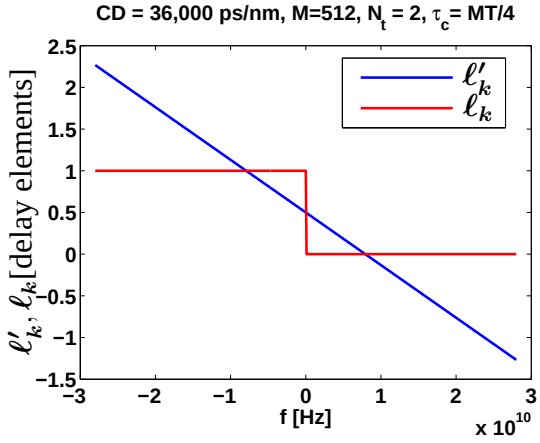

(c) ℓ_k and ℓ'_k for CD = 36,000 ps/nm, $M = 512$, $N_t = 2$ and $\tau_c = MT/4$

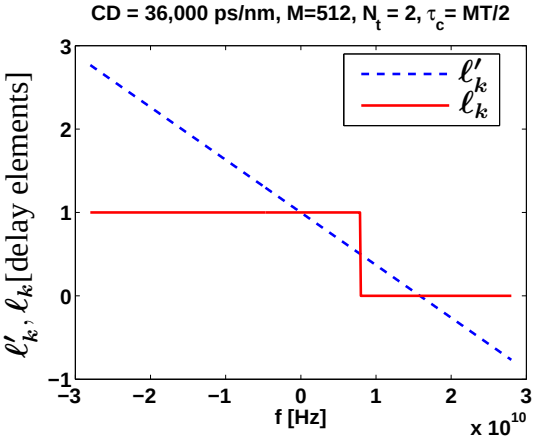

(d) ℓ_k and ℓ'_k for CD = 36,000 ps/nm, $M = 512$, $N_t = 2$ and $\tau_c = MT/2$

Fig. 3.11. ℓ_k and ℓ'_k for CD = 36,000 ps/nm, $M = 512$, $N_t = 2$ and different τ_c values

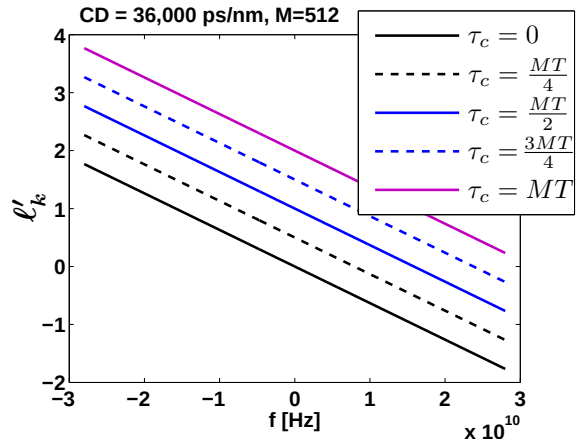

(a) ℓ'_k for CD = 36,000 ps/nm, $M = 512$ and different τ_c values

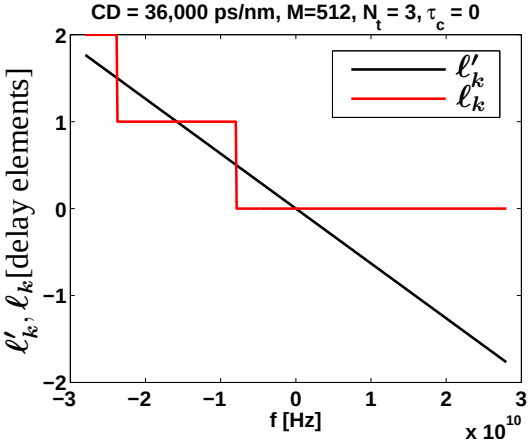

(b) ℓ_k and ℓ'_k for CD = 36,000 ps/nm, $M = 512$, $N_t = 3$ and $\tau_c = 0$

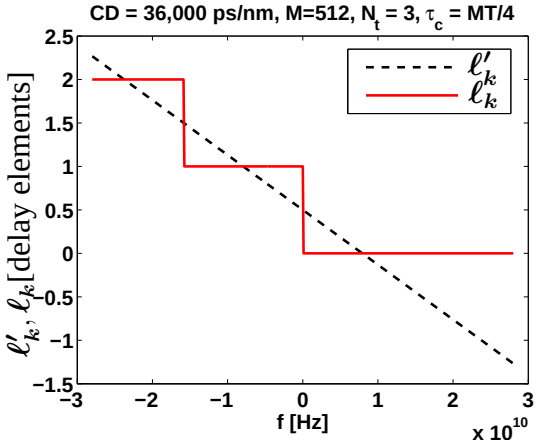

(c) ℓ_k and ℓ'_k for CD = 36,000 ps/nm, $M = 512$, $N_t = 3$ and $\tau_c = MT/4$

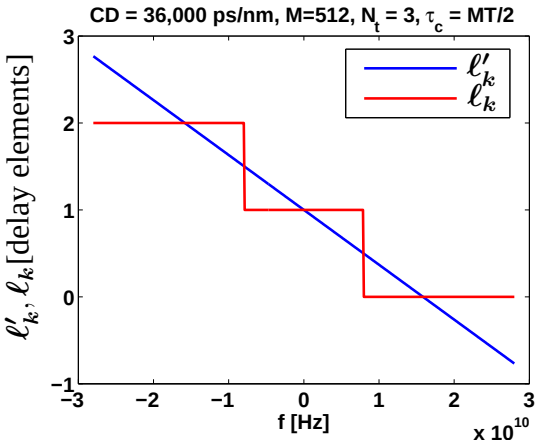

(d) ℓ_k and ℓ'_k for CD = 36,000 ps/nm, $M = 512$, $N_t = 3$ and $\tau_c = MT/2$

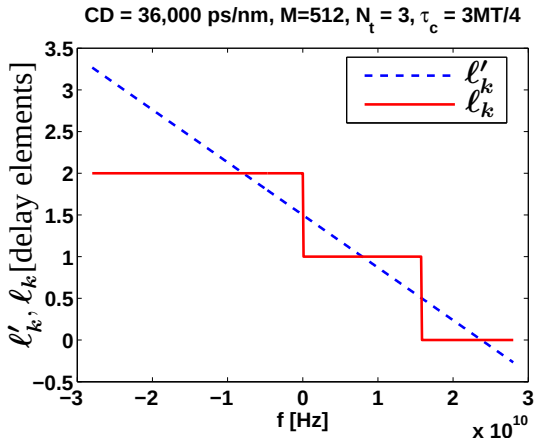

(e) ℓ_k and ℓ'_k for CD = 36,000 ps/nm, $M = 512$, $N_t = 3$ and $\tau_c = 3MT/4$

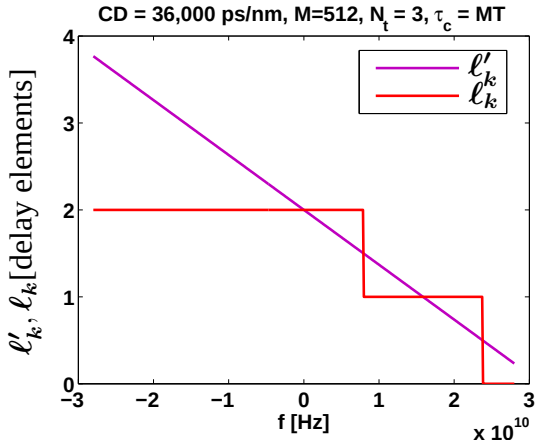

(f) ℓ_k and ℓ'_k for CD = 36,000 ps/nm, $M = 512$, $N_t = 3$ and $\tau_c = MT$

Fig. 3.12. ℓ_k and ℓ'_k for CD = 36,000 ps/nm, $M = 512$, $N_t = 3$ and different τ_c values

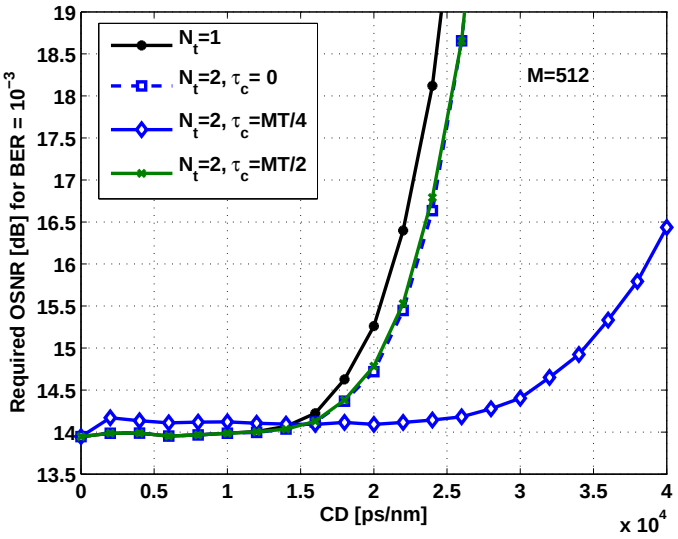

Fig. 3.13. Required OSNR for different CD values with $M = 512$, $N_t = 2$ and different τ_c values

structure of the equalizer (see Figs. 3.11(b) and 3.11(d)). Additionally, no penalty in performance for small CD values is obtained for these values of τ_c. As a conclusion, for an even N_t the value of τ_c has to be optimized for each CD value: for small CD values to obtain the minimum required OSNR and for large CD values to increase CD tolerance.

In Fig. 3.14, the required OSNR value to achieve a BER of 10^{-3} to compensate for different CD values is plotted for $M = 512$, $N_t = 3$ and the different τ_c values considered for Fig. 3.12. The advantage of a delayed single-tap equalizer can be clearly seen where significantly larger CD values are compensated for with any value of τ_c as compared to the system with a single-tap equalizer. For $\tau_c = \frac{MT}{2}$, corresponding to $\tau_c = \frac{N_t-1}{2}\frac{MT}{2}$ the maximum CD tolerance is obtained as compared to other τ_c values and there is no penalty in the required OSNR for small CD values as compared to the system performance with other τ_c values and even when using a single-tap equalizer. For $\tau_c > \frac{MT}{2}$, the CD tolerance does not increase and the system performance is the same for $\tau_c < \frac{MT}{2}$. For example the values of $\tau_c = 0$ and $\tau_c = \frac{2MT}{2}$ deliver the same system performance as can be seen in Fig. 3.14. This also the case for $\tau_c = \frac{1}{2}\frac{MT}{2}$ and $\tau_c = \frac{3}{2}\frac{MT}{2}$. For both pairs of τ_c values, the structure of the equalizer is the same (see Figs. 3.12(b) and 3.12(f) and 3.12(c) and 3.12(e), respectively). As a conclusion, for an odd N_t, the optimum τ_c over all CD values is $\tau_c = \frac{N_t-1}{2}\frac{MT}{2}$.

In Fig. 3.15, the required OSNR is plotted for different number of taps N_t for the equalizer per sub-band. For the case of even N_t, the value of τ_c is optimized for each CD value to get the least required OSNR. For odd N_t, the value of $\tau_c = \frac{N_t-1}{2}\frac{MT}{2}$ is the optimum for all CD values. The advantage of a delayed single-tap equalizer can be clearly seen where significantly higher CD values are compensated for the same FFT length when increasing N_t as long as $N_t \ll M$. The equalizer memory can be significantly increased by the combination of the group delay elements and the phase rotation. This is a clear benefit compared to a single tap equalizer with only phase filtering. For a given maximum N_t, a lower number of active taps is automatically applied at low CD values. In other words, as CD increases, the number of required taps for equalization increases linearly until the maximum N_t is reached.

The simulations in Fig. 3.16 show the required OSNR for the same N_t value but with different I/FFT-length M. As a benchmark, we choose the I/FFT length $M = 1024$ and a single-tap equalizer

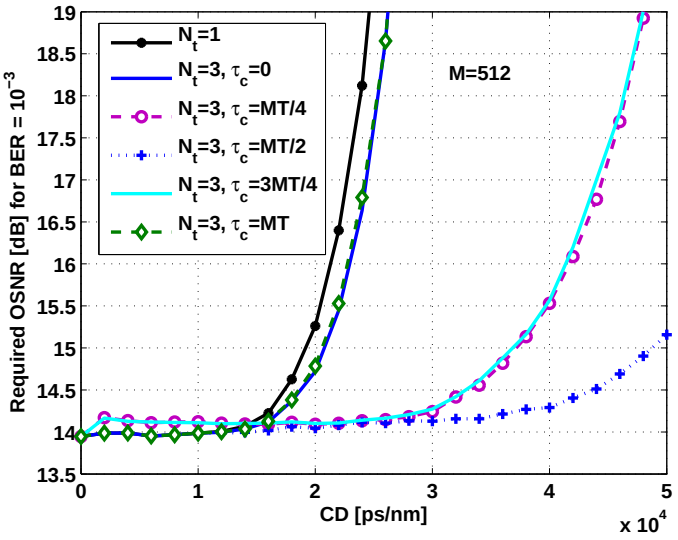

Fig. 3.14. Required OSNR for different CD values with $M = 512$, $N_t = 3$ and different τ_c values

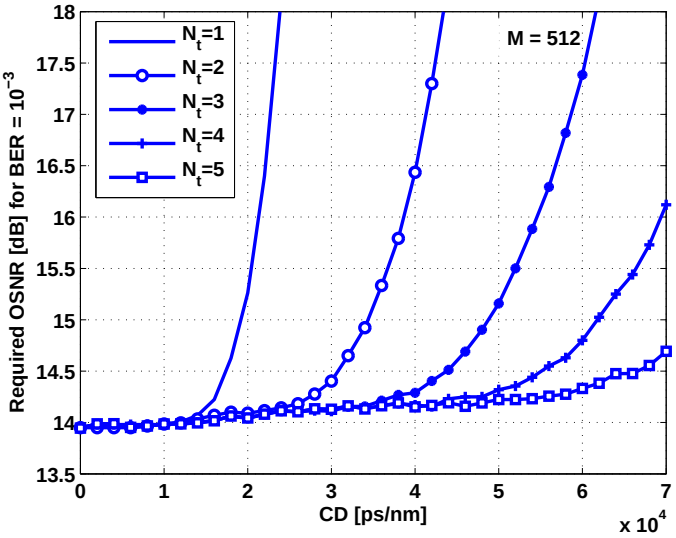

Fig. 3.15. Required OSNR for different CD values with a delayed single-tap per sub-band CD equalizer with the optimum τ_c for all CD values for odd N_t and optimizing τ_c for each CD value for an even N_t: advantage of a delayed-single tap equalizer.

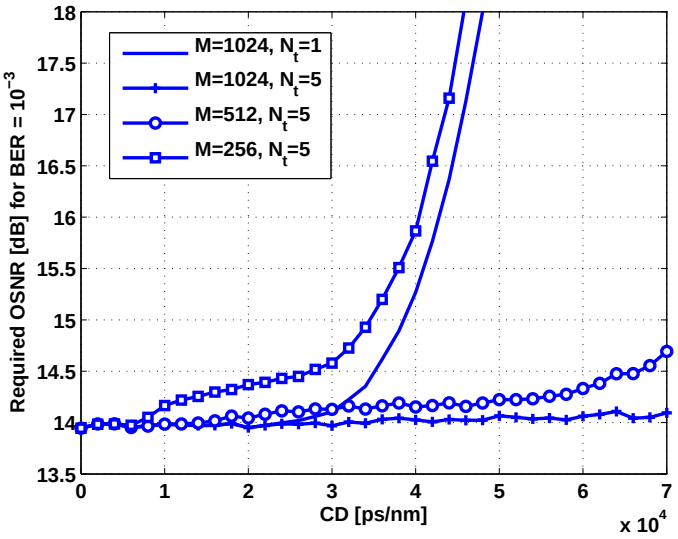

Fig. 3.16. Required OSNR for different CD values: larger CD values are compensated for $N_t > 1$ at the cost of small penalty and additional memory elements.

i.e. $N_t = 1$. Significant smaller FFT lengths as compared to the benchmark for $N_t = 5$ (and optimum τ_c) is needed to tolerate the same CD value. For example, to tolerate a CD value of 32,000 ps/nm, it is sufficient to have an I/FFT length of $M = 256$ with $N_t = 5$ taps with less than 1-dB OSNR penalty. With $M = 1024$ and $N_t = 5$, a negligible OSNR penalty is observed even outperforming the benchmark.

In Fig. 3.17, the required OSNR is plotted with $M = 1024$ and $N_t = 9$. The linear increase of filtering penalty up to 200,000 ps/nm results from the decomposition of the signal into an increasing number of sub-bands. It results from slight phase imperfections between adjacent sub-bands after signal decomposition. Above 200,000 ps/nm the channel memory starts to exceed the filter memory with the typical rapid penalty accumulation. For an OSNR filtering penalty of 0.5 dB more than 240,000 ps/nm can be equalized which refers to a trans-Pacific distance around 15,000 km with standard single-mode fiber.

3.5.3 Delayed Dual-tap Equalizer for FD CD Compensation

3.5.3.1 Derivation

Although the delayed single-tap equalizer already tries to compensate not only the phase but also the group delay of the CD channel at each discrete frequency point f_k, which is the center of each frequency subband, it can perform this for the group delay only in a coarsely quantized way, i.e. in steps of $MT/2$. This quantization can be reduced by introducing the delayed dual-tap equalizer which reduces the step-size to $MT/4$. This is achieved by utilizing two taps with a delay of $MT/2$ in between, thereby, interpolating the group delay compensation between $\ell_u MT/2$ and $(\ell_u \pm 1)MT/2$. This interpolation is specially useful in those frequency sub-bands where the quantization error due to rounding (3.45) is almost $MT/2$.

The design of the delayed dual-tap equalizer is originated from the delayed single-tap concept (Sec. 3.5.2). There we observe the quantization error defined as

$$q_k = \ell_k - \ell'_k \tag{3.47}$$

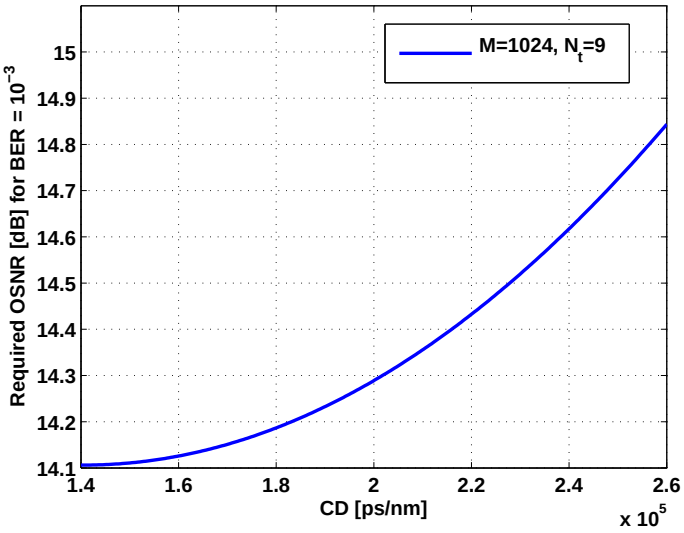

Fig. 3.17. Comparison of basic CD model with extended channel model for widely considered I/FFT length of $M = 1024$ and $N_t = 9$.

which is bounded to $-1/2 < q_k \leq 1/2$. A change in the sign from q_k to q_{k+1} corresponding to an abrupt change in the group delay compensation caused by the change from ℓ_k to ℓ_{k+1} points to these frequency sub-bands is where the concept of dual-tap is most useful. All those index pairs $(k, k+1)$ are denoted by $(u, u+1)$ and are collected in the set S_D. We exclude the index pair $(M/2-1, M/2)$ which comprises the two frequency bins at the upper and lower end of the baseband spectrum.

The mathematical expression of the delayed dual-tap equalizer is obtained by modifying (3.40) as follows

$$E_u^{\mathrm{D}}(f) = e'_u[\ell_u]\exp\left(-j2\pi f \ell_u MT/2\right) + e'_u[\ell_u \pm 1]\exp\left(-j2\pi f(\ell_u \pm 1)MT/2\right), u \in S_D. \quad (3.48)$$

The active tap $e'_u[\ell_u - 1]$ is placed at position $\ell_u - 1$ for a positive q_u whereas the active tap $e'_u[\ell_u + 1]$ is placed at position $\ell_u + 1$ for a negative q_u.

In order to find the value of the two active taps $e'_u[\ell_u]$ and $e'_u[\ell_u \pm 1]$, we recall that in general the desired equalizer in each sub-band u aims at equalizing the CD channel as given in (3.41). The equalizer $E'_u(f)$ in (3.41) can be rewritten as follows

$$\begin{aligned} E'_u(f) &= H_{\mathrm{CD}}^{-1}(f_u)\exp\left(-j2\pi f_u \tau_c\right) \\ &= aH_{\mathrm{CD}}^{-1}(f_u)\exp\left(-j2\pi f_u \tau_c\right) + (1-a)H_{\mathrm{CD}}^{-1}(f_u)\exp\left(-j2\pi f_u \tau_c\right) \\ &= aH_{\mathrm{CD}}^{-1}(f_u)\exp\left(-j2\pi f_u \ell_u MT/2\right)\exp\left(+j2\pi f_u \ell_u MT/2\right)\exp\left(-j2\pi f_u \tau_c\right) \\ &\quad + (1-a)H_{\mathrm{CD}}^{-1}(f_u)\exp\left(-j2\pi f_u \tau_c\right) \\ &\quad \times \exp\left(-j2\pi f_u(\ell_u \pm 1)MT/2\right)\exp\left(+j2\pi f_u(\ell_u \pm 1)MT/2\right) \end{aligned} \quad (3.49)$$

where $0 < a < 1$ is an amplitude factor assigned to the tap derived for the delayed single-tap equalizer. By setting (3.49) and (3.48) equal, the value of the two active taps $e'_u[\ell_u]$ and $e'_u[\ell_u \pm 1]$

is

$$e'_u[\ell_u] = aH_{\text{CD}}^{-1}(f_u)\text{exp}\left(+j2\pi f_u\left(\frac{MT}{2}\ell_u - \tau_{\text{c}}\right)\right), \tag{3.50}$$

$$e'_u[\ell_u \pm 1] = (1-a)H_{\text{CD}}^{-1}(f_u)\text{exp}\left(+j2\pi f_u\left(\frac{MT}{2}(\ell_u \pm 1) - \tau_{\text{c}}\right)\right). \tag{3.51}$$

Both active taps $e'_u[\ell_u]$ and $e'_u[\ell_u \pm 1]$ of the delayed dual-tap equalizer can be expressed as function of the active tap $e_u[\ell_u]$ of the delayed single-tap equalizer as

$$e'_u[\ell_u] = ae_u[\ell_u], \tag{3.52}$$

$$e'_u[\ell_u \pm 1] = \begin{cases} (1-a) \times e_u[\ell_u], & \text{for } u \text{ even}, \\ -(1-a) \times e_u[\ell_u], & \text{for } u \text{ odd}. \end{cases} \tag{3.53}$$

In order to keep the same complexity in terms of multiplications for the delayed dual-tap equalizer and the delayed single-tap equalizer, both active taps are chosen to be equal[1]. This is achieved by having

$$a = \frac{1}{2}. \tag{3.54}$$

With this assumption, the delayed dual-tap equalizer $E_u^{\text{D}}(z_{M/2})$ in (3.48) can be rewritten as

$$E_u^{\text{D}}(f) = \begin{cases} \frac{1}{2}e_u[\ell_u]\text{exp}\left(-j2\pi f\ell_u MT/2\right)\Big(1 + \text{exp}\left(\mp j2\pi fMT/2\right)\Big), & \text{for } u \text{ even}, \\ \frac{1}{2}e_u[\ell_u]\text{exp}\left(-j2\pi f\ell_u MT/2\right)\Big(1 - \text{exp}\left(\mp j2\pi fMT/2\right)\Big), & \text{for } u \text{ odd}. \end{cases} \tag{3.55}$$

In general, for even u the term $\Big(1 + \text{exp}\left(\mp j2\pi fMT/2\right)\Big)$ can be rewritten as

$$\begin{aligned} 1 + \text{exp}\left(\mp j2\pi fTM/2\right) &= \text{exp}\left(\mp j2\pi fTM/4\right)\left(\text{exp}\left(\pm j2\pi fTM/4\right) + \text{exp}\left(\mp j2\pi fTM/4\right)\right) \\ &= 2 \times \text{exp}\left(\mp j2\pi fTM/4\right)\cos(2\pi fTM/4) \end{aligned} \tag{3.56}$$

and for odd u the term $\Big(1 - \text{exp}\left(\mp j2\pi fMT/2\right)\Big)$ can be rewritten as

$$\begin{aligned} 1 - \text{exp}\left(\mp j2\pi fTM/2\right) &= \text{exp}\left(\mp j2\pi fTM/4\right)\left(\text{exp}\left(\pm j2\pi fTM/4\right) - \text{exp}\left(\mp j2\pi fTM/4\right)\right) \\ &= \pm 2j \times \text{exp}\left(\mp j2\pi fTM/4\right)\sin(2\pi fTM/4). \end{aligned} \tag{3.57}$$

This leads actually to the following two important conclusions for the delayed dual-tap equalizer with $a = \frac{1}{2}$. Firstly, in the sub-bands where it is applied, there are $(\ell_u \pm \frac{1}{2})MT/2$ delay elements represented by the terms $(-j2\pi fTM/2)$ and $(\mp j2\pi fTM/4)$, respectively. This is illustrated in Fig. 3.18. The delay elements realize a sub-band group delay necessary to compensate the normalized group delay of the CD channel $\tau_{\text{CD}}(f)$ and the latency time τ_c in (3.23). Thus the sub-band group delay is now smoothed where the delayed dual-tap equalizer is applied. The second conclusion is that the delayed dual-tap equalizer is not an all-pass filter since its amplitude is not equal to one; it has a sinusoidal shape represented by the terms $\cos(2\pi fTM/4)$ and $\sin(2\pi fTM/4)$ for even and odd u, respectively.

[1]For odd u, both taps have equal magnitudes but opposite signs.

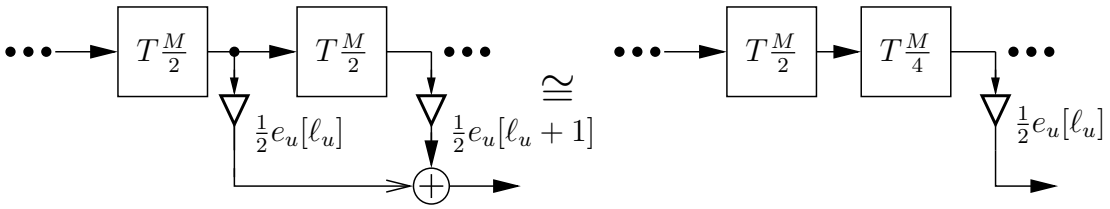

Fig. 3.18. Delayed dual-tap equalizer with taps of same amplitude: an integer and a fractional group delay

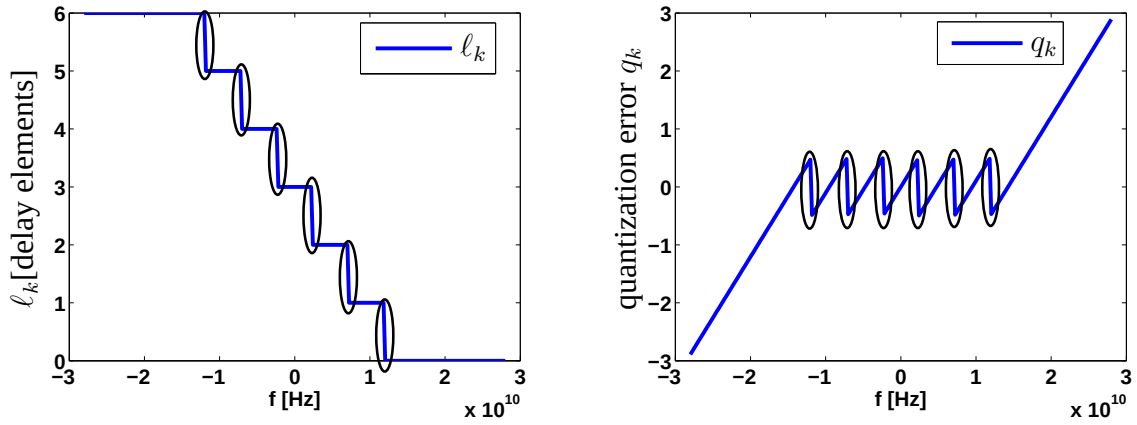

(a) ℓ'_k for CD= 60,000 ps/nm, $M = 256$, $N_t = 7$: discontinuity of ℓ_k

(b) q_k for CD= 60,000 ps/nm, $M = 256$, $N_t = 7$: discontinuity of the quantization error q_k

Fig. 3.19. Delayed dual-tap equalizer for CD= 60,000 ps/nm, $M = 256$, $N_t = 7$: the frequencies at which it is applied

3.5.3.2 Performance Analysis

The performance of the system with delayed dual-tap equalizer and with delayed single-tap equalizer is evaluated for compensating different CD values.

In a first set of simulations, in Fig. 3.19 we plot ℓ_k and and the quantization error q_k for CD value of 60,000 ps/nm, $M = 256$ and $N_t = 7$ (correspondingly optimum τ_c). The discontinuity (as marked in the figures) in ℓ_k and q_k highly depends on the quantization method (rounding in our case) chosen to get ℓ_k for a given CD value, M and N_t. There is a total of twelve sub-bands where the discontinuity occurs. This defines the elements of the set S_D which has the following indexes $S_D = \{10, 11, 32, 33, 54, 55, 201, 202, 223, 224, 245, 246\}$. In these frequency sub-bands, the delayed dual-tap equalizer is applied to smooth ℓ_k.

For the same settings as in Fig. 3.19, the smoothing of ℓ_k is shown in Fig. 3.20 by applying the delayed dual-tap equalizer at the corresponding sub-bands. We show just the frequency range $f \in [0 \cdots 10]$ GHz. At the even indexes of the set S_D, the delayed dual-tap equalizer has the additional active tap at position $\ell_k - 1$. At the odd indexes of the set S_D, the delayed dual-tap equalizer has the additional active tap at position $\ell_k + 1$. Fractional values of $\ell_{u=k}$ are noticed in the sub-bands of S_D.

In a second set of simulations, the required OSNR is plotted in Fig. 3.21 for $M = 256$, $N_t = 7$ (and optimum τ_c) and $a = \frac{1}{2}$ for different CD values. The performance of the system with a delayed dual-tap equalizer further improves as compared to the system with delayed single-tap equalizer. This is due to the finer quantization of ℓ_k by smoothing it in the sub-bands where it is discontinuous. The improvement in performance in terms of the required OSNR can be observed when

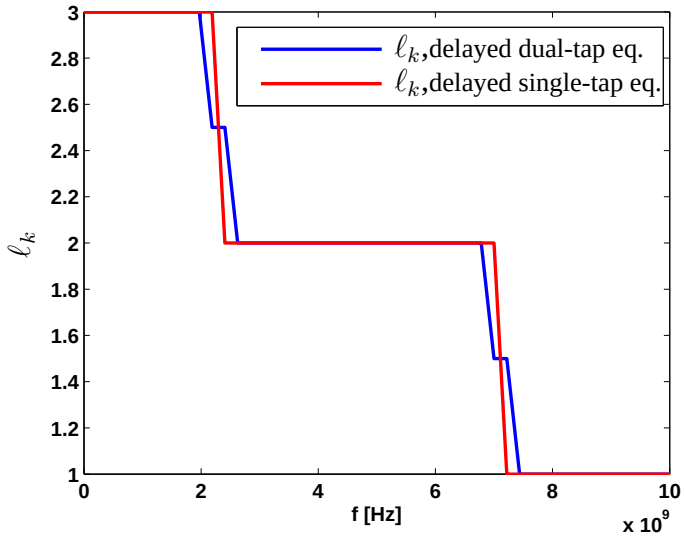

Fig. 3.20. Delayed dual-tap equalizer for for CD= 60,000 ps/nm, $M = 256$, $N_t = 7$: Smoothing of ℓ_k at the frequency sub-bands where discontinuity occurs; integer and fractional values of ℓ_k

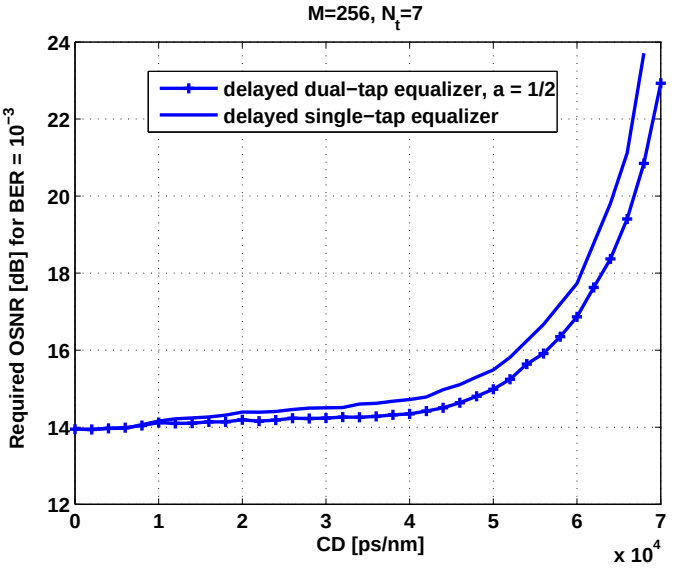

Fig. 3.21. Required OSNR for different CD values: Delayed Dual-tap equalizer and single-tap equalizer having the same complexity in terms of multiplications.

compensating for large CD values with small M. Actually, as long as N_t stays small (and accordingly the number of sub-bands at which the delayed dual-tap equalizer is applied) as compared to M, there is an improvement in performance.

3.6 Frequency Domain Equalization of the Complete System

The FD equalization of the signal $x_{\mathrm{q}}[m]$ in Fig. 3.1 considered in the previous sections accounted for the effects of the propagating CD channel for the equalizer design. In this section, we design an MMSE equalizer in the FD that equalizes the total channel including the response of the transmit

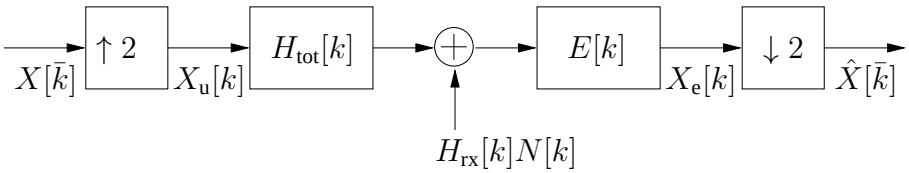

Fig. 3.22. System Model for FD equalizer design

and receive filters. Moreover, the equalizer takes into account the aliasing terms that arise due to the electrical (Bessel) filter. The criterion which we use for equalization reduces to filtering at each discrete frequency point. In other words, we aim at designing a fractionally spaced MMSE equalizer $E[k]$ at each discrete frequency point $k, k = 0, 1, \cdots, M-1$ taking into account the aliasing terms that arise due to the Bessel filter. A simplified model of the system in Fig. 3.1 necessary for the derivation of the point-wise equalizer $E[k]$ is shown in Fig. 3.22.

We consider that the TD signals and the noise in Fig. 3.1 maintain their energy when transformed to the FD according to Parseval's theorem. Given that the TD input signal $x[n]$ has variance σ_x^2, the $\bar{k}$-th point of the discrete Fourier transform of $x[n]$ denoted as $X[\bar{k}], \bar{k} = 0, 1, \cdots, M/2-1$ has the same variance of σ_x^2. The discrete TD signal $x[n]$ after upsampling by a factor of 2 is denoted as $x_{\mathrm{u}}[m]$. The latter thus has a variance of $\sigma_X^2 = \frac{1}{2}\sigma_x^2$ according to (B.4). Therefore, it follows that the k-th point of the discrete Fourier transform of $x_{\mathrm{u}}[m]$ denoted as $X_{\mathrm{u}}[k], k = 0, 1, \cdots, M-1$ has the same variance of value

$$\sigma_X^2 = \frac{1}{2}\sigma_x^2. \tag{3.58}$$

The $\bar{k}$-th point of the discrete Fourier transform of $\hat{x}[n]$ in Fig. 3.1 is denoted as $\hat{X}[\bar{k}]$ in Fig. 3.22. The aliasing terms present due to the downsampling appear when expressing the output signal $\hat{X}[\bar{k}]$ as function of the equalized signal $X_{\mathrm{e}}[k]$ [113]

$$\hat{X}[\bar{k}] = \begin{cases} \frac{1}{2}\left(X_{\mathrm{e}}[k] + X_{\mathrm{e}}\left[k + \frac{M}{2}\right]\right), & \text{for } 0 \le k \le M/2-1, 0 \le \bar{k} \le M/4-1, \\ \frac{1}{2}\left(X_{\mathrm{e}}[k] + X_{\mathrm{e}}\left[k - \frac{M}{2}\right]\right), & \text{for } M/2 \le k \le M-1, M/4 \le \bar{k} \le M/2-1. \end{cases} \tag{3.59}$$

The continuous TD representation of the total channel denoted as $\bar{h}_{\mathrm{tot}}(t)$ is obtained by convolving the impulse response of the pulse shaper $h_{\mathrm{p}}(t)$, CD channel $h_{\mathrm{CD}}(t)$ and the receive filter $h_{\mathrm{rx}}(t)$ defined in Sec. 3.2

$$\bar{h}_{\mathrm{tot}}(t) = h_{\mathrm{rx}}(t) * h_{\mathrm{CD}}(t) * h_{\mathrm{p}}(t). \tag{3.60}$$

It follows that the discrete-time representation of $\bar{h}_{\mathrm{tot}}(t)$ is obtained by sampling it at twice the symbol rate as follows

$$h_{\mathrm{tot}}[m] = \bar{h}_{\mathrm{tot}}(mT_s/2). \tag{3.61}$$

Therefore, $H_{\mathrm{tot}}[k]$ representing the k-th point of the discrete Fourier transform of $h_{\mathrm{tot}}[m]$ is obtained according to (1.7)

$$H_{\mathrm{tot}}[k] = \sum_{m=0}^{M-1} h_{\mathrm{tot}}[m] W_M^{km}. \tag{3.62}$$

The impulse response of the receive filter $h_{\mathrm{rx}}(t)$ defined in Sec. 3.2 is sampled at twice the symbol rate $\bar{h}_{\mathrm{rx}}[m] = h_{\mathrm{rx}}(mT_s/2)$ in order to get the corresponding discrete Fourier transform

representation $H_{\text{rx}}[k]$ according to (1.7)

$$H_{\text{rx}}[k] = \sum_{m=0}^{M-1} \bar{h}_{\text{rx}}[m] W_M^{km}. \tag{3.63}$$

The k-th (frequency) point of the discrete Fourier transform of the noise denoted as $N[k]$ is obtained in the same way as $H_{\text{tot}}[k]$ and $H_{\text{rx}}[k]$ by first sampling the noise $n(t)$ in Fig. 3.1 at twice the symbol rate and then transforming it according to (1.7)

$$N[k] = \sum_{m=0}^{M-1} n(mT_s/2) W_M^{km}. \tag{3.64}$$

The variance of $N[k]$ denoted as σ_N^2 is derived as in (3.8) over a frequency bandwidth of $2B$.

We can, thus, express the k-th (frequency) point representation of the equalized signal $X_{\text{e}}[k]$ as function of $H_{\text{tot}}[k]$, $H_{\text{rx}}[k]$, $X_{\text{u}}[k]$, $N[k]$ and $E[k]$ as follows

$$X_{\text{e}}[k] = E[k] H_{\text{tot}}[k] X_{\text{u}}[k] + E[k] H_{\text{rx}}[k] N[k]. \tag{3.65}$$

For $0 \leq \bar{k} \leq M/4 - 1$, the output signal $\hat{X}[\bar{k}]$ in (3.59) when substituting (3.65) can be expressed in a matrix-vector notation as follows

$$\hat{X}[\bar{k}] = \frac{1}{2} \left(\boldsymbol{e}[k] \boldsymbol{h}[k] X_{\text{u}}[k] + \boldsymbol{e}[k] \boldsymbol{H}_{\text{R}}[k] \boldsymbol{n}[k] \right) \tag{3.66}$$

where $0 \leq k \leq M/2 - 1$ with the following definitions

$$\boldsymbol{e}[k] = \begin{bmatrix} E[k] & E\left[k + \frac{M}{2}\right] \end{bmatrix}, \tag{3.67}$$

$$\boldsymbol{h}[k] = \begin{bmatrix} H_{\text{tot}}[k] & H_{\text{tot}}\left[k + \frac{M}{2}\right] \end{bmatrix}^{\text{T}}, \tag{3.68}$$

$$\boldsymbol{H}_{\text{R}}[k] = \begin{bmatrix} H_{\text{rx}}[k] & 0 \\ 0 & H_{\text{rx}}\left[k + \frac{M}{2}\right] \end{bmatrix}, \tag{3.69}$$

$$\boldsymbol{n}[k] = \begin{bmatrix} N[k] & N\left[k + \frac{M}{2}\right] \end{bmatrix}^{\text{T}}, \tag{3.70}$$

and we used the fact that $X_{\text{u}}\left[k + \frac{M}{2}\right] = X_{\text{u}}[k]$ since $X_{\text{u}}[k]$ is periodic with period $M/2$.

We design $\boldsymbol{e}[k]$ according to the FD MMSE criterion. For this the mean squared error denoted as $J(\boldsymbol{e}[k])$ at each discrete frequency point $\bar{k}$ is built between $X[\bar{k}]$ and $\hat{X}[\bar{k}]$ which is function of $\boldsymbol{e}[k]$ as given in (3.66). It reads as

$$\begin{aligned}
J(\boldsymbol{e}[k]) &= \text{E}\left[\left| \hat{X}[\bar{k}] - X[\bar{k}] \right|^2 \right] \\
&= \text{E}\left[\left| \frac{1}{2} \Big(\left(\boldsymbol{e}[k] \boldsymbol{h}[k] - 2 \right) X_{\text{u}}[k] + \boldsymbol{e}[k] \boldsymbol{H}_{\text{R}}[k] \boldsymbol{n}[k] \Big) \right|^2 \right] \\
&= \text{E}\left[\frac{1}{4} \Big(\left(\boldsymbol{e}[k] \boldsymbol{h}[k] - 2 \right) X_{\text{u}}[k] + \boldsymbol{e}[k] \boldsymbol{H}_{\text{R}}[k] \boldsymbol{n}[k] \Big) \times \right. \\
&\qquad \left. \Big(\left(\boldsymbol{e}[k] \boldsymbol{h}[k] - 2 \right) X_{\text{u}}[k] + \boldsymbol{e}[k] \boldsymbol{H}_{\text{R}}[k] \boldsymbol{n}[k] \Big)^{\text{H}} \right] \\
&= \frac{1}{4} \left(\sigma_X^2 \left(\boldsymbol{e}[k] \boldsymbol{h}[k] - 2 \right) \left(\boldsymbol{e}[k] \boldsymbol{h}[k] - 2 \right)^{\text{H}} + \sigma_N^2 \boldsymbol{e}[k] \boldsymbol{H}_{\text{R}}[k] \boldsymbol{H}_{\text{R}}[k]^{\text{H}} \boldsymbol{e}[k]^{\text{H}} \right),
\end{aligned} \tag{3.71}$$

where $X[\bar{k}] = X_u[k]$ [113] for $\bar{k} = 0, 1, \cdots, M/4 - 1$ and $k = 0, 1, \cdots, M/2 - 1$ but the latter has a variance of σ_X^2 given in (3.58). The expectation is taken over the signal $X_u[k]$ and over the noise term $\boldsymbol{n}[k]$ with the following noise correlation matrix

$$\mathrm{E}\left[\boldsymbol{n}[k]\boldsymbol{n}[k]^{\mathrm{H}}\right] = \begin{bmatrix} \mathrm{E}\left[|N[k]|^2\right] & 0 \\ 0 & \mathrm{E}\left[|N[k+\frac{M}{2}]|^2\right] \end{bmatrix} = \sigma_N^2 \mathbf{1}_{2\times 2}, \tag{3.72}$$

and it is assumed that signal $X_{\mathrm{u}}[k]$ and the noise components of $\boldsymbol{n}[k]$ are uncorrelated.

The optimum $\boldsymbol{e}[k]$ is the one that minimizes $J(\boldsymbol{e}[k])$ in (3.71)

$$\boldsymbol{e}[k] = \underset{\boldsymbol{e}[k]}{\operatorname{argmin}}\, J(\boldsymbol{e}[k]) \tag{3.73}$$

which is found by taking the derivative of $J(\boldsymbol{e}[k])$ with the respect to $\boldsymbol{e}[k]$ and setting it to zero

$$\frac{\partial}{\partial \boldsymbol{e}[k]} J(\boldsymbol{e}[k]) = \sigma_X^2 \left(\boldsymbol{e}[k]^* \boldsymbol{h}[k]^* - 2\right) \boldsymbol{h}[k]^{\mathrm{T}} + \sigma_N^2 \boldsymbol{e}[k]^* \boldsymbol{H}_{\mathrm{R}}[k]^* \boldsymbol{H}_{\mathrm{R}}[k]^{\mathrm{T}} = \mathbf{0}_{1\times 2}. \tag{3.74}$$

Therefore, the optimum $\boldsymbol{e}[k]$ for $k = 0, \cdots, M/2 - 1$ reads as

$$\boldsymbol{e}[k] = 2\sigma_X^2 \boldsymbol{h}[k]^{\mathrm{H}} \left(\sigma_X^2 \boldsymbol{h}[k]\boldsymbol{h}[k]^{\mathrm{H}} + \sigma_N^2 \boldsymbol{H}_{\mathrm{R}}[k]\boldsymbol{H}_{\mathrm{R}}[k]^{\mathrm{H}}\right)^{-1}. \tag{3.75}$$

For $k = M/2, \cdots, M - 1$, the vector-equalizer $\boldsymbol{e}^-[k] = \begin{bmatrix} E[k] & E\left[k - \frac{M}{2}\right] \end{bmatrix}$ can be similarly derived. It reads as

$$\boldsymbol{e}^-[k] = 2\sigma_X^2 \boldsymbol{h}^-[k]^{\mathrm{H}} \left(\sigma_X^2 \boldsymbol{h}^-[k]\boldsymbol{h}^-[k]^{\mathrm{H}} + \sigma_N^2 \boldsymbol{H}_{\mathrm{R}}^-[k]\boldsymbol{H}_{\mathrm{R}}^-[k]^{\mathrm{H}}\right)^{-1} \tag{3.76}$$

where

$$\boldsymbol{h}^-[k] = \begin{bmatrix} H_{\text{tot}}[k] & H_{\text{tot}}\left[k - \frac{M}{2}\right] \end{bmatrix}^{\mathrm{T}}, \tag{3.77}$$

$$\boldsymbol{H}_{\mathrm{R}}^-[k] = \begin{bmatrix} H_{\text{rx}}[k] & 0 \\ 0 & H_{\text{rx}}\left[k - \frac{M}{2}\right] \end{bmatrix}. \tag{3.78}$$

The matrix inversion lemma of the form (E.1) [142] is finally applied to (3.75) and (3.76) to get the expression of the fractionally spaced equalizer $E[k]$ at each discrete frequency point k

$$E[k] = \begin{cases} \dfrac{\dfrac{2H_{\text{tot}}[k]^*}{|H_{\text{rx}}[k]|^2}}{\dfrac{|H_{\text{tot}}[k]|^2}{|H_{\text{rx}}[k]|^2} + \dfrac{\left|H_{\text{tot}}\left[k+\frac{M}{2}\right]\right|^2}{\left|H_{\text{rx}}\left[k+\frac{M}{2}\right]\right|^2} + \dfrac{\sigma_N^2}{\sigma_X^2}}, & \text{for} \quad 0 \le k \le M/2 - 1, \\ \dfrac{\dfrac{2H_{\text{tot}}[k]^*}{|H_{\text{rx}}[k]|^2}}{\dfrac{|H_{\text{tot}}[k]|^2}{|H_{\text{rx}}[k]|^2} + \dfrac{\left|H_{\text{tot}}\left[k-\frac{M}{2}\right]\right|^2}{\left|H_{\text{rx}}\left[k-\frac{M}{2}\right]\right|^2} + \dfrac{\sigma_N^2}{\sigma_X^2}}, & \text{for} \quad M/2 \le k \le M - 1. \end{cases} \tag{3.79}$$

The proof is given in Appendix E.

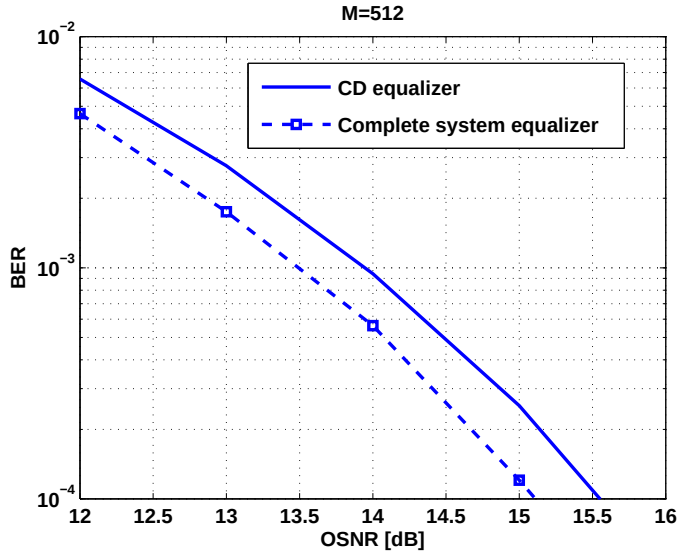

Fig. 3.23. Frequency domain equalizer of the complete system: advantage over benchmark equalizer at back-to-back connection of the transmitter and receiver i.e. no CD channel between them

The performance of the system with the equalizer designed according to (3.79) is examined in terms of ROSNR to get a BER of 10^{-3} to compensate different CD values for a given M as compared to a system with the benchmark design given in (3.16) and also other designs for the equalizer derived from (3.79) as we present later.

In Fig. 3.23, the BER vs. OSNR is plotted for back-to-back connection of the transmitter ($h_{\rm p}(t)$ in (3.2)) and the receiver (the opto-electronic front-end of the coherent receiver $h_{\rm rx}(t)$ in Fig. 3.1) i.e. without CD channel between them. The equalization is done either through the proposed equalizer in (3.79) or the benchmark in (3.16) for $M = 512$. As it can be seen, less ROSNR values is needed with the proposed equalizer as compared to the benchmark. Concretely, a 0.5 dB improvement in ROSNR is attained to get a BER of 10^{-3}. This is because the equalizer in (3.79) can be interpreted as a pre-whitening filter that whitens the colored noise (with power spectral density of $\sigma_N^2 \, |H_{\rm rx}[k]|^2$) input to the equalizer.

In Fig. 3.24 the ROSNR to get BER of 10^{-3} is plotted for different CD values with both equalizer designs as in Fig. 3.23. For CD values less than or equal 14,000 ps/nm, the ROSNR values with the proposed equalizer are less than the values with the benchmark equalizer. This is because the proposed equalizer equalizes not only the propagating CD channel but also the transmit and receive filters (given by the term $H_{\rm tot}[k]^*$ in (3.79)). However, for CD values greater than 14,000 ps/nm, the ROSNR values for the system with the proposed equalizer become greater than for the system with the benchmark equalizer since the former equalizer causes noise enhancement at certain frequency components which deteriorates the overall performance. In other words, the optimum equalizer design depends on the CD value (correspondingly on the length of the optical fiber).

Finally, in Fig. 3.25 the ROSNR to get BER of 10^{-3} is plotted for different CD values with the proposed equalizer design in (3.79) and a pre-whitening equalizer expressed by $E_{p.w.}[k] = \frac{H_{\rm tot}[k]^*}{|H_{\rm rx}[k]|^2}$ which does not take into account both the aliasing terms due to downsampling and the regularization term due to FD MMSE design in the denominator of (3.79). As it can be seen, for $M = 512$ the ROSNR values with the proposed equalizer in (3.79) are less than the values when a pre-whitening equalizer is used such that a gain of 0.5 dB values is obtained for CD values

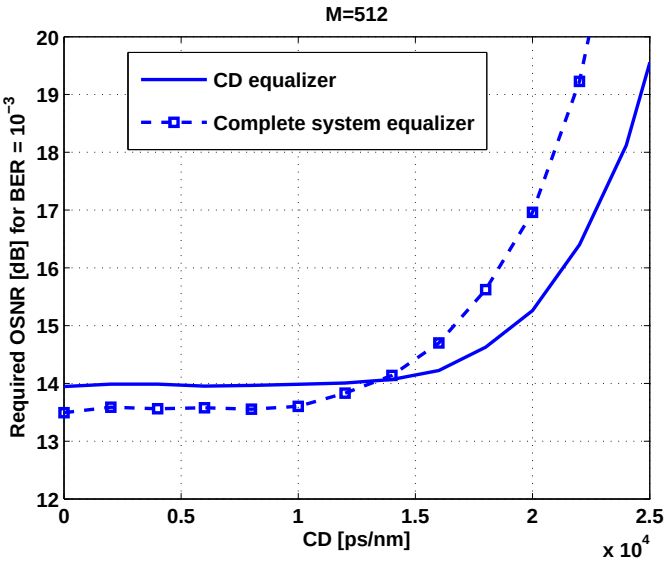

Fig. 3.24. Required OSNR for different CD values: advantage of the frequency domain equalizer of the complete system over benchmark equalizer for low and moderate CD values

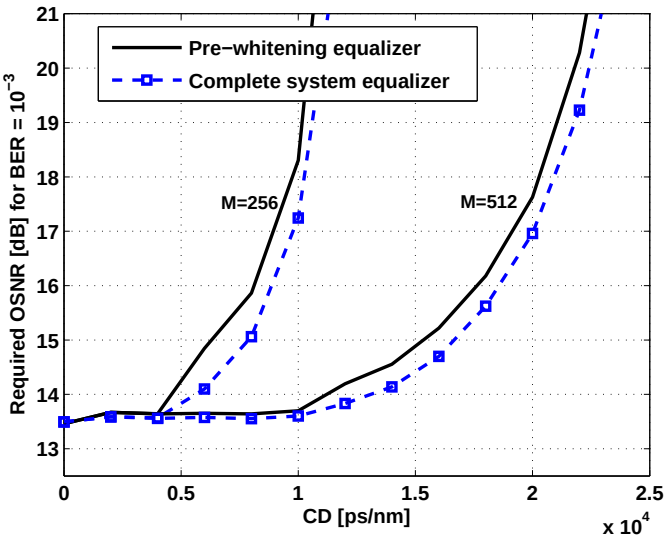

Fig. 3.25. Frequency Domain Equalizer with Oversampling vs Pre-whitening Equalizer: advantage of FDE with oversampling over all CD values

greater than 10,000 ps/nm. This is because the noise enhancement with the proposed equalizer is less when compared to the pre-whitening filter. This gain in ROSNR values is more obvious when decreasing M where at least a 1-dB gain is obtained for $M = 256$ for CD values greater than 4,000 ps/nm. Lastly, the equalizer can be designed without taking into account the aliasing terms due to downsampling and thus the $k \pm \frac{M}{2}$ components in (3.79) can be ignored. The obtained equalizer for the given transmit and receive filter delivers not only high ROSNR values for small CD values as compared to all aforementioned designs of the equalizer but also it is not able to compensate large CD values. This concludes the superiority and the advantages of the proposed equalizer in (3.79).

3.7 Summary

Coherent detection with digital signal processing algorithms took advantage from the continuously increasing electrical processing speed. In this chapter we presented various DSP algorithms associated with PDM-QPSK-RZ-50% optical transmission coherent systems to enhance data rates of 112 Gbit/s and beyond per wavelength channel. The DSP algorithms are used to compensate for CD among other transmission impairments in optical fibers. The main obstacle for implementation at such high data rates is the complexity of the filtering algorithms in terms of multiplications and thus power consumption and the availability of DSP circuits that offer both very high gate density and processing speed. FD equalization by means of linear all-pass filters has been shown to have the least implementation complexity compared to TD implementation for large dispersion values where the equalizer has many taps. Overlap FDE is one configuration of SC-FDE which perform linear convolution in FD.

In this chapter, first, we interpreted the well known OLS-50% method applied so far for FD CD compensation as a non-maximally decimated DFT FB with trivial prototype filters and a single-tap filter per sub-band equalizing the propagating CD channel. Next, due to the nature of the CD channel which distorts not only the phase of the signal but also its group delay, we proposed and derived a delayed single-tap equalizer in the FD. It is a multi-tap filter applied in each frequency sub-band but has only one active tap and several delay elements accounting to the quantized (normalized) group delay of the inverse of the CD channel. With this design larger CD values can be compensated with a smaller I/DFT length. This is simply done by increasing the number of delay elements of the equalizer in each sub-band as long as the maximum number of delay elements remains negligible as compared to the I/DFT length. An important advantage of such a filter design is that its complexity in terms of multiplications remains the same as the benchmark (OLS-50%) apart from the needed additional delay elements. The quantized (normalized) group delay function derived for the delayed single-tap equalizer can be smoothed to provide a better (normalized) group delay approximation around the frequency points where the (normalized) group delay function is discontinuous. We proposed, therefore, a delayed dual-tap equalizer applied at the these frequency points which can also has the same complexity as the delayed single-tap equalizer apart from some adders/subtractors by adjusting the amplitude of the two active taps. The (normalized) group delay at the frequency points where this equalizer is applied is finer quantized by having an and integer and fractional (normalized) group delay. This improves the performance of the system by requiring lower ROSNR values specially when concurrently the I/DFT length is small and the CD values are large. Finally, we derived a FD MMSE equalizer compensating the total channel composed of the impulse response of both the transmitter and receiver and the propagating CD channel. The designs takes into account as well the aliasing terms that arise due to the electrical filter. The results showed lower ROSNR values of the system compared to the benchmark for low and moderate CD values.

4. Baud-rate Channel Spacing in Wavelength Division Multiplexing Systems

In this chapter, we adopt baud-rate channel spacing in wavelength division multiplexing (WDM) systems as a way to efficiently use the available optical bandwidth. Due to the baud-rate spacing of WDM channels, there is a considerable overlap between adjacent channel spectra. This gives rise to interchannel interference (ICI) degrading system performance. Therefore, we present three different approaches to mitigate or minimize ICI. These approaches employ either standard or orthogonal modulation schemes. In standard quadrature amplitude modulation (QAM) WDM systems, we develop two receiver-side approaches to mitigate ICI. In offset QAM WDM systems, there is no ICI despite spectra overlap because of the orthogonality between the wavelength channels. Channel orthogonality is achieved theoretically through staggering and destaggering, in the transmitter and receiver, respectively, of the real and imaginary parts of the signal. We demonstrate through simulations the feasibility of offset QAM WDM systems. We compare these different approaches in terms of performance, system requirements and complexity. For all the different techniques for ICI mitigation or minization, a digital root-raised-cosine (RRC) pulse shaper is implemented in the transmitter and in the receiver since the overall resulting RC response satisfies the first Nyquist criterion for intersymbol interference (ISI)-free transmission.

4.1 Introduction

In WDM optical communication systems, multiple optical carriers are modulated individually at relatively lower symbol rates, and then multiplexed together delivering the desired net data-rate. Enhancing the spectral efficiency (SE) in WDM systems is the key to meet the growing traffic demands and higher capacity requirements. The SE determines not only the maximum theoretical data throughput of a system, but also how efficiently the total available bandwidth is being used. After the commercialization of 112 Gbit/s PDM-QPSK per wavelength channel systems and in order to enhance the SE in WDM systems, approaches for the efficient use of the available optical bandwidth are to be investigated. These approaches allow existing modulation formats, baud-rate and components to be exploited without the need to utilize additional fibers and amplifier infrastructures, without employing high order modulation schemes, without an increase in the baud-rate, without limiting the reach and without incurring unacceptable complexities. Therefore, a way to achieve high SE is by reducing the channel spacing, defined as the frequency separation between two optical carriers, to the baud-rate. Three major competitive technologies for generating baud-rate spaced channels in WDM systems can be identified.

The first one is the orthogonal frequency-division multiplexing (OFDM) technology [16–33]. It makes use of the orthogonality between the channels to allow for spectral overlapping through utilizing a sinc-function spectrum in the frequency-domain (FD). In the time-domain (TD), the modulated symbols in each channel have rectangular shape. A diversity of implementation methods of OFDM has been proposed, such as electro-optical hybrid OFDM [24, 25], and all-optical OFDM or namely no-guard-interval OFDM (NGI-OFDM) [19, 21, 30, 32]. Theoretically, OFDM belongs to the class of orthogonal systems with ICI-free transmission. However in practical systems, the generation and maintenance of ideally orthogonal channels is quite difficult. The transmitting end in an optical OFDM system must use optical oscillators with frequency locking to get carrier spacing equal to the baud-rate with sufficient accuracy. Additionally, OFDM systems require accurate timing alignment of the symbols at the demultiplexing stage to maintain the orthogonality between the channels. Any slight imperfection in maintaining orthogonal channels results in severe performance degradation mainly ICI from the cross-talk from neighboring channels. Moreover, there is a long oscillating tail in the FD which implies that sufficient bandwidth is needed at the transmitter and the receiver to modulate each channel. Furthermore, channel separation at the receiver side is not trivial, requiring a fast Fourier transform (FFT) either in the electrical domain [25, 26] or in the optical domain [22, 27]. For the electrical channel separation, a simultaneous detection scheme is usually used for detecting more than one channel per digital sampling, which further reduces the achievable baud-rate per each channel due to the limitation of the sampling rates of the analog-to-digital converters (ADCs). In addition to these practical implementation issues, the use of GI in OFDM systems reduces the SE. Finally, conventional OFDM typically has a large peak-to-average power ratio (PAPR) leading to high fiber nonlinear impairments in fiber links. For these reasons, we do not consider OFDM further in this thesis.

The second technology to generate baud-rate spaced channels is the Nyquist WDM approach [34–47]. It is complementary to OFDM where each channel has an ideal rectangular shaped spectrum in FD with bandwidth equal to the baud-rate obtained by employing optical, analog or digital electrical filters in the transmitter [36, 38–41, 143–146]. In the TD, the pulse within each channel has a sinc-shape with zero-crossings at integer multiples of the symbol period T_s. This simply characterizes a Nyquist pulse which achieves inter-symbol interference (ISI)-free transmission. ISI is one of the major intrachannel impairments caused by the limited channel bandwidth. In Sec. 4.2, we review the concept of ISI-free transmission obtained by utilizing different Nyquist pulses each characterized by a roll-off factor. Theoretically, Nyquist WDM systems are both ISI and ICI free. However, practical issues raise such as the imperfect generation of an ideal rectangular spectrum and the difficulty to maintain it over the transmission system due to the impact of cascaded filters along the transmission line. These issues degrade the performance due to the inevitable induced ISI and ICI effects since there is no GI. Thus, practical WDM systems are not ideal Nyquist systems although it is common to refer to them as Nyquist WDM systems. One challenge in Nyquist WDM systems with baud-rate spacing of the channels is to simultaneously minimize ISI and ICI impairments. This can be achieved by adopting transmitter-side and receiver-side approaches. At the transmitter side, pulse shaping is performed according to the Nyquist criterion to generate ISI-free signals rather than sinc pulses. The class of root raised cosine (RRC) filters is of particular interest for pulse shaping. This is because they satisfy the Nyquist criterion of zero ISI (in the case of an ideal channel) whatever the roll-off is when applied at the transmitter and receiver. The sinc-function has a raised cosine spectrum with zero roll-off. Optical methods such as Nyquist optical filter [144] or an ordinary optical filter and a pulse carver [145] to generate Nyquist WDM signals have been demonstrated. Electrical pulse shaping [40, 146, 147] implemented either

in the analog or in the digital domain can be alternatively done to delicately constitute the spectrum in electrical domain. Digital filtering approaches require digital-to-analog converter (DAC) at the transmitter. Compared with optical approaches, DSP-based pulse shaping solutions are more flexible as the same hardware can be used to generate different filter shapes and modulation formats [148]. These approaches can be implemented either in the TD with finite impulse response (FIR) filters or in the FD using discrete Fourier transform (DFT), inverse DFT (IDFT) and pointwise multiplication for filtering. Allowing for non-zero roll-offs relaxes the constraints on the filter length and the tolerable jitter at the expense of non-negligible ICI degrading the performance. This requires adopting receiver-side approaches to mitigate not only ICI but also ISI that arises due to the propagating channel between the transmitter and receiver. In general for ISI and ICI equalization receiver-side approaches are more flexible and adaptable to the overall channel variations than transmitter-side approaches. We present two designs for the equalizer in the digital domain requiring an ADC at the receiver side. The first equalization method which we propose in Sec. 4.6.1 is based on the conventional minimum mean squared error (MMSE) design for the equalizer in the FD which is modified such that the ICI of adjacent channels is also introduced in the optimization procedure. This is achieved by making use of the statistical information of the symbols of the immediately adjacent channels in order to get a regularization term for the resulting expression of the MMSE equalizer. Thus, the interference is taken into account in the optimization process in a very similar way to the noise. The equalization is carried out independently in each channel of interest i.e. a single-receiver equalization technique. The second equalization approach that we propose in Sec. 4.6.2 is referred to as multi-receiver equalization (MRE) method. It is based on a super-receiver architecture which builds on conventional Nyquist WDM systems such that the received signals of the neighboring channels are fed into the receiver of the channel of interest to eliminate ICI in this channel. This method has been previously demonstrated as an ICI cancellation method in coherent OFDM systems [149]. By taking advantage of information from neighboring channels using joint DSP to cancel ICI, greatly improved performance can be achieved as compared to conventional receivers which process each channel independently. In general, compared to no GI OFDM systems, Nyquist WDM systems relax the bandwidth requirement of the receiver and exhibits better non-linearity tolerance due to lower PAPR values [33].

The third technology to generate baud-rate spaced channels is by employing offset QAM (OQAM) as modulation scheme in Nyquist WDM systems [48–53]. In OQAM Nyquist WDM systems as opposed to SQAM Nyquist WDM systems, the multiplexing of the channels at the baud-rate allows for spectral overlap without ideally resulting in ICI which impairs the received constellations. Channel orthogonality is achieved through the use of OQAM as modulation scheme by offsetting the inphase and quadrature tributaries that alternate for odd and even channels. In Sec. 4.3, we review the principle of OQAM for ICI-free transmission in baud-rate channel spaced systems. Originally, OQAM was proposed by Chang [54] and Saltzberg [55] for parallel data transmission systems over bandlimited dispersive transmission media. Later it was applied in radio frequency (RF) wireless communications [150–155], in powerline communications [156, 157], and in optical wireless [158, 159]. The concept of OQAM in Nyquist WDM systems can be implemented either in the optical [48, 51] or in the electrical domain [49, 50]. As opposed to no GI OFDM, OQAM Nyquist WDM systems use bandwidth-limited pulse shapes. Therefore, the bandwidth requirements of the involved electrical and electro-optical components are reduced accordingly. In Sec. 4.5, we introduce the OQAM Nyquist WDM system and demonstrate through simulations the feasibility of the OQAM principle under the assumption of perfect synchronization of frequency, phase and time.

In this chapter, we consider three isolated wavelength channels in the transmitter of a WDM system which are multiplexed at baud-rate spacing. We investigate Nyquist WDM systems which employ either standard or offset QAM as modulation schemes. We consider baud-rate of value $B = 28$ GBaud. The signal generated by the transmitter is then coupled into the standard single mode fiber which is modeled as a linear CD channel whose frequency response is given in (3.5). The received signal then enters coherent receiver(s) for further processing. We present a detailed description of the different approaches necessary to mitigate ICI in Nyquist WDM system with SQAM and OQAM as modulation scheme in the following sections.

4.2 Principle of ISI-free Transmission in Single-channel Transmission Systems

According to Nyquist theorem [58], ISI-free transmission in single-channel systems can be achieved if the spectrum of a signal $H_s(f)$ satisfies

$$\sum_{m_s=-\infty}^{\infty} H_s(f + m_s/T_s) = T_s \tag{4.1}$$

at the slicer where T_s is the symbol period of the signal. The smallest bandwidth of a signal with zero ISI is $1/T_s$. The frequency spectrum of such signal is rectangular and its correspondingly pulse shape is a sinc function

$$h_s(t) = \text{sinc}\left(\frac{\pi t}{T_s}\right) = \frac{\sin(\pi t/T_s)}{\pi t/T_s}. \tag{4.2}$$

One difficulty with the impulse response in (4.2) is that it is fundamentally impossible to obtain because it is infinitely long. Additionally, the tails of $h_s(t)$ decay as $1/t$ which means that a large number of taps are required in practice to approximate it and any small sampling timing error can cause ISI.

A widely used and more practical pulse that satisfies Nyquist theorem is the raised cosine (RC) filter with a roll-off factor $0 < \rho \leq 1$. It can expressed by

$$h_{\text{RC}}(t) = \frac{\sin(\pi t/T_s)}{\pi t/T_s} \frac{\cos(\pi \rho t/T_s)}{1 - 4\pi\rho^2 t^2/T_s^2}. \tag{4.3}$$

The tails of $h_{\text{RC}}(t)$ in (4.3) decay as $1/t^3$ for $\rho > 0$. Consequently, as compared to the sinc function in (4.2), the impulse response decays faster and an error in sampling time causes less ISI. However, the RC pulse occupies ρ/T_s extra bandwidth.

According to the requirement that the receive filter should be matched to the transmit filter, the impulse response of the RC filter is factored into a RRC filter in both entities. Besides, the cascade of the transmit and receive filters must satisfy the first Nyquist criterion in order to avoid ISI. By taking the square root of (4.3), the impulse response of an RRC filter can be expressed by

$$h_{\text{RRC}}(t) = \frac{4\rho\frac{t}{T_s}\cos(\pi\frac{t}{T_s}(1+\rho)) + \sin(\pi\frac{t}{T_s}(1-\rho))}{\pi\frac{t}{T_s}(1-(4\rho\frac{t}{T_s})^2)}. \tag{4.4}$$

The frequency response of the continuous-time RC filter can be found by taking the Fourier transform of (4.3). It reads as

$$H_{\mathrm{RC}}(f) = \begin{cases} T_s, & 0 \le |f| < f_N(1-\rho), \\ \frac{T_s}{2}\cos\left(\frac{\pi}{2\rho}\left(\frac{|f|}{f_N} - (1-\rho)\right)\right), & f_N(1-\rho) \le |f| \le f_N(1+\rho), \\ 0, & |f| > f_N(1+\rho). \end{cases} \tag{4.5}$$

where $f_N = 1/(2T_s)$ is the Nyquist frequency. The frequency response of the continuous-time RRC filter can be found by taking the square root of (4.5). It reads as

$$H_{\mathrm{RRC}}(f) = \begin{cases} \sqrt{T_s}, & 0 \le |f| < f_N(1-\rho), \\ \sqrt{T_s}\cos\left(\frac{\pi}{4\rho}\left(\frac{|f|}{f_N} - (1-\rho)\right)\right), & f_N(1-\rho) \le |f| \le f_N(1+\rho), \\ 0, & |f| > f_N(1+\rho). \end{cases} \tag{4.6}$$

4.3 Principle of ICI-free Transmission in Multi-channel Transmission Systems

In multi-channel transmission system where each user transmits with a signaling rate of B bit/s, an efficient use of the available spectrum for channel multiplexing is achieved when the channels of the different users are placed at the baud-rate. This introduces considerable ICI. Chang and Saltzberg developed independently in [54, 55] an orthogonal signaling method that leads to zero crosstalk i.e. zero ICI despite baud-rate channel multiplexing when the transmission medium is distortionless. We briefly review here the proposed orthogonal signaling in [54, 55] .

Fig. 4.1 shows the block diagram of an analog continuous *frequency division multiplexed* transmission system. It is assumed that the spectral shape of the signal is identical in all channels and is symmetrical around the center frequency of the channel of each user. Each user transmits two independent data streams I and Q, each of which modulates one of a pair of carriers whose frequency is equal to the center frequency of the channel of each user. Each data stream has a signaling rate of $B/2$ and the timing of the two streams is staggered by $1/B$. The signal in adjacent channels is staggered oppositely, so that the data streams which modulate the cosine carriers of the even numbered users' channels are in phase with the data streams that modulate the sine carriers of the odd numbered users' channels and conversely. All the pulse shaping filters $H(\omega)$ in the transmitter and receiver are identical and assumed to be real. They are bandlimited to the signaling rate in order to avoid the interference from non immediately adjacent channels.

Since the system is linear and time-invariant, the distortion in one channel can be determined from the response to a single pulse transmitted on each subchannel. The channel could have an even or odd number and the subchannel could be either the cosine or the sine subchannel. There are six components that constitute the distortion in each channel. Two components comprise ISI from the inphase and quadrature components of the channel itself due to the dispersive media. The other four components comprise ICI of the immediate adjacent upper and lower channel specifically from the inphase and quadrature components of the immediately adjacent channels. In case the transmission medium is distortionless and when $H(\omega)$ is chosen such that it satisfies the Nyquist criterion i.e. an RRC filter, there is no ISI in the system. By the staggering and the destaggering operations performed in the transmitter and receiver, respectively, Saltzberg showed in his paper [55] that the four terms consituting ICI are zero.

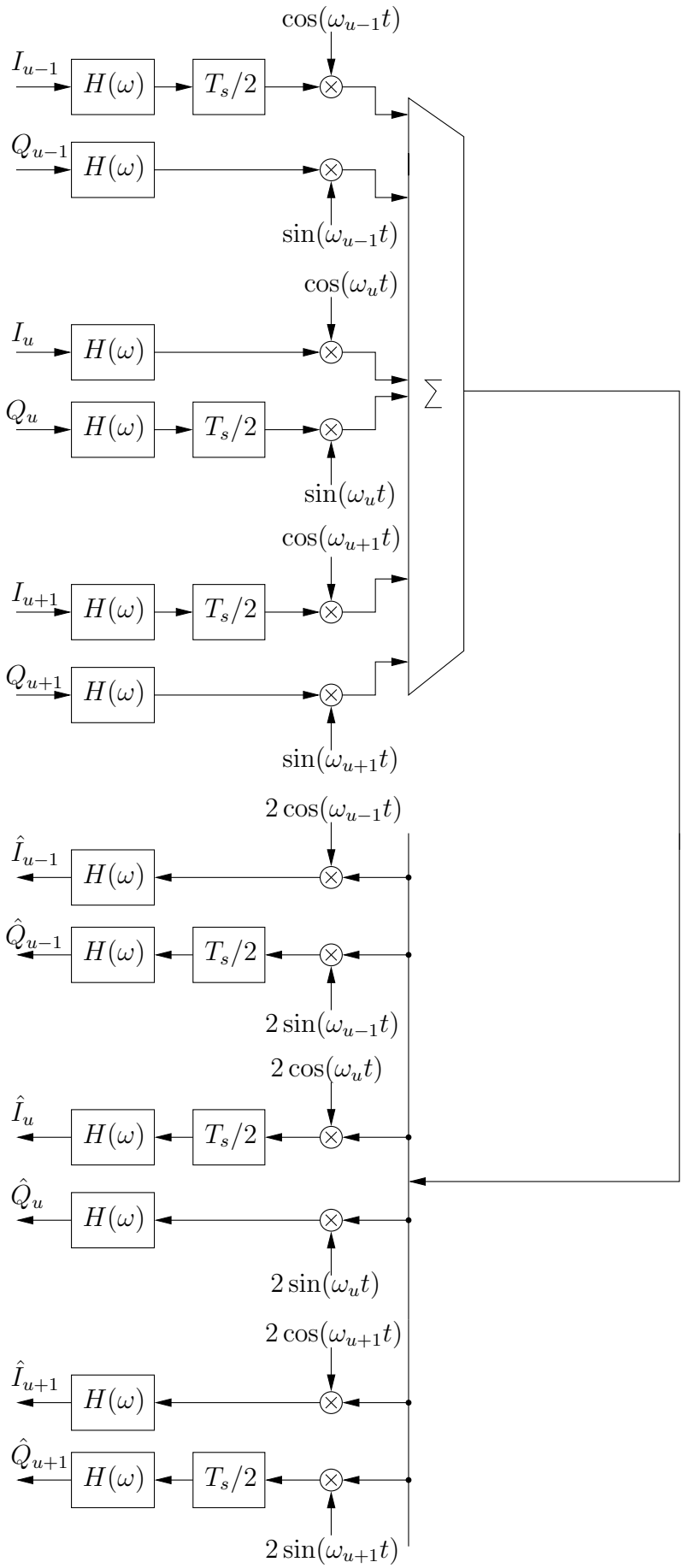

Fig. 4.1. Analog Orthogonal FDM system; distortionless transmission medium

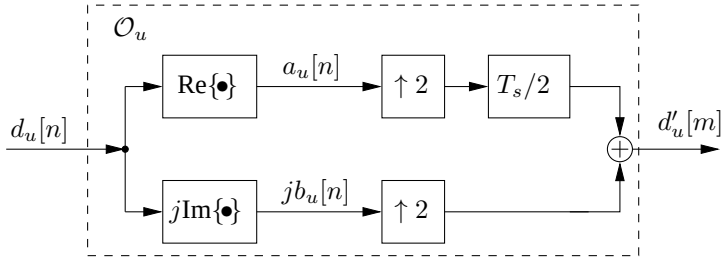

(a) OQAM Staggering, u odd

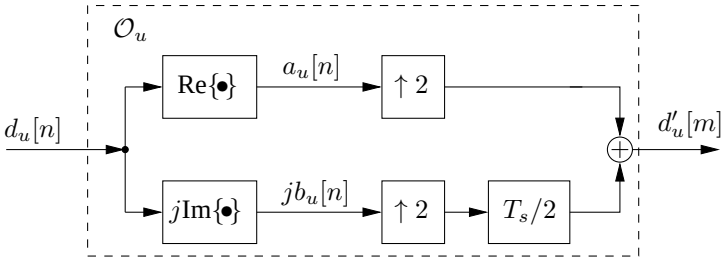

(b) OQAM Staggering, u even

Fig. 4.2. OQAM Staggering in odd- and even-numbered channels

In the discrete-time domain, the process of offsetting the real and imaginary part of the signals in the channels is carried out by the OQAM modulators in the transmitter and OQAM demodulators in the receiver. The OQAM staggering of the symbols in each channel is carried out according to Figs. 4.2(a) and 4.2(b). The OQAM modulators denoted as $\mathcal{O}_u$ inherently include an upsampler which increases the sampling rate of the signal by a factor of 2. The role of the real and imaginary part has to be interchanged from one channel to the other. This means the OQAM modulation of the odd numbered channels delays the real part of the signal according to Fig. 4.2(a), whereas it delays the imaginary part (multiplied by j) in the even numbered channels according to Fig. 4.2(b). The OQAM destaggering of the symbols in each channel is carried out according to Figs. 4.3(a) and 4.3(b). The OQAM demodulators denoted as $\mathcal{O}'_u$ inherently include a decimation by the factor 2. Similar to the OQAM staggering, the role of the real and imaginary part has to be interchanged from one channel to the other. Hence, the OQAM demodulation of the odd numbered channels delays the imaginary part (multiplied by j) part of the signal according to Fig. 4.3(a), whereas it delays the real part in the even numbered channels according to Fig. 4.3(b).

4.4 Transmit Processing in Nyquist WDM Systems

In the transmitter of a Nyquist WDM system, three separate wavelength channels are firstly generated and then multiplexed before being sent over the same optical channel.

4.4.1 Generic Digital Pulse Shaper Module

Pulse shaping is performed according to the Nyquist criterion to generate ISI-free signals. Optical methods such as Nyquist optical filter [144] or an ordinary optical filter and a pulse carver [145] to generate Nyquist WDM signals have been demonstrated. Electrical pulse shaping [40, 146, 147] implemented either in the analog or in the digital domain can be alternatively done to delicately constitute the spectrum in electrical domain. Digital filtering approaches require a DAC at the transmitter which incurs additional complexity due to DSP processing. As compared with optical

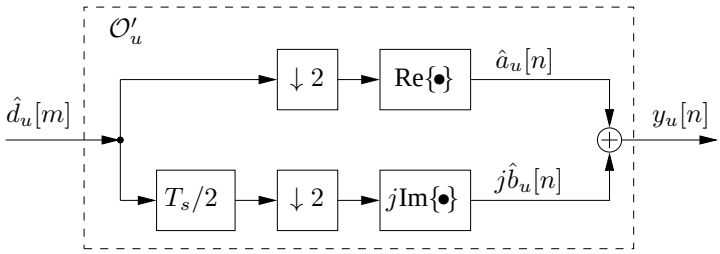

(a) OQAM Destaggering, u odd

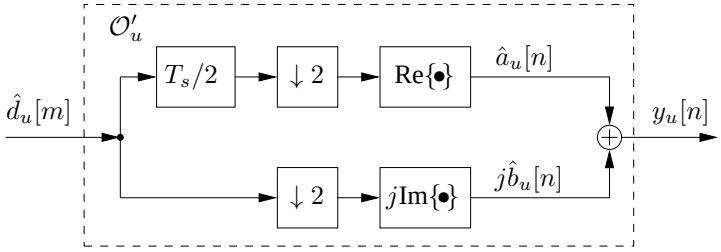

(b) OQAM Destaggering, u even

Fig. 4.3. OQAM Destaggering in odd- and even-numbered channels

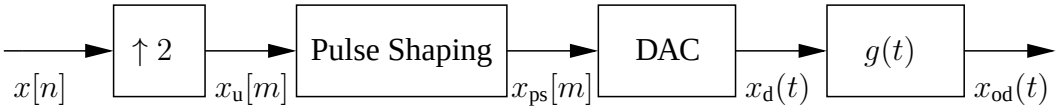

Fig. 4.4. Generic Digital Spectral Shaping Module

approaches, DSP-based pulse shaping solutions are more flexible as the same hardware can be used to generate different filter shapes and modulation formats [148]. We therefore present and adopt digital filtering for pulse shaping of the input signal.

A generic module for digital pulse shaping is shown in Fig. 4.4. The input signal $x[n]$ is upsampled to avoid aliasing in the bandwidth B before being pulse shaped. We choose an upsampling factor of 2. Due to the reasons we mentioned in Sec. 4.2, an RRC filter is our choice for the pulse shaper in the transmitter of each wavelength channel. In order to relax the constraints on the filter length and the tolerable jitter, we opt for a non-zero roll-off factor ρ for the RRC filter.
RRC filtering for digital pulse shaping can be performed either in the TD or in the FD. In the TD, the upsampled input signal $x_{\mathrm{u}}[m]$ is linearly convolved with a digital FIR RRC filter to obtain the RRC-shaped signal. An FIR RRC filter is obtained from the continuous time RRC impulse response of infinite support in (4.4) by firstly sampling it at $T_s/2$ spacing and then truncating it by a discrete-time window function of length $M_p/2+1$. In the FD, the overlap techniques perform linear convolution of the signal with the RRC pulse shaper. Two overlap methods exist in the literature: the overlap-and-save and overlap-and-add. We deploy the overlap-and-save method with 50% overlap (OLS-50%) for filtering in the FD. A schematic of the OLS-50% method is shown in Fig. 3.2 where the length of DFT and IDFT is M_p. The M_p coefficients of the RRC filter in the FD necessary for pulse shaping are obtained by evaluating $H_{\mathrm{RRC}}(f)$ in (4.6) at M_p discrete frequency points $f_p, p = 0, 1, \cdots, M_p - 1$ defined in (3.17). Since all M_p degrees of freedom are used in the design of the FD RRC filter, the system is no longer a linear time invariant system but rather a linear time variant one. However, for the FIR design of the RRC filter in TD, the system is linear time invariant since $M_p/2+1$ degrees of freedom has been used for the design.

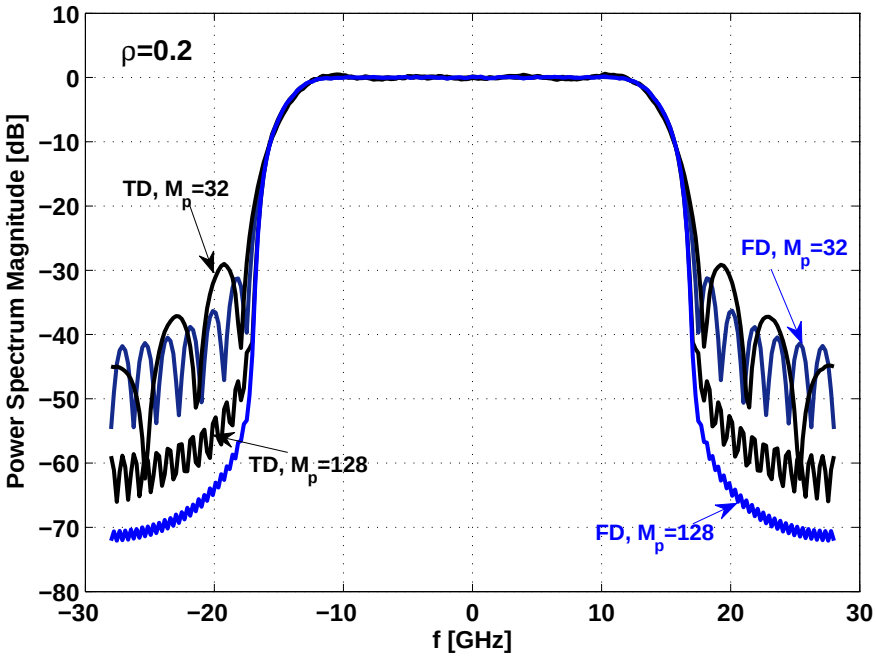

Fig. 4.5. Power spectral density of the input signal pulse shaped with an RRC filter of $\rho = 2$ designed in the FD and TD

Different figures of merit determine whether to perform TD or FD filtering for pulse shaping the upsampled signal $x_{\mathrm{u}}[m]$. Complexity in terms of the number of required real multiplications per output symbol is one figure of merit. As we showed in Sec. 3.3.3, when $M_p \geq 4$, which is the case for pulse shaping to design an RRC filter, the multiplication complexity for filtering in the FD is much less than the complexity in the TD. Another important figure of merit that drives the use of FD filtering rather than TD filtering is the power of the sidelobes of the attained RRC pulse-shaped signal. This is an important attribute in baud-rate spaced systems because the power of the sidelobes causes out-of-band radiation. Since the out-of-band radiation leaks to adjacent channels, it leads to ICI in baud-rate spaced Nyquist WDM systems. We plot in Fig. 4.5 the power spectral density of the signal $x_{\mathrm{ps}}[m]$ obtained by either TD or FD RRC filtering of the signal $x_{\mathrm{u}}[m]$ for different values of M_p and with a roll-off value of $\rho = 0.2$. As it can be seen in the plot, the power of the sidelobes of the pulse-shaped signal $x_{\mathrm{ps}}[m]$ is larger with TD filtering than with FD filtering. Additionally, as M_p increases, the power of the sidelobes of the RRC-pulsed signal $x_{\mathrm{ps}}[m]$ obtained by both methods for filtering decreases, but with FD filtering the signal has lower sidelobes than with TD filtering. Therefore, throughout this thesis we choose FD filtering with the method of OLS-50% for performing RRC pulse shaping of each user's upsampled signal not only because it has lower computational complexity than TD filtering but also because it delivers lower power of the sidelobes of the generated signal; an essential parameter in baud-rate spaced Nyquist WDM systems.

The pulse shaped signal $x_{\mathrm{ps}}[m]$ is then converted to the analog domain through a DAC to get the signal $x_{\mathrm{d}}(t)$ in order to further modulate it onto an optical carrier. The DAC holds each digital value for half a symbol period and then filters it. Because the DAC is suppressing the periodic repetitions inherent to its input sequence, a filter denoted as $g(t)$ is employed as part of the digital

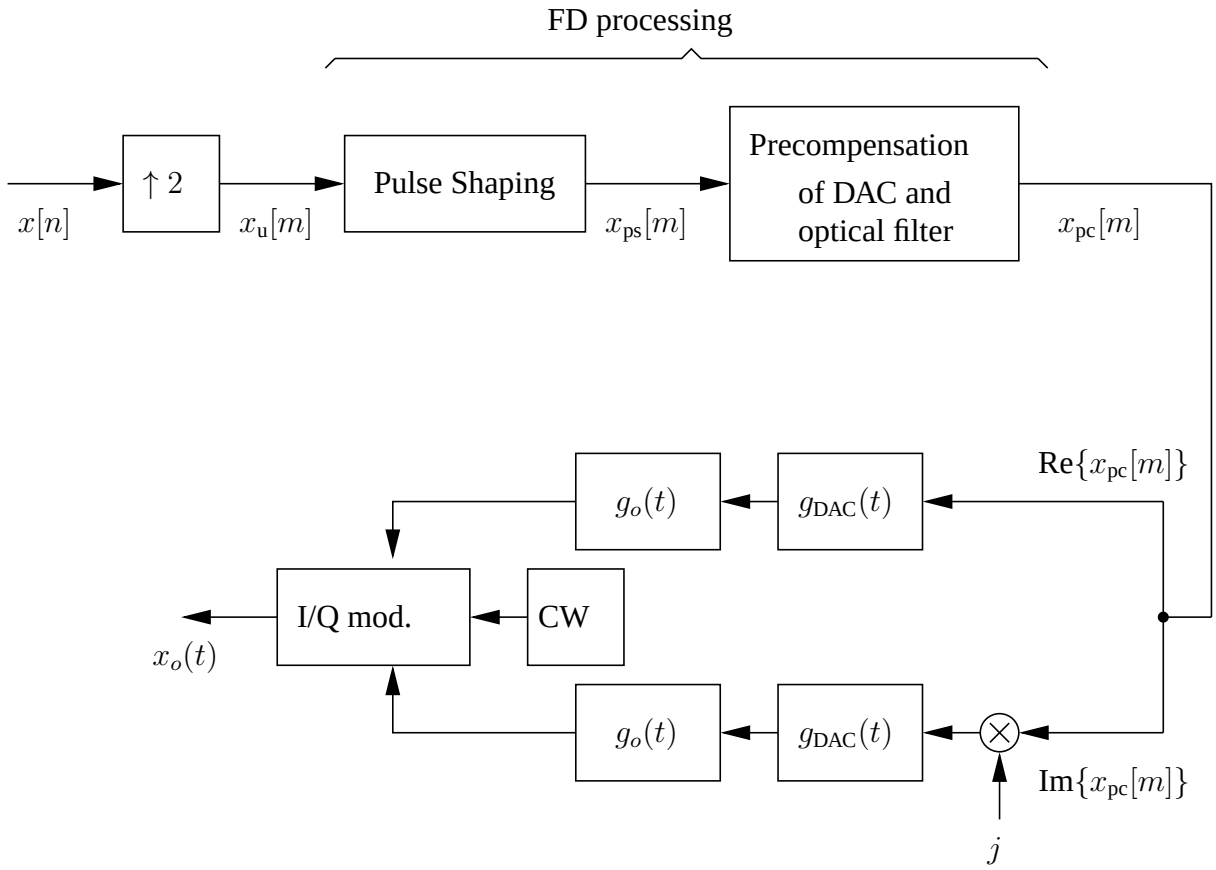

Fig. 4.6. Transmitter module per wavelength channel: digital pulse shaping and precompensation of the DAC and the optical filter and optical modulation

pulse shaper module. Realistic models for the DAC and the filter $g(t)$ for suppressing the periodic repetitions of the input signal to the DAC are given in the following section.

4.4.2 Transmitter Design per Wavelength-channel of WDM System

The transmitter in each wavelength channel constitutes of a digital pulse shaper, a digital predistorter and an optical signal modulator.

The input signal $x[n]$ in each wavelength channel is digitally pulse shaped in the FD as we presented in Sec. 4.4.1 to get the signal $x_{\mathrm{od}}(t)$. However, the signal $x_{\mathrm{od}}(t)$ is distorted by the DAC and the optical filter. This induces ISI and degrades the performance of the overall system. These distortions can be compensated at either the transmitter or at the receiver. It is intuitively reasonable to compensate the distortions already at the transmitter i.e. at the origin where they are introduced. When the compensation is performed at the receiver, the distorted signal propagates through the time-invariant or -variant channel making the compensation complicated. Accordingly, we adopt a transmitter model per wavelength channel shown in Fig. 4.6. A detailed description of precompensation is explained in the following paragraph. After pulse shaping and precompensation, the real and the imaginary part of the signal $x_{\mathrm{pc}}[m]$ are fed into the DAC. They are filtered with the impulse response of the DAC and finally with the optical filter. The real and imaginary part of the analog electric signal are then used for the optical PDM-QPSK modulation by ideal IQ modulators.

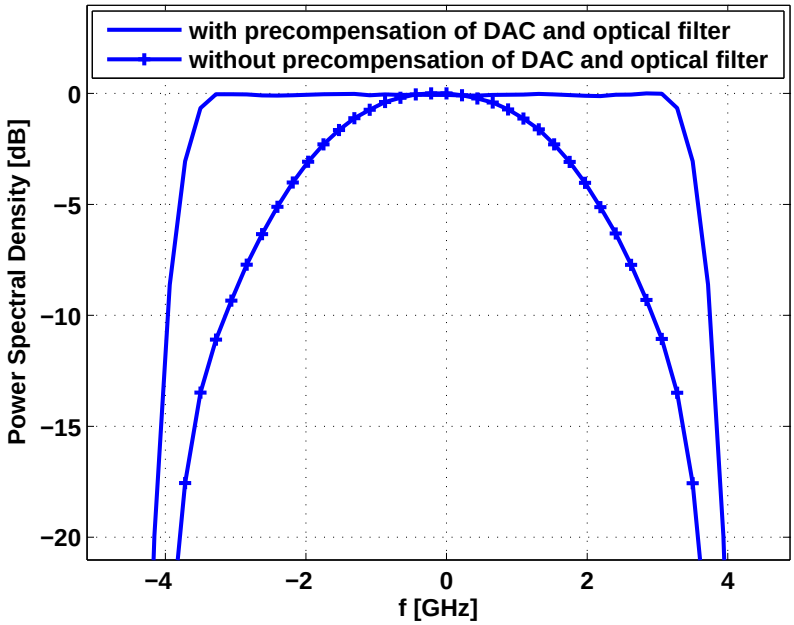

Fig. 4.7. Power spectral density of the signal with and without predistortion of the DAC and the optical filter

One advantage of filtering (pulse shaping) the signal $x_{\mathrm{u}}[m]$ in the FD in the transmitter is that it is relatively straightforward to pre-distort it as well in the FD. Provided that the transfer function of DAC and the filter $g(t)$ are known beforehand, RRC pulse-shaped signal $x_{\mathrm{ps}}[m]$ is pre-distorted in the FD with the OLS-50%. In this case, the frequency transformed overlapping blocks formed from $x_{\mathrm{ps}}[m]$ are point-wise multiplied by the inverse of the transfer function of the DAC and by the inverse of the transfer function of the filter $g(t)$ at each discrete frequency point f_p for pre-distortion. We model the DAC in the FD as a fifth-order Bessel function $H_{\mathrm{DAC}}(f)$ defined in (2.7) with single-sided 3-dB bandwidth of $B_{\mathrm{DAC}} = 0.25 \times B = 7$ in GHz. We model the filter suppressing the periodic repetitions inherent to the input sequence of the DAC as a Gaussian filter denoted as $g_o(t)$ which has a frequency response $H_o(f)$ defined in (2.6) with order $n_{\mathrm{od}} = 2$. We choose $B_{\mathrm{O3dB}} = 35$ GHz for the double-sided 3-dB bandwidth of $H_o(f)$. The FD digital pulse shaping and predistortion is carried out with the same FFT and IFFT in order to save computational complexity. In other words, for OLS-50% method, the overlapping blocks formed from the upsampled signal $x_{\mathrm{u}}[m]$ which when transformed to the FD by an FFT of length M_p are point-wise multiplied by $H_{\mathrm{RRC}}(f)/\left(H_{\mathrm{DAC}}(f)H_o(f)\right)$ evaluated at discrete frequency points $f_p, p = 0, 1, \cdots, M_p - 1$.

In Fig. 4.7, the power spectral density of the signal $x_{\mathrm{o}}(t)$ generated in each wavelength channel is plotted with and without the predistortion of the DAC and the optical filter. The loss in power of the spectrum of the non predistorted RRC pulse-shaped signal causes ISI. A consequence of predistortion of the transfer function of the DAC and the optical filter is that the 3-dB bandwidth of either the DAC or the optical filter has no influence on the performance of the system in the case of infinite resolution of the DAC i.e. no quantization error effects.

4.4.3 Wavelength Division Multiplexing with Baud-rate Spacing of the Channels

Multiplexing is the process of combining two or more signals into a single transmission line. Wavelength division multiplexing belongs to the class of optical multiplexing techniques where each wavelength channel is assigned a unique carrier frequency f_c (or correspondingly a unique wavelength λ_c) and the independent wavelength channels are transmitted at the same time on the same fiber link. The use of WDM therefore allows for a manifold increase in the data-rates of long-haul optical transmission systems. Even more importantly, it allows for a tremendous decrease in the cost per transmitted bit.

Multiplexing enhances the efficient use of the available optical bandwidth. An optical multiplexer combines the output of several transmitters such that the frequency separation $\Delta f = f_c^{u+1} - f_c^u$ between the neighboring carrier frequencies f_c^{u-1} and f_c^u of user $u-1$ and u, respectively, is only a fraction α_{sp} of the inverse of the symbol period $T_s = 1/B$, i.e.

$$\alpha_{\text{sp}} = \Delta f T_s \tag{4.7}$$

where α_{sp} could be equal to, less than or greater than 1. The ultimate capacity of WDM fiber links depends on how closely the wavelength channels can be packed. The minimum channel spacing Δf is limited by ISI and ICI. A measure of the spectral efficiency of a WDM system is given as $\eta_{\text{sp}} = \frac{1}{\alpha_{\text{sp}}}$. Attempts are made to make η_{sp} as large as possible.

In this thesis, we consider three isolated wavelength channels and a fixed channel spacing between the neighboring channels at the baud-rate. This means that $\Delta f = B$ and consequently the efficiency is $\eta_{\text{sp}} = 1$. The wavelength channel of user 2 is in the baseband and the wavelength channel of users 1 and 3 are considered as the immediate neighboring channels. The optical signal generated in each of these wavelength channels denoted as $x_{\text{o},1}(t)$ and $x_{\text{o},3}(t)$, respectively, are modulated as

$$x_1(t) = x_{\text{o},1}(t)\exp(j2\pi Bt), \tag{4.8}$$
$$x_3(t) = x_{\text{o},3}(t)\exp(-j2\pi Bt). \tag{4.9}$$

Fig. 4.8 shows the transmitter of a Nyquist WDM system consisting of the individual transmitters of each wavelength channel, and an optical multiplexer. The signal $x(t)$ transmitted over the same fiber link can be expressed by

$$x(t) = x_1(t) + x_2(t) + x_3(t) \tag{4.10}$$

where $x_2(t) = x_{\text{o},2}(t)$ represents the baseband optical signal of user 2.

A baud-rate multiplexing of the adjacent wavelength channels causes inevitable ICI due to spectra overlap. We prove this by examining the relationship between α_{sp} and the roll-off factor ρ of the RRC pulse-shaper. In general, the spectra of adjacent channels overlap when $\alpha_{\text{sp}} - (1+\rho)/2 < (1+\rho)/2$ and consequently when

$$\alpha_{\text{sp}} < 1 + \rho. \tag{4.11}$$

In baud-rate channel spaced WDM system where $\alpha_{\text{sp}} = 1$, equation (4.11) always holds since $\rho > 0$. Therefore, baud-rate spacing causes considerable ICI which demands developing receive methods to mitigate it.

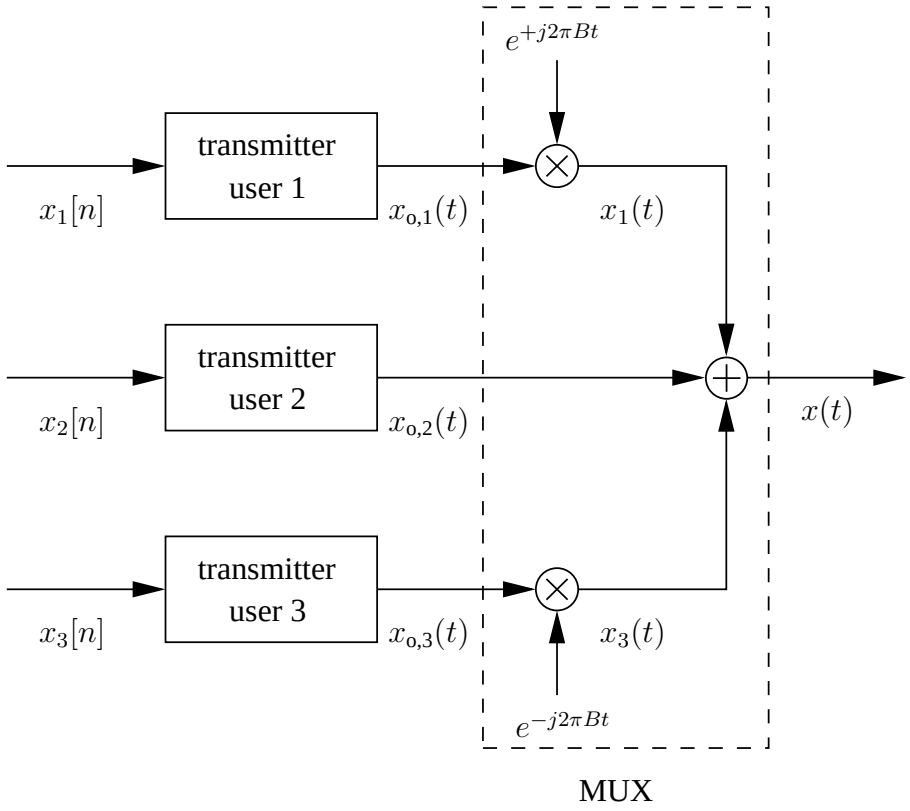

Fig. 4.8. Nyquist WDM Transmitter Model: individual wavelength channel transmitter and an optical transmitter

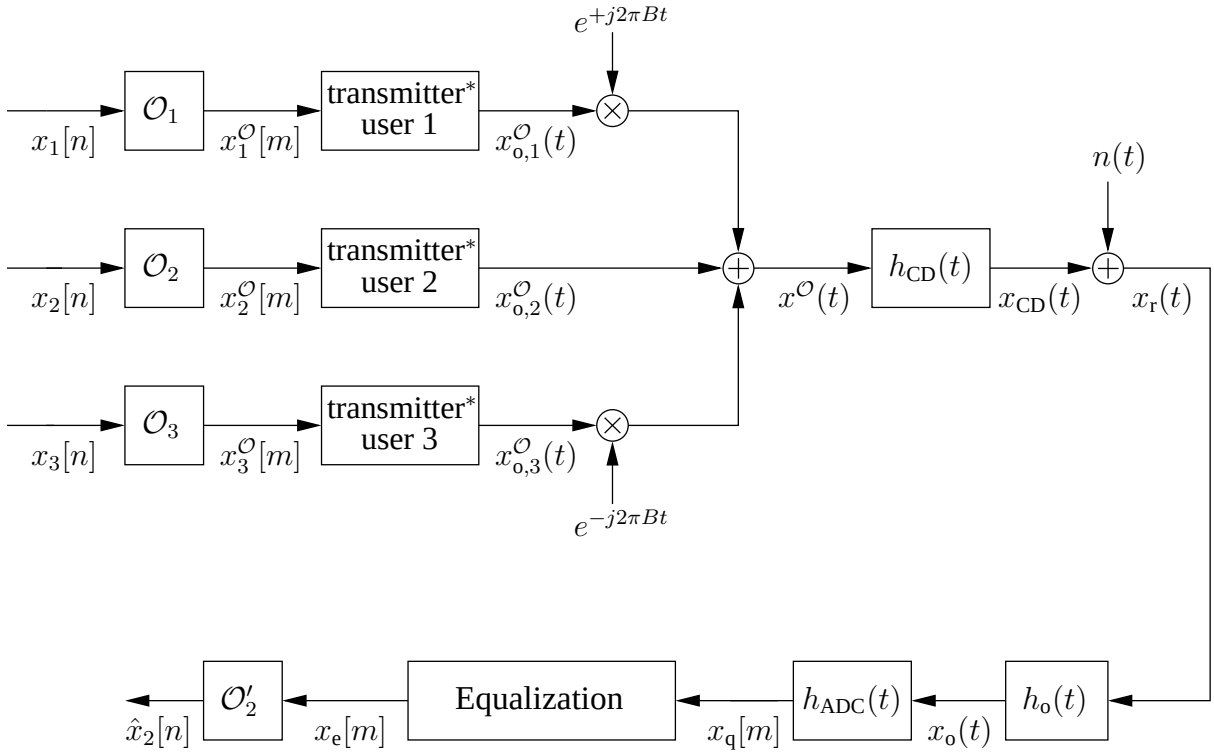

Fig. 4.9. OQAM Nyquist WDM system model of three isolated wavelength channels in the transmitter and one wavelength channel (central channel) in the receiver

4.5 Nyquist WDM Systems with Offset QAM Modulation Scheme

4.5.1 System Model

We show in Fig. 4.9 the schematic block diagram of an OQAM WDM system. In the transmitter side, the discrete-time input signal $x_u[n], u = \{1, 2, 3\}$ in the wavelength channel of each user u, respectively, is firstly staggered in the electrical domain. This is done through OQAM modulators $\mathcal{O}_u$ according to Figs. 4.2(a) and 4.2(b) depending whether the wavelength channel is odd- or even-numbered, respectively. The signal $x_u[n]$ has a variance $\mathrm{E}[|x_u[n]|^2] = \sigma_x^2$. The output signal of the OQAM modulator in each wavelength channel denoted as $x_u^{\mathcal{O}}[m]$ forms the input signal to the transmitter module for pulse shaping as we explained in Sec. 4.4. The transmitter module in each wavelength channel of the OQAM WDM system differs from the transmitter module in Fig. 4.6 in Sec. 4.4 because in the former the upsampling operation is already included in the OQAM modulators. Therefore, the staggered signal $x_u^{\mathcal{O}}[m]$ in each wavelength channel is directly operated by the pulse shaper in the transmitter module presented in Fig. 4.6. The analog output signal in each wavelength channel is denoted as $x_{\mathrm{o},u}^{\mathcal{O}}(t)$. The transmitted signal $x^{\mathcal{O}}(t)$ obtained as in (4.10) comprises the differently modulated signals of $x_{\mathrm{o},u}^{\mathcal{O}}(t)$ in each wavelength channel according to (4.8) and (4.9). It is then coupled into the standard single mode fiber which is modeled as a linear CD channel $h_{\mathrm{CD}}(t)$ to get the signal $x_{\mathrm{CD}}(t) = h_{\mathrm{CD}}(t) * x^{\mathcal{O}}(t)$.

At the receiver side, the signal of each wavelength channel is first demultiplexed separately for further processing before noise $n(t)$ from different sources explained in Sec. 2.4 is loaded to it. We consider the receiver of the baseband channel i.e. the receiver of user 2. The input signal to the receiver of user 2 is the perturbed signal $x_{\mathrm{r}}(t) = x_{\mathrm{CD}}(t) + n(t)$. The noise $n(t)$ has variance σ_n^2 and is related to optical signal-to-noise ratio (OSNR) commonly used in optical communication systems given in (3.8). The signal $x_{\mathrm{r}}(t)$ is then optically filtered by $h_o(t)$ to get the signal $x_{\mathrm{o}}(t) = h_o(t) * x_{\mathrm{r}}(t)$. The equivalent low-pass transfer function of the optical filter $h_o(t)$ denoted as $H_o(f)$ is modeled in the FD as a Gaussian function given in (2.6) with order $n_{\mathrm{od}} = 2$ and $B_{\mathrm{O3dB}} = 35$ GHz. Afterward, the optical signal $x_{\mathrm{o}}(t)$ is converted into an electrical signal denoted as $x_{\mathrm{ro}}(t)$ by an electrical filter $h_e(t)$. It is modeled in the FD as a 5th-order Bessel function denoted as $H_e(f)$ defined in (2.7) with $B_{\mathrm{E3dB}} = 0.7 \times B = 19.6$ GHz. We assume that the electrical filter represents a realistic model of an ADC which samples the signal at double the symbol-rate. The optical and electrical filters define the opto-electronic front-end of the coherent receiver modeled by $h_{\mathrm{rx}}(t) = h_o(t) * h_e(t)$ which has the frequency response of $H_{\mathrm{rx}}(f) = H_o(f)H_e(f)$. The real and imaginary tributaries of the sampled signal are added together to get $x_{\mathrm{q}}[m]$ which is at this stage equalized to get the signal $x_{\mathrm{e}}[m]$. After equalization, the signal $x_{\mathrm{e}}[m]$ is then destaggered through OQAM demodulators according to Fig 4.3(b) since the wavelength channel of user 2 is even-numbered to get finally the symbol-based signal $\hat{x}_2[n]$.

4.5.2 Equalizer Design

We adopt, in the same way as we did in Chapter 3, the OLS-50% method with an I/FFT of length M for the FD equalization of $x_{\mathrm{q}}[m]$ to get the signal $x_{\mathrm{e}}[m]$. We aim thus at deriving a FD equalizer at each discrete frequency point $k = 0, 1, \cdots, M-1$ in the wavelength channel of user 2 denoted as $E_2^{\mathrm{OQAM}}[k]$. As we showed in Sec. 4.3, in OQAM WDM systems the ICI induced to the baseband channel of user 2 from the two neighboring channels is eliminated[1] through the staggering and destaggering operations in the transmitter and receiver, respectively. In other words, the tolerance

[1] in the absence of any system imperfection like for example quantization errors, frequency, phase and time offset

to dispersion in OQAM WDM systems is equivalent to the dispersion tolerance in systems with a single wavelength channel. This simplifies the design of the equalizer $E_2^{\text{OQAM}}[k]$. It is therefore straightforward to design the FD MMSE equalizer $E_2^{\text{OQAM}}[k]$ with single-tap in the same way as we did in Sec. 3.6. For this, the MSE expression needed for the derivation of $E_2^{\text{OQAM}}[k]$ is built between the sent signal $x_2[n]$ and the detected signal $\hat{x}_2[n]$ on the wavelength channel of user 2 without including the signals from the immediate neighbouring channels. The equalizer $E_2^{\text{OQAM}}[k]$ at each discrete frequency point $k = 0, 1, \cdots, M-1$ employed in the wavelength channel of user 2 can be expressed by

$$E_2^{\text{OQAM}}[k] = H_{\text{RRC}}(f)H_{\text{CD}}^{-1}(f)H_{\text{rx}}^{-1}(f)\big|_{f=f_k}. \tag{4.12}$$

It is a simplified expression of (3.79) since the FD expression of the total channel in this case is $H_{\text{tot}}(f) = H_{\text{RRC}}(f)H_{\text{CD}}(f)H_{\text{rx}}(f)$. For (4.12) we also considered that $\sigma_N^2/\sigma_X^2 \to \infty$ in (3.79) and f_k is defined in (3.17) with an oversampling factor $o_s = 2$. Note that one complex-valued equalizer $E_2^{\text{OQAM}}[k]$ is needed and derived at each discrete frequency point k to equalize the complex signal $x_{\text{q}}[m]$. In other words, we do not need to derive two different equalizers each aimed to equalize either the real or the imaginary tributary of $x_{\text{q}}[m]$.

4.5.3 Performance Analysis

The performance of the OQAM WDM system is examined in terms of the required OSNR (ROSNR) for a BER value of 10^{-3} for back-to-back connection of the transmitter and receiver i.e. without CD channel in between. It is compared to that of an OQAM single wavelength channel system with the same settings. In OQAM single wavelength channel system, only one channel is present in the transmitter i.e. there are no interfering channels and in the receiver the equalizer derived in (4.12) is applied. We use for the simulations QPSK modulation scheme and $B = 28$ GHz.

In the simulations in Fig. 4.10, the BER vs. OSNR is plotted for $M_p = 256$ and $M = 512$. As it can be seen in the figure, both systems deliver the same performance for any value of ρ with a required OSNR value of 13.3 dB to get a BER of 10^{-3}. This is also the theoretical OSNR value required for the given BER in case of QPSK modulation scheme. The simulation results prove the theoretical assumption that OQAM WDM systems are ICI-free systems in the absence of a propagating channel and any other distortion in the system.

To examine the effects of M_p on the performance of the overall system, we plot in Fig. 4.11 the ROSNR for BER of 10^{-3} with different values of ρ and M_p (given that M is simultaneously large enough for the design of the RRC filter with the same ρ in the receiver). Specifically, we plot for $\rho = 0.01, 0.05, 0.1$ and $M_p = 64, 128, 256$ the ROSNR values in a back-to-back connection of the transmitter and the receiver i.e. without CD channel in between. In the receiver where also an RRC filter is employed with the same ρ value as the pulse shaper in the transmitter, we choose $M = 512$ for its design. As it can be seen in the figure, for small ρ values, for example $\rho = 0.01$ and 0.05, there is degradation in the overall performance of the system. This is because the impulse response of the RRC filter for such ρ values is long and an I/FFT length of $M_p = 64$ or even smaller in the transmitter is not sufficient to approximate it leading to ISI in the wavelength channel of user 2 and ICI from the interfering channels. For the case of $M_p = 64$ and $\rho = 0.01$ for example, a 0.5 dB penalty in OSNR is incurred given that the theoretical value of the ROSNR is 13.3 dB for QPSK modulation schemes to get a BER of 10^{-3}. In order to avoid this degradation, M_p should be chosen large enough for small ρ values. For example, for $\rho = 0.01$, an I/FFT length of $M_p = 256$ is sufficient to avoid degradation in the performance of the system. For $\rho = 0.1$ and larger, $M_p = 128$

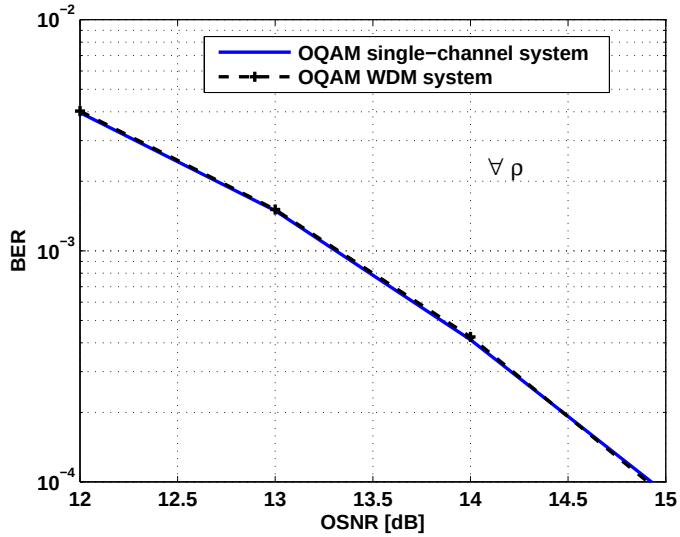

Fig. 4.10. BER vs. OSNR: performance of single wavelength channel vs. OQAM WDM system

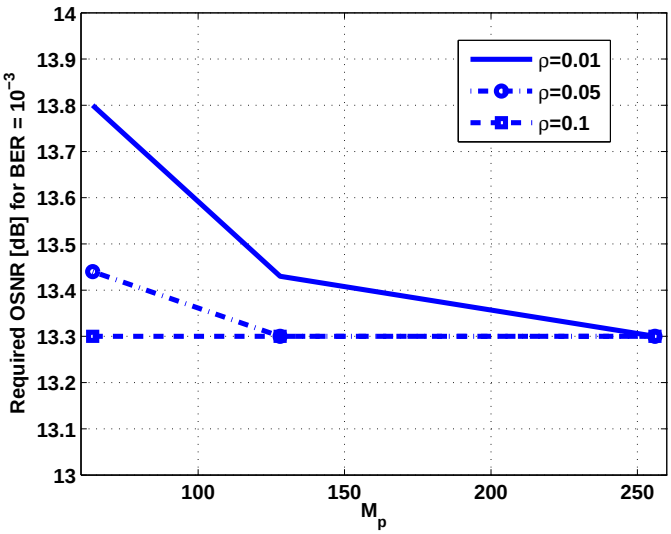

Fig. 4.11. Effects of M_p on the overall performance of an OQAM WDM system for different ρ values for the pulse shaper

is already sufficient to avoid degradation in performance. As a consequence, a system employing an RRC filter with a small ρ values experiences an increase in complexity at the transmitter side as compared to a system with large ρ values because of the additional DSP processing.

4.6 Nyquist WDM Systems with Standard QAM Modulation Scheme

In ideal Nyquist WDM systems with standard QAM modulation (SQAM) schemes where the wavelength channels are packed with a channel spacing equal to the baud-rate, it is difficult to realize a rectangular spectrum even with high cost. The latter is a necessary requirement to eliminate the effects of ICI in these systems. Moreover, in these systems where there is no guard interval, any slight spectral imperfection results in ICI which degrades the performance of the system. In this

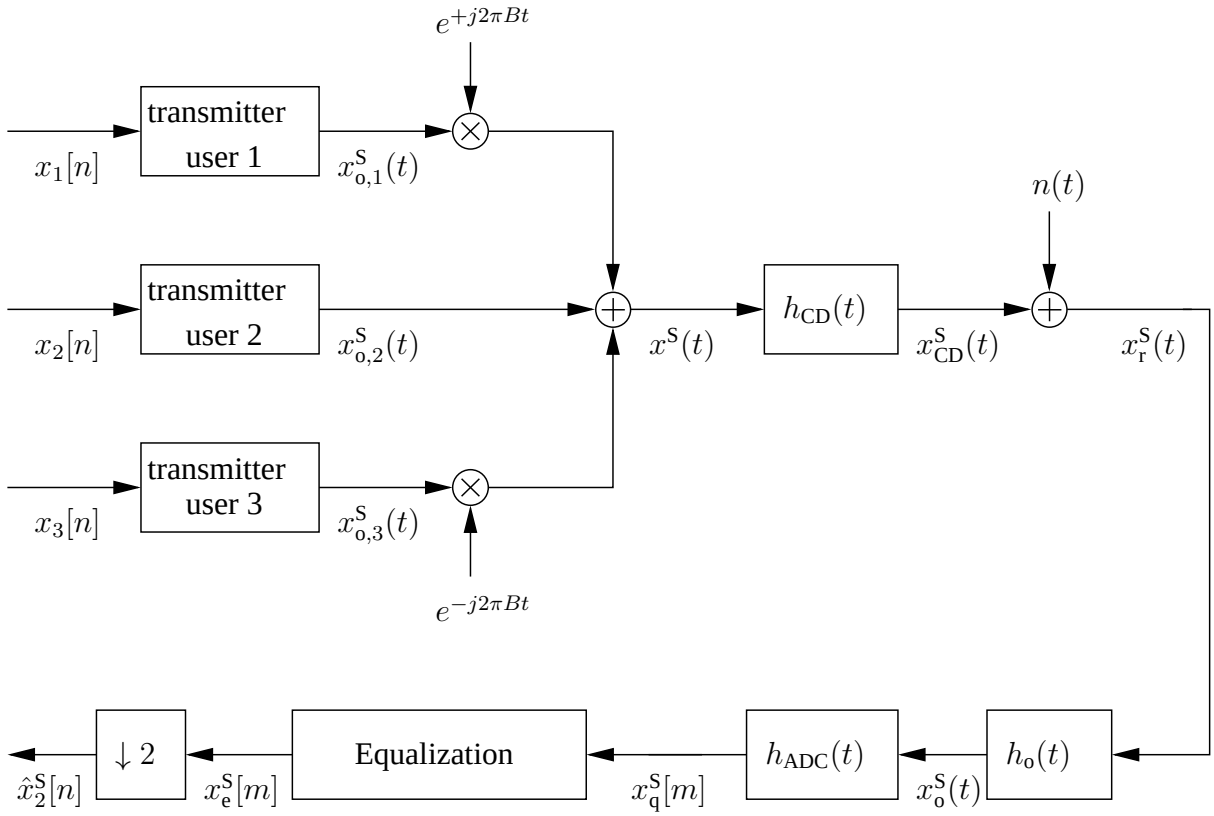

Fig. 4.12. Standard QAM Nyquist WDM system model of three isolated channels in the transmitter and one channel (central channel) in the receiver

section, we relax the requirement of a tight roll-off factor for the RRC pulse shaper by allowing $\rho > 0$ in Nyquist SQAM WDM systems. This leads to considerable ICI in the system requiring receiver-side approaches to mitigate it. We present, therefore, two approaches for ICI equalization. The first one is a single-receiver equalizer where the equalization is carried out independently in each channel of interest such that ICI is taken into account in the optimization process very similar to the noise. The second approach is multi-receiver equalization method where the information of the signals in adjacent channels are used to eliminate ICI in each channel of interest.

4.6.1 SQAM WDM Single-receiver System Model

We show in Fig. 4.12 the schematic block diagram of a SQAM WDM system with three isolated transmitters and the receiver of one channel of interest for equalization which is the baseband channel of user 2. In the transmitter side, the discrete-time input signal $x_u[n], u = \{1, 2, 3\}$ in the wavelength channel of each user u, respectively, forms the input signal to the transmitter module for pulse shaping as we explained in Sec. 4.4. The signal $x_u[n]$ has a variance $\mathrm{E}[|x_u[n]|^2] = \sigma_x^2$. The transmitter module in each wavelength channel of the SQAM WDM system is shown in Fig. 4.6. The analog output signal in each wavelength channel is denoted as $x^{\mathrm{S}}_{\mathrm{o},u}(t)$. The transmitted signal $x^{\mathrm{S}}(t)$ obtained as in (4.10) comprises the differently modulated signals of $x^{\mathrm{S}}_{\mathrm{o},u}(t)$ in each wavelength channel according to (4.8) and (4.9). It is then coupled into the standard single mode fiber which is modeled as a linear CD channel $h_{\mathrm{CD}}(t)$ to get the signal $x^{\mathrm{S}}_{\mathrm{CD}}(t) = h_{\mathrm{CD}}(t) * x^{\mathrm{S}}(t)$.

At the receiver side, the signal of each wavelength channel is first demultiplexed separately for further processing before noise $n(t)$ from different sources explained in Sec. 2.4 is loaded to it. In

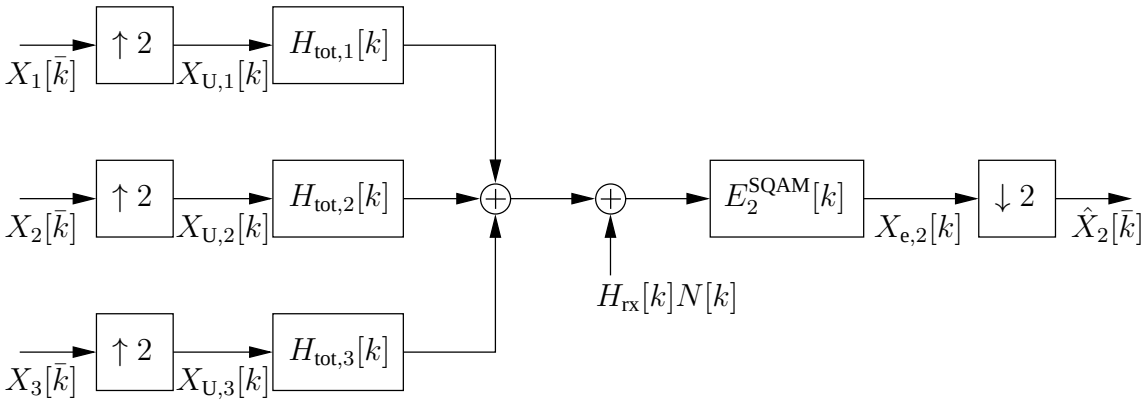

Fig. 4.13. Simplified model of a SQAM WDM system with single-receiver for FD equalizer design

a SQAM WDM system with a single-receiver structure for equalization, we consider the receiver of the baseband channel. The baseband perturbed signal denoted as $x_{\mathrm{r}}^{\mathrm{S}}(t) = x_{\mathrm{CD}}^{\mathrm{S}}(t) + n(t)$ serves as the input signal to the coherent receiver of the wavelength channel of user 2. The noise $n(t)$ of variance σ_n^2 is related to OSNR commonly used in optical communication systems given in (3.8). The signal $x_{\mathrm{r}}^{\mathrm{S}}(t)$ is then optically filtered by $h_o(t)$ to get the signal $x_{\mathrm{o}}^{\mathrm{S}}(t) = h_o(t) * x_{\mathrm{r}}^{\mathrm{S}}(t)$. The equivalent low-pass transfer function of the optical filter $h_o(t)$ is modeled in the FD as a Gaussian function denoted as $H_o(f)$ given in (2.6) with order $n_{\mathrm{od}} = 2$ and $B_{\mathrm{O3dB}} = 35$ GHz. Afterward, the optical signal is converted into an electrical signal denoted as $x_{\mathrm{ro}}^{\mathrm{S}}(t)$ by an electrical filter $h_e(t)$. It is modeled in the FD as a 5th-order Bessel function denoted as $H_e(f)$ defined in (2.7) with $B_{\mathrm{E3dB}} = 0.7 \times B = 19.6$ GHz. We assume that the electrical filter represents a realistic model of an ADC which samples the signal at double the symbol-rate. The optical and electrical filters define the opto-electronic front-end of the coherent receiver modeled by $h_{\mathrm{rx}}(t) = h_o(t) * h_e(t)$ which has the frequency response of $H_{\mathrm{rx}}(f) = H_o(f)H_e(f)$. The real and imaginary tributaries of the sampled signal are added together to get $x_{\mathrm{q}}^{\mathrm{S}}[m]$. The latter is equalized to get the signal $x_{\mathrm{e}}^{\mathrm{S}}[m]$ which is finally downsampled by a factor of 2 to get the symbol-based signal $\hat{x}_2^{\mathrm{S}}[n]$.

4.6.1.1 Equalizer Design

For the equalization of $x_{\mathrm{q}}^{\mathrm{S}}[m]$, we adopt in the same way as we did in Chapter 3 the OLS-50% method with an I/FFT of length M. We aim thus at deriving a FD equalizer at each discrete frequency point $k = 0, 1, \cdots, M-1$ in the wavelength channel of user 2 denoted as $E_2^{\mathrm{SQAM}}[k]$. The crucial idea in the design of $E_2^{\mathrm{SQAM}}[k]$ in SQAM WDM systems with single-receiver for equalization is that the ICI of the neighboring channels to the wavelength channel of user 2, which is in the baseband, is also introduced in the optimization procedure. We, therefore, use the statistical information of the symbols on the immediately adjacent neighboring channels i.e. the wavelength channel of users 1 and 3 in order to get a regularization term for the resulting Wiener-Hopf equation of the MSE minimization. Thus the interference is taken into account in the optimization process very similar to the noise.

A simplified model of the SQAM WDM system with single-receiver for equalization necessary for the derivation of the equalizer $E_2^{\mathrm{SQAM}}[k], k = 0, 1, \cdots, M-1$ is shown in Fig. 4.13.

The $\bar{k}$-th frequency point of the discrete Fourier transform of the discrete-time input signal $x_u[m], u \in \{1, 2, 3\}$ in Fig. 4.12 is denoted as $X_u[\bar{k}], \bar{k} = 0, 1, \cdots, M/2-1$ in Fig. 4.13. The TD and FD signals have the same variance of σ_x^2 according to Parseval's theorem. The discrete TD signal $x_u[n], u \in \{1, 2, 3\}$ after upsampling by a factor of 2 is denoted as $x_{\mathrm{U},u}[m]$, respec-

tively. The latter thus has a variance of $\sigma_X^2 = \frac{1}{2}\sigma_x^2$ according to (B.4). Therefore, it follows that the k-th (frequency) point of the discrete Fourier transform of $x_{\mathrm{U},u}[m], u \in \{1,2,3\}$ denoted as $X_{\mathrm{U},u}[k], k = 0, 1, \cdots, M-1$, respectively, has the same variance of value $\sigma_X^2 = \frac{1}{2}\sigma_x^2$.

We denote $H_{\text{tot},2}[k]$ as the k-th frequency point of the discrete Fourier transform of the discrete TD representation of the total channel of user 2 in the baseband comprising the pulse shaper, the CD channel and the opto-electro receive filter. It can be obtained as follows

$$H_{\text{tot},2}[k] = H_{\text{RRC}}(f)H_{\text{CD}}(f)H_{\text{rx}}(f)\Big|_{f=f_k} \tag{4.13}$$

where f_k is defined in (3.17) with an oversampling factor $o_s = 2$.

The k-th frequency point of the discrete Fourier transform of the interfering channels i.e. wavelength channel of user 1 and 3 denoted, respectively as, $H_{\text{tot},1}[k]$ and $H_{\text{tot},3}[k]$ can be obtained from (4.13) as

$$H_{\text{tot},1}[k] = \begin{cases} 0, & \text{for} \quad k = 0, 1, \cdots, M/2-1, \\ H_{\text{tot},2}[k - M/2], & \text{for} \quad k = M/2, \cdots, M-1, \end{cases} \tag{4.14}$$

$$H_{\text{tot},3}[k] = \begin{cases} H_{\text{tot},2}[k + M/2], & \text{for} \quad k = 0, 1, \cdots, M/2-1, \\ 0, & \text{for} \quad k = M/2, \cdots, M-1, \end{cases} \tag{4.15}$$

since the TD transmit filter in each interfering channel represents a modulated version of the transmit filter in the baseband channel i.e. the wavelength channel of user 2.

The discrete Fourier transform representation $H_{\text{rx}}[k]$ of the receiver filter is obtained by first sampling $h_{\text{rx}}(t)$ at double the symbol rate and then transforming it according to (1.7).

The k-th frequency point of the discrete Fourier transform of the noise denoted as $N[k]$ represents a FD representation of the noise $n(t)$ over a bandwidth of $2B$. The variance of $N[k]$ denoted as σ_N^2 is derived as in (3.8) over a frequency bandwidth of $2B$.

We can, therefore, express the k-th frequency point representation of the equalized signal $X_{\text{e},2}[k]$ as function of the total channel of user 2 i.e. $H_{\text{tot},2}[k]$, the interfering channels $H_{\text{tot},1}[k]$ and $H_{\text{tot},3}[k]$, the receive filter $H_{\text{rx}}[k]$, the upsampled signal of the desired user denoted as $X_{\mathrm{U},2}[k]$, the upsampled signal of the interfering users denoted as $X_{\mathrm{U},1}[k]$ and $X_{\mathrm{U},3}[k]$ the noise $N[k]$ and the equalizer $E_2^{\text{SQAM}}[k]$ as follows

$$\begin{aligned} X_{\text{e},2}[k] = {} & E_2^{\text{SQAM}}[k]H_{\text{tot},2}[k]X_{\mathrm{U},2}[k] + E_2^{\text{SQAM}}[k]\left(H_{\text{tot},1}[k]X_{\mathrm{U},1}[k] + H_{\text{tot},3}[k]X_{\mathrm{U},3}[k]\right) \\ & + E_2^{\text{SQAM}}[k]H_{\text{rx}}[k]N[k]. \end{aligned} \tag{4.16}$$

Taking into account the aliasing terms arising in the system arising from the optical filter, the k-th point of the discrete Fourier transform of the output signal in the wavelength channel of user 2 denoted as $\hat{X}_2[\bar{k}]$ can be written as function of the equalized signal $X_{\text{e},2}[k]$ as follows

$$\hat{X}_2[\bar{k}] = \begin{cases} \frac{1}{2}\left(X_{\text{e},2}[k] + X_{\text{e},2}\left[k + \frac{M}{2}\right]\right), & \text{for} \;\; 0 \le k \le M/2-1, 0 \le \bar{k} \le M/4-1, \\ \frac{1}{2}\left(X_{\text{e},2}[k] + X_{\text{e},2}\left[k - \frac{M}{2}\right]\right), & \text{for} \;\; M/2 \le k \le M-1, M/4 \le \bar{k} \le M/2-1. \end{cases} \tag{4.17}$$

For $0 \le \bar{k} \le M/4-1$, the output signal $\hat{X}_2[\bar{k}]$ in (4.17) when substituting (4.16) can be expressed in a matrix-vector notation as follows

$$\hat{X}_2[\bar{k}] = \frac{1}{2}\left(\boldsymbol{e}_{\text{D}}[k]\boldsymbol{h}_{\text{D}}[k]X_{\mathrm{U},2}[k] + \boldsymbol{H}_{\text{I}}[k]\boldsymbol{x}_{\mathrm{U,I}}[k] + \boldsymbol{H}_{\text{R}}[k]\boldsymbol{n}[k]\right) \tag{4.18}$$

where $0 \leq k \leq M/2-1$ with the following definitions of the vector-equalizer $\boldsymbol{e}_{\mathrm{D}}[k]$ and vector-channel $\boldsymbol{h}_{\mathrm{D}}[k]$, respectively, for the desired channel i.e. the wavelength channel of user 2

$$\boldsymbol{e}_{\mathrm{D}}[k] = \left[E_2^{\mathrm{SQAM}}[k] \quad E_2^{\mathrm{SQAM}}\left[k+\tfrac{M}{2}\right]\right], \tag{4.19}$$

$$\boldsymbol{h}_{\mathrm{D}}[k] = \left[H_{\mathrm{tot},2}[k] \quad H_{\mathrm{tot},2}\left[k+\tfrac{M}{2}\right]\right]^{\mathrm{T}}, \tag{4.20}$$

and the following definitions of the channel-matrix $\boldsymbol{H}_{\mathrm{I}}[k]$ and signal-vector $\boldsymbol{x}_{\mathrm{U,I}}[k]$, respectively, for the interfering channels i.e. the wavelength channel of users 1 and 3

$$\boldsymbol{H}_{\mathrm{I}}[k] = \begin{bmatrix} H_{\mathrm{tot},1}[k] & H_{\mathrm{tot},3}[k] \\ H_{\mathrm{tot},1}[k+\frac{M}{2}] & H_{\mathrm{tot},3}\left[k+\frac{M}{2}\right] \end{bmatrix}, \tag{4.21}$$

$$\boldsymbol{x}_{\mathrm{U,I}}[k] = \left[X_{\mathrm{U},1}[k] \quad X_{\mathrm{U},3}[k]\right]^{\mathrm{T}}, \tag{4.22}$$

and the receive filter matrix and noise vector, respectively,

$$\boldsymbol{H}_{\mathrm{R}}[k] = \begin{bmatrix} H_{\mathrm{rx}}[k] & 0 \\ 0 & H_{\mathrm{rx}}\left[k+\frac{M}{2}\right] \end{bmatrix}, \tag{4.23}$$

$$\boldsymbol{n}[k] = \left[N[k] \quad N\left[k+\tfrac{M}{2}\right]\right]^{\mathrm{T}}. \tag{4.24}$$

We used the fact that $X_{\mathrm{U},u}\left[k+\frac{M}{2}\right] = X_{\mathrm{U},u}[k], u = \{1,2,3\}$ since $X_{\mathrm{U},u}[k]$ is periodic with period $M/2$.

In a similar way to the criterion we developed in Sec. 3.6, we design the equalizer $E_2^{\mathrm{SQAM}}[k]$ at each discrete frequency point k according to the FD MMSE criterion. For this we build the mean squared error denoted as $J(\boldsymbol{e}_{\mathrm{D}}[k])$ at each discrete frequency point $\bar{k}$ between $\hat{X}_2[\bar{k}]$ and $\hat{X}_2[\bar{k}]$ as follows

$$\begin{aligned}
J(\boldsymbol{e}_{\mathrm{D}}[k]) &= \mathrm{E}\left[\left|\hat{X}_2[\bar{k}] - X_2[\bar{k}]\right|^2\right] \\
&= \mathrm{E}\left[\left|\frac{1}{2}\Big((\boldsymbol{e}_{\mathrm{D}}[k]\boldsymbol{h}_{\mathrm{D}}[k]-2)\, X_{\mathrm{U},2}[k] + \boldsymbol{e}_{\mathrm{D}}[k]\boldsymbol{H}_{\mathrm{I}}[k]\boldsymbol{x}_{\mathrm{U,I}}[k] + \boldsymbol{e}_{\mathrm{D}}[k]\boldsymbol{H}_{\mathrm{R}}[k]\boldsymbol{n}[k]\Big)\right|^2\right] \\
&= \mathrm{E}\Bigg[\frac{1}{4}\Big((\boldsymbol{e}_{\mathrm{D}}[k]\boldsymbol{h}_{\mathrm{D}}[k]-2)\, X_{\mathrm{U},2}[k] + \boldsymbol{e}_{\mathrm{D}}[k]\boldsymbol{H}_{\mathrm{I}}[k]\boldsymbol{x}_{\mathrm{U,I}}[k] + \boldsymbol{e}_{\mathrm{D}}[k]\boldsymbol{H}_{\mathrm{R}}[k]\boldsymbol{n}[k]\Big)\times \\
&\qquad \Big((\boldsymbol{e}_{\mathrm{D}}[k]\boldsymbol{h}_{\mathrm{D}}[k]-2)\, X_{\mathrm{U},2}[k] + \boldsymbol{e}_{\mathrm{D}}[k]\boldsymbol{H}_{\mathrm{I}}[k]\boldsymbol{x}_{\mathrm{U,I}}[k] + \boldsymbol{e}_{\mathrm{D}}[k]\boldsymbol{H}_{\mathrm{R}}[k]\boldsymbol{n}[k]\Big)^{\mathrm{H}}\Bigg] \\
&= \frac{1}{4}\Big(\sigma_X^2\, (\boldsymbol{e}_{\mathrm{D}}[k]\boldsymbol{h}_{\mathrm{D}}[k]-2)\, (\boldsymbol{e}_{\mathrm{D}}[k]\boldsymbol{h}_{\mathrm{D}}[k]-2)^{\mathrm{H}} + \sigma_X^2 \boldsymbol{e}_{\mathrm{D}}[k]\boldsymbol{H}_{\mathrm{I}}[k]\boldsymbol{H}_{\mathrm{I}}[k]^{\mathrm{H}}\boldsymbol{e}_{\mathrm{D}}[k]^{\mathrm{H}} \\
&\quad + \sigma_N^2 \boldsymbol{e}_{\mathrm{D}}[k]\boldsymbol{H}_{\mathrm{R}}[k]\boldsymbol{H}_{\mathrm{R}}[k]^{\mathrm{H}}\boldsymbol{e}_{\mathrm{D}}[k]^{\mathrm{H}}\Big),
\end{aligned} \tag{4.25}$$

where $X_u[\bar{k}] = X_{\mathrm{U},u}[k], u \in \{1,2,3\}$ for $\bar{k} = 0,1,\cdots,M/4-1$ and consequently $k = 0,1,\cdots,M/2-1$ [113] but the latter has a variance of σ_X^2 given in (3.58). The expectation is taken over the signals $X_{\mathrm{U},u}[k], u \in \{1,2,3\}$ and over the noise term $\boldsymbol{n}[k]$ with the following noise correlation matrix

$$\mathrm{E}\left[\boldsymbol{n}[k]\boldsymbol{n}[k]^{\mathrm{H}}\right] = \begin{bmatrix} \mathrm{E}\left[|N[k]|^2\right] & 0 \\ 0 & \mathrm{E}\left[|N[k+\frac{M}{2}]|^2\right] \end{bmatrix} = \sigma_N^2 \mathbf{1}_{2\times 2}. \tag{4.26}$$

It is assumed that the signals are uncorrelated i.e. $\mathrm{E}[X_{\mathrm{U},u}[k]X_{\mathrm{U},v}[k]^*] = 0$ when $u \neq v$ and that signals $X_{\mathrm{U},u}[k], u \in \{1,2,3\}$ and the noise components of $\boldsymbol{n}[k]$ are uncorrelated.

The optimum $\boldsymbol{e}_{\mathrm{D}}[k]$ is the one that minimizes $J(\boldsymbol{e}_{\mathrm{D}}[k])$ in (4.25)

$$\boldsymbol{e}_{\mathrm{D}}[k] = \underset{\boldsymbol{e}_{\mathrm{D}}[k]}{\operatorname{argmin}}\, J(\boldsymbol{e}_{\mathrm{D}}[k]). \tag{4.27}$$

It is found by taking the derivative of $J(\boldsymbol{e}_{\mathrm{D}}[k])$ with the respect to $\boldsymbol{e}_{\mathrm{D}}[k]$ and setting it to zero

$$\begin{aligned}\frac{\partial}{\partial \boldsymbol{e}_{\mathrm{D}}[k]} J(\boldsymbol{e}_{\mathrm{D}}[k]) &= \sigma_X^2 \left(\boldsymbol{e}_{\mathrm{D}}[k]^* \boldsymbol{h}_{\mathrm{D}}[k]^* - 2\right) \boldsymbol{h}_{\mathrm{D}}[k]^{\mathrm{T}} + \sigma_X^2 \boldsymbol{e}_{\mathrm{D}}[k]^* \boldsymbol{H}_{\mathrm{I}}[k]^* \boldsymbol{H}_{\mathrm{I}}[k]^{\mathrm{T}} \\ &\quad + \sigma_N^2 \boldsymbol{e}_{\mathrm{D}}[k]^* \boldsymbol{H}_{\mathrm{R}}[k]^* \boldsymbol{H}_{\mathrm{R}}[k]^{\mathrm{T}} \\ &= \mathbf{0}_{1\times 2}. \end{aligned} \tag{4.28}$$

Therefore, the optimum $\boldsymbol{e}_{\mathrm{D}}[k]$ for $k = 0, \cdots, M/2-1$ reads as

$$\boldsymbol{e}_{\mathrm{D}}[k] = 2\sigma_X^2 \boldsymbol{h}_{\mathrm{D}}[k]^{\mathrm{H}} \left(\sigma_X^2 \boldsymbol{h}_{\mathrm{D}}[k] \boldsymbol{h}_{\mathrm{D}}[k]^{\mathrm{H}} + \sigma_X^2 \boldsymbol{H}_{\mathrm{I}}[k] \boldsymbol{H}_{\mathrm{I}}[k]^{\mathrm{H}} + \sigma_N^2 \boldsymbol{H}_{\mathrm{R}}[k] \boldsymbol{H}_{\mathrm{R}}[k]^{\mathrm{H}}\right)^{-1}. \tag{4.29}$$

For $k = M/2, \cdots, M-1$, the vector-equalizer defined as $\boldsymbol{e}_{\mathrm{D}}^{-}[k] = \left[E_2^{\mathrm{SQAM}}[k] \quad E_2^{\mathrm{SQAM}}\left[k - \frac{M}{2}\right]\right]$ can be similarly derived. It reads as

$$\boldsymbol{e}_{\mathrm{D}}^{-}[k] = 2\sigma_X^2 \boldsymbol{h}_{\mathrm{D}}^{-}[k]^{\mathrm{H}} \left(\sigma_X^2 \boldsymbol{h}_{\mathrm{D}}^{-}[k] \boldsymbol{h}_{\mathrm{D}}^{-}[k]^{\mathrm{H}} + \sigma_X^2 \boldsymbol{H}_{\mathrm{I}}^{-}[k] \boldsymbol{H}_{\mathrm{I}}^{-}[k]^{\mathrm{H}} + \sigma_N^2 \boldsymbol{H}_{\mathrm{R}}^{-}[k] \boldsymbol{H}_{\mathrm{R}}^{-}[k]^{\mathrm{H}}\right)^{-1} \tag{4.30}$$

with the following definitions

$$\boldsymbol{h}_{\mathrm{D}}^{-}[k] = \left[H_{\text{tot},2}[k] \quad H_{\text{tot},2}\left[k - \tfrac{M}{2}\right]\right]^{\mathrm{T}}, \tag{4.31}$$

$$\boldsymbol{H}_{\mathrm{I}}^{-}[k] = \begin{bmatrix} H_{\text{tot},1}[k] & H_{\text{tot},3}[k] \\ H_{\text{tot},1}\left[k - \frac{M}{2}\right] & H_{\text{tot},3}\left[k - \frac{M}{2}\right] \end{bmatrix}, \tag{4.32}$$

$$\boldsymbol{H}_{\mathrm{R}}^{-}[k] = \begin{bmatrix} H_{\text{rx}}[k] & 0 \\ 0 & H_{\text{rx}}\left[k - \frac{M}{2}\right] \end{bmatrix}. \tag{4.33}$$

By applying the inverse of a 2×2 matrix to (4.29) and (4.30), the expression of the fractionally spaced equalizer $E_2^{\mathrm{SQAM}}[k]$ at each discrete frequency point k applied in the channel of user 2 can be finally expressed by

$$E_2^{\mathrm{SQAM}}[k] = \begin{cases} 2\sigma_X^2 \left(\dfrac{\theta\left[k+\frac{M}{2}\right] H_{\text{tot},2}^*[k] - \beta_1^*[k] H_{\text{tot},2}^*\left[k+\frac{M}{2}\right]}{\theta[k]\theta\left[k+\frac{M}{2}\right] - \beta_1[k]\beta_1^*[k]}\right), & \text{for} \quad 0 \le k \le M/2-1, \\ 2\sigma_X^2 \left(\dfrac{\theta\left[k-\frac{M}{2}\right] H_{\text{tot},2}^*[k] - \beta_2^*[k] H_{\text{tot},2}^*\left[k-\frac{M}{2}\right]}{\theta[k]\theta\left[k-\frac{M}{2}\right] - \beta_2[k]\beta_2^*[k]}\right), & \text{for} \quad M/2 \le k \le M-1. \end{cases} \tag{4.34}$$

where

$$\theta[k] = \sigma_X^2 \sum_{u=1}^{3} \left|H_{\text{tot},u}[k]\right|^2 + \sigma_N^2 \left|H_{\text{rx}}[k]\right|^2, \text{for} \quad 0 \le k \le M-1, \tag{4.35}$$

$$\beta_1[k] = \sigma_X^2 \sum_{u=1}^{3} H_{\text{tot},u}[k] H_{\text{tot},u}^*\left[k + \frac{M}{2}\right], \text{for} \quad 0 \le k \le M/2-1, \tag{4.36}$$

$$\beta_2[k] = \sigma_X^2 \sum_{u=1}^{3} H_{\text{tot},u}[k] H_{\text{tot},u}^*\left[k - \frac{M}{2}\right], \text{for} \quad M/2 \le k \le M-1. \tag{4.37}$$

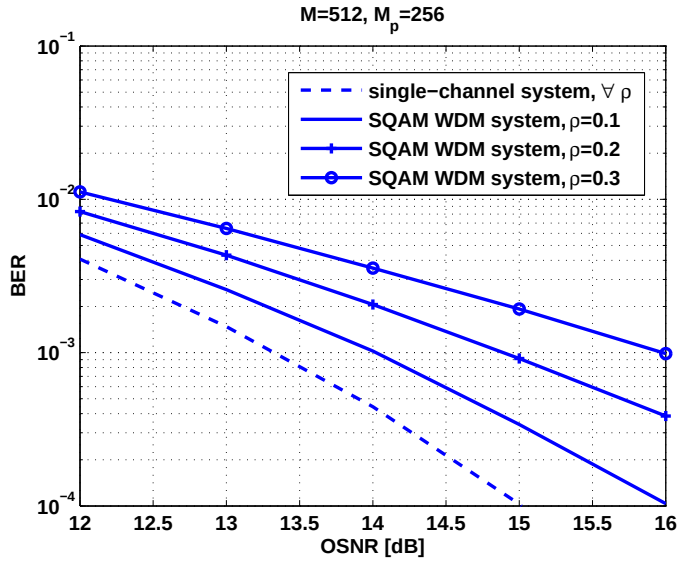

Fig. 4.14. BER vs. OSNR: SQAM WDM system with a single-receiver equalizer for ICI mitigation and SQAM single wavelength-channel system at back-to-back connection of the transmitter and receiver i.e. without CD channel: $M = 512$ and $M_p = 256$.

4.6.1.2 Performance Analysis

The performance of the SQAM WDM system is examined in terms of the ROSNR to get a BER value of 10^{-3} for back-to-back connection of the transmitter and receiver i.e. without CD channel in between. It is compared to an SQAM single wavelength-channel system with the same settings. In SQAM single wavelength-channel system, only one channel is present in the transmitter i.e. there are no interfering channels and in the receiver the equalizer derived in (3.79) is applied. We use for the simulations QPSK modulation scheme and $B = 28$ GHz.

In the simulations in Fig. 4.14, we plot the BER vs. OSNR for $M_p = 256$ and $\rho = 0.1, 0.2, 0.3$ for the pulse shaper and $M = 512$ for the equalizer. As it can be seen in the figure, for the SQAM single wavelength-channel system, an OSNR of value 13.3 dB is needed to get a BER of 10^{-3} for all ρ values. This value represents as well the theoretical OSNR value for the given BER. For a SQAM WDM system, the performance degrades by increasing ρ as compared to a SQAM single wavelength-channel system such that the penalty in the required OSNR values increases. This is the case since the power of the ICI increases by increasing ρ. For large ρ values, for example $\rho = 0.9$, a BER of 10^{-3} can not be even reached.

4.6.2 SQAM WDM Multi-receiver System Model

We show in Fig. 4.15 the schematic block diagram of a SQAM WDM system with three isolated wavelength channels in the transmitter and the receiver with a multi-receiver structure for ICI cancellation. We refer to this system as SQAM MRE WDM system. The ICI cancellation processing is illustrated for the baseband channel i.e. the wavelength channel of user 2. The structure of the transmitter is the same as that of a SQAM WDM with single-receiver system in Sec. 4.6.1. The multi-receiver structure retains the functions of a single-receiver structure but performs ICI cancellation jointly on multiple wavelength channels. Thus, after transmission over the optical fiber, the received signal of each channel enters independent but synchronized coherent receivers. The optical signal of each channel is firstly separately downconverted to the baseband. The baseband

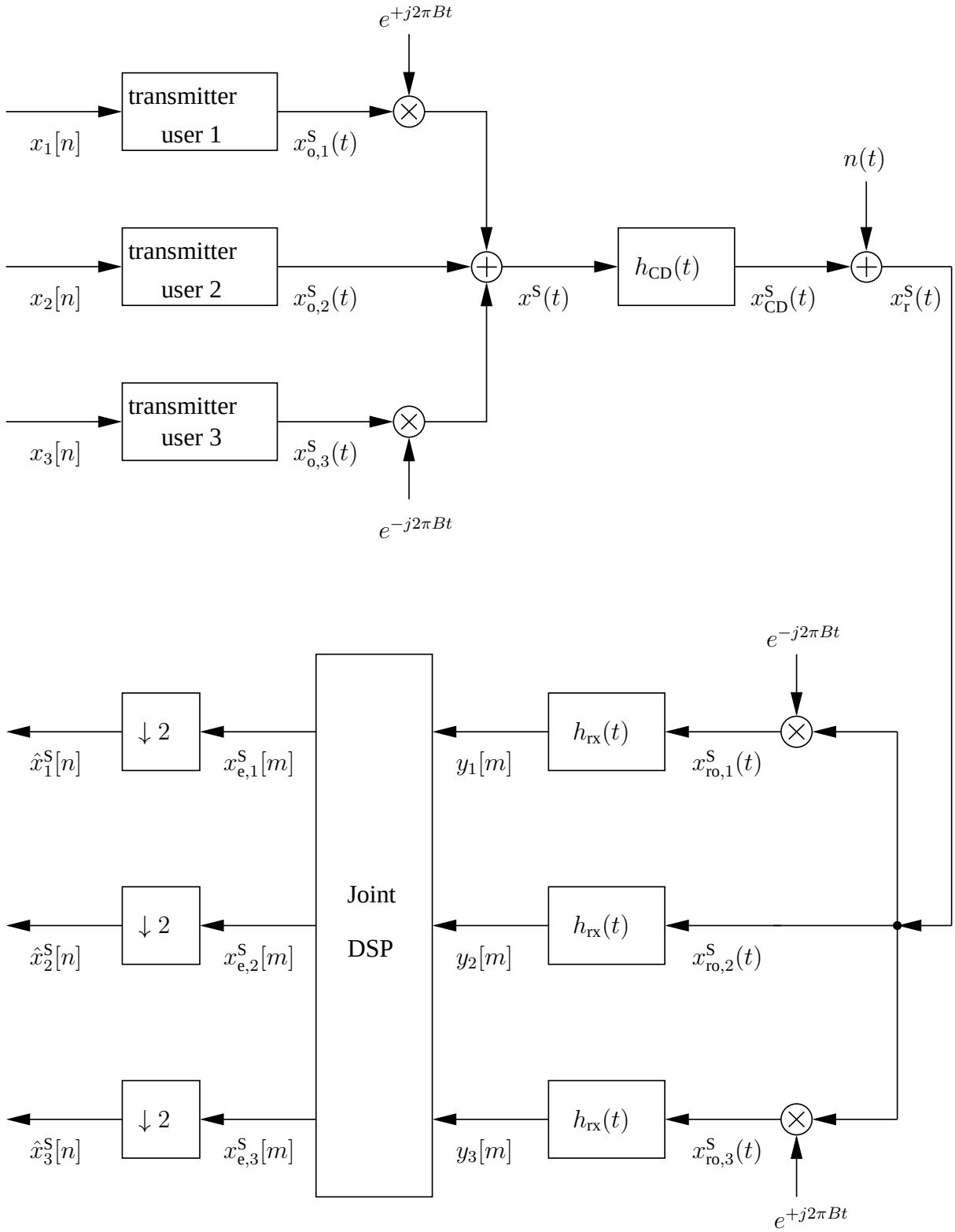

Fig. 4.15. Standard QAM Nyquist WDM system model of three isolated channels in the transmitter and in the receiver for ICI cancellation evaluated for baseband wavelength channel of user 2

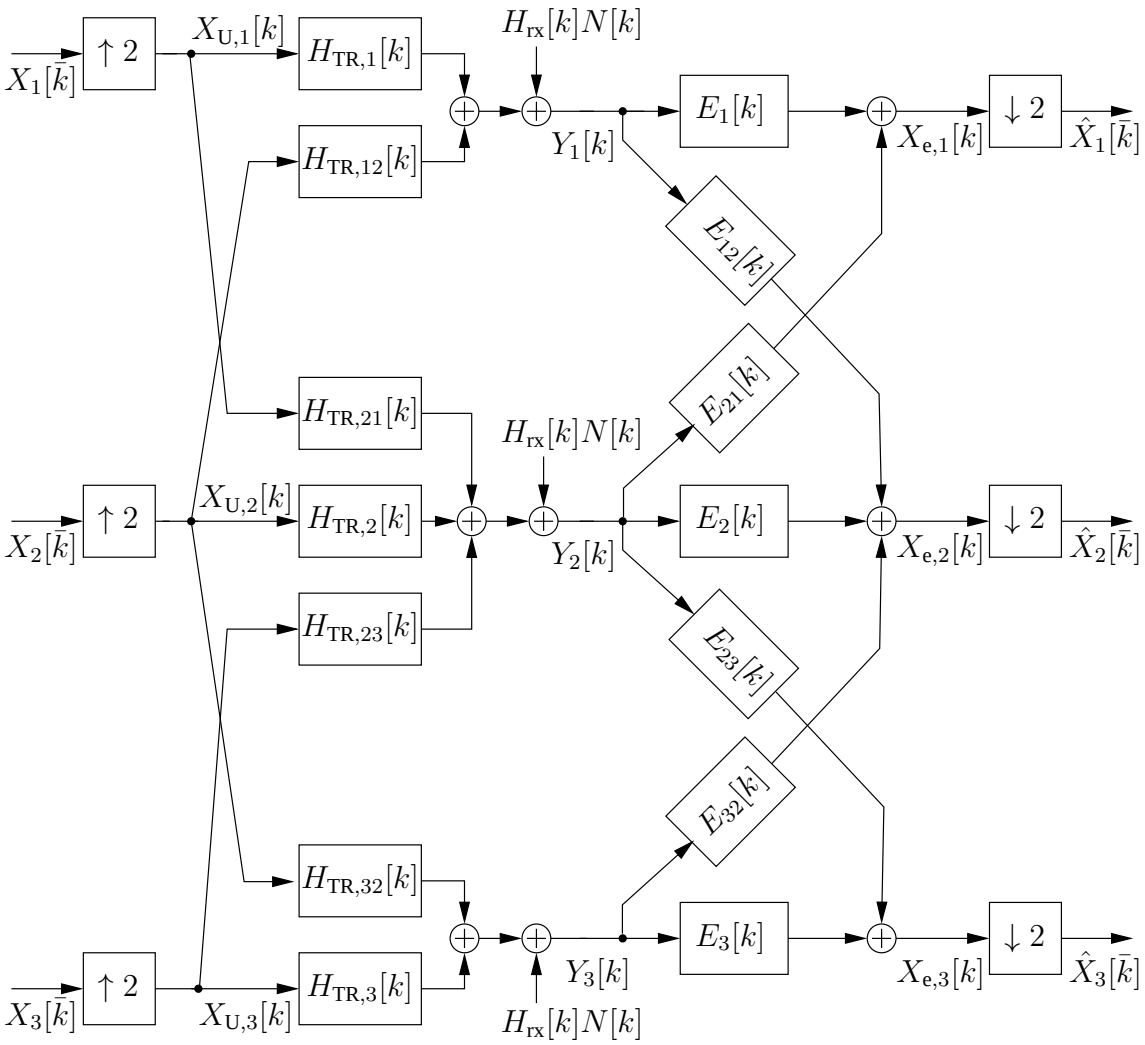

Fig. 4.16. Simplified model of a SQAM MRE WDM system for FD ICI equalizer design

signal in each channel is denoted as $x^{\mathrm{S}}_{\mathrm{ro},u}(t), u = \{1,2,3\}$ which is filtered by an optical filter $h_o(t)$ modeled in the FD as a Gaussian function given in (2.6) with order $n_{\mathrm{od}} = 2$ and $B_{\mathrm{O3dB}} = 35$ GHz. Each optical signal is then converted to an electrical signal by the filter $h_e(t)$ which represents the low-pass characteristics of the electrical components. It can be modeled in the FD as a 5th-order Bessel function defined in (2.7) with $B_{\mathrm{E3dB}} = 0.7 \times B = 19.6$ GHz. The optical and electrical filters define the opto-electronic front-end of the coherent receiver modeled by $h_{\mathrm{rx}}(t) = h_o(t) * h_e(t)$ in Fig. 4.15 which has the frequency response of $H_{\mathrm{rx}}(f) = H_o(f)H_e(f)$. The electrical signals of the multiple channels are then synchronously sampled at double the symbol rate i.e. at 56 Gsamples/s to get the signals $y_u[m]$. These are fed into the joint DSP block and processed offline for ICI cancellation to get the equalized signals $x^{\mathrm{S}}_{\mathrm{e},u}[m]$. After equalization, the signal $x^{\mathrm{S}}_{\mathrm{e},u}[m]$ is downsampled by a factor of 2 to get finally the symbol-based signal $\hat{x}^{\mathrm{S}}_u[n]$.

4.6.2.1 Equalizer Design

The crucial idea in SQAM MRE WDM system is that the signals $y_1[m]$, $y_2[m]$ and $y_3[m]$ are jointly processed for canceling the ICI introduced in the channel of user 2. In the same way as in Sec. 4.6.1, we adopt the OLS-50% with an I/FFT of length M for the joint equalization of $y_1[m]$, $y_2[m]$ and

$y_3[m]$. Therefore, we present a FD design at each discrete frequency point $k = 0, 1, \cdots, M-1$ of the necessary equalizers for ICI cancellation. We show in Fig. 4.16 a simplified model of the SQAM MRE WDM system necessary for the derivation of the equalizers. Since we evaluate the performance for the baseband wavelength channel of user 2, we aim at designing the equalizers $E_2[k], E_{12}[k], E_{32}[k]$ at each discrete frequency point $k = 0, 1, \cdots, M-1$.

The $\bar{k}$-th frequency point of the discrete Fourier transform of the discrete-time input signal $x_u[m]$ in Fig. 4.15 is denoted as $X_u[\bar{k}], \bar{k} = 0, 1, \cdots, M/2-1$ in Fig. 4.16. The TD and FD signals have the same variance of σ_x^2 according to Parseval's theorem. The discrete TD signal $x_u[n], u \in \{1, 2, 3\}$ after upsampling by a factor of two is denoted as $x_{\mathrm{U},u}[m]$, respectively. The latter thus has a variance of $\sigma_X^2 = \frac{1}{2}\sigma_x^2$ according to (B.4). Therefore, it follows that the k-th frequency point of the discrete Fourier transform of $x_{\mathrm{U},u}[m]$ denoted as $X_{\mathrm{U},u}[k], k = 0, 1, \cdots, M-1$, respectively, has the same variance of value $\sigma_X^2 = \frac{1}{2}\sigma_x^2$.

We denote $H_{\mathrm{TR},u}[k]$ as the k-th frequency point of the discrete Fourier transform of the discrete TD representation of the total base-band channel of user u comprising the pulse shaper and the opto-electro receive filter. It can be obtained as follows

$$H_{\mathrm{TR},u}[k] = H_{\mathrm{RRC}}(f)H_{\mathrm{rx}}(f)\Big|_{f=f_k} \tag{4.38}$$

where f_k is defined in (3.17) with an oversampling factor $o_s = 2$.

We denote $H_{\mathrm{TR},uv}[k], u, v \in \{1, 2, 3\}, u \neq v$ as the k-th (frequency) point of the discrete Fourier transform of the interfering channel v to the wavelength channel u. It is defined as

$$H_{\mathrm{TR},uv}[k] = H_{\mathrm{RRC},v}(f)H_{\mathrm{rx},u}(f)\Big|_{f=f_k} \tag{4.39}$$

where $H_{\mathrm{rx},u}(f) = H_{\mathrm{rx}}(f), \forall u$ and $H_{\mathrm{RRC},v}(f)$ forms the interfering part at the transmitter obtained in the same way as in (4.14) or (4.15). Note that $H_{\mathrm{TR},13}[k] = H_{\mathrm{TR},31}[k] = 0, \forall k$ since the interference is just from the neighboring channels.

We can now give the expression of k-th frequency point of the discrete Fourier transform of the discrete-time signal $y_u[m]$ for equalization denoted as $Y_u[k]$ as function of $H_{\mathrm{TR},u}[k], H_{\mathrm{TR},uv}[k], X_{\mathrm{U},u}[k], H_{\mathrm{rx}}[k]$ and $N[k]$ as follows

$$Y_1[k] = H_{\mathrm{TR},1}[k]X_{\mathrm{U},1}[k] + H_{\mathrm{TR},12}[k]X_{\mathrm{U},2}[k] + H_{\mathrm{rx}}[k]N[k], \tag{4.40}$$
$$Y_2[k] = H_{\mathrm{TR},21}[k]X_{\mathrm{U},1}[k] + H_{\mathrm{TR},2}[k]X_{\mathrm{U},2}[k] + H_{\mathrm{TR},23}[k]X_{\mathrm{U},3}[k] + H_{\mathrm{rx}}[k]N[k], \tag{4.41}$$
$$Y_3[k] = H_{\mathrm{TR},32}[k]X_{\mathrm{U},2}[k] + H_{\mathrm{TR},3}[k]X_{\mathrm{U},3}[k] + H_{\mathrm{rx}}[k]N[k]. \tag{4.42}$$

The joint processing of $Y_1[k], Y_2[k]$ and $Y_3[k]$ for ICI cancellation is shown in Fig. 4.16 where for the wavelength channel of user 2, the following three equalizers $E_2[k], E_{12}[k]$ and $E_{32}[k]$ are applied. The two equalizers $E_{12}[k]$ and $E_{32}[k]$ represent the ICI cancelers. We can therefore express the k-th frequency point representation of the equalized signal $X_{\mathrm{e},u}[k]$ as function of $Y_u[k]$ and the corresponding equalizers in the wavelength channels as follows

$$X_{\mathrm{e},1}[k] = E_1[k]Y_1[k] + E_{21}[k]Y_2[k] \tag{4.43}$$
$$X_{\mathrm{e},2}[k] = E_{12}[k]Y_1[k] + E_2[k]Y_2[k] + E_{32}[k]Y_3[k] \tag{4.44}$$
$$X_{\mathrm{e},3}[k] = E_3[k]Y_3[k] + E_{23}[k]Y_2[k]. \tag{4.45}$$

The k-th frequebcy point of the discrete Fourier transform of the output signal in each wavelength channel u denoted as $\hat{X}_u[\bar{k}]$ can be written as function of the equalized signal $X_{\mathrm{e},u}[k]$ taking into account the aliasing terms that arise in the system due to downsampling as follows

$$\hat{X}_u[\bar{k}] = \begin{cases} \frac{1}{2}\left(X_{\mathrm{e},u}[k] + X_{\mathrm{e},u}\left[k+\frac{M}{2}\right]\right), & \text{for } 0 \le k \le M/2-1, 0 \le \bar{k} \le M/4-1, \\ \frac{1}{2}\left(X_{\mathrm{e},u}[k] + X_{\mathrm{e},u}\left[k-\frac{M}{2}\right]\right), & \text{for } M/2 \le k \le M-1, M/4 \le \bar{k} \le M/2-1. \end{cases} \tag{4.46}$$

The vector of the output signals is denoted as $\hat{\boldsymbol{x}}[\bar{k}] = \begin{bmatrix}\hat{X}_1[\bar{k}] & \hat{X}_2[\bar{k}] & \hat{X}_3[\bar{k}]\end{bmatrix}^{\mathrm{T}}$ which can be expressed in a matrix-vector notation when substituting (4.43), (4.44) and (4.44) in (4.46) as follows

$$\hat{\boldsymbol{x}}[\bar{k}] = \frac{1}{2}\boldsymbol{E}^{\mathrm{MRE}}[k]\boldsymbol{y}[k] \tag{4.47}$$

for $0 \le \bar{k} \le M/4-1$ with the following definitions, respectively, for the matrix-equalizer $\boldsymbol{E}^{\mathrm{MRE}}[k]$ and the vector-signal $\boldsymbol{y}[k]$

$$\boldsymbol{E}^{\mathrm{MRE}}[k] = \begin{bmatrix} E_1[k] & E_1[k+M/2] & E_{21}[k] & E_{21}[k+M/2] & 0 & 0 \\ E_{12}[k] & E_{12}[k+M/2] & E_2[k] & E_2[k+M/2] & E_{32}[k] & E_{32}[k+M/2] \\ 0 & 0 & E_{23}[k] & E_{23}[k+M/2] & E_3[k] & E_3[k+M/2] \end{bmatrix}, \tag{4.48}$$

$$\boldsymbol{y}[k] = \begin{bmatrix} Y_1[k] & Y_1[k+M/2] & Y_2[k] & Y_2[k+M/2] & Y_3[k] & Y_3[k+M/2] \end{bmatrix}^{\mathrm{T}}. \tag{4.49}$$

The signal-vector $\boldsymbol{y}[k]$ can be expressed by

$$\boldsymbol{y}[k] = \boldsymbol{H}^{\mathrm{MRE}}[k]\boldsymbol{X}_{\mathrm{U}}[k] + \boldsymbol{H}_{\mathrm{RR}}[k]\boldsymbol{N}_{\mathrm{RR}}[k] \tag{4.50}$$

based on (4.40), (4.41) and (4.42) with the channel-matrix $\boldsymbol{H}^{\mathrm{MRE}}[k]$ defined as

$$\boldsymbol{H}^{\mathrm{MRE}}[k] = \begin{bmatrix} H_{\mathrm{TR},1}[k] & H_{\mathrm{TR},12}[k] & 0 \\ H_{\mathrm{TR},1}[k+M/2] & H_{\mathrm{TR},12}[k+M/2] & 0 \\ H_{\mathrm{TR},21}[k] & H_{\mathrm{TR},2}[k] & H_{\mathrm{TR},23}[k] \\ H_{\mathrm{TR},21}[k+M/2] & H_{\mathrm{TR},2}[k+M/2] & H_{\mathrm{TR},23}[k+M/2] \\ 0 & H_{\mathrm{TR},32}[k] & H_{\mathrm{TR},3}[k] \\ 0 & H_{\mathrm{TR},32}[k+M/2] & H_{\mathrm{TR},3}[k+M/2] \end{bmatrix}, \tag{4.51}$$

and the receive filter matrix and noise vector, respectively, defined as

$$\boldsymbol{H}_{\mathrm{RR}}[k] = \begin{bmatrix} H_{\mathrm{rx}}[k] & 0 & 0 & 0 & 0 & 0 \\ 0 & H_{\mathrm{rx}}[k+M/2] & 0 & 0 & 0 & 0 \\ 0 & 0 & H_{\mathrm{rx}}[k] & 0 & 0 & 0 \\ 0 & 0 & 0 & H_{\mathrm{rx}}[k+M/2] & 0 & 0 \\ 0 & 0 & 0 & 0 & H_{\mathrm{rx}}[k] & 0 \\ 0 & 0 & 0 & 0 & 0 & H_{\mathrm{rx}}[k+M/2] \end{bmatrix}, \tag{4.52}$$

$$\boldsymbol{n}_{\mathrm{RR}}[k] = \begin{bmatrix} N[k] & N[k+M/2] & N[k] & N[k+M/2] & N[k] & N[k+M/2] \end{bmatrix}^{\mathrm{T}} \tag{4.53}$$

and signal-vector $\boldsymbol{x}_{\mathrm{U}}[k]$ defined as

$$\boldsymbol{x}_{\mathrm{U}}[k] = \begin{bmatrix} X_{\mathrm{U},1}[k] & X_{\mathrm{U},2}[k] & X_{\mathrm{U},3}[k] \end{bmatrix}^{\mathrm{T}} \tag{4.54}$$

with the fact that $X_{\mathrm{U},u}\left[k+\frac{M}{2}\right] = X_{\mathrm{U},u}[k]$ since $X_{\mathrm{U},u}[k]$ is periodic with period $M/2$,

In order to design the equalizers $E_2[k], E_{12}[k], E_{32}[k]$ for ICI cancellation, $\boldsymbol{x}[\bar{k}]$ and $\hat{\boldsymbol{x}}[\bar{k}]$ are jointly processed. Note that the input signals $X_1[\bar{k}], X_2[\bar{k}]$ and $X_3[\bar{k}]$ are stacked in the vector $\boldsymbol{x}[\bar{k}] = \begin{bmatrix} X_1[\bar{k}] & X_2[\bar{k}] & X_3[\bar{k}] \end{bmatrix}^{\mathrm{T}}$ which is equivalent to $\boldsymbol{x}_{\mathrm{U}}[k]$ for $\bar{k} = 0, 1, \cdots, M/4-1$ and $k = 0, 1, \cdots, M/2-1$ but the latter has covariance matrix $\boldsymbol{R}_{\mathrm{XX}} = \sigma_X^2 \times \mathbf{1}_{3\times 3}$ where σ_X^2 is given in (3.58). The signal components of $\boldsymbol{x}_{\mathrm{U}}[k]$ are uncorrelated i.e. $\mathrm{E}[X_{\mathrm{U},u}[k]X_{\mathrm{U},v}[k]^*] = 0, u \neq v$. For a FD MMSE design of $\boldsymbol{E}^{\mathrm{MRE}}[k]$, we build the mean squared error denoted as $J(\boldsymbol{E}^{\mathrm{MRE}}[k])$ between $\boldsymbol{x}[\bar{k}]$ and $\hat{\boldsymbol{x}}[\bar{k}]$ as follows

$$J(\boldsymbol{E}^{\mathrm{MRE}}[k]) = \mathrm{E}\left[\left|\left|\hat{\boldsymbol{x}}[\bar{k}] - \boldsymbol{x}[\bar{k}]\right|\right|_2^2\right] \tag{4.55}$$

which when substituting (4.47) and taking the expectation over the signal-vector $\boldsymbol{x}_{\mathrm{U}}[k]$ and over the noise term $\boldsymbol{n}_{\mathrm{RR}}[k]$, it reduces to

$$\begin{aligned} J(\boldsymbol{E}^{\mathrm{MRE}}[k]) = \frac{1}{4}\mathrm{tr}\Big\{ & \sigma_X^2 \left(\boldsymbol{E}^{\mathrm{MRE}}[k]\boldsymbol{H}^{\mathrm{MRE}}[k] - 2\times\mathbf{1}_{3\times 3}\right)\left(\boldsymbol{E}^{\mathrm{MRE}}[k]\boldsymbol{H}^{\mathrm{MRE}}[k] - 2\times\mathbf{1}_{3\times 3}\right)^{\mathrm{H}} \\ & + \sigma_N^2 \boldsymbol{E}^{\mathrm{MRE}}[k]\boldsymbol{H}_{\mathrm{RR}}[k]\boldsymbol{H}_{\mathrm{RR}}[k]^{\mathrm{H}}\boldsymbol{E}^{\mathrm{MRE}}[k]^{\mathrm{H}}\Big\}. \end{aligned} \tag{4.56}$$

The noise term $\boldsymbol{n}_{\mathrm{RR}}[k]$ has the following noise correlation matrix

$$\begin{aligned} &\mathrm{E}\left[\boldsymbol{n}_{\mathrm{RR}}[k]\boldsymbol{n}_{\mathrm{RR}}[k]^{\mathrm{H}}\right] = \\ &\begin{bmatrix} \mathrm{E}\left[|N[k]|^2\right] & 0 & 0 & 0 & 0 & 0 \\ 0 & \mathrm{E}\left[|N[k+\frac{M}{2}]|^2\right] & 0 & 0 & 0 & 0 \\ 0 & 0 & \mathrm{E}\left[|N[k]|^2\right] & 0 & 0 & 0 \\ 0 & 0 & 0 & \mathrm{E}\left[|N[k+\frac{M}{2}]|^2\right] & 0 & 0 \\ 0 & 0 & 0 & 0 & \mathrm{E}\left[|N[k]|^2\right] & 0 \\ 0 & 0 & 0 & 0 & 0 & \mathrm{E}\left[|N[k+\frac{M}{2}]|^2\right] \end{bmatrix} \\ &= \sigma_N^2 \mathbf{1}_{6\times 6}. \end{aligned} \tag{4.57}$$

and it is assumed that signal-vector $\boldsymbol{x}_{\mathrm{U}}[k]$ and the noise components of $\boldsymbol{n}_{\mathrm{RR}}[k]$ are uncorrelated.

The *Karush-Kuhn-Tucker* (KKT) condition necessary for the optimum of (4.56) reads as

$$\begin{aligned} \frac{\partial}{\partial \boldsymbol{E}^{\mathrm{MRE}}[k]} J(\boldsymbol{E}^{\mathrm{MRE}}[k]) &= \sigma_X^2 \left(\boldsymbol{E}^{\mathrm{MRE}}[k]^*\boldsymbol{H}^{\mathrm{MRE}}[k]^* - 2\times\mathbf{1}_{3\times 3}\right)\boldsymbol{H}^{\mathrm{MRE}}[k]^{\mathrm{T}} \\ &\quad + \sigma_N^2 \boldsymbol{E}^{\mathrm{MRE}}[k]^*\boldsymbol{H}_{\mathrm{RR}}[k]^*\boldsymbol{H}_{\mathrm{RR}}[k]^{\mathrm{T}} \\ &= \mathbf{0}_{3\times 6}. \end{aligned} \tag{4.58}$$

It delivers the final expression of the FD MMSE equalizer $\boldsymbol{E}^{\mathrm{MRE}}[k], k = 0, 1, \cdots, M/2-1$

$$\boldsymbol{E}^{\mathrm{MRE}}[k] = 2\sigma_X^2 \boldsymbol{H}^{\mathrm{MRE}}[k]^{\mathrm{H}}\left(\sigma_X^2 \boldsymbol{H}^{\mathrm{MRE}}[k]\boldsymbol{H}^{\mathrm{MRE}}[k]^{\mathrm{H}} + \sigma_N^2 \boldsymbol{H}_{\mathrm{RR}}[k]\boldsymbol{H}_{\mathrm{RR}}[k]^{\mathrm{H}}\right)^{-1}. \tag{4.59}$$

Given the definition of $\boldsymbol{E}^{\mathrm{MRE}}[k]$ in (4.48), the equalizers $E_2[k], E_{12}[k]$ and $E_{32}[k]$ necessary to cancel ICI in the wavelength channel of user 2 are obtained. This definition also delivers these equalizers at the discrete frequency points $k = M/2, \cdots, M-1$ through the terms $E_2[k+M/2], E_{12}[k+M/2]$ and $E_{32}[k+M/2]$. Therefore, the equalizers $E_2[k], E_{12}[k]$ and $E_{32}[k]$ for $k = 0, 1, \cdots, M-1$ are obtained from (4.59).

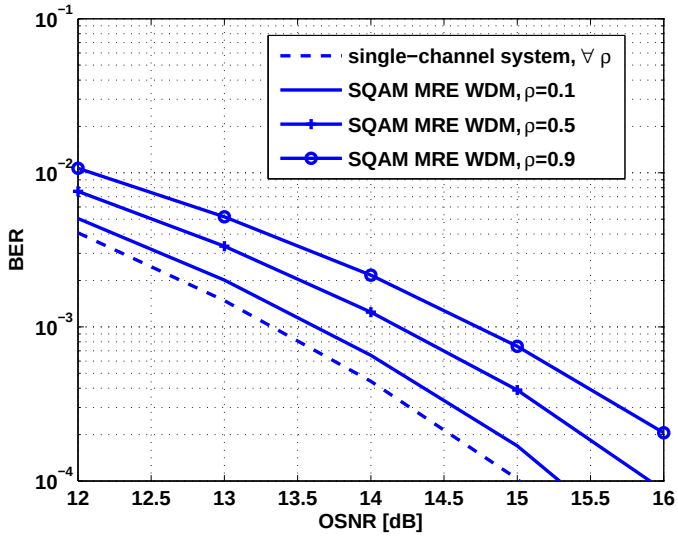

Fig. 4.17. BER vs. OSNR: SQAM WDM system with a multiple-receiver equalizer for ICI cancellation and SQAM single wavelength-channel system at back-to-back connection of the transmitter and receiver i.e. without CD channel: $M = 512$ and $M_p = 256$.

4.6.2.2 Performance Analysis

The performance of the SQAM MRE WDM system is examined in terms of the ROSNR to get a BER value of 10^{-3} for the back-to-back connection of the transmitter and the receiver i.e. without CD channel between them with $M_p = 256$ and $\rho = 0.1, 0.5, 0.9$ for the pulse shaper and $M = 512$ for the equalizer. The performance is compared to the performance of an SQAM single wavelength-channel system with the same settings. In SQAM single wavelength-channel system, only one channel is present in the transmitter i.e. there are no interfering channels and in the receiver the equalizer derived in (3.79) is applied. We deploy for the simulations QPSK modulation schemes and $B = 28$ GHz.

We plot in Fig. 4.17 the BER vs. OSNR for both systems. As compared to a SQAM single wavelength-channel system, there is a penalty in performance with a SQAM MRE WDM system. The required OSNR value increases by increasing ρ since the power of the ICI increases. However, the penalty is not extremely high for large ρ values. For large ρ values, for example $\rho = 0.9$, the penalty as compared to a SQAM single wavelength-channel system is 1.4 dB. We compare in Fig. 4.18, the performance of the SQAM MRE WDM system and the SQAM WDM system with single-receiver for equalization. For the latter system where ρ should be kept small as possible to get the smallest penalty in OSNR, moderate or even large ρ values can be utilized in the former system. This will neither lead to increased peak values nor to reduced eye-opening in time and therefore provide a robust solution for the ICI problem. However, this comes at the expense of increased complexity in the digital signal processing in the receiver.

4.7 Summary

As WDM systems move to tighter channel spacing in search for high spectrally-efficient transmissions, ICI is likely to incur a significant penalty due to the considerable overlap between adjacent channel spectra. We addressed and demonstrated three different approaches to minimize or com-

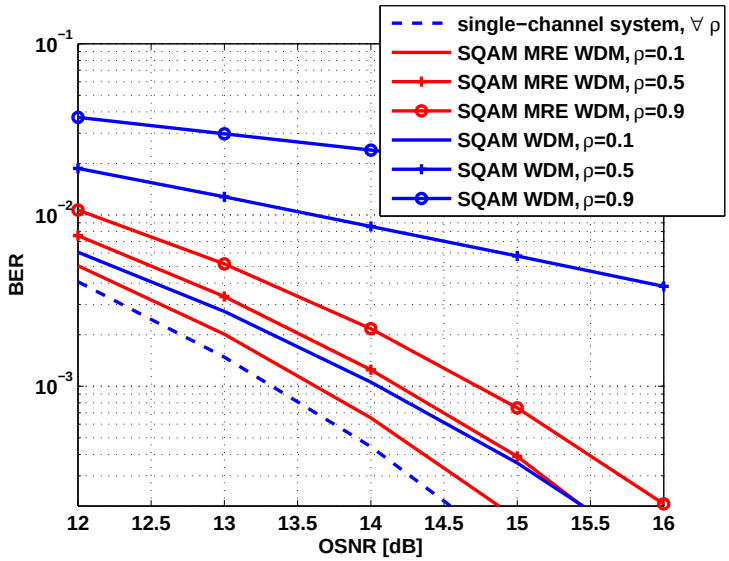

Fig. 4.18. BER vs. OSNR: Performance comparison between SQAM WDM system with a multiple-receiver equalizer, SQAM WDM with single-receiver equalizer and SQAM single wavelength-channel system at back-to-back connection of the transmitter and receiver i.e. without CD channel: $M = 512$ and $M_p = 256$.

pensate ICI in baud-rate channel-spaced WDM systems. In the transmitter of these WDM systems regardless of the techniques used to compensate ICI, a RRC pulse shaper characterized by its roll-off factor is employed since it satisfies Nyquist criterion for ISI-free transmission. The first technique for ICI mitigation is a WDM system utilizing OQAM as modulation format. In this technique, which is known from the perfect reconstruction filter banks, the achieved orthogonality hinges on a strict frequency-, phase- and timing synchronization which may be hard to achieve in a practical system. Nevertheless, if it is achieved ICI is zeroed out. We demonstrated through simulations that in the absence of any imperfections in the system, the performance is the same of a single wavelength-channel system i.e. there are no effects from ICI. The second technique to compensate for ICI in baud-rate channel spacing WDM system is to utilize SQAM as modulation format and to design an equalizer in the receiver of the wavelength channel of interest. The crucial idea about the design of this equalizer is that the ICI of the neighboring channel is introduced in the optimization process and it is treated similar to noise. ICI is minimized by simply reducing the spectral overlap with an extremely small roll-off factor. This comes with the expense of increased peak values of the transmit signal possibly leading to nonlinear distortion not only in the electronic part but also in the fiber. In addition the eye-opening will also be reduced in time, increasing the vulnerability to timing jitter. Finally, we investigated a third approach for ICI compensation. It is based on a WDM system utilizing SQAM as modulation format and a joint processing of the three received signals is carried out for ICI cancellation. In this case, moderate or even large roll-off factor can be utilized to enhance the performance. This will neither lead to increased peak values nor to reduced eye-opening in time providing a robust solution for the ICI problem. However, this method requires that the received signals are perfectly synchronized. This comes therefore at the expense of increased complexity of the digital signal processing in the receiver. Among these three different approaches for ICI equalization or cancellation, an OQAM WDM system with a moderate roll-off provide the compromise between performance and complexity.

5. Conclusions and Outlook

We proposed various DSP algorithms to enhance the performance in long-haul coherent optical transmission systems carrying data rates of 112 Gbit/s per wavelength channel. The DSP algorithms aim at compensating CD among other transmission impairments in optical fibers. The main obstacle for implementation at such high data rates is the complexity of the filtering algorithms in terms of multiplication. Thus, power consumption and the availability of DSP circuits which offer both very high gate density and processing speeds are of concern at such high data rates. Since FD equalization of CD becomes more efficient than TD equalization over a wide range of CD values, the FD OLS-50% method is considered as the benchmark for CD compensation. We were able to interpret the OLS-50% as a non-maximally decimated DFT FB with trivial prototype filters and the equalization is done per frequency sub-band. This paved the way for more sophisticated sub-band processing. We, therefore, derived and implemented a delayed single-tap equalizer. It is a multi-tap filter applied in each frequency sub-band but has only one active tap and several delay elements accounting to the quantized group delay of the inverse of the CD channel. The incentive for such a design is the nature of the CD channel which distorts not only the phase of the signal but also its group delay. With this design, we showed that larger CD values can be compensated with a smaller I/DFT size as compared to the benchmark. This is simply done by increasing the number of delay elements of the equalizer in each sub-band as long as the maximum number of delay elements remains negligible as compared to the I/DFT size. With this design, trans-Pacific distance of around 15,000 km with standard single-mode fiber accounting for more than 240,000 ps/nm can be equalized with an OSNR filtering penalty of 0.5 dB. An important advantage of such a filter design is that its complexity in terms of multiplications remains the same as compared to the benchmark apart from the needed additional delay elements. To further improve the performance, we proposed to smooth the quantized group delay of the delayed single-tap equalizer. We therefore designed a delayed dual-tap equalizer derived from the from the delayed single-tap equalizer. It is applied in the frequency sub-bands where the group delay function of the delayed single-tap equalizer is discontinuous. By setting the amplitude of the two active taps equal, the delayed dual-tap equalizer that we proposed keeps the same complexity as the delayed single-tap equalizer apart from some adders and/or subtractors. The performance of the system was improved by requiring lower ROSNR values specially when concurrently the I/DFT size is small and the CD values are large. As a way to further improve the performance of the system for low and moderate CD values, we designed a MMSE FD equalizer that equalizes not only the propagating CD channel but also the transfer function of the transmitter and receiver. Additionally, the aliasing terms that arise due to the optical filter in the receiver are also accounted for in the equalizer design.

For WDM systems with baud-rate channel spacing, we proposed three different approaches which minimize or compensate for ICI. Baud-rate channel spaced WDM systems enable an effi-

cient use of the available optical bandwidth as a way to enhance SE. However, due to the spectra overlap considerable ICI arises. In the first approach for ICI equalization OQAM is used as modulation format. OQAM is employed through staggering and destaggering, in the transmitter and receiver, respectively, of the real and imaginary parts of the signal. In this technique, which is known from the perfect reconstruction filter banks, the achieved orthogonality hinges on a strict frequency-, phase- and timing synchronization which may be hard to achieve in a practical system. Nevertheless, if it is achieved ICI is zeroed out. We demonstrated this through simulations. In a second approach SQAM is used as modulation scheme. We designed an MMSE equalizer which treats ICI in the same way as noise for the regularization term of the equalizer. With this technique, ICI is minimized by simply reducing the spectral overlap with an extremely small roll-off factor. This comes with an increased peak values of the transmit signal possibly leading to nonlinear distortions not only in the electronic part but also in the fiber. In addition the eye-opening will also be reduced in time, increasing the vulnerability to timing jitter. The third approach is based on utilizing SQAM with a moderate or even large roll-off factor where ICI cancellation is done with the help of digital signal processing. The proposed algorithm is based on a super-receiver architecture which builds on conventional Nyquist WDM systems where the received signals of the neighboring channels are fed into the receiver of the channel of interest for multi-receiver equalization. Moderate or even large roll-off factors will neither lead to increased peak values nor to reduced eye-opening in time and therefore provide a robust solution for the ICI problem. However, this approach comes at the expense of increased complexity of the digital signal processing in the receiver and strict synchronization requirements. For all these different approaches for ICI minimization or cancellation, an RRC pulse shaper characterized by its roll-off factor is implemented in the transmitter and in the receiver. This is the choice because the overall resulting RC response satisfies the first Nyquist criterion for ISI-free transmission. Among these approaches for ICI minimization or cancellation it is reasonable to adopt the first approach for ICI equalization since it provides the best compromise between performance and complexity.

These novel DSP algorithms for CD compensation and ICI equalization and cancellation are essential to reduce complexity and energy efficient for any future coherent optical transceivers to cope with the ever increasing demands for high throughput for tomorrow's Internet applications.

As an outlook, the proposed algorithms for CD compensation and ICI mitigation must consider real-time compatibility where the effects of frequency-, phase- and timing synchronization should be considered. A natural extension of this work is to include polarization effects and quantify the penalty that the systems incur with respect to different PMD values. Additionally, compensation algorithms for non-linear transmission impairments have to be considered.

A. Polyphase Decomposition

A.1 Type-1

This is the normal polyphase representation and it is referred to as polyphase decomposition of type-1 [160, 161].

Any sequence $x[n]$ can be decomposed in the time-domain into L polyphase components $x_\lambda[n], \lambda = 0, 1, \cdots, L-1$ that differ in their phase offset

$$x[n] = \sum_{\lambda=0}^{L-1} x_\lambda[n] = \sum_{\lambda=0}^{L-1} x[n] w_L[n-\lambda], \tag{A.1}$$

where

$$w_L[n-\lambda] = \frac{1}{L}\sum_{\ell=0}^{L-1} W_L^{-\ell(n-\lambda)} = \begin{cases} 1, & n = mL+\lambda, -\infty < m < +\infty \\ 0, & \text{elsewhere.} \end{cases}$$

Each polyphase component $x_\lambda[n]$ can be expressed by

$$x_\lambda[n] = x[n] w_L[n-\lambda] = \begin{cases} x[n], & n = mL+\lambda, -\infty < m < +\infty \\ 0, & \text{elsewhere.} \end{cases} \tag{A.2}$$

The z-transform representation of each polyphase component in (A.2) results in

$$\begin{aligned} X_\lambda(z) &= \mathcal{Z}\{x_\lambda[n]\} = \sum_{n=-\infty}^{+\infty} x_\lambda[n] z^{-n} = \sum_{m=-\infty}^{+\infty} x[mL+\lambda] z^{-(mL+\lambda)} \\ &= z^{-\lambda} \sum_{m=-\infty}^{+\infty} x[mL+\lambda](z^L)^{-m} \\ &= z^{-\lambda} X'_\lambda(z^L), \end{aligned} \tag{A.3}$$

with $X'_\lambda(z^L) = \sum_{m=-\infty}^{+\infty} x[mL+\lambda](z^L)^{-m}$. The sum of the z-transform representations of all polyphase components obviously results in the original signal $X(z)$ proven in what follows:

$$\begin{aligned}
\sum_{\lambda=0}^{L-1} z^{-\lambda} X'_\lambda(z^L) &= \sum_{\lambda=0}^{L-1} z^{-\lambda} \sum_{m=-\infty}^{+\infty} x[mL+\lambda](z^L)^{-m} \\
&= \sum_{\lambda=0}^{L-1} \sum_{m=-\infty}^{+\infty} x[mL+\lambda] z^{-(mL+\lambda)} = \sum_{m=-\infty}^{+\infty} \sum_{\lambda=0}^{L-1} x[mL+\lambda] z^{-(mL+\lambda)} \\
&= \sum_{n=-\infty}^{+\infty} \sum_{\lambda=0}^{L-1} x_\lambda[n] z^{-n} = \sum_{n=-\infty}^{+\infty} x[n] z^{-n} \\
&= X(z). \quad \text{q.e.d.}
\end{aligned} \tag{A.4}$$

In addition to polyphase decomposition of type-1, there are also two other decompositions that are defined in the literature, namely, polyphase decomposition of type-2 [162] and type-3 [112, 115, 116]. These three decompositions are different representations of $x[n]$, but they are all equivalent.

A.2 Type-2

Type-2 polyphase components $x_\lambda^{(2)}[n], \lambda = 0, 1, \cdots, L-1$ of $x[n]$ are obtained by replacing λ with $(L-1-\lambda)$ for (A.2) [162], i.e.

$$\begin{aligned}
x_\lambda^{(2)}[n] &= x[n] w_L[n-(L-1-\lambda)] \\
&= \begin{cases} x[n], & n = mL + (L-1-\lambda), -\infty < m < +\infty \\ 0, & \text{elsewhere.} \end{cases}
\end{aligned} \tag{A.5}$$

The z-transform representation of the type-2 polyphase component $x_\lambda^{(2)}[n]$ in (A.5) results in

$$X_\lambda^{(p2)}(z) = \sum_{n=-\infty}^{+\infty} x_\lambda^{(2)}[n] z^{-n}. \tag{A.6}$$

Therefore, the signal $X(z)$ can be expressed as function of $X_\lambda^{(p2)}(z)$ as

$$X(z) = \sum_{\lambda=0}^{L-1} z^{-(L-1-\lambda)} X_\lambda^{(p2)}(z^L). \tag{A.7}$$

The relationship between type-2 polyphase components and type-1 polyphase components is constructed as follows

$$X_\lambda^{(p2)}(z) = X_{L-1-\lambda}(z). \tag{A.8}$$

A.3 Type-3

Type-3 polyphase components $x_\lambda^{(3)}[n], \lambda = 0, 1, \cdots, L-1$ of $x[n]$ are obtained by replacing λ with $-\lambda$ for (A.2) [112, 115, 116], i.e.

$$x_\lambda^{(3)}[n] = x[n] w_L[n+\lambda] = \begin{cases} x[n], & n = mL - \lambda, -\infty < m < +\infty \\ 0, & \text{elsewhere.} \end{cases} \tag{A.9}$$

The z-transform representation of the type-3 polyphase component $x_\lambda^{(3)}[n]$ in (A.9) results in

$$X_\lambda^{(p3)}(z) = \sum_{n=-\infty}^{+\infty} x_\lambda^{(3)}[n] z^{-n}. \tag{A.10}$$

Therefore, the signal $X(z)$ can be expressed as function of $X_\lambda^{(p3)}(z)$ as

$$X(z) = \sum_{\lambda=0}^{L-1} z^\lambda X_\lambda^{(p3)}(z^L). \tag{A.11}$$

The relationship between type-3 polyphase components and type-1 polyphase components is constructed as follows

$$X_0^{(p3)}(z) = X_0(z), \tag{A.12}$$

$$X_\lambda^{(p3)}(z) = z^{-L} X_{L-\lambda}(z), \quad \lambda = 1, 2, \cdots, L-1. \tag{A.13}$$

B. Multi-rate Processing

We define a complex valued signal $x[n]$ which is sampled at a rate of $R_s = 1/T$ where T is the symbol period in seconds. The spectrum $X(\omega)$ of $x[n]$ is defined over the non-normalized continuous angular frequency axis $-\frac{\pi}{T} \leq \omega \leq +\frac{\pi}{T}$ where ω is the angular frequency defined by $\omega = 2\pi f$ in rad/s and f is the fundamental frequency in Hz $= s^{-1}$.

Multi-rate processing of $x[n]$ involves upsampling and downsampling it.

B.1 Upsampling

In the time-domain, upsampling of the signal $x[n]$ by a factor of L fills $L-1$ zero valued samples inbetween the samples of $x[n]$. This leads to increasing the sampling rate of $x[n]$ by L which means that the temporal spacing between its subsequent samples becomes T/L. The new obtained sequence denoted as $y[m]$ is given by

$$y[m] = \begin{cases} x[n], & m = nL, \\ 0, & \text{elsewhere}, \end{cases}$$

The z-transform representation $Y(z')$ of $y[m]$ is expressed by

$$Y(z') = \mathcal{Z}\{y[m]\} = \sum_{m=-\infty}^{+\infty} y[m](z')^{-m}, \tag{B.1}$$

with $z' = e^{j\omega\frac{T}{L}}$. Since the $\lambda = 0$ polyphase component of type-1 of $y[m]$ is nonzero and all other polyphase components are zero valued, eq. (B.1) can be simplified to

$$Y(z') = \sum_{m=-\infty}^{+\infty} y[m](z')^{-m} = \sum_{n=-\infty}^{+\infty} x[n](z')^{-nL} = \sum_{n=-\infty}^{+\infty} x[n]z^{-n} = X(z). \tag{B.2}$$

In the ω-domain, the spectrum of the upsampled signal $\hat{Y}(\omega)$ is identical to the spectrum of the original signal $\hat{X}(\omega)$

$$\hat{Y}(\omega) = \hat{X}(\omega). \tag{B.3}$$

However, what differs after upsampling is the Nyquist bandwidth (bandwidth of uniqueness) of both signals since the sampling rate has changed.

Given that the variance of the signal $x[n]$ is σ_{xn}^2, the variance of the upsampled signal $y[m]$ denoted as σ_y^2 is given by

$$\begin{aligned}\sigma_y^2 &= \lim_{NL\to\infty}\frac{1}{NL}\sum_{m=0}^{NL} y[m] \\ &= \lim_{NL\to\infty}\frac{1}{NL}\sum_{n=0}^{N} x[n] \\ &= \lim_{NL\to\infty}\frac{1}{L}\lim_{NL\to\infty}\frac{1}{N}\sum_{n=0}^{N} x[n] \\ &= \lim_{L\to\infty}\frac{1}{L}\lim_{N\to\infty}\frac{1}{N}\sum_{n=0}^{N} x[n] \\ &= \frac{1}{L}\sigma_{xn}^2. \end{aligned} \tag{B.4}$$

B.2 Downsampling

In the time-domain, downsampling of the signal $x[n]$ by a factor L keeps every L-th sample and deletes the $(L-1)$ in between samples of the input signal $x[n]$. This leads to decreasing the sampling rate of the signal by L which means that the temporal spacing between the subsequent samples becomes TL.

There are L different possible ways to perform downsampling of $x[n]$ to get $y[m]$ depending on the time instant when the downsampling starts. Using the theory of polyphase decomposition, the different outputs of downsampling are obtained by dropping the zero-valued elements of the L polyphase components $x_\lambda[n], \lambda = 0, 1, \cdots, L-1$ of $x[n]$. Since for each λ the impulse response of $x_\lambda[n]$ is different, downsampling operation is not time-invariant. It belongs to the class of linear periodically time varying systems of period L.

In this thesis, we consider for downsampling the $\lambda = 0$ polyphase component of $x[n]$ which has the following z-transform representation

$$\begin{aligned} X_0(z) &= \sum_{m=-\infty}^{+\infty} x[mL](z^L)^{-m} = \sum_{n=-\infty}^{+\infty} x[n]\frac{1}{L}\sum_{\ell=0}^{L-1} W_L^{-\ell n} z^{-n} \\ &= \frac{1}{L}\sum_{\ell=0}^{L-1}\sum_{n=-\infty}^{+\infty} x[n]\left(zW_L^{\ell}\right)^{-n} = \frac{1}{L}\sum_{\ell=0}^{L-1} X(zW_L^{\ell}). \end{aligned} \tag{B.5}$$

In order to get the spectrum of the downsampled signal $\tilde{Y}(z_L) = \mathcal{Z}\{y[m]\}$, the zero-valued terms of $X_0(z)$ are dropped

$$\tilde{Y}(z_L) = \tilde{X}_0(z^L) = X_0(z),$$

where $z_L = z^L = e^{j\omega TL}$ (see App. B.3) and taking into account that the spacing between samples is now LT.

For the specific case of $L = 2$, $X_0(z)$ becomes

$$X_0(z) = \frac{1}{2}\left(X(z) + X(-z)\right). \tag{B.6}$$

In $X_0(z)$, the terms with odd exponents of z are zero valued such that $X_0(z) = \tilde{X}_0(z^2)$. Dropping the zero valued terms of $X_0(z)$, the following spectrum of the downsampled signal $\tilde{Y}(z_2)$ is obtained

$$\tilde{Y}(z_2) = \tilde{X}_0(z^2) = X_0(z),$$

where $z_2 = z^2 = e^{j2\omega T}$ and taking into account that the spacing between samples is now $2T$. The spectrum of $X_0(z)$ can be expressed in the ω-domain as follows

$$\hat{X}_0(\omega) = \frac{1}{2}\left(\hat{X}(\omega) + \hat{X}(\omega + \frac{\pi}{T})\right), \quad \omega \in \left[-\frac{\pi}{T}, \cdots, \frac{\pi}{T}\right], \tag{B.7}$$

with $\hat{X}(\omega) = \sum_{n=-\infty}^{+\infty} x[n]e^{-j\omega nT}$.

B.3 Difference between z_L and z^L

Mathematically, $z_L = z^L$ but physically z^{-L} is a cascade of L delay elements each with delay time T whereas z_L^{-1} is a single delay element with delay time TL. This is shown in Fig. B.1.

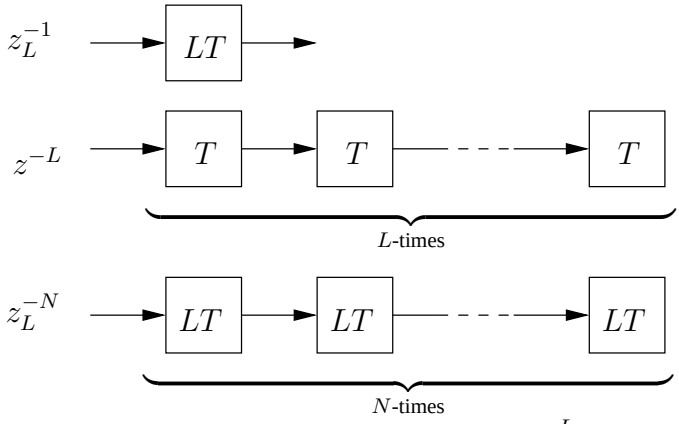

Fig. B.1. Difference between z_L and z^L

B.4 Noble Identity for Upsampling

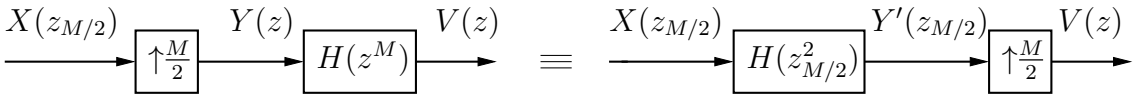

Fig. B.2. Noble identities for upsampling

The input-output relation between $X(z_{M/2})$ and $V(z)$ of the subbfigure on the left-hand side of Fig. B.2 is obtained by inserting

$$Y(z) = X(z_{M/2}) \tag{B.8}$$

into

$$V(z) = H(z^M)Y(z) \tag{B.9}$$

as

$$V(z) = H(z^M)X(z_{M/2}). \tag{B.10}$$

The input-output relation between $X(z_{M/2})$ and $V(z)$ of the subbfigure on the right-hand side of Fig. B.2 is cascaded into

$$Y'(z_{M/2}) = H(z_{M/2}^2)X(z_{M/2}) \tag{B.11}$$

and

$$V(z) = Y'(z_{M/2}). \tag{B.12}$$

Combining both (B.11) and (B.12) leads to

$$V(z) = H(z_{M/2}^2)X(z_{M/2}) = H(z^M)X(z_{M/2}) \tag{B.13}$$

which is identical to (B.10) and proves the equivalence relation of the Noble Identities [115] for upsampling in Fig. B.2 .

B.5 Noble Identity for Downsampling

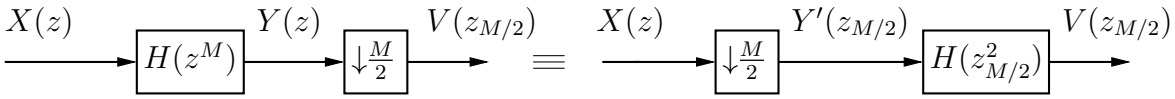

Fig. B.3. Noble identities for downsampling

The input-output relation between $X(z)$ and $Y(z)$ of the subfigure on the left-hand side of Fig. B.3 is obtained by inserting

$$Y(z) = H(z^M)X(z) \tag{B.14}$$

into

$$V(z_{M/2}) = \frac{2}{M}\sum_{\ell=0}^{M/2-1} Y(zW_{M/2}^{\ell}) \tag{B.15}$$

as

$$V(z_{M/2}) = \frac{2}{M}\sum_{\ell=0}^{M/2-1} H(z^M \underbrace{W_{M/2}^{\ell M}}_{=1\forall\ \ell})X(zW_{M/2}^{\ell}) = \frac{2}{M}H(z^M)\sum_{\ell=0}^{M/2-1} X(zW_{M/2}^{\ell}). \tag{B.16}$$

The relations for the subfigure on the right-hand side of Fig.B.3 are given by

$$Y'(z_{M/2}) = \frac{2}{M}\sum_{\ell=0}^{M/2-1} X(zW_{M/2}^{\ell}) \tag{B.17}$$

and

$$V(z_{M/2}) = H(z_{M/2}^2)Y'(z_{M/2}). \tag{B.18}$$

Equations (B.17) and (B.18) can be combined into

$$V(z_{M/2}) = \frac{2}{M}H(z^M)\sum_{\ell=0}^{M/2-1} X(zW_{M/2}^{\ell}) \tag{B.19}$$

confirming the equivalence relation of the Noble Identities [115] for downsampling of both subfigures in Fig. B.3.

C. Perfect Reconstruction Filter Bank

C.1 Uniform Exponentially Modulated Non-maximally Decimated Filter Bank

A general structure of a filter bank system is sketched in Fig. C.1. It is characterized by having M subbands and a rate-changing factor of L in each subband. We consider the case of a non-maximally decimated filter bank structure which is characterized by having $L < M$. We choose $L = M/2$.

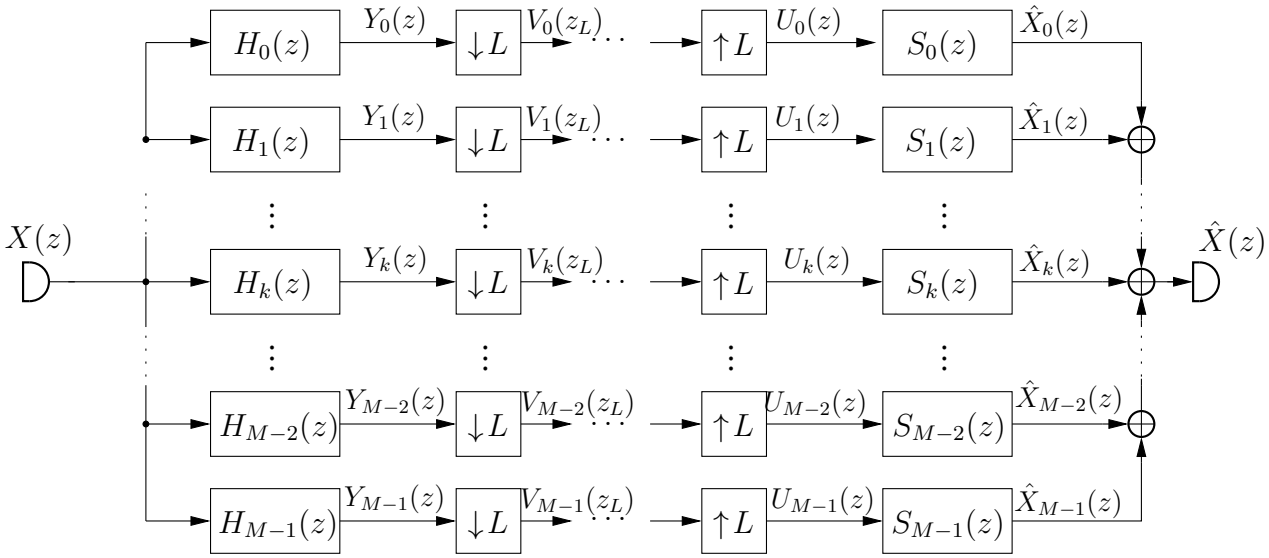

Fig. C.1. General M-channel Filterbank with sampling-rate change factor of L. Non-maximally Decimated FB necessitate $L < M$. We choose $L = M/2$.

The filters

$$H_k(z) = \mathcal{Z}\{h_k[l]\}, \quad k = 0, 1, \cdots, M-1, \quad \text{and} \tag{C.1}$$

$$S_k(z) = \mathcal{Z}\{s_k[l]\}, \quad k = 0, 1, \cdots, M-1 \tag{C.2}$$

represent the analysis and synthesis filters, respectively.

We consider exponentially modulated filter bank systems which are characterized by the modulation of suitably chosen prototype filters $h_{\text{P}}[l]$ and $s_{\text{P}}[l]$ with length P to get $h_k[l]$ and $s_k[l]$,

respectively, in the following way

$$h_k[l] = h_{\mathrm{P}}[l]\exp(j[\alpha_k l + \beta_k]) \tag{C.3}$$

$$s_k[l] = s_{\mathrm{P}}[l]\exp(j[\alpha_k l + \beta_k]) \tag{C.4}$$

where $l = 0, 1, \cdots, P-1$, k represents the corresponding subcarrier, α_k is the modulation factor and β_k determines the phase offset of the subcarriers. We always assume that the prototype filters $h_{\mathrm{P}}[l]$ and $s_{\mathrm{P}}[l]$ have only real coefficients and are symmetrical.

Even stacked subcarrier modulation results in

$$\alpha_k = \frac{2\pi}{M}k. \tag{C.5}$$

The factor β_k ensures that the complex valued subband filters have a strictly linear phase and not an affine phase. This is attained by having the following value for β_k

$$\beta_k = -\frac{2\pi}{M}\frac{P-1}{2}k. \tag{C.6}$$

For perfect reconstruction of the output signal $\hat{x}[n] = \mathcal{Z}^{-1}\{\hat{X}(z)\}$, which means that the output signal $\hat{x}[n]$ is only a time-delayed version of the input signal $x[n] = \mathcal{Z}^{-1}\{X(z)\}$, the subband analysis filters $h_k[l]$ and synthesis filters $s_k[l]$ have to be set equal and they are derived from a common prototype filter denoted as $b_{\mathrm{P}}[l]$

$$h_k[l] = s_k[l] = b_{\mathrm{P}}[l]\exp(j[\alpha_k l + \beta_k]). \tag{C.7}$$

The z-transform representation of the even-stacked linear phase subcarrier filters $H_k(z)$ and $S_k(z)$ is obtained from (C.7) with (C.5) and (C.6) in the form

$$\begin{aligned} H_k(z) = S_k(z) &= \sum_{l=0}^{P-1} b_{\mathrm{P}}[l]\exp(j[\alpha_k l + \beta_k])z^{-l} \\ &= \exp\Big(-j\frac{2\pi}{M}\frac{P-1}{2}k\Big)B_{\mathrm{P}}\Big(z\underbrace{\exp\big(-j\frac{2\pi}{M}k\big)}_{W_M^k}\Big). \end{aligned} \tag{C.8}$$

We will derive an efficient implementation [115] of this filter bank structure. Efficient means that the computational complexity in terms of multiplications per symbol is minimal. The efficient implementation is attained through polyphase decomposition (presented in Appendix A) of the prototype filter and using Noble Identities for upsampling (presented in Appendix B.4) and downsampling (presented in Appendix B.5) .

C.2 Efficient Implementation of the Analysis Filter Bank

The efficient analysis filter bank structure is obtained through polyphase decomposition of the prototype filter $B_{\mathrm{P}}(z)$ and the use of Noble Identities for downsampling presented in Appendix B.5.

As we aim at having a DFT in the analysis filter bank, type-3 polyphase decomposition of $B_{\mathrm{P}}(z)$ is chosen. The z-transform representation of type-3 polyphase components denoted as $G_m^{(p3)}(z^M)$ of $B_{\mathrm{P}}(z)$ are expressed as in (A.11)

$$B_{\mathrm{P}}(z) = \sum_{m=0}^{M-1} z^{+m} G_m^{(p3)}(z^M). \tag{C.9}$$

We use the relation for $H_k(z)$ in (C.8) and (C.9) in

$$Y_k(z) = H_k(z)X(z) = \exp\Big(-j\frac{2\pi}{M}\frac{P-1}{2}k\Big) B_{\mathrm{P}}(zW_M^k)X(z) \tag{C.10}$$

to obtain the following expression for $Y_k(z)$

$$\begin{aligned} Y_k(z) &= X(z)\exp\Big(-j\frac{2\pi}{M}\frac{P-1}{2}k\Big) \sum_{m=0}^{M-1} \big(zW_M^k\big)^{+m} G_m^{(3)}\big((zW_M^k)^M\big) \\ &= X(z)\exp\Big(-j\frac{2\pi}{M}\frac{P-1}{2}k\Big) \left(G_0(z^M) + \sum_{m=1}^{M-1} z^{-(M-m)} W_M^{mk} G_{M-m}(z^M)\right), \end{aligned} \tag{C.11}$$

where $W_M^{kM} = e^{-j\frac{2\pi}{M}kM} = e^{-j2\pi k} = 1, \forall k$ and type-3 to type-1 transformation in (A.12) was used to solve the problem of the non-causal delays that arise in type-3 polyphase decomposition (also later in Sec. C.3 polyphase decomposition of type-1 in the synthesis filter bank will be used).

Introducing the vector $\boldsymbol{g}_3(z)$ with the polyphase components of $B_{\mathrm{P}}(zW_M^k)$ as entries according to

$$\boldsymbol{g}_3(z) = \big[G_0(z^M), z^{-(M-1)}G_{M-1}(z^M), z^{-(M-2)}G_{M-2}(z^M), \cdots, z^{-1}G_1(z^M)\big]^{\mathrm{T}}, \tag{C.12}$$

and the diagonal matrix $\boldsymbol{D} = \text{diag }[d_k], k = 0, 1, \cdots, M-1$,

$$\boldsymbol{D} = \begin{bmatrix} 1 & & & \\ & \exp(-j\frac{2\pi}{M}\frac{P-1}{2}) & & \\ & & \ddots & \\ & & & \exp(-j\frac{2\pi}{M}(M-1)\frac{P-1}{2}) \end{bmatrix} \tag{C.13}$$

the vector $\boldsymbol{y}(z)$ which comprises the subcarrier signals $Y_k(z)$ in the form

$$\boldsymbol{y}(z) = [Y_0(z), Y_1(z), \cdots, Y_{M-1}(z)]^{\mathrm{T}} \tag{C.14}$$

can be expressed in the matrix-vector notation

$$\boldsymbol{y}(z) = \sqrt{M}\boldsymbol{D}\boldsymbol{W}_M\boldsymbol{g}_3(z)X(z), \tag{C.15}$$

where $\boldsymbol{W}_M$ is the DFT matrix defined in (1.5).

To this end, we can interpret analysis filter bank of the (non-maximally) decimated uniform exponentially modulated filter bank as an DFT filter bank, where the input signal $X(z)$ is first filtered with the polyphase vector $\boldsymbol{g}_3(z)$, then the result is multiplied with the DFT matrix and the phase factors and finally downsampled by $M/2$.

If the number of subcarriers M is power of two, the structure is already more efficient than the original one because of the DFT block which can be implemented as fast Fourier transform (FFT). The structure can be further efficiently implemented. The efficient structure of the analysis filter bank can be obtained by applying the Noble Identities [115] as in Appendix B.5 to exchange the filtering by the polyphase components and downsampling operation. This can be done in this case since DFT is a memoryless operation. The resulting efficient structure of the analysis DFT filter bank is shown in Fig. C.2.

The delay elements z^{-1} followed by downsampling by $M/2$ in Fig. C.2 can be interpreted as a serial to parallel convertor of the serial input signal $x[n] = \mathcal{Z}\{X(z)\}$. Overlapping blocks each of length M are formed where consecutive blocks overlap by $M/2$ samples. The overlapping blocks in the time-domain serve as input to the polyphase components $\boldsymbol{g}_3(z)$.

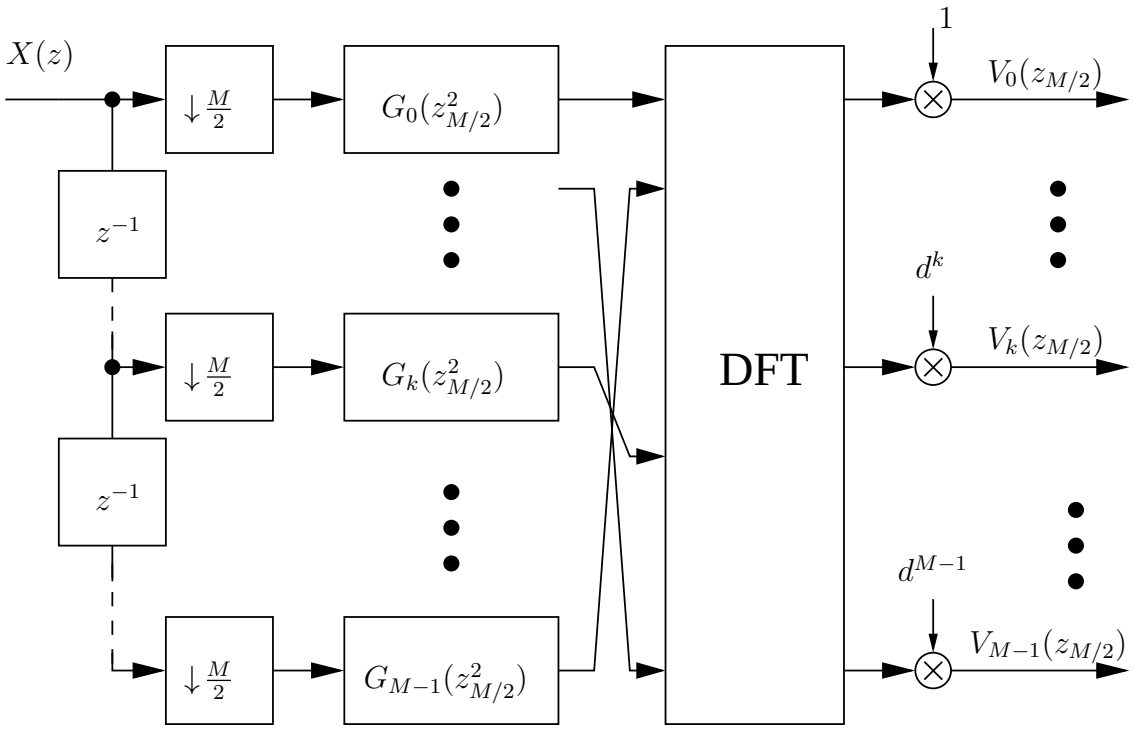

Fig. C.2. Efficient Implementation of the Analysis Filter Bank

C.3 Efficient Implementation of the Synthesis Filter Bank

The efficient synthesis filter bank structure is obtained through polyphase decomposition of the prototype filter $B_{\mathrm{P}}(z)$ and the use of Noble Identities for upsampling presented in B.4.

As we aim at having an IDFT in the synthesis filter bank, type-1 polyphase decomposition of $B_{\mathrm{P}}(z)$ is chosen. The z-transform representation of type-1 polyphase components denoted as $G_m(z^M)$ of $B_{\mathrm{P}}(z)$ are expressed as in (A.3) as

$$B_{\mathrm{P}}(z) = \sum_{m=0}^{M-1} z^{-m} G_m(z^M). \tag{C.16}$$

We use the relation for $S_k(z)$ in (C.8) and (C.16) to express the k-th output signal $\hat{X}_k(z)$ in each sub-band as

$$\hat{X}_k(z) = S_k(z)U_k(z) = \exp\Big(-j\frac{2\pi}{M}\frac{P-1}{2}k\Big) B_{\mathrm{P}}(zW_M^k)U_k(z). \tag{C.17}$$

Introducing the vector $\boldsymbol{g}(z)$ with the polyphase components of $B_{\mathrm{P}}(zW_M^k)$ as entries according to

$$\boldsymbol{g}(z) = \left[G_0(z^M), z^{-1}G_1(z^M), z^{-2}G_2(z^M), \cdots, z^{-(M-1)}G_{M-1}(z^M)\right]^{\mathrm{T}}, \tag{C.18}$$

and the vector $\boldsymbol{u}(z)$ which comprises the sub-band signals $U_k(z)$ in the form

$$\boldsymbol{u}(z) = [U_0(z), U_1(z), \cdots, U_{M-1}(z)]^{\mathrm{T}}, \tag{C.19}$$

the reconstructed signal $\hat{X}(z) = \sum_{k=0}^{M-1} \hat{X}_k(z)$ can be compactly expressed by

$$\hat{X}(z) = \sum_{k=0}^{M-1} \hat{X}_k(z) = \sqrt{M}\boldsymbol{g}^{\mathrm{T}}(z)\boldsymbol{D}\boldsymbol{W}_M^*\boldsymbol{u}(z), \tag{C.20}$$

where $\boldsymbol{W}_M^*$ is the IDFT matrix defined in (1.6) and $\boldsymbol{D}$ in (C.13).

To this end, each input signal to the synthesis filter bank is upsampled by factor $M/2$, transformed by the DFT and then filtered by the polyphase components $\boldsymbol{g}(z)$.

If the number of subcarriers M is power of two, the structure is already more efficient than the original one because of the DFT block which can be implemented as fast Fourier transform (FFT). The structure can be further efficiently implemented. The efficient structure of the synthesis filter bank can be obtained by applying the Noble Identities [115] as in Appendix B.4 to exchange the upsampling operation by $M/2$ and filtering by the polyphase components $\boldsymbol{g}(z)$. This can be done in this case since IDFT is a memoryless operation. The resulting efficient structure of the analysis DFT filter bank is shown in Fig. C.3.

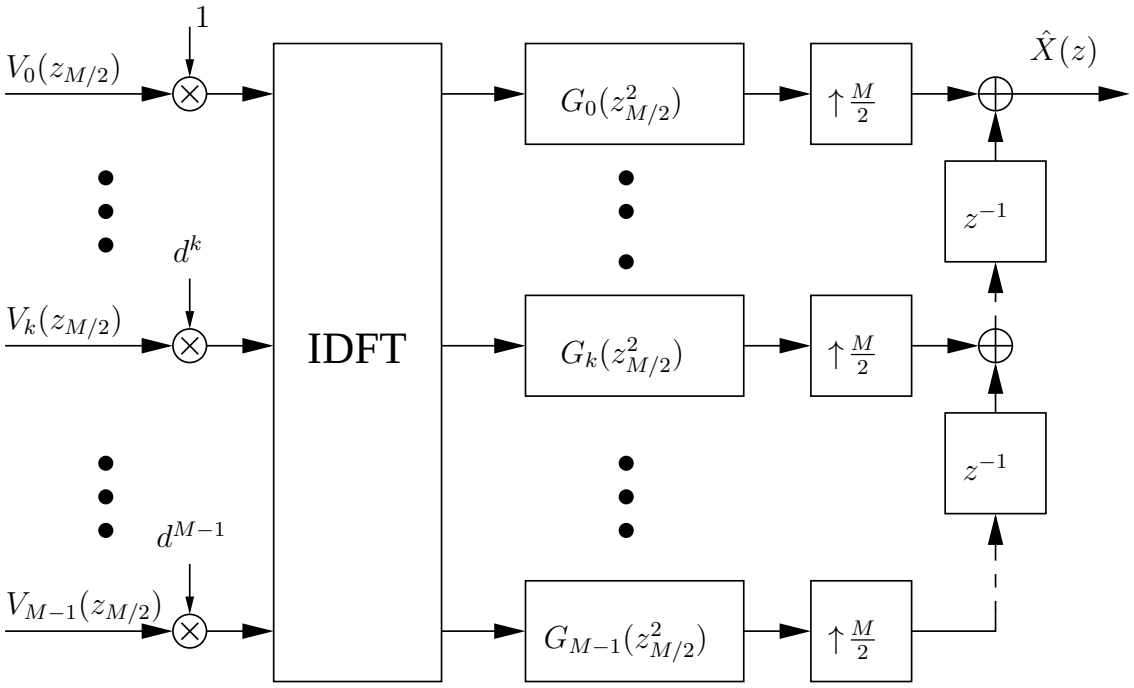

Fig. C.3. Efficient Implementation of the Synthesis Filter Bank

The upsamplering by $M/2$ followed by the delay elements z^{-1} in Fig. C.3 can be interpreted as a parallel to serial converter of the output blocks of the polyphase components $\boldsymbol{g}(z)$. The filtered blocks each of length M are overlapped such that the tail $M/2$ samples of each block are added to the $M/2$ head samples of the adjacent blocks. The overlapped blocks are finally serialized to get the reconstructed signal $\hat{x}[n] = \mathcal{Z}\{\hat{X}(z)\}$.

C.4 Prototype Filter Designs

For the design of the prototype filter $b_{\mathrm{P}}[l]$ in (C.7) the perfect reconstruction condition should be fullfilled.

An example for a perfect reconstruction prototype filter $b_{\mathrm{P}}[l]$ of length $P = 2M$ is defined by [163, 164] and used in *extended lapped transforms* (ELT). It has the following closed form expression

$$b_{\mathrm{P}}[l] = \frac{\sqrt{2}}{4} - \frac{1}{2}\cos\left(l + \frac{1}{2}\frac{\pi}{M}\right), \quad l = 0, 1, \cdots, 2M-1. \tag{C.21}$$

Another possibility for the design of the prototype filter is to abandon the strict PR condition and only achieve an approximate reconstruction or nearly PR. This prototype filter is studied in the literature under the term nearly perfect reconstruction filter banks. The RRC filter is a good example of a NPR prototype filter. It reads as

$$g_{\text{RRC}}(t) = \frac{4\rho\frac{t}{T}\cos(\pi\frac{t}{\pi}(1+\rho)) + \sin(\pi\frac{t}{\pi}(1-\rho))}{\pi\frac{t}{T}(1-(4\rho\frac{t}{T})^2)} \tag{C.22}$$

with roll-off factor ρ.

The finite impulse response (FIR) RRC filter can be obtained from (C.22) by e. g. the following steps

- sampling of the continuous-time impulse response by a suitable oversampling factor (at least factor 2), $o_f = T/T_s, k \geq 2, o_f \in \mathbb{N}$

$$g_{\text{RRC}}^{(\infty)}[l] = g_{\text{RRC}}(tT_s), \tag{C.23}$$

- truncation of the infinitely long filter by a discrete-time window function $w[l]$ of length P

$$b_{\text{P}}[l] = g_{\text{RRC}}^{(\infty)}[l]w[l]. \tag{C.24}$$

We assume that the window function is a rectangular (symmetric) window with an odd P.

For the case that the prototype filter $b_{\text{P}}[l]$ has $P = KM$ coefficients expressed by

$$b_{\text{P}}[l] = \sum_{p=0}^{P-1} b[p]\delta[l-p], \tag{C.25}$$

each polyphase component of type-1 $G_m(z^M)$ (cf. (C.16)) will have K coefficients as

$$G_m(z^M) = \left(\sum_{i=0}^{K-1} g_m[i]z^{-Mi}\right), \tag{C.26}$$

where $g_m[i] = b[p]$ and $p = m + iM$ for $m = 0, 1, \cdots, M-1$.

For the case that $P = KM + 1$, just the first polyphase component $G_0(z^M)$ has $K + 1$ coefficients whereas the rest polyphase components will have K coefficients.

D. Proof of (3.29) and (3.30)

Using the Geometric series

$$\sum_{k=0}^{M-1} l^k = \frac{1-l^M}{1-l} \tag{D.1}$$

in (3.27) with $z = \mathrm{e}^{j\omega T}$ results in

$$\begin{aligned} H_{\mathrm{p}}(z = e^{j\omega T}) &= \frac{1}{\sqrt{M}} \sum_{k=0}^{M-1} e^{-j\omega Tk} = \frac{1}{\sqrt{M}} \frac{1-\mathrm{e}^{-j\omega TM}}{1-\mathrm{e}^{-j\omega T}} \\ &= \frac{1}{\sqrt{M}} \frac{\mathrm{e}^{-j\omega M\frac{T}{2}} \left(\mathrm{e}^{+j\omega M\frac{T}{2}} - \mathrm{e}^{-j\omega M\frac{T}{2}}\right)}{\mathrm{e}^{-j\omega\frac{T}{2}} \left(\mathrm{e}^{+j\omega\frac{T}{2}} - \mathrm{e}^{-j\omega\frac{T}{2}}\right)} \\ &= \frac{1}{\sqrt{M}} \mathrm{e}^{-j\omega(M-1)\frac{T}{2}} \frac{\sin(\omega M\frac{T}{2})}{\sin(\omega\frac{T}{2})}. \quad \text{q.e.d} \end{aligned} \tag{D.2}$$

For the prototype filter in (3.27), we start by using the equality (D.1) with $z = \mathrm{e}^{j\omega T}$ in

$$S'_{\mathrm{p}}(z = e^{j\omega T}) = \frac{1}{\sqrt{M}} \sum_{k=0}^{M/2-1} e^{-j\omega Tk} \tag{D.3}$$

to get

$$\begin{aligned} S'_{\mathrm{p}}(z = e^{j\omega T}) &= \frac{1}{\sqrt{M}} \frac{1-\mathrm{e}^{-j\omega M\frac{T}{2}}}{1-\mathrm{e}^{-j\omega T}} \\ &= \frac{1}{\sqrt{M}} \frac{\mathrm{e}^{-j\omega M\frac{T}{4}} \left(\mathrm{e}^{+j\omega M\frac{T}{4}} - \mathrm{e}^{-j\omega M\frac{T}{4}}\right)}{\mathrm{e}^{-j\omega\frac{T}{2}} \left(\mathrm{e}^{+j\omega\frac{T}{2}} - \mathrm{e}^{-j\omega\frac{T}{2}}\right)} \\ &= \frac{1}{\sqrt{M}} \mathrm{e}^{-j\omega(\frac{M}{2}-1)\frac{T}{2}} \frac{\sin(\omega M\frac{T}{4})}{\sin(\omega\frac{T}{2})}. \end{aligned} \tag{D.4}$$

The z-transform representation of $S_{\mathrm{P}}(z = e^{j\omega T})$ is

$$\begin{aligned} S_{\mathrm{P}}(z = e^{j\omega T}) &= \frac{1}{\sqrt{M}} \sum_{k=\frac{M}{4}}^{\frac{3M}{4}-1} e^{-j\omega Tk} = \mathrm{e}^{-j\omega M\frac{T}{4}} S'_{\mathrm{P}}(z = e^{j\omega T}) \\ &= \frac{1}{\sqrt{M}} \mathrm{e}^{-j\omega(M-1)\frac{T}{2}} \frac{\sin(\omega M\frac{T}{4})}{\sin(\omega\frac{T}{2})}. \quad \text{q.e.d} \end{aligned} \tag{D.5}$$

E. Proof of (3.79)

The matrix inversion lemma of the following form [142]

$$\boldsymbol{A}^{\mathrm{H}}\left(\boldsymbol{A}\boldsymbol{A}^{\mathrm{H}}+\boldsymbol{B}\right)^{-1}=\left(\boldsymbol{A}^{\mathrm{H}}\boldsymbol{B}^{-1}\boldsymbol{A}+\mathbf{1}\right)^{-1}\boldsymbol{A}^{\mathrm{H}}\boldsymbol{B}^{-1} \tag{E.1}$$

is used to derive $E[k]$ for $k=0,1,\cdots,\frac{M}{2}-1$ in (3.79). The same procedure can be used to get $E[k]$ for $k=\frac{M}{2}-1,\cdots,M-1$.

The matrices $\boldsymbol{A}$ and $\boldsymbol{B}$ in (E.1) correspond to

$$\boldsymbol{A}=\boldsymbol{h}[k] \tag{E.2}$$

$$\boldsymbol{B}=\sigma_N^2\boldsymbol{H}_{\mathrm{R}}[k]\boldsymbol{H}_{\mathrm{R}}[k]^{\mathrm{H}} \tag{E.3}$$

in (3.79).

Therefore, the vector-equalizer $\boldsymbol{e}[k]$ in (3.75) can be expressed as

$$\begin{aligned}\boldsymbol{e}[k]&=2\sigma_X^2\boldsymbol{h}[k]^{\mathrm{H}}\left(\sigma_X^2\boldsymbol{h}[k]\boldsymbol{h}[k]^{\mathrm{H}}+\sigma_N^2\boldsymbol{H}_{\mathrm{R}}[k]\boldsymbol{H}_{\mathrm{R}}[k]^{\mathrm{H}}\right)^{-1}\\&=2\sigma_X^2\left(\sigma_X^2\boldsymbol{h}[k]^{\mathrm{H}}\left(\sigma_N^2\boldsymbol{H}_{\mathrm{R}}[k]\boldsymbol{H}_{\mathrm{R}}[k]^{\mathrm{H}}\right)^{-1}\boldsymbol{h}[k]+1\right)^{-1}\boldsymbol{h}[k]^{\mathrm{H}}\left(\sigma_N^2\boldsymbol{H}_{\mathrm{R}}[k]\boldsymbol{H}_{\mathrm{R}}[k]^{\mathrm{H}}\right)^{-1}\\&=2\left(\boldsymbol{h}[k]^{\mathrm{H}}\left(\boldsymbol{H}_{\mathrm{R}}[k]\boldsymbol{H}_{\mathrm{R}}[k]^{\mathrm{H}}\right)^{-1}\boldsymbol{h}[k]+\frac{\sigma_N^2}{\sigma_X^2}\right)^{-1}\boldsymbol{h}[k]^{\mathrm{H}}\left(\boldsymbol{H}_{\mathrm{R}}[k]\boldsymbol{H}_{\mathrm{R}}[k]^{\mathrm{H}}\right)^{-1}.\end{aligned} \tag{E.4}$$

By substituting (3.68) and (3.69) in (E.4), the latter becomes

$$\begin{aligned}\boldsymbol{e}[k]&=\begin{bmatrix}E[k] & E\left[k+\frac{M}{2}\right]\end{bmatrix}\\&=2\left(\begin{bmatrix}H_{\text{tot}}[k]^* & H_{\text{tot}}[k+\frac{M}{2}]^*\end{bmatrix}\begin{bmatrix}\frac{1}{|H_{\text{rx}}[k]|^2} & 0\\0 & \frac{1}{\left|H_{\text{rx}}\left[k+\frac{M}{2}\right]\right|^2}\end{bmatrix}\begin{bmatrix}H_{\text{tot}}[k]\\H_{\text{tot}}[k+\frac{M}{2}]\end{bmatrix}+\frac{\sigma_N^2}{\sigma_X^2}\right)^{-1}\\&\quad\times\begin{bmatrix}H_{\text{tot}}[k]^* & H_{\text{tot}}\left[k+\frac{M}{2}\right]^*\end{bmatrix}\begin{bmatrix}\frac{1}{|H_{\text{rx}}[k]|^2} & 0\\0 & \frac{1}{\left|H_{\text{rx}}\left[k+\frac{M}{2}\right]\right|^2}\end{bmatrix}\\&=\frac{2}{\frac{|H_{\text{tot}}[k]|^2}{|H_{\text{rx}}[k]|^2}+\frac{\left|H_{\text{tot}}\left[k+\frac{M}{2}\right]\right|^2}{\left|H_{\text{rx}}\left[k+\frac{M}{2}\right]\right|^2}+\frac{\sigma_N^2}{\sigma_X^2}}\begin{bmatrix}\frac{H_{\text{tot}}[k]^*}{|H_{\text{rx}}[k]|^2} & \frac{H_{\text{tot}}\left[k+\frac{M}{2}\right]^*}{\left|H_{\text{rx}}\left[k+\frac{M}{2}\right]\right|^2}\end{bmatrix}.\end{aligned} \tag{E.5}$$

Therefore, the equalizer $E[k]$ for $k = 0, 1, \cdots, \frac{M}{2} - 1$ reads as

$$E[k] = \frac{\frac{2H_{\text{tot}}[k]^*}{|H_{\text{rx}}[k]|^2}}{\frac{|H_{\text{tot}}[k]|^2}{|H_{\text{rx}}[k]|^2} + \frac{\left|H_{\text{tot}}\left[k+\frac{M}{2}\right]\right|^2}{\left|H_{\text{rx}}\left[k+\frac{M}{2}\right]\right|^2} + \frac{\sigma_N^2}{\sigma_X^2}}. \tag{E.6}$$

The same steps can be followed to derive $E[k]$ for $k = \frac{M}{2}, \cdots, M - 1$. This proves (3.79).

F. List of Used Symbols and Acronyms

F.1 List of Used Symbols

Symbol	Description
a	amplitude of the main active tap of the delayed dual-tap equalizer
a_{co}	radius of the core
$A_x(z,t), A_y(z,t)$	slowly varying amplitude envelopes
$\tilde{A}(z,\omega)$	frequency transform of $A(z,t)$
B	Baud-rate, noise bandwidth at the receiver
B_{DAC}	single-sided 3-dB bandwidth of the DAC
B_{E3dB}	single-sided 3-dB bandwidth of the electrical filter
B_{O3dB}	double-sided 3-dB bandwidth of the optical filter
B_{ref}	reference bandwidth
c	speed of light in vacuum in m/s
$C_{\text{FD-OLS/OLA}}$	number of real multiplications needed by the OLS and OLA method
$C_{\text{I/FFT}}$	number of real multiplications for an M-point I/FFT using split-radix algorithm
$C_{\text{TD-FIR}}$	number of real multiplications per output symbol
CD	chromatic dispersion coefficient
d^k	phase factor
D_{CD}	chromatic dispersion parameter
D_{PMD}	polarization mode dispersion coefficient
D_{M}	material dispersion
D_{W}	waveguide dispersion
$\boldsymbol{D}$	matrix of the phase factors
$e_k[\ell]$	value of the ℓ-th tap of the FIR CD equalizer in sub-band k
$e_k[\ell_k]$	value of the ℓ_k-th active tap of the delayed single-tap CD equalizer in sub-band k
$e'_u[\ell_u]$	value of the ℓ_u-th active tap of the delayed dual-tap CD equalizer in sub-band u
$e'_u[\ell_u \pm 1]$	value of the $\ell_u \pm 1$-th active tap of the delayed dual-tap CD equalizer in sub-band u
$E[k], E_2^{\text{SQAM}}[k], E_2^{\text{OQAM}}[k]$	k-th discrete frequency point of the equalizer
$E_u[k], E_{uv}[k]$	k-th discrete frequency point of the multi-receiver equalizer
$\boldsymbol{e}[k]$	vector equalizer

Symbol	Description
$E_{\text{in}}(t)$	continuous wave light of the laser
$E_k(z_{M/2})$	per sub-band FIR CD equalizer
$E_k^{\text{S}}(z_{M/2})$	delayed single-tap equalizer per sub-band k
$E_{\text{out}}(t)$	output signal of the modulator
$E_u^{\text{D}}(z_{M/2})$	delayed dual-tap equalizer per sub-band u
$E_x(z,t), E_y(z,t)$	transverse components of the optical field
$E'_k(z_{M/2})$	desired equalizer per sub-band k
$\mathbf{E}$	strength of the electric field
$\boldsymbol{e}[k], \boldsymbol{e}^-[k], \boldsymbol{e}_{\text{D}}[k], \boldsymbol{e}_{\text{D}}^-[k]$	vector equalizer in FD
$\boldsymbol{E}^{\text{MRE}}[k]$	matrix equalizer in FD
f	frequency argument
f_c	carrier frequency
f_k, f_p	discrete frequency point
f_{N}	Nyquist frequency
f_s, f'_s	sampling frequency
F	$= \frac{K_{\text{3dB}}}{B_{\text{E3dB}}} f$ a simplified argument
$g(t)$	impulse response of the suppressor of periodic repetitions in DAC
$g_o(t)$	low-pass equivalent of the optical filter
$G_k(z_{M/2}^2)$	k-th polyphase component of the prototype filter
$h[k]$	k-th coefficient of the prototype filter in the analysis filter bank
$h_{\text{CD}}(t)$	base-band linear time-invariant CD channel
$h_{\text{e}}(t)$	low-pass characteristics of the electrical components
$h_{\text{o}}(t)$	low-pass equivalent of the optical filter
$h_{\text{p}}(t)$	continuous-time representation of the waveform generator
$h_{\text{P}}[\ell]$	ℓ-th coefficient of the prototype filter in the analysis filter bank
$h_{\text{RC}}(t)$	impulse response of an RC filter
$h_{\text{RRC}}(t)$	impulse response of an RRC filter
$h_{\text{rx}}(t)$	impulse response of the electro-optic receiver front-end
$h_s(t)$	impulse response of a pulse shaper
$h_{\text{tot}}[m]$	discrete-time domain representation of the total channel
$\bar{h}_{\text{rx}}[m]$	discrete time domain representation of the receive filter
$\bar{h}_{\text{tot}}(t)$	continuous time domain representation of the total channel
$H(\omega)$	response of the pulse shaping filter
$H_{\text{CD}}(f)$	frequency domain response of the CD channel
$H_{\text{DAC}}(f)$	frequency domain response of DAC
$H_{\text{e}}(f)$	frequency domain response of the electrical filter
$H_{\text{FSM}}(f)$	frequency domain response of the CD equalizer
$H_k(z)$	z-transform representation of the analysis filter in the k-th subband
$H_{\text{o}}(f)$	frequency domain response of the optical filter
$H_{\text{P}}(z)$	z-transform representation of the prototype filter in the analysis filter bank
$H_{\text{RC}}(f)$	frequency response of an RC filter
$H_{\text{RRC}}(f)$	frequency response of an RRC filter

Symbol	Description
$H_{\text{rx}}(f)$	frequency domain response of the electro-optic receiver front-end
$H_{\text{rx}}[k]$	k-th point of the discrete Fourier transform of $h_{\text{rx}}[m]$
$H_s(f)$	spectrum of the signal
$H_{\text{tot}}(f)$	frequency response of $h_{\text{tot}}(t)$
$H_{\text{tot}}[k]$, $H_{\text{tot},u}[k]$	k-th point of the discrete Fourier transform of the total channel
$H_{\text{TR},u}[k]$, $H_{\text{TR},uv}[k]$	k-th point of the discrete Fourier transform of the convolved transmit and receive filter
$\boldsymbol{h}[k], \boldsymbol{h}^{-}[k], \boldsymbol{h}_{\text{D}}[k], \boldsymbol{h}_{\text{D}}^{-}[k]$	channel vector in FD
$\boldsymbol{H}^{\text{MRE}}[k]$	channel matrix in FD
$\boldsymbol{H}_{\text{I}}[k], \boldsymbol{H}_{\text{I}}^{-}[k]$	interfering channel matrix in FD
$\boldsymbol{H}_{\text{R}}[k], \boldsymbol{H}_{\text{R}}^{-}[k], \boldsymbol{H}_{\text{RR}}[k]$	receive filter matrix in FD
I_s	data stream sent in the inphase subchannel
$\hat{I}_s$	data stream detected in the inphase subchannel
$J(\boldsymbol{E}[k])$	mean squared error expression as function of $\boldsymbol{E}[k]$
k, k	index of the discrete frequency point
K	number of the non-zero coefficients of the polyphase component
K_{ch}	number of WDM channels
K_{3dB}	3-dB normalization constant of the electrical filter
ℓ_k	position of the active tap of the delayed single-tap equalizer in sub-band k
ℓ_k'	non-integer multiple of the sampling rate
L	downsampling rate
L_{B}	beat length of the fiber
L_E	length of the equalizer
L_{F}	fiber length where birefringence can be considered constant
L_h	length of the prototype filter in the analysis filter bank
L_s	length of the prototype filter in the synthesis filter bank
m	sample index
M, M_p	I/DFT and I/FFT size
$n(t)$	white Gaussian noise
$n(\omega)$	refractive index
n_{cl}	refractive index of the cladding layer
n_{co}	refractive index of the core layer
n_g	group index
n_{od}	order of the Gaussian function
n_{H}	modal refractive index of the horizontal polarization
n_{V}	modal refractive index of the vertical polarization
N_{cp}	number of symbols for cyclic prefix
N_{PMD}	PMD sections
N_{spans}	fiber spans
N_t	number of coefficients for the equalizer
$N_{\text{TD-FIR}}$	maximum required number of taps for time-domain FIR CD equalizer

Symbol	Description
$N_{\text{TD-IIR}}$	maximum required number of taps for time-domain IIR CD equalizer
$N[k]$	k-th point of the discrete Fourier transform of the noise
$\boldsymbol{n}[k]$	noise vector in FD
$\boldsymbol{n}_{\text{RR}}[k]$	noise vector in FD
o_s	oversampling factor
$\mathcal{O}_u$	OQAM modulation
$\mathcal{O}'_u$	OQAM demodulation
$p(\Delta\tau)$	probability density function for the DGD
P	length of the prototype filter
P_{in}	power launched at the input end of an optical fiber
$P(\ell)$	signal power after traveling distance ℓ over the optical fiber
$\mathbf{P}$	induced electric polarization
q	maximum quantization error
q_k	quantization error in subband k
Q_s	data stream sent in the out-of-phase subchannel
$\hat{Q}_s$	data stream detected in the out-of-phase subchannel
r	integer value
$r_{\text{V}}^{\text{R}}[n] + jr_{\text{V}}^{\text{I}}[n]$	input signal to the DSP module in the vertical polarization
$\mathbf{r}$	Cartesian coordinates
$\boldsymbol{R}_{\text{XX}}$	covariance matrix
$s[k]$	k-th coefficient of the prototype filter in the synthesis filter bank
$s_{\text{H}}^{\text{R}}[n] + js_{\text{H}}^{\text{I}}[n]$	input signal to the DSP module in the horizontal polarization
$s_{\text{P}}[\ell]$	prototype filter in the synthesis filter bank
S	dispersion slope parameter
S_D	set of subband indexes
$S_k(z)$	z-transform representation of the synthesis filter in the k-th subband
$S_{\text{P}}(z)$	z-transform representation of the prototype filter in the synthesis filter bank
t	time index
T	double-symbol period
T_s	symbol period
u	subband index at which delayed dual-tap equalizer is applied, user's channel index
$v(t)$	applied voltage
v_{bias}	bias voltage
v_g	group velocity
$v_1(t)$, $v_2(t)$	externally applied voltages
$V_\pi, V_{\pi 1}, V_{\pi 2}$	drive voltage
V_p	peak voltage
$\mathbf{W}_M$	DFT matrix
$x[n], x_u[n]$	n-th sample of the discrete-time complex QAM input signal
$x_{\text{CD}}(t), x_{\text{CD}}^{\text{S}}(t)$	continuous-time transmitted signal over the CD channel
$x_{\text{d}}(t)$	continuous-time output signal of the DAC

Symbol	Description
$x_{\mathrm{e}}[m], x_{\mathrm{e}}^{\mathrm{S}}[m], x_{\mathrm{e},u}^{\mathrm{S}}[m]$	m-th sample of the discrete-time equalized signal
$x_{\mathrm{H}}^{\mathrm{R}}[n], x_{\mathrm{H}}^{\mathrm{I}}[n]$	bit sequence in the horizontal polarization
$x_{\mathrm{o}}(t), x_{\mathrm{o}}^{\mathcal{O}}(t), x_{\mathrm{o},u}^{\mathcal{O}}(t), x_{\mathrm{o},u}^{\mathrm{S}}(t)$	continuous-time optical signal
$x_{\mathrm{od}}(t)$	continuous-time filtered signal after DAC
$x_{\mathrm{oe}}(t)$	continuous-time base-band electrical signal
$x_{\mathrm{p}}(t), x^{\mathcal{O}}(t), x^{\mathrm{S}}(t)$	continuous-time complex signal sent over CD channel
$x_{\mathrm{ps}}[m]$	m-th sample of the discrete-time pulse-shaped signal
$x_{\mathrm{q}}[m], x_{\mathrm{q}}^{\mathrm{S}}[m]$	m-th sample of the electrical signal after the receive filter
$x_{\mathrm{r}}(t), x_{\mathrm{r}}^{\mathrm{S}}(t)$	continuous-time signal perturbed with noise
$x_{\mathrm{ro}}(t), x_{\mathrm{ro}}^{\mathrm{S}}(t), x_{\mathrm{ro}}(t), x_{\mathrm{ro},u}^{\mathrm{S}}(t)$	continuous-time optical signal in the receiver
$x_{\mathrm{u}}[n]$	n-th sample of the discrete-time upsampled signal
$x_u^{\mathcal{O}}[m]$	m-th sample of the discrete-time staggered input signal
$x_1(t), x_2(t), x_3(t)$	modulated optical signal
$\bar{x}_{\mathrm{H}}^{\mathrm{R}}(t), \bar{x}_{\mathrm{H}}^{\mathrm{I}}(t)$	continuous-time signal representation in the horizontal polarization
$\hat{x}[n], \hat{x}_u[n], \hat{x}_u^{\mathrm{S}}[n]$	n-th sample of the discrete-time downsampled equalized signal
$\hat{x}_{\mathrm{H}}^{\mathrm{I}}[n] + j\hat{x}_{\mathrm{H}}^{\mathrm{R}}[n]$	equalized signal in the horizontal polarization
$X_{\mathrm{e}}[k], X_{\mathrm{e},u}[k]$	k-th discrete frequency point representation of the equalized signal
$X_{\mathrm{e}}(z)$	z-transform representation of the (equalized) signal $x_{\mathrm{e}}[m]$
$X_{\mathrm{q}}(z)$	z-transform representation of the signal $x_{\mathrm{q}}[m]$
$X[\bar{k}]$	k-th point of the discrete Fourier transform of $x[n]$
$X_{\mathrm{u}}[k], X_{\mathrm{U,u}}[k]$	k-th point of the discrete Fourier transform of the upsampled signal
$\hat{X}[\bar{k}], \hat{X}_u[\bar{k}]$	$\bar{k}$-th discrete point of the output signal
$\hat{\boldsymbol{x}}[\bar{k}]$	vector of the output signals in FD
$\boldsymbol{x}_{\mathrm{U}}[k]$	vector of the upsampled input signal in FD
$\boldsymbol{x}_{\mathrm{U,I}}[k]$	interfering signal vector in FD
$y_u[m]$	discrete-time complex signal for equalization
$y_{\mathrm{V}}^{\mathrm{R}}[n], y_{\mathrm{V}}^{\mathrm{I}}[n]$	bit sequence in the vertical polarization
$\bar{y}_{\mathrm{V}}^{\mathrm{R}}(t), \bar{y}_{\mathrm{V}}^{\mathrm{I}}(t)$	continuous-time signal representation in the vertical polarization
$\hat{y}_{\mathrm{V}}^{\mathrm{R}}[n] + j\hat{y}_{\mathrm{V}}^{\mathrm{I}}[n]$	equalized signal in the vertical polarization
$Y_u[k]$	k-th discrete frequency point representation of the discrete-time signal $y_u[m]$
$\boldsymbol{Y}[k]$	signal vector in the FD of the signals for equalization
z^{-1}	delay element
$\lfloor x \rfloor$	floor operator
α_{att}	attenuation coefficient in the optical fiber
α_{CD}	CD coefficient
α_{IR}	intrinsic absorption losses dominating for long wavelengths
α_{OH}	extrinsic absorption
α_{sp}	fraction of frequency separation
α_{UV}	intrinsic absorption losses dominating for short wavelengths
$\beta(\omega)$	propagation constant
β_0	constant phase shift
β_1	group-velocity

Symbol	Description
β_2	group-velocity dispersion
β_3	third-order dispersion
$\beta_1[k], \beta_2[k]$	defined in (4.36) and (4.37)
β_1^{H}	group velocity of the fundamental mode of the horizontal polarization
β_1^{V}	group velocity of the fundamental mode of the vertical polarization
Δf	frequency separation
Δn	strength of the modal dispersion
$\Delta\tau$	differential group delay
$\Delta\varphi$	phase shift
η_{sp}	measure of the spectral efficiency
ϵ_0	vacuum permittivity
λ_c	carrier wavelength in nm
μ_0	vacuum permeability
∇	nabla operator
ω	angular frequency
∂	partial operator
$\phi_{\mathrm{CD}}(f)$	phase of the CD channel
ϕ	phase
ρ	roll-off factor
σ_n^2, σ_N^2	noise variance
σ_t^2	variance of the signal $x_p(t)$
σ_x^2	variance of the input signal $x[n]$
σ_X^2	variance of the upsampled signal in the TD and FD
τ_c	latency time
$\tau_{\mathrm{CD}}(f)$	group delay of the CD channel
$\tau'_{\mathrm{Eq}}(f_k)$	group delay of the desired equalizer
τ_{FB}	delay introduced by the filter bank
$\theta[k]$	defined in (4.35)

F.2 List of Used Acronyms

Acronym	Description
ADC	analog-to-digital converter
AFB	analysis filter bank
ASE	amplified spontaneous emission
ASIC	application specific integrated circuit
AWG	arrayed waveguide gratings
BER	bit-to-error ratio
CD	chromatic dispersion
CMA	constant modulus algorithm
CP	cyclic-prefix
CP-FDE	cyclic prefix - frequency-division equalization

Acronym	Description
CW	continuous wave
C-band	conventional band
DAC	digital-to-analog converter
DCF	dispersion compensating fiber
DCM	dispersion compensating module
DFB	distributed feedback laser
DFT	discrete Fourier transform
DGD	differential group delay
DMUX	demultiplexer
DP	dual-polarization
DSP	digital signal processing
EAMs	electro-absorption modulators
ECL	external cavity laser
EDFA	Erbium-doped fiber amplifier
ELT	extended lapped transform
ENOBs	effective number of bits
EOMs	electro-optic modulators
E-band	extended band
FB	filter bank
FD	frequency-domain
FDE	frequency-domain equalizer
FFE	feed-forward equalizer
FFT	fast Fourier transform
FIR	finite impulse response
FPGA	field programmable gate array
FSE	fractionally spaced equalizer
FSM	frequency sampling method
FTN	faster-than-Nyquist
FWM	four wave mixing
GLSE	generalized linear Schrödinger equation
GVD	group velocity dispersion
IBI	inter-block-interference
ICI	interchannel interference
IDFT	inverse discrete Fourier transform
IFFT	inverse fast Fourier transform
IIR	infinite impulse response
IQ	inphase-quadrature
IQM	in-phase and quadrature modulator
ISI	intersymbol interference
ITU	International Telecommunication Union
KKT	Karush-Kuhn-Tucker
laser	Light Amplification by Stimulated Emission of Radiation
LO	local oscillator
LMS	least mean squared

Acronym	Description
LS	least-squares
LTI	linear time invariant
L-band	long-wavelength band
MAC	multiplier-accumulator
MC	multi-carrier
MF	matched filter
MIMO	multiple-input multiple-output
MLSE	maximum likelihood sequence estimation
MMFs	multimode fibers
MMSE	minimum mean square error
MRE	multi-receiver equalization
MUX	multiplexer
MZM	Mach-Zehnder modulator
NGI-OFDM	no-guard-interval orthogonal frequency division multiplexing
NRZ	non return-to-zero
NTF	non-trivial prototype filters
OA	optical amplifier
OFDE	overlap frequency domain equalization
OFDM	orthogonal frequency division multiplexing
OLA	overlap-and-add
OLA-OSZP	overlap-and-add one-side zero-padding
OLS	overlap-and-save
OQAM	offset QAM
OSNR	optical signal to noise ratio
OPLLs	optical phase-locked loops
O-band	original band
PAPR	peak-to-average power ratio
PBC	polarization beam combiner
PBS	polarization beam splitter
PDF	power density function
PDM	polarization division multiplexed
PLL	phase-locked loop
PolMUX	polarization multiplexing
PM	phase modulator
PMD	polarization mode dispersion
PSD	power spectral density
QAM	quadrature amplitude modulation
QPSK	quadrature phase shift keying
RC	raised cosine
RF	radio frequency
RRC	root raised cosine
RZ	return-to-zero
SE	spectral efficiency
SFB	synthesis filter bank

Acronym	Description
SMFs	single-mode fibers
SPM	self-phase modulation
SQAM	standard QAM
SSMF	standard single-mode fiber
S-band	short-wavelength band
TD	time-domain
UW	unique word
U-band	ultra long-wavelength band
WDM	wavelength division multiplexing
WGN	white Gaussian noise
WSS	wavelength selective switching
XPolM	cross-polarization modulation
XPM	cross-phase modulation
ZF	zero-forcing

Bibliography

[1] Cisco Systems, Inc., White Paper, *Cisco Visual Networking Index Forecast and Methodology, 2015-2020*, 2016.

[2] Infinera Corporation, White Paper, *DWDM Coherent Technology*, 2009.

[3] A. Chralyvy, "The coming capacity crunch," in *Proc. European Conference on Optical Communication (ECOC 2009)*, September 2009.

[4] Y. Yamamoto and T. Kimura, "Coherent optical fiber transmission systems," *IEEE Journal of Quantum Electronics*, vol. 17, no. 06, pp. 919–935, June 1981.

[5] G.-D. Khoe, "Lightwave technology: expectations, problems, and achievements," *IEEE Journal on Selected Topics of Quantum Electronics*, vol. 06, no. 06, pp. 1265–1272, November 2000.

[6] R. A. Linke and A. H. Gnauck, "High-capacity coherent lightwave systems," *IEEE/OSA Journal of Lightwave Technology*, vol. 6, pp. 1750–1769, 1988.

[7] K. Kikuchi, "Coherent transmission systems," in *Proc. European Conference on Optical Communication (ECOC 2008)*, September 2008.

[8] L. G. Kazovsky, S. Benedetto, and A. E. Willner, *Optical Fiber Communication Systems*. Artech House, 1996.

[9] G. P. Agrawal, *Fiber-optic Communication Systems*, 2nd ed. John Wiley and Sons, 1997.

[10] D. N. Payne and R. I. Laming, "Optical amplifier-a telecommunications revolution," *International Electron Devices Meeting*, pp. 3–4, 1991.

[11] I. P. Kaminov, T. Li, and A. E. Willne, *Optical Fiber Telecommunications V B: Systems and networks*. San Diego: Academic Press, 2008.

[12] T. Pfau, "Carrier recovery algorithms and real-time DSP implementation for coherent receivers," in *Proc. Optical Fiber Communication Conference (OFC 2014)*, 2014, p. W4K.1.

[13] J. E. Mazo, "Faster-than-Nyquist Signaling," *Bell System Technical Journal*, vol. 54, pp. 1451–1462, October 1975.

[14] F. Rusek and J. B. Anderson, "Successive interference cancellation in multistream faster-than-Nyquist Signaling," in *Proc. International Conference on Wireless Communications and Mobile Computing (IWCMC 2006)*, New York, NY, USA, 2006, pp. 1021–1026.

[15] S. B. Weinstein and P. M. Ebert, "Data Transmission by Frequency-domain Multiplexing using the Discrete Fourier Transform," *IEEE Transactions on Communication Technology*, vol. 19, pp. 628–628, October 1971.

[16] W. Shieh, H. Bao, and Y. Tang, "Coherent optical OFDM: Theory and design," *Optics Express*, vol. 16, no. 2, pp. 841–859, 2008.

[17] W. Shieh, Q. Yang, and Y. Ma, "107 Gb/s coherent optical OFDM transmission over 1000-km SSMF fiber using orthogonal band multiplexing," *Optics Express*, vol. 16, no. 9, pp. 6378–6386, 2008.

[18] W. Shieh, X. Yi, Y. Ma, and Q. Yang, "Coherent optical OFDM: has its time come?" *Journal of Optical Networking*, vol. 7, no. 3, pp. 235–255, March 2008.

[19] S. Chandrasekhar, X. Liu, B. Zhu, and D. W. Peckham, "Transmission of a 1.2 Tbit/s 24-carrier no GI-OFDM superchannel over 7200-km of ultra-large area fiber," in *Proc. European Conference on Optical Communication (ECOC 2009)*, September 2009.

[20] S. Chandrasekhar and X. Liu, "Experimental investigation on the performance of of closely spaced multi-carrier PDM-QPSK with digital coherent detection," *Optics Express*, vol. 17, no. 24, pp. 21 350–21 361, 2009.

[21] A. Sano, E. Yamada, H. Masuda, E. Yamazaki, T. Kobayashi, E. Yoshida, Y. Miyamoto, R. Kudo, K. Ishihara, and Y. Takatori, "No-Guard-Interval coherent optical OFDM for 100-Gb/s long-haul WDM Transmission," *IEEE/OSA Journal of Lightwave Technology*, vol. 27, no. 16, pp. 3705–3713, 2009.

[22] K. Takiguchi, M. Oguma, T. Shibata, and H. Takahashi, "Optical OFDM demultiplexer using silica PLC based optical FFT circuit," in *Proc. Optical Fiber Communication Conference (OFC 2009)*, 2009.

[23] X. Liu, S. Chandrasekhar, B. Zhu, P. J. Winzer, A. H. Gnauck, and D. W. Peckham, "Transmission of 448-Gb/s reduced-GI CO-OFDM with a 60-GHz optical BW over 2000 km of ULAF and five 80-GHz-grid ROADMs," in *Proc. Optical Fiber Communication Conference (OFC 2010)*, 2010.

[24] Y. Ma, Q. Yang, Y. Tang, S. Chen, and W. Shieh, "1-Tb/s single-channel coherent optical OFDM transmission with orthognal-band multiplexing and subwavelength BW access," *IEEE/OSA Journal of Lightwave Technology*, vol. 28, no. 4, pp. 308–315, August 2010.

[25] X. Liu, S. Chandrasekhar, B. Zhu, P. J. Winzer, A. H. Gnauck, and D. W. Peckham, "Transmission of a 448-Gb/s reduced-guard-interval CO-OFDM signal with a 60-GHz optical bandwidth over 2000 km of ULAF and five 80-GHz-grid ROADMs," in *Proc. Optical Fiber Communication Conference (OFC 2010)*, 2010.

[26] S. Chandrasekhar and X. Liu, "Terabit superchannels for high spectral efficiency transmission," in *Proc. European Conference on Optical Communication (ECOC 2010)*, 2010.

[27] D. Hillerkuss, M. Winter, M. Teschke, A. Marculescu, J. Li, G. Sigurdsson, K. Worms, W. Freude, and J.Leuthold, "Low-complexity optical FFT scheme enabling Tbit/s all-optical OFDM communication," in *ITG Symposium on Photonic Networks*, 2010.

[28] J. Yu, Z. Dong, X. Xiao, Y. Xia, S. Shi, C. Ge, W. Zhou, N. Chi, and Y. Shao, "Generation, transmission, and coherent detection of 11.2 Tb/s (112x100 Gb/s) single source optical OFDM superchannel," in *Proc. Optical Fiber Communication Conference (OFC 2011)*, 2011.

[29] B. Inan, S. Adhikari, O. Karakaya, P. Kainzmaier, M. Mocker, H. von Kirchbauer, N. Hanik, and S. L. Jansen, "Real-time 93.8-Gb/s polarization-multiplexed OFDM transmitter with 1024-point IFFT," *Optics Express*, vol. 19, no. 26, pp. B64–B68, 2011.

[30] D. Hillerkuss, R. Schmogrow, T. Schellinger, M. Jordan, M. Winter, G. Huber, T. Vallaitis, R. Bonk, P. Kleinow, F. Frey, M. Roeger, and S. Koenig, "26 Tbit/s line-rate superchannel transmission utilizing all-optical fast Fourier transform processing," *Nature Photonics*, vol. 5, no. 6, pp. 364–371, 2011.

[31] E. Giacoumidis, A. Tsokanos, C. Mouchos, G. Zardas, C. Alves, J. L. Wei, J. M. Tang, C. Gosset, Y. Jaouen, and I. Tomkos, "Extensive comparison of optical fast OFDM and conventional OFDM for local and access networks," *IEEE/OSA Journal of Optical Communications and Networking*, vol. 4, no. 10, pp. 724–733, 2012.

[32] J. Zhao and A. D. Ellis, "Advantage of optical fast OFDM over OFDM in residual frequency offset compensation," *IEEE Photonics Technology Letters*, vol. 24, no. 24, pp. 2284–2287, 2012.

[33] S. Chandrasekhar and X. Liu, "OFDM Based Superchannel Transmission Technology," *IEEE/OSA Journal of Lightwave Technology*, vol. 30, no. 24, pp. 3816–3823, 2012.

[34] G. Gavioli, E. Torrengo, G. Bosco, A. Carena, V. Curri, V. Miot, and P. Poggiolini, "Investigation of the impact of ultra-narrow carrier spacing on the transmission of a 10-carrier 1 Tb/s superchannel," in *Proc. Optical Fiber Communication Conference (OFC 2010)*, March 2010.

[35] G. Bosco, A. Carena, V. Curri, P. Poggiolini, E. Torrengo, and F. Forghieri, "Investigation of the robustness of a Nyquist-WDM terabit superchannel to transmitter and receiver non-linearities," in *Proc. European Conference on Optical Communication (ECOC 2010)*, September 2010.

[36] E. Torrengo, R. Cigliutti, G. Bosco, G. Gavioli, S. Abrate, A. Carena, V. Curri, F. Forghieri, S. Piciaccia, M. Belmonte, A. Brinciotti, A. L. Porta, A. Alaimo, and P. Poggiolini, "Transoceanic PM-QPSK terabit superchannel transmission experiments at the Baud-rate subcarrier spacing," in *Proc. European Conference on Optical Communication (ECOC 2010)*, September 2010.

[37] Y. Cai, J. X. Cai, C. R. Davidson, D. Foursa, A. Lucero, O. Sinkin, A. Pilipetskii, G. Mohs, and N. S. Bergano, "High spectral efficiency long-haul transmission with pre-filtering and maximum a posteriori probability detection," in *Proc. European Conference on Optical Communication (ECOC 2010)*, September 2010.

[38] G. Bosco, A. Carena, V. Curri, and F. Forghieri, "Performance limits of N-WDM and CO-OFDM in the high speed PM-QPSK systems," *IEEE Photonics Technology Letters*, vol. 22, no. 10, pp. 1129–1131, 2010.

[39] Z. Dong, J. Yu, H. C. Chien, N. Chi, L. Chen, and G. K. Chang, "Ultra-dense WDM-PON delivering carrier-centralized Nyquist-WDM uplink with digital coherent detection," *Optics Express*, vol. 19, no. 12, pp. 11 100–11 105, 2011.

[40] K. Igarashi, Y. Mori, K. Katoh, and K. Kikuchi, "BER performance of Nyquist-WDM QPSK optical signals," in *Proc. Optical Fiber Communication Conference (OFC 2011)*, 2011.

[41] X. Zhou, L. Nelson, P. Magill, R. Isaac, B. Zhu, and D. W. Peckham, "8x450-Gb/s, 50-GHz-spaced, PDM-32 QAM transmission over 400 km and one 50-GHz grid ROADM," in *Proc. Optical Fiber Communication Conference (OFC 2011)*, 2011.

[42] G. Bosco, V. Curri, A. Carena, and F. Forghieri, "On the performance of Nyquist-WDM terabit superchannels based on the PM-BPSK, PM-QPSK, PM-8QAM, PM-16QAM subcarriers," *IEEE/OSA Journal of Lightwave Technology*, vol. 29, no. 1, pp. 53–61, January 2011.

[43] J. Zhao and A. Ellis, "Electronic impairment mitigation in optically multiplexed multicarrier systems," *IEEE/OSA Journal of Lightwave Technology*, vol. 29, no. 2, pp. 278–290, January 2011.

[44] D.Hillerkuss, R. Schmogrow, M. Meyer, S. Wolf, M. Jordan, P. Kleinow, N.Lindenmann, P. C. Schindler, A. Melikyan, and X.Yang, "Single-Laser 32.5 Tbit/s Nyquist WDM Trans-

mission," *Journal of Optical Communications and Networking*, vol. 4, no. 10, pp. 715–723, 2012.

[45] J. Li, E. Tipsuwannakul, T. Eriksson, M. Karlsson, and P. A. Andrekson, "Approaching Nyquist Limit in WDM Systems by Low-Complexity Receiver-Side Duobinary Shaping," *IEEE/OSA Journal of Lightwave Technology*, vol. 30, no. 11, pp. 1664–1676, 2012.

[46] J. Fickers, A.Ghazisaeidi, M. Salsi, G. Charlet, F. Horlin, P. Emplit, and S. Bigo, "Design Rules for Pulse Shaping in PDM-QPSK and PDM-16QAM Nyquist-WDM Coherent Optical Transmission Systems ," in *Proc. Optical Fiber Communication Conference (OFC 2012)*, 2012.

[47] Z. Dong, X. Li, J. Yu, and N. Chi, "6x144 Gb/s Nyquist WDM PDM-64QAM generation and transmission on a 12-GHz WDM grid equipped with Nyquist band pre-equalization," *IEEE/OSA Journal of Lightwave Technology*, vol. 30, no. 23, pp. 3687–3692, 2012.

[48] J. Zhao and A. D. Ellis, "Offset-QAM based coherent WDM for spectral efficiency enhancement," *Optics Express*, vol. 19, no. 15, pp. 14 617–14 631, 2011.

[49] S. Randel, A. Sierra, X. Liu, S. Chandrasekhar, and P. J. Winzer, "Study of multicarrier offset-QAM for spectrally efficient coherent optical communications," in *Proc. European Conference on Optical Communication (ECOC 2011)*, 2011.

[50] S. Randel, S. Corteselli, S. Chandrasekhar, A. Sierra, X. Liu, P. J. Winzer, T. Ellermeyer, J. Lutz, and R. Schmid, "Generation of 224-Gb/s multicarrier offset-QAM using a real-time transmitter," in *Proc. Optical Fiber Communication Conference (OFC 2012)*, March 2010.

[51] F. Horlin, J. Fickers, P. Emplit, A. Bourdoux, , and J. Louveaux, "Dual-polarization OFDM-OQAM for communications over optical fibers with coherent detection," *Optics Express*, vol. 21, no. 5, pp. 6409–6421, 2013.

[52] Z. Li, T. Jiang, H. Li, X. Zhang, C. Li, C. Li, R. Hu, M. Luo, X. Zhang, X. Xiao, Q. Yang, and S. Yu, "Experimental demonstration of 110-Gb/s unsynchronized band-multiplexed superchannel coherent optical OFDM/OQAM system," *Optics Express*, vol. 21, no. 19, pp. 21 924–21 931, 2013.

[53] S. M. Bilal and G. Bosco, "Pilot tones based polarization rotation, frequency offset and phase estimation for polarization multiplexed Offset-QAM Multi-Subcarrier coherent optical systems," in *Proc. International Conference on Transparent Optical Networks (ICTON 2016)*, 2016.

[54] R. W. Chang, "Synthesis of bandlimited orthogonal signals for multi-channel data transmission," *Bell System Technical Journal*, vol. 45, pp. 1775–1796, December 1966.

[55] B. Saltzberg, "Performance of an efficient parallel data transmission systems," *IEEE Transactions on Communications*, vol. 15, no. 6, pp. 805–811, December 1967.

[56] M. Seimetz, *High-Order Modulation for Optical Fiber Transmission*, 1st ed. Springer, 2009.

[57] D. van den Borne, "Robust optical transmission systems," Dissertation, Technische Universiteit Eindhoven, March 2008.

[58] H. Nyquist, "Certain topics in telegraph transmission theory," *Proceedings of the IEEE*, vol. 90, no. 2, pp. 280–305, February 2002.

[59] J. L. Vossen and W. Kern, *Thin film processes*, 1st ed. Academic express, 1978.

[60] G. P. Agrawal, *Nonlinear Fiber Optics*, 4th ed. Academic Press, 2007.

[61] F. M. Gardner, "BPSK/QPSK Timing-Error Detector for Sampled Receivers," *IEEE Transaction on Communications*, vol. COM-34, pp. 423–429, 1986.

[62] M. Oerder and H. Meyr, "Digital filter and square timing recovery," *IEEE Transaction on Communications*, vol. COM-36, pp. 605–612, 1988.

[63] K. Mueller and M. Mueller, "Timing recovery in digital synchronous data receivers," *IEEE Transaction on Communications*, vol. COM-24, pp. 516–531, 1976.

[64] M. Kuschnerov, F. Hauske, E. Gourdon, K. Piyawanno, B. Lankl, and B. Spinnler, "Digital Timing Recovery for Coherent Fiber Optic Systems," in *Proc. Optical Fiber Communication Conference (OFC 2008)*, San Diego, CA, U.S.A., March 2008, paper JThA63.

[65] M. Kuschnerov, F. Hauske, K. Piyawanno, B. Spinnler, E.-D. Schmidt, and B. Lankl, "Joint Equalization and Timing Recovery for Coherent Fiber Optic Receivers," in *Proc. European Conference on Optical Communication (ECOC 2008)*, Brussel, Belgium, September 2008, paper Mo.3.D.3.

[66] D. N. Godard, "Self-recovering equalization and carrier tracking in two-dimensional data communication systems," *IEEE Transaction on Communications*, vol. COM-28, pp. 1867–1875, 1980.

[67] B. Widrow and M. E. Hoff, "Adaptive switching circuits," *IRE WESCON Convention record*, vol. 4, pp. 96–104, 1960.

[68] D. N. Godard, "Synthesis of a nonlinear Bayes detector for Gaussian signal and noise fields using Wiener filters," *IEEE Transactions on Information Theory*, vol. IT-13, pp. 116–118, 1967.

[69] K. C. Kao and G. A. Hockham, "Dielectric-fibre surface waveguides for optical frequencies," *Proceedings of the Institution of Electrical Engineers*, vol. 113, no. 7, pp. 1151–1158, 1966.

[70] G. Keiser, *Optical Fiber Communications*, 3rd ed. McGraw-Hill, 2000.

[71] *Optical system design and engineering considerations*, vol. G. Sup. 39 ed., International Telecommunication Union ITU, October 2003.

[72] M. Nakamura, H. Ueda, S. Makino, T. Yokotani, and K. Oshima, "Proposal of networking by PON technologies for full and Ethernet services in FFTx," *IEEE/OSA Journal of Lightwave Technology*, vol. 22, no. 11, pp. 2631–2640, November 2004.

[73] M. Abrams, P. Becker, Y. Fujimoto, Oapos, V. Byrne, and D. Piehler, "FTTP deployments in the United States and Japan-equipment choices and service providers imperatives," *IEEE/OSA Journal of Lightwave Technology*, vol. 23, no. 1, pp. 236–246, January 2005.

[74] H. Thiele, P. Winzer, J. Sinsky, L. Stulz, L. Nelson, and F. Fidler, "160-Gb/s CWDM capacity upgrade using 2.5-Gb/s rated uncooled directly modulated lasers," *IEEE Photonics Technology Letters*, vol. 16, no. 10, pp. 2389–2391, 2004.

[75] M. Duelk, "Next-Generation 100G Ethernet," in *Proc. European Conference on Optical Communication (ECOC 2005)*, vol. 2, 2005.

[76] A. Galtarossa, L. Palmieri, A. Pizzinat, M. Schiano, and T. Tambosso, "Measurement of local beat length and differential group delay in installed single-mode fibers," *IEEE/OSA Journal of Lightwave Technology*, vol. 18, no. 10, pp. 1389–1394, October 2000.

[77] I. P. Kaminow and T. L. Koch, *Optical Fiber Telecommunication*. Academic Press, 1997, vol. IIIa.

[78] C. R. S. Fludger, T. Duthel, D. van den Borne, C. Schulien, E.-D. Schmidt, T. Wuth, J. Geyer, E. D. Man, G.-D. Khoe, and H. de Waardt, "Coherent equalization and POLMUX-RZ-DQPSK for robust 100-GE transmission," *IEEE/OSA Journal of Lightwave Technology*, vol. 26, no. 1, pp. 64–72, January 2008.

[79] F. Buchali and H. Bülow, "Adaptive PMD compensation by electrical and optical techniques," *IEEE/OSA Journal of Lightwave Technology*, vol. 22, no. 4, pp. 1116–1126, April 2004.

[80] M. Bohn, G. Mohs, C. Scheerer, C. Glingener, C. Wree, and W. Rosenkranz, "An adaptive optical equalizer concept for single-channel distortion compensation," in *Proc. European Conference on Optical Communication (ECOC 2001)*, Amsterdam, The Netherlands, September 2001, paper Mo.F.2.3.

[81] M. Secondini, E. Forestieri, and G. Prati, "Adaptive minimum MSE controlled PLC optical equalizer for chromatic dispersion compensation," *IEEE/OSA Journal of Lightwave Technology*, vol. 21, no. 10, pp. 2322–2311, 2003.

[82] D. Stahl, P. J. Winzer, C. R. Doerr, and S. Chandrasekhar, "Extending the chromatic dispersion tolerance by optical equalization at 43 Gb/s," in *Proc. Optical Fiber Communication Conference (OFC 2003)*, Atlanta, GA, U.S.A., March 2003, paper ThU5.

[83] S. H. Lawan and M. Ajiya, "Dispersion compensating fibers for non-zero dispersion fibers," in *Proc. IEEE International Conference on Emerging and Sustainable Technologies for Power and ICT in a Developing Society (NIGERCON 2013)*, 2013, pp. 93–95.

[84] M. Wandel, P. Kristensen, T. Veng, Y. Qian, Q. Lea, and L. Gruner-Nielsen, "Dispersion management in a single-mode optical fiber communication system using dispersion compensating fiber," in *Optical Fiber Communication Conference (OFC 2002)*, 2002, pp. 327–329.

[85] F. Gerome, J. L. Auguste, J. Maury, J. M. Blondy, and J. Marcou, "Theoretical and experimental analysis of a chromatic dispersion compensating module using a dual concentric core fiber," *IEEE/OSA Journal of Lightwave Technology*, vol. 24, no. 1, pp. 442–448, 2006.

[86] H. Nakaji, "Lossless dispersion compensating fibre module for wavelength-management networks," *Electronics Letter*, vol. 40, no. 12, pp. 756–758, 2004.

[87] V. Curri, P. Poggiolini, A. Carena, and F. Forghieri, "Dispersion compensation and mitigation of nonlinear effects in 111-Gb/s WDM coherent PM-QPSK systems," *IEEE Photonics Technology Letters*, vol. 20, no. 17, pp. 1473–1475, 2008.

[88] C. C. Davis and T. Murphy, "Fiber-optic communications," *IEEE Signal Processing Magazine*, vol. 28, no. 4, pp. 147–150, July 2011.

[89] P. Bower and I. Dedic, "High speed converters and DSP for 100G and beyond," *Optical Fiber Technology*, vol. 17, no. 5, pp. 464–471, October 2011.

[90] H. Bülow, F. Buchali, and A. Klekamp, "Electronic dispersion compensation," *IEEE/OSA Journal of Lightwave Technology*, vol. 26, no. 1, pp. 158–167, 2008.

[91] A. Färbert, S. Langenbach, N. Stojanovic, C. Dorschky, T. Kupfer, C. Schulien, J. P. Elbers, H. Wernz, H. Griesser, , and C. Glingener, "Performance of a 10.7 Gb/s receiver with digital equalizer using maximum likelihood sequence estimation," in *Proc. European Conference on Optical Communication (ECOC 2004)*, 2004, paper Th4.1.5.

[92] T. Xu, G. Jacobsen, S. Popov, J. Li, E. Vanin, K. Wang, A. T. Friberg, and Y. Zhang, "Chromatic dispersion compensation in coherent transmission system using digital filters," *Optics Express*, vol. 18, no. 15, pp. 16 234–16 257, 2010.

[93] T. Xu, G. Jacobsen, S. Popov, J. Li, K. Wang, and A. T. Friberg, "Normalized LMS digital filter for chromatic dispersion equalization in 112-Gbit/s PDM-QPSK coherent optical transmission system," *Optical Communications*, vol. 283, no. 6, pp. 963–967, 2010.

[94] S. J. Savory, G. Gavioli, R. I. Killey, and P. Bayvel, "Digital filters for coherent optical receivers," *Optics Express*, vol. 15, no. 5, pp. 2120–2126, 2007.

[95] S. J. Savory, "Digital filters for coherent optical receivers," *Optics Express*, vol. 16, no. 2, pp. 804–817, 2008.

[96] ——, "Compensation of fibre impairments in digital coherent systems," in *Proc. European Conference on Optical Communication (ECOC 2008)*, 2008, paper Mo.3.D.1.

[97] A. Eghbali, H. Johansson, O. Gustafsson, and S. J. Savory, "Optimal least-squares FIR digital filters for compensation of chromatic dispersion in digital coherent optical receivers," *IEEE/OSA Journal of Lightwave Technology*, vol. 32, no. 8, pp. 1449–1456, April 2014.

[98] G. Goldfarb and G. Li, "Chromatic dispersion compensation using digital IIR filtering with coherent detection," *IEEE Photonics Technology Letters*, vol. 19, no. 13, pp. 969–971, 2007.

[99] G. Goldfarb, "Digital Signal Processing Techniques for Coherent Optical Communication," Dissertation, Department of Optics in the College of Optics and Photonics at the University of Central Florida, 2008.

[100] J. Munir, A. Mezghani, I. Slim, and J. A. Nossek, "Chromatic dispersion compensation using complex-valued all-pass filter," in *Proc. European Signal Processing Conference (Eusipco 2014)*, 2014.

[101] J. Munir, A. Mezghani, H. Khawar, I. Slim, and J. A. Nossek, "Chromatic dispersion compensation using filter bank based complex-valued all-pass filter," in *Proc. 10th International ITG Conference on Systems, Communications and Coding (SCC 2015)*, 2015, paper 1403.

[102] S. L. Jansen, I. Morita, K. Forozesh, S. Randel, D. van den Borne, and H. Tanaka, "Optical OFDM, a hype or is it for real," in *Proc. European Conference on Optical Communication (ECOC 2008)*, 2008, paper Mo.3.E.3.

[103] A. Sano, E. Yamada, H. Masuda, E. Yamazaki, T. Kobayashi, E. Yoshida, Y. Miyamoto, S. Matsuoka, R. Kudo, K. . Ishihara, Y. Takatori, M. Mizoguchi, K. Okada, K. Hagimoto, H. Yamazaki, S. Kamei, and H. Ishii, "13.4-Tb/s (134 x 111-Gb/s/ch) no-guard-interval coherent OFDM Transmission over 3,600 km of SMF with 19-ps average PMD," in *Proc. European Conference on Optical Communication (ECOC 2008)*, 2008.

[104] K. Ishihara, T. Kobayashi, R. Kudo, Y. Takatori, A. Sano, E. Yamada, H. Masuda, and Y. Miyamoto, "Frequency-domain equalisation for optical transmission systems," *Electronics Letters*, vol. 44, no. 14, pp. 870–871, July 2008.

[105] R. Kudo, T. Kobayashi, K. Ishihara, Y. Takatori, A. Sano, and Y. Miyamoto, "Coherent Optical Single Carrier Transmission using overlap FD equalization for long haul Optical Systems," *IEEE/OSA Journal of Lightwave Technology*, vol. 27, no. 16, pp. 3721–3728, 2009.

[106] R. Kudo, T. Kobayashi, K. Ishihara, Y. Takatori, A. Sano, E. Yamada, H. Masuda, Y. Miyamoto, and Mizoguchi, "Single carrier Transmission with two-stage overlap frequency domain equalisation for long-haul optical systems," *Electronics Letters*, vol. 45, no. 3, pp. 180–182, 2009.

[107] ——, "Frequency-domain equalization without guard interval for optical transmission systems," *Electronics Letters*, vol. 44, no. 25, pp. 1480–1482, 2009.

[108] B. Spinnler, F. N. Hauske, , and M. Kuschnerov, "Adaptive equalizer complexity in coherent optical receivers," in *Proc. European Conference on Optical Communication (ECOC 2008)*, 2008, paper We.2.E.4.

[109] M. Kuschnerov, F. N. Hauske, K. Piyawano, B. Spinnler, M. Alfiad, A. Napoli, and B. Lankl, "DSP for coherent single-carrier receivers," *IEEE/OSA Journal of Lightwave Technology*, vol. 27, no. 16, pp. 3614–3622, 2009.

[110] B. Spinnler, "Equalizer Design and Complexity for Digital Coherent Receiver," *IEEE Journal of Selected Topics in Quantum Electronics*, vol. 16, no. 5, pp. 1180–1192, 2010.

[111] L. K. Rabiner and B. Gold, *Theory and Application of Digital Signal Processing*. Englewood Cliffs: Prentice-Hall, 1975.

[112] R. Crochier and L. Rabiner, *Multirate Digital Signal Processing*. Englewood Cliffs: Prentice-Hall, 1983.

[113] A. Oppenheim and R. Schafer, *Discrete-Time Signal Processing*. Upper Saddle River: Prentice-Hall, 1989.

[114] J. J. Shynk, "Frequency-domain and multi-rate adaptive filtering," *IEEE Signal Processing Magazine*, vol. 9, no. 1, pp. 14–37, 1992.

[115] P. P. Vaidyanathen, *Multirate Systems and Filter Banks*. Prentice-Hall, 1993.

[116] N. J. Fliege, *Multirate Digital Signal Processing*. JohnWiley and Sons, 1994.

[117] K. P. Ho, "Subband equalizer for chromatic dispersion of optical fibre," *IEEE Electronics Letters*, vol. 45, no. 24, 2009.

[118] J. G. Proakis, *Digital Communications*. 3rd ed. New York: McGraw-Hill, 1995.

[119] R. D. Gitlin and S. B. Weinstein, "Fractionally spaced equalization: An improved digital transversal equalizer," *Bell System Technical Journal*, vol. 60, no. 2, pp. 275–296, February 1981.

[120] G. Ungerboeck, "Fractional tap-spacing equalizer and consequences for clock recovery in data modems," *IEEE Transactions on Communication*, vol. COM-24, no. 8, pp. 856–864, August 1976.

[121] S. Qureshi, "Adaptive equalization," *Proceedings of the IEEE*, vol. 73, no. 9, pp. 1349–1387, September 1985.

[122] J. H. Winters, "Equalization in coherent lightwave systems using a fractionally spaced equalizer," *IEEE/OSA Journal of Lightwave Technology*, vol. 8, no. 10, pp. 1487–1491, 1990.

[123] S. Tsukamoto, K. Katoh, , and K. Kikuchi, "Unrepeated transmission of 20-Gb/s optical quadrature phase-shift-keying signal over 200-km standard single-mode fiber based on digital processing of homodyne-detected signal for group-velocity dispersion compensation," *IEEE Photonics Technology Letters*, vol. 18, no. 9, pp. 1016–1018, 2006.

[124] ——, "Coherent demodulation of optical multilevel phase-shift-keying signals using homodyne detection and digital signal processing," *IEEE Photonics Technology Letters*, vol. 18, no. 10, pp. 1131–1133, May 2006.

[125] M. G. Taylor, "Coherent detection method using DSP for demodulation of signal and subsequent equalization of propagation impairments," *IEEE Photonics Technology Letters*, vol. 16, no. 2, pp. 674–676, February 2004.

[126] G. Ungerboeck, "Adaptive Maximum-Likelihood Receiver for Carrier-Modulated Data Transmission Systems," *IEEE Transactions on Communications*, vol. 22, no. 5, pp. 624–636, 1974.

[127] A. Carena, V. Curri, R. Gaudino, P. A. P. P. Poggiolini, and S. A. B. S. Benedettok, "A time-domain optical transmission system simulation package accounting for nonlinear and polarization-related effects in fiber," *IEEE Journal on Selected Areas in Communications*, vol. 15, no. 4, pp. 751–765, 1997.

[128] J. G. Proakis and D. K. Manolakis, *Digital Signal Processing: principles, algorithms and applications*, 4th ed. Prentice Hall, 2006.

[129] N. Benvenuto and G. Cherubini, *Algorithms for Communications Systems and their Applications*. John Wiley and Sons, 2005.

[130] D. Falconer, S. L. Ariyavisitakul, A. Benyamin-Seeyar, and B. Edison, "Frequency domain equalization for single-carrier broadband wireless systems," *IEEE Communications Magazine*, vol. 40, no. 4, pp. 58–66, 2002.

[131] K. Takeda, Y. Kojima, and F. Adachi, "Performance comparison between CDTD and STTD for DS-CDMA/MMSE-FDE with frequency-domain ICI cancellation," *IEEE Communications Magazine*, vol. 92, no. 9, pp. 2882–2890, 2009.

[132] D. Lowe and X. Huang, "Adaptive overlap-add equalization for MB-OFDM ultra-wideband," in *IEEE International Symposium on Communications and Information Technologies*, 2006, pp. 664–648.

[133] M. V. Clark, "Adaptive frequency-domain equalisation and diversity combining for broadband wireless communications," *IEEE Journal on Selected Areas in Communications*, vol. 16, no. 8, pp. 1385–1395, 1998.

[134] K. Ishihara, Y. Takatori, S. Kubota, and M. Umehira, "Comparison of SCFDE and OFDM with adaptive modulation and coding in nonlinear fading channel," *Electronics Letters*, vol. 43, no. 3, pp. 174–175, 2007.

[135] K. Ishihara, T. Kobayashi, R. Kudo, Y. Takatori, A. Sano, and Y. Miyamoto, "Frequency-domain equalization for coherent optical single-carrier transmission systems," *IEICE Transactions on Communications*, vol. E92-B, no. 12, pp. 3736–3743, 2009.

[136] I. Martoyo, T. Weiss, F. Capar, and F. Jondral, "Low complexity CDMA downlink receiver based on frequency domain equalization," in *Proc. IEEE Vehicular Technology Conference (VTC 2003-Fall)*, 2003.

[137] M. Vetterli and H. J. Nussbaumer, "Simple FFT and DCT algorithms with reduced number of operations," *Elsevier Science Publishers in Signal Processing*, vol. 6, pp. 267–278, 1984.

[138] I. Slim, L. G. Baltar, A. Mezghani, F. N. Hauske, and J. A. Nossek, "Modified DFT Filter Bank with One-tap per Subchannel Equalizer for Frequency Domain Chromatic Dispersion Compensation," in *Conference Photonische Netze - 13. ITG-Fachtagung*, May 2012.

[139] I. Slim, A. Mezghani, L. G. Baltar, J. A. Nossek, F. N. Hauske, and F. Pittala, *Method for digitally compensating a phase response of an optical channel*, Int. Publ. Numb. WO 2013/139395 A1.

[140] I. Slim, A. Mezghani, L. G. Baltar, J. Qi, F. N. Hauske, and J. A. Nossek, "Delayed Single-tap Frequency Domain Chromatic Dispersion Compensation," *IEEE Photonics Technology Letters*, vol. 25, no. 2, pp. 167–170, January 2013.

[141] ——, "Delayed Single-tap Subband Processing for Chromatic Dispersion Compensation," in *Proc. Signal Processing in Photonic Communications (SppCom 2013)*, 2013, paper SPM2E.6.

[142] S. R. Searle, *Matrix Algebra Useful for Statistics*. John Wiley and Sons, 1982.

[143] J. X. Cai, Y. Cai, C. R. Davidson, D. Foursa, A. Lucero, O. Sinkin, W. Patterson, A. Pilipetskii, G. Mohs, and N. S. Bergano, "Transmission of 96x100G prefiltered PDM-RZ-QPSK channels with 300efficiency over 4368 km," in *Proc. Optical Fiber Communication Conference (OFC 2010)*, March 2010.

[144] M. Salsi, C. Koebele, P. Tran, H. Mardoyan, E. Dutisseuil, J. Renaudier, M. Bigot-Astruc, L. Provost, S. Richard, and P. Sillard, "Transmission of 96x100G pre-filtered with 23spectral engineering," in *Proc. Optical Fiber Communication Conference (OFC 2011)*, 2011.

[145] C. Xie, G. Raybon, and P. J. Winzer, "Hybrid 224-Gbit/s and 112 Gb/s PDM-QPSK transmission at 50-GHz channel spacing over 1200-km dispersion managed LEAF spans and 3 ROADMs," in *Proc. Optical Fiber Communication Conference (OFC 2011)*, 2011.

[146] R. Schomogrow, S. Ben-Ezra, P. C. Schindler, B. Nebendahl, C. Koos, W. Freude, and J. Leuthold, "Pulse-Shaping with Digital, Electrical, and Optical Filters-A Comparison," *IEEE/OSA Journal of Lightwave Technology*, vol. 31, no. 15, pp. 2570–2577, August 2013.

[147] B. Chatelian, C. Laperle, K. Roberts, X. Xu, and M. Chagnon, "Optimized pulse shaping for inta-channel non-linearities mitigation in a 10 GBaud dual-polarization 16-QAM system," in *Proc. Optical Fiber Communication Conference (OFC 2011)*, 2011.

[148] G. Bosco, "Spectral shaping in ultra-dense WDM systems: Optical vs. electrical approaches," in *Proc. Optical Fiber Communication Conference (OFC 2011)*, 2012.

[149] M. Yan, Z. Tao, W. Yan, L. Li, T. Hoshida, and J. C. Rasmussen, "Intercarrier interference suppression in No-Gaurd-Interval Orthogonal-Frequency-Division-Multiplexing Systems," *IEEE Photonics Technology Letters*, vol. 24, no. 7, pp. 563–565, April 2012.

[150] A. I. Perez-Neira, M. Caus, R. Zakaria, D. L. Ruyet, E. Kofidis, M. Haardt, X. Mestre, and Y. Cheng, "MIMO Signal Processing in Offset-QAM Based Filter Bank Multicarrier Systems," *IEEE Transactions on Signal Processing*, vol. 64, no. 21, pp. 5733–5762, 2016.

[151] T. Ihalainen, A. Ikhlef, J. Louveaux, and M. Renfors, "Channel Equalization for Multi-Antenna FBMC/OQAM Receivers," *IEEE Transactions on Vehicular Technology*, vol. 60, no. 5, pp. 2070– 2085, 2011.

[152] H. Saeedi-Sourck, Y. Wu, J. W. M. Bergmans, S. Sadri, and B. Farhang-Boroujeny, "Complexity and Performance Comparison of Filter Bank Multicarrier and OFDM in Uplink of Multicarrier Multiple Access Networks," *IEEE Transactions on Signal Processing*, vol. 59, no. 4, pp. 1907–1912, 2011.

[153] D. Mattera, M. Tanda, and M. Bellanger, "Performance Analysis of the Frequency-Despreading Structure for OFDM/OQAM Systems," in *IEEE Proc. Semiannual Vehicular Technology Conference (VTC 2013-Spring)*, vol. 3, 2013, pp. 1581–1585.

[154] D. Waldhauser, L. Baltar, and J. A. Nossek, "MMSE subcarrier equalization for filter bank based multicarrier systems," in *IEEE Proc. Signal Processing Advances in Wireless Communications (SPAWC 2008)*, 2008.

[155] H. Bölcskei, P. Duhamel, and R. Hleiss, "Design of pulse shaping OFDM/OQAM systems for high data-rate transmission over wireless channels," in *IEEE Proc. International Conference on Communications (ICC 1999)*, vol. 1, 1999, pp. 559–564.

[156] P. Achaichia, M. L. Bot, and P. Siohan, "OFDM/OQAM: A Solution to Efficiently Increase the Capacity of Future PLC Networks," *IEEE Transactions on Power Delivery*, vol. 26, no. 4, pp. 2443–2455, 2011.

[157] J. Javaudin, D. Lacroix, and A. Rouxel, "Pilot-aided channel estimation for OFDM/OQAM," in *IEEE Proc. Semiannual Vehicular Technology Conference (VTC 2003-Spring)*, vol. 3, 2003, pp. 1581–1585.

[158] M. E. Tabach, P. Tortelier, R. Pyndiah, and O. Bouchet, "Modified OFDM/OQAM for Personal Optical Wireless with Direct Detection," in *Information and Communication Technologies: From Theory to Applications (ICTTA 2008)*, 2008.

[159] ——, "Diffuse Infrared Personal optical wireless based on modified OFDM/OQAM," in *Proc. International Symposium on Communication Systems, Networks and Digital Signal Processing (CSNDSP 2008)*, 2008, pp. 161–164.

[160] M. G. Bellanger, G. Bonnerot, and M. Coudreuse, "Digital Filtering by polyphase network: Application to sample-rate alteration and filter banks," *IEEE Transactions on Acoustics, Speech, and Signal Processing*, vol. 24, no. 2, pp. 109–114, April 1976.

[161] M. G. Bellanger and J. L. Daguet, "TDM-FDM Transmultiplexer: Digital Polyphase and FFT," *IEEE Transactions on Communications*, vol. 22, no. 9, pp. 1199–1205, September 1974.

[162] P. P. Vaidyanathen and S. K. Mitra, "Polyphase Networks, Block Digital Filtering LPTV Systems, and Alias-Free QMF Bank: A unified approach based on Pseudocirculants," *IEEE Transactions on Acoustics, Speech, and Signal Processing*, vol. 36, pp. 381–391, March 1988.

[163] H. S. Malvar, "Extended Lapped Transforms: properties, applications, and fast algorithms," *IEEE Transactions on Signal Processing*, vol. 40, no. 11, pp. 2703–2714, November 1992.

[164] ——, *Signal Processing with Lapped Transforms*. Artech House, 1992.